ADVANCES IN POLYMER SCIENCE 227

Volume Editors A.H.E. Müller · H.-W. Schmidt

Complex Macromolecular Systems I

Springer

227

Advances in Polymer Science

Advances in Polymer Science

Recently Published and Forthcoming Volumes

Complex Macromolecular Systems II
Volume Editors: Müller, A.H.E., Schmidt, H.-W.
Vol. 228, 2010

Complex Macromolecular Systems I
Volume Editors: Müller, A.H.E., Schmidt, H.-W.
Vol. 227, 2010

Shape-Memory Polymers
Volume Editor: Lendlein, A.
Vol. 226, 2010

Polymer Libraries
Volume Editors: Meier, M.A.R., Webster, D.C.
Vol. 225, 2010

Polymer Membranes/Biomembranes
Volume Editors: Meier, W.P., Knoll, W.
Vol. 224, 2010

Organic Electronics
Volume Editors: Meller, G., Grasser, T.
Vol. 223, 2010

Inclusion Polymers
Volume Editor: Wenz, G.
Vol. 222, 2009

Advanced Computer Simulation Approaches for Soft Matter Sciences III
Volume Editors: Holm, C., Kremer, K.
Vol. 221, 2009

Self-Assembled Nanomaterials II
Nanotubes
Volume Editor: Shimizu, T.
Vol. 220, 2008

Self-Assembled Nanomaterials I
Nanofibers
Volume Editor: Shimizu, T.
Vol. 219, 2008

Interfacial Processes and Molecular Aggregation of Surfactants
Volume Editor: Narayanan, R.
Vol. 218, 2008

New Frontiers in Polymer Synthesis
Volume Editor: Kobayashi, S.
Vol. 217, 2008

Polymers for Fuel Cells II
Volume Editor: Scherer, G.G.
Vol. 216, 2008

Polymers for Fuel Cells I
Volume Editor: Scherer, G.G.
Vol. 215, 2008

Photoresponsive Polymers II
Volume Editors: Marder, S.R., Lee, K.-S.
Vol. 214, 2008

Photoresponsive Polymers I
Volume Editors: Marder, S.R., Lee, K.-S.
Vol. 213, 2008

Polyfluorenes
Volume Editors: Scherf, U., Neher, D.
Vol. 212, 2008

Chromatography for Sustainable Polymeric Materials
Renewable, Degradable and Recyclable
Volume Editors: Albertsson, A.-C., Hakkarainen, M.
Vol. 211, 2008

Wax Crystal Control · Nanocomposites Stimuli-Responsive Polymers
Vol. 210, 2008

Functional Materials and Biomaterials
Vol. 209, 2007

Phase-Separated Interpenetrating Polymer Networks
Authors: Lipatov, Y.S., Alekseeva, T.
Vol. 208, 2007

Hydrogen Bonded Polymers
Volume Editor: Binder, W.
Vol. 207, 2007

Oligomers · Polymer Composites Molecular Imprinting
Vol. 206, 2007

Polysaccharides II
Volume Editor: Klemm, D.
Vol. 205, 2006

Neodymium Based Ziegler Catalysts – Fundamental Chemistry
Volume Editor: Nuyken, O.
Vol. 204, 2006

Complex Macromolecular Systems I

Volume Editors: Axel H.E. Müller
Hans-Werner Schmidt

With contributions by

V. Altstädt · A. Böker · H.R. Brand · A. Fery
P. Gutmann · A. Horn · W. Köhler · G. Krausch
A. Krekhov · A.H.E. Müller · V. Olszowka · H. Ruckdäschel
H. Schmalz · K. Schmidt · H.G. Schoberth · A. Schweikart
G.J.A. Sevink · D. Svenšek · L. Tsarkova · W. Zimmermann

Springer

Editors
Prof. Axel H.E. Müller
Universität Bayreuth
Lehrstuhl für Makromolekulare Chemie II
Universitätsstr. 30
95440 Bayreuth
Germany
axel.mueller@uni-bayreuth.de

Prof. Hans-Werner Schmidt
Universität Bayreuth
Lehrstuhl für Makromolekulare Chemie I
Universitätsstr. 30
95440 Bayreuth
Germany
hans-werner.schmidt@uni-bayreuth.de

ISSN 0065-3195 e-ISSN 1436-5030
ISBN 978-3-642-12875-2 e-ISBN 978-3-642-12876-9
DOI 10.1007/978-3-642-12876-9
Springer Heidelberg Dordrecht London New York

Library of Congress Control Number: 2010926686

Cover design: WMXDesign GmbH, Heidelberg

Printed on acid-free paper

Springer is part of Springer Science+Business Media (www.springer.com)

Volume Editors

Prof. Axel H.E. Müller

Universität Bayreuth
Lehrstuhl für Makromolekulare Chemie II
Universitätsstr. 30
95440 Bayreuth
Germany
axel.mueller@uni-bayreuth.de

Prof. Hans-Werner Schmidt

Universität Bayreuth
Lehrstuhl für Makromolekulare Chemie I
Universitätsstr. 30
95440 Bayreuth
Germany
hans-werner.schmidt@uni-bayreuth.de

Editorial Board

Advances in Polymer Sciences Also Available Electronically

Advances in Polymer Sciences is included in Springer's eBook package *Chemistry and Materials Science*. If a library does not opt for the whole package the book series may be bought on a subscription basis. Also, all back volumes are available electronically.

For all customers who have a standing order to the print version of *Advances in Polymer Sciences*, we offer the electronic version via SpringerLink free of charge.

If you do not have access, you can still view the table of contents of each volume and the abstract of each article by going to the SpringerLink homepage, clicking on "Browse by Online Libraries", then "Chemical Sciences", and finally choose *Advances in Polymer Science*.

You will find information about the

- Editorial Board
- Aims and Scope
- Instructions for Authors
- Sample Contribution

at springer.com using the search function by typing in *Advances in Polymer Sciences*.

Color figures are published in full color in the electronic version on SpringerLink.

Aims and Scope

The series *Advances in Polymer Science* presents critical reviews of the present and future trends in polymer and biopolymer science including chemistry, physical chemistry, physics and material science. It is addressed to all scientists at universities and in industry who wish to keep abreast of advances in the topics covered.

Review articles for the topical volumes are invited by the volume editors. As a rule, single contributions are also specially commissioned. The editors and publishers will, however, always be pleased to receive suggestions and supplementary information. Papers are accepted for *Advances in Polymer Science* in English.

In references *Advances in Polymer Sciences* is abbreviated as *Adv Polym Sci* and is cited as a journal.

Special volumes are edited by well known guest editors who invite reputed authors for the review articles in their volumes.

Impact Factor in 2008: 6.802; Section “Polymer Science”: Rank 2 of 73

Preface

A promising approach and ongoing challenge in macromolecular science exploits the formation of complex ordered structures by (macro)molecular self-assembly. The various examples of biomacromolecules in nature impressively demonstrate how a well-defined primary molecular structure can lead to a rich complexity of structure and function on a hierarchy of different length scales. Our growing ability to control molecular structures in synthetic macromolecules opens new pathways toward novel complex macromolecular architectures, where hierarchical organization and long-range interactions enable to design new functions and tailor physical and chemical properties. The combination and interplay of these well-balanced "internal fields" with "external fields" such as mechanical, electrical, magnetic, electromagnetic, and/or the interactions with surfaces are a powerful tool to create defect-free and perfectly ordered macromolecular structures on a macroscopic scale, leading to new material properties, processes, and applications.

Therefore, the scientific understanding, control and manipulation of macromolecules, and the implementation in devices and applications of higher complexity are of critical importance for advances and breakthroughs of emerging technologies. Complex macromolecular systems play a key role in technology areas such as the generation, conversion, storage, and conservation of energy, organic electronics, photonics, information storage, and communication and display technology.

Within this context, the German Research Foundation (Deutsche Forschungsgemeinschaft) established in 1998 at the University of Bayreuth the Collaborative Research Centre (Sonderforschungsbereich) SFB 481 on *Complex Macromolecular and Hybrid Systems in Internal and External Fields*. The basis for this Collaborative Research Centre was the long-term interdisciplinary research focus on "Macromolecular and Colloid Research" at the University of Bayreuth. This focus included research groups from macromolecular chemistry, physical chemistry, experimental physics, theoretical physics, and materials science & engineering. After a maximal funding period of 12 years, members of SFB 481 now present highlights of their scientific achievements in the form of review articles in Volumes 227 and 228 of *Advances in Polymer Science*.

The first volume contains review articles on electric field-induced effects on block copolymer microdomains (by H. Schoberth, V. Olszowka, K. Schmidt, and A. Böker); on experiments and simulations of the nanopattern evolution in block

copolymer thin films (by L. Tsarkova, G.J.A. Sevink, and G. Krausch); on non-lithographic approaches for topographical structuring of polymer surfaces utilizing external mechanical fields and buckling instabilities (by A. Schweikart, A. Horn, A. Böker, and A. Fery); on a generalization of the usual hydrodynamic description of destabilization and reorientation of layered systems under shear flow (by D. Svenšek and H.R. Brand); on the thermal diffusion in polymer blends, focusing on experimental and theoretical investigations on the patterning and structure formation processes (by W. Köhler, W. Zimmermann, and A. Krekhov); and on foaming of polymer blends, microstructured and nanostructured by triblock terpolymers (by H. Ruckdäschel, P. Gutmann, V. Altstädt, H. Schmalz, and A.H.E. Müller).

The second volume provides review articles on recent advances in polyelectrolyte stars and cylindrical brushes (by Y. Xu, F. Plamper, M. Ballauff, and A.H.E. Müller); on various aspects of interfacial self-assembly of nanoparticles in liquid–liquid interfaces and in block copolymers (by N. Popp, S. Kutuzov, and A. Böker); on the materials development and photophysics of azobenzene-containing block copolymers as potential media for reversible volume holographic data storage and azobenzene-containing molecular glasses for the controlled formation of surface relief gratings (by H. Audorff, K. Kreger, R. Walker, D. Haarer, L. Kador, and H.-W. Schmidt); on donor–acceptor block copolymers with nanoscale morphology for photovoltaic applications (by M. Sommer, S. Hüttner, and M. Thelakkat); and on recent advances in the improvement of polymer electret films with potential applications in microphones, sensor devices, electret filters, and in energy-harvesting devices (by D.P. Erhard, D. Lovera, C. von Salis-Soglio, R. Giesa, V. Altstädt, and H.-W. Schmidt).

On behalf of all members of the Collaborative Research Centre 481 on *Complex Macromolecular and Hybrid Systems in Internal and External Fields*, we wish to thank the Deutsche Forschungsgemeinschaft for financial and administrative support, the voluntary reviewers of the proposals for their invaluable judgment and advice, the Bavarian State Ministry of Sciences, Research and the Arts, and the University of Bayreuth for their ongoing support to continuously develop and strengthen the interdisciplinary research focus on "Macromolecular and Colloid Research" at the University of Bayreuth. Undoubtedly, all of these measures helped to advance the impact and international visibility.

Bayreuth, April 2010

Hans-Werner Schmidt
Axel Müller

The authors would like to dedicate these two volumes of Advances in Polymer Science to their colleagues and friends, Prof. Raimund Stadler and Prof. Lorenz Kramer, members of this Collaborative Research Centre, who passed away much too early. Their scientific vision and inspiring research had a great impact on progress and success of this Collaborative Research Centre.

Contents

Adv Polym Sci (2010) 227: 1–31
DOI:10.1007/12_2010_51

Published online: 25 March 2010

Effects of Electric Fields on Block Copolymer Nanostructures

Heiko G. Schoberth, Violetta Olszowka, Kristin Schmidt, and Alexander Böker

Abstract In this chapter we overview electric-field-induced effects on block copolymer microdomains. First, we will consider the thin film behavior and elucidate the parameters governing electric-field-induced alignment. We describe the structural evolution of the alignment in an electric field via quasi in situ scanning force microscopy (SFM) using a newly developed SFM setup that allows solvent vapor treatment in the presence of high electric fields. Second, we will turn to bulk structures and show novel effects of high field strengths on the block copolymer phase behavior. We will describe a procedure that allows tuning the morphology and size of the nanoscopic patterns by application of high electric fields and present experimental evidence for the electric-field-induced decrease of the order–disorder transition temperature in a block copolymer.

Keywords Electric field · Block copolymers · Microdomain orientation · In situ SFM · Orientation mechanism

Contents

H.G. Schoberth, V. Olszowka, and K. Schmidt
Lehrstuhl für Physikalische Chemie II, Universität Bayreuth, 95440 Bayreuth, Germany
e-mail: heiko.schoberth@uni-bayreuth.de; violetta.olszowka@uni-bayreuth.de; kristin.schmidt@uni-bayreuth.de

A. Böker (✉)
Lehrstuhl für Makromolekulare Materialien und Oberflächen and DWI an der RWTH Aachen e.V., RWTH Aachen University, 52056 Aachen, Germany
and
Lehrstuhl für Physikalische Chemie II, Universität Bayreuth, 95440 Bayreuth, Germany
e-mail: boeker@dwi.rwth-aachen.de

Abbreviations

1D	One-dimensional
2D	Two-dimensional
CCD	Charge-coupled device
E	Electric field
F	Free energy
M_n	Number-average molecular weight
M_w	Weight-average molecular weight
ODT	Order–disorder transition
P_2	Orientational order parameter
PHEMA	Poly(2-hydroxyethyl methacrylate)
PI	Polyisoprene
PMMA	Poly(methyl methacrylate)
PS	Polystyrene
PVP	Poly(2-vinyl pyridine)
$S_{47}H_{10}M_{43}$ [82]	Polystyrene-*block*-poly (2-hydroxyethyl methacrylate)-*block*-poly(methyl methacrylate)
$S_{50}V_{50}$ [78]	Polystyrene-*block*-poly(2-vinyl pyridine)
SAXS	Small-angle X-ray scattering
SFM	Scanning force microscopy
SI	Polystyrene-*block*-polyisoprene diblock copolymer
TEM	Transmission electron microscopy
THF	Tetrahydrofuran
T_{ODT}	Order–disorder transition temperature

1 Introduction

Block copolymers are ideal candidates for the structuring of surfaces on the nanometer scale because they form highly regular microdomain structures via self-assembly (in the order of some tens of nanometers) both in bulk as well as in thin films. Unfortunately, these microdomains only exhibit short-range order within a grain and it is still a challenge to align the microdomains in such a way as to yield macroscopic orientation or even a single domain structure. Various methods have been devised to induce long-range orientation and order in thin block

copolymer films. External fields such as shear fields [1, 2], temperature gradients [3], selective solvent evaporation [4], directional solidification [5], or graphoepitaxy [6] have been employed successfully. In addition, the large potential of electric fields for the generation of in-plane and out-of-plane alignment of block copolymer microdomains has been shown [7–10].

This chapter deals with the behavior of block copolymer nanostructures subjected to electric fields. We will consider the thin film behavior, elucidate the parameters governing the electric-field-induced alignment, and finally turn to bulk structures and show novel effects of high field strengths on block copolymer phase behavior.

2 Control of Orientational Order in Thin Films

First, we turn to the electric field strength at which interfacial interactions are overcome, allowing the microdomains to orient along the electric field vector [11–15]. This field strength is known as the threshold electric field strength, E_{thresh}, and can be described with respect to the difference between the interfacial energy of each block with the substrate, $\Delta\gamma$, the static dielectric constants of the respective blocks, ε_A and ε_B, and the film thickness, d [15, 16]:

$$E_{\text{thresh}} = \Delta\gamma^{1/2} \frac{2(\varepsilon_A + \varepsilon_B)^{1/2}}{\varepsilon_A - \varepsilon_B} d^{-1/2}. \tag{1}$$

From (1) it can be seen that a small film thickness, a large $\Delta\gamma$ and a small dielectric contrast between the blocks, $\Delta\varepsilon$ (given by $\varepsilon_A - \varepsilon_B$), lead to an increase of E_{thresh}. In order to decide whether a given block copolymer system can be aligned using an electric field, many tedious and time-consuming experiments are usually required to determine a minimum field strength at which the nanostructure orients in the applied field. The same holds true for the maximum possible degree of order in the aligned thin films. In this chapter, we demonstrate a combinatorial approach allowing the simultaneous determination of the above-described parameters in one experiment under constant environmental conditions (e.g., temperature, solvent vapor) by a fixed voltage as a function of the electrode distance.

Two lamellar block copolymers will now be discussed. Polystyrene-*block*-poly(2-hydroxyethyl methacrylate)-*block*-poly(methyl methacrylate) [$S_{47}H_{10}M_{43}^{82}$; consisting of 47 wt% polystyrene (PS), 10 wt% poly(2-hydroxyethyl methacrylate) (PHEMA) and 43 wt% poly(methyl methacrylate) (PMMA) with a total number-average molecular weight (M_n) of 82 kg/mol] and polystyrene-*block*-poly(2-vinyl pyridine) ($S_{50}V_{50}^{78}$; consisting of 50% PS and 50% PVP with M_n of 78 kg/mol) were synthesized by sequential living anionic polymerization as described in detail elsewhere [9, 12, 17]. The static dielectric constants of the PS, PMMA, and PVP were 2.4, 3.6, and 7.5, respectively [18]. Thus, the dielectric contrast $\Delta\varepsilon$ between the respective blocks yields 1.2 for PS/PMMA and 5.1 for PS/PVP. For the electric field studies, films of the respective block copolymers with lamellar orientations

perpendicular to the substrate were prepared as reported earlier. This resulted in film thicknesses (d) of 37 ± 2 nm for $S_{47}H_{10}M_{43}{}^{82}$ and 745 ± 2 nm for $S_{50}V_{50}{}^{78}$ [9, 17, 19].

In order to study the influence of the electric field strength on the degree of alignment, ex situ experiments with gradient gold electrodes on a glass substrate were performed. The electrode distance was chosen as a linear gradient ranging from 5 to 50 µm. The height of the electrodes was around 55 nm (this height corresponds to the film thickness of the $S_{47}H_{10}M_{43}{}^{82}$ block copolymer film swollen during the solvent vapor treatment) [9]. The limited electrode height does not influence the electric-field-induced ordering process due to the dominating in-plane component of the electric field on and between the electrodes, even in the case of films that are significantly thicker than those used here. A schematic of the electrode geometry is shown in Fig. 1. Due to the very small aspect ratio between electrode spacing and the electrode length (6 mm), the electric field can be considered homogeneous. A voltage of either 75 or 150 V was applied, resulting in a field strength gradient of 1.5–30 V/µm.

The microdomain orientation as a function of the electric field strength was monitored by a series of scanning force microscopy (SFM) images taken in the center between the electrodes. The entire electrode length of 6 mm was screened in steps of a few tens of microns. From the azimuthal intensity distribution of the 2D Fourier transformations of the SFM images, the orientational order parameter P_2 was calculated according to:

$$P_2 = \frac{3 < \cos^2 \phi > -1}{2} \tag{2}$$

with

$$< \cos^2 \phi > = \frac{\int_0^{2\pi} \mathrm{d}\phi \left(I_q(\phi) \cdot \cos^2 \phi \cdot |\sin(\phi)| \right)}{\int_0^{2\pi} \mathrm{d}\phi \left(I_q(\phi) \cdot |\sin(\phi)| \right)}. \tag{3}$$

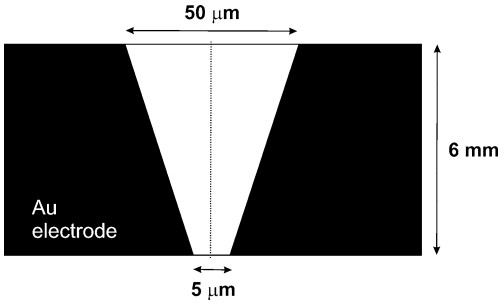

Fig. 1 Top view of gradient electrodes on a glass substrate. The height of the electrodes is 55 nm. The electrode gap is not true to scale and the gradient (5–50 µm) has been exaggerated for clarity. The *dotted line* shows the axis along which the SFM images were taken. Reprinted with permission from Macromolecules [20]. Copyright 2008 American Chemical Society

The angle φ quantifies the in-plane direction, with $\varphi = 0°$ corresponding to the direction along the stripe-like electrodes. For an alignment of the lamellae along the field direction (maximum azimuthal intensity distribution of the 2D Fourier transform intensity at $\varphi = 90°$), P_2 ranges from 0 to -0.5 with $P_2 = -0.5$ corresponding to the fully oriented case.

To achieve in-plane alignment in a lamellar block copolymer thin film, the lamellae have to be oriented perpendicular to the plane of the film in the first place. As we have shown earlier, in the block copolymer system $S_{47}H_{10}M_{43}{}^{82}$ perpendicular alignment of the lamellae is achieved spontaneously at zero electric field [9, 17]. In short, a thin brush layer of the block copolymer is adsorbed onto the (polar) substrate via the PHEMA middle block, resulting in a stripe pattern of the two majority components PS and PMMA. In thicker films, this brush layer seems to serve as a template for perpendicular lamellae [21, 22]. This can be seen in Fig. 2a, which shows SFM images of a thin $S_{47}H_{10}M_{43}{}^{82}$ film annealed for

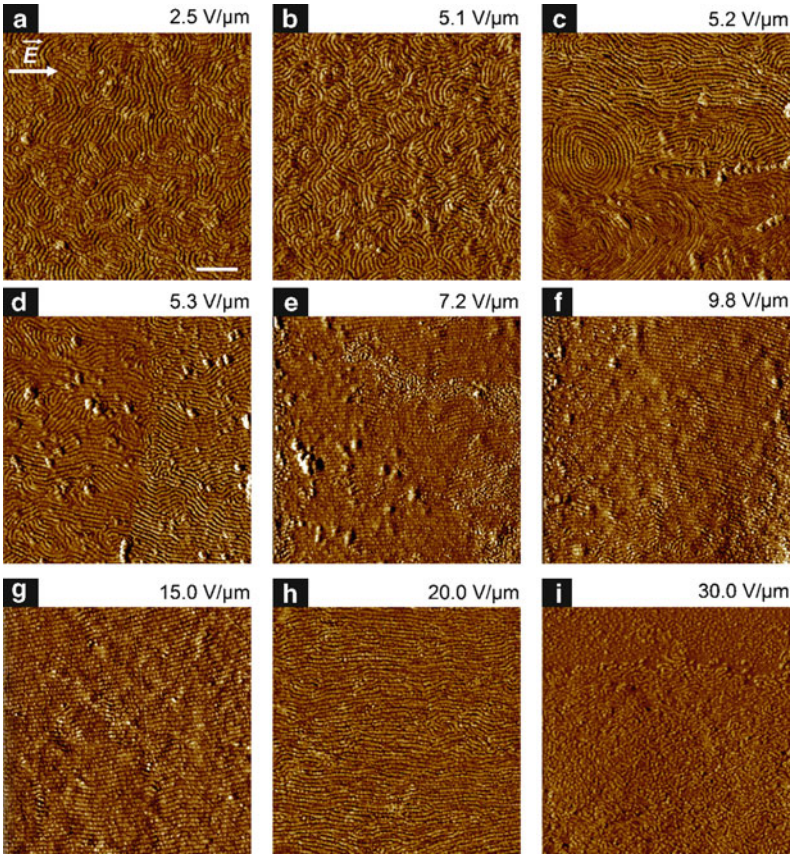

Fig. 2 (**a–i**) Series of SFM phase images (z-range: 0°–10°) of a 39-nm thick $S_{47}H_{10}M_{43}{}^{82}$ film after annealing for 6.5 h in saturated toluene vapor in the gradient electrode setup. The *arrow* in (**a**) indicate the direction of the electric field vector. *Scale bar*: 500 nm. Reprinted with permission from Macromolecules [20]. Copyright 2008 American Chemical Society

6.5 h in saturated toluene vapor at a position between the gradient electrodes with an electric field strength of 2.5 V/μm. The image exhibits a striped surface structure, which can be interpreted as upstanding lamellae. The characteristic lateral spacing amounts to some 55 ± 8 nm, in reasonable agreement with the spacing of 49 ± 6 nm for the dried bulk material [17]. However, the stripe pattern exhibits a large number of defects and does not show any long-range order. Increasing the electric field strength E from 5.1 to 5.2 V/μm yields some grains with a preferred orientation of the lamellae parallel to the electric field vector.

This onset of alignment is not markedly reflected in a decrease of the order parameter, which yields $P_2 = -0.11$ for the image in Fig. 2b and $P_2 = -0.12$ for the image in Fig. 2c (P_2 data are shown in Fig. 3). At a slightly larger electric field strength of 5.3 V/μm (Fig. 2d) the predominant alignment of the lamellae parallel to the electric field vector is found to be more pronounced, which is also reflected in the decrease of P_2 to -0.16, which is about 50% of the value finally achieved in this experiment. Thus, from the SFM images and the onset of the ordering process, the threshold field (E_{thresh}) that is required for parallel alignment of the lamellae of the polymer $S_{47}H_{10}M_{43}{}^{82}$ with respect to the electric field lines (under the given environmental conditions and in the time frame of our experiment) is $5.2 - 5.3$ V/μm. For electric field strengths less than 5.2 V/μm, an alignment of the lamellae parallel to the electric field lines cannot be achieved, even after longer annealing times. Increasing the electric field strength further from 7.2 to 15 V/μm (as shown in Fig. 2e–g), leads to a structure with a rather limited number of defects and a predominant alignment parallel to the electric field lines. This is also reflected in a continuing decrease of P_2 from -0.20 (Fig. 2e and Fig. 3) to -0.31 (Fig. 2g and Fig. 3). We note here that even longer annealing times at $E = 15$ V/μm

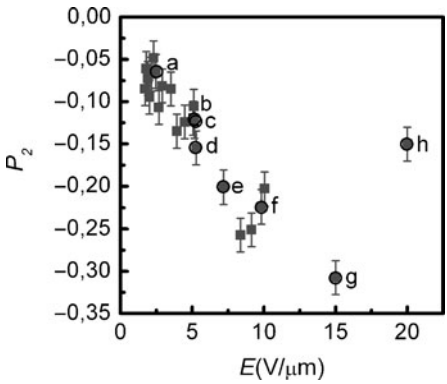

Fig. 3 Evolution of orientational order parameter P_2 at different electrode distances plotted versus the electric field strength E. The *letters* next to the marked values correspond to the SFM images in Fig. 2a–h. The error of P_2 due to inhomogeneities in the film and the phase contrast can be estimated to be about ± 0.02. Reprinted with permission from Macromolecules [20]. Copyright 2008 American Chemical Society

did not improve the orientational order significantly. The block copolymer film was therefore subjected to higher field strengths; however, $20\,\mathrm{V}/\mu\mathrm{m}$ and more lead to a decrease in P_2 to -0.15 (Fig. 2h and Fig. 3).

From the SFM image in Fig. 2h, it is found that the intensity of the phase signal strongly decreases, pointing to changes in the polymeric structure. This observation is supported by the SFM image of the film at $30\,\mathrm{V}/\mu\mathrm{m}$, where severe damage to the film can be seen (Fig. 2i). Moreover, a significant decrease in film thickness is observed with time. In this high voltage range, the electric breakdown voltage has been reached, leading to ionization of the surrounding gas atmosphere, which finally results in the formation of a gas plasma. Thus, we can deduce that the film is ablated by a plasma etching process. As a result, besides the threshold field, an upper limit of the field strengths in the range of 20–$30\,\mathrm{V}/\mu\mathrm{m}$ can also be identified. The fact that the ideal value of $P_2 = -0.5$, describing perfect alignment, is not reached during the experiments can be explained as follows: From a technical point of view, the low contrast ratio between the different polymer phases in the raw data leads to a rather noisy Fourier spectrum, which deteriorates the numerical value of P_2. In addition, we note that the value of P_2 is similar to those determined for bulk solutions of the same polymer via real-time small-angle X-ray scattering (SAXS) measurements [11]. This finding points towards a more fundamental reason. Since the electrodynamic driving force scales with $\cos^2\theta$, where θ is the tilt angle of the lamellar normal vector with respect to the electric field vector, the energy gain for improved alignment is expected to continuously decrease as the angle between the lamellae and the electric field direction approaches zero [23]. Therefore, within finite annealing times, no "perfect alignment" is to be expected. The observed limiting value for P_2 is likely to be determined by a combination of the above reasons.

The evolution of the order parameter as a function of the electric field strength (as plotted in Fig. 3) shows a linear dependence up to the onset of polymer decomposition. With increasing electric field strengths the order parameter decreases, i.e., the lamellar structure increasingly aligns parallel to the electric field vector. The difference in the free energy between the aligned and nonaligned state, ΔF, is predicted to be proportional to $[(\varepsilon_\mathrm{A} - \varepsilon_\mathrm{B})^2/(\varepsilon_\mathrm{A} + \varepsilon_\mathrm{B})]E^2$ [23, 24]. However, there is no direct link to the expected degree of order, especially as the electric-field-induced driving force strongly depends on the tilt angle of the lamellar normal vector with respect to the electric field vector, as pointed out above.

In order to demonstrate the applicability of our method to other block copolymer systems, we exposed a thick diblock copolymer film of $S_{50}V_{50}{}^{78}$ with upstanding lamellae (generated by selective solvent vapor treatment in toluene [19]) to an electric field in the same gradient electrode geometry as described above. As the dielectric contrast between the PS and the PVP is larger than that for PS and PMMA, if we consider the dielectric term in (1), a threshold field for $S_{50}V_{50}{}^{78}$ would be expected that is about three times lower than for $S_{47}H_{10}M_{43}{}^{82}$. In addition, according to the larger dielectric contrast between the blocks in $S_{50}V_{50}{}^{78}$ compared to $S_{47}H_{10}M_{43}{}^{82}$, the gain in free energy and thus the electrodynamic driving force is about an order of magnitude larger for the PVP-based block copolymer. Figure 4 shows a series of SFM phase images of a $745 \pm 2 - \mathrm{nm}$ thick $S_{50}V_{50}{}^{78}$ film after

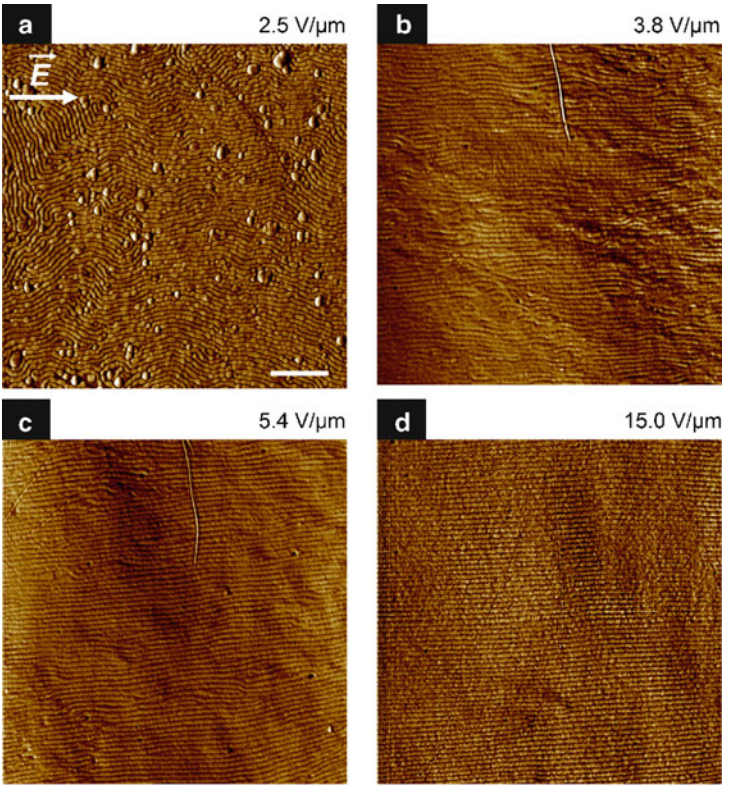

Fig. 4 (**a–d**) Series of SFM phase images (z-range: 0–20°) of a 745 ± 2-nm thick $S_{50}V_{50}$[78] film after annealing for 20 h in saturated toluene vapor in the gradient electrode setup. The *arrow* in (**a**) indicate the direction of the electric field vector. *Scale bar*: 500 nm. Reprinted with permission from Macromolecules [20]. Copyright 2008 American Chemical Society

20 h of annealing with saturated toluene vapor under a gradient electric field. All images reveal a stripe pattern of upstanding lamellae. Even at the largest electrode spacing of the gradient electrode (which corresponds to an electric field strength of 2.5 V/μm) a preferential orientation of the lamellae parallel to the electric field lines is observed (Fig. 4a). Therefore, the threshold electric field strength for the alignment of the lamellae of $S_{50}V_{50}$[78] is smaller than 2.5 V/μm. Larger field strengths lead to a significant increase of the degree of orientation (Fig. 4b–d). At $E = 15$ V/μm, an almost defect-free structure is found (Fig. 4d). These observations are in good agreement with the predictions from theory [15, 23]. Unfortunately, due to the low contrast between the different polymer phases in the raw data of the SFM images, leading to a Fourier spectrum with a low signal-to-noise ratio, a reliable order parameter P_2 could not be determined from the images. However, our data clearly show that by increasing the dielectric contrast of the polymer blocks, a reduced threshold field strength and an improved orientation of the lamellae can be achieved. This valuable information was gained in a single combinatorial

experiment using a gradient electric field setup under constant environmental conditions, thereby establishing an efficient testing method for the processability of various polymer systems with electric fields and their applicability for electric-field-based surface patterning procedures.

3 In Situ Observation of Domain Orientation

The key to an understanding of the orientation behavior of block copolymer microdomains in thin films is knowledge of the underlying microscopic mechanisms that contribute to the rearrangement of domains. Although shear and electric field alignment of block copolymers in bulk have been studied by a variety of different techniques such as in situ birefringence [25], in situ small angle neutron scattering [26], ex situ [27–29] and in situ small-angle scattering (SAXS) [12, 30, 31], little is known about the relevant processes of block copolymer alignment under electric fields in thin films.

We observed the structural evolution of the alignment in an electric field via quasi in situ SFM using a newly developed SFM setup that allows solvent vapor treatment in the presence of high electric fields. Quasi in situ SFM imaging, firstly demonstrated by successive plasma etching of thin polymer films [32], provides the possibility to reposition the SFM probe on a specific sample spot after ex situ treatment with high accuracy with respect to the lateral displacement between tip and sample. This technique allows straightforward examination of the same sample spot prior to and after treatment. Using the above approach, we compared the density of two particular defect types with the evolution of the orientational order parameter during the alignment process. This revealed the essential role of tori defects for the lamella-reorientation mechanism. Further, the quasi in situ technique allowed elucidation of the influence of the electric field strength on the propagation velocity of the topological defects.

For the alignment experiments, gold electrodes were evaporated onto a glass substrate. The electrode distance was chosen as 10 µm. The height of the electrodes was around 55 nm to compensate for swelling of the film in the presence of solvent vapor, allowing the thin film treatment under a homogeneous electric field. A schematic of the electrode geometry is shown in Fig. 5.

The quasi in situ SFM setup utilizes a modified commercial SFM (Dimension 3100 equipped with a NanoScope IV SPM controller and a XY closed-loop scanner, all from Veeco Instruments.). A detailed description of the setup is reported elsewhere [9, 32, 34]. Si_3N_4 cantilevers from Olympus were used (OMCL-AC160TS, spring constant $\sim$40 N/m, resonance frequency 200–300 kHz). All measurements were performed at free amplitudes of about 30–50 nm and a relative set point of about 0.95.

Figure 6 shows a schematic setup and a photograph of the SFM setup. The original sample holder system of the SFM (chuck and chuck-base) was replaced by a special air bearing table, which can be controlled by an external vacuum pump

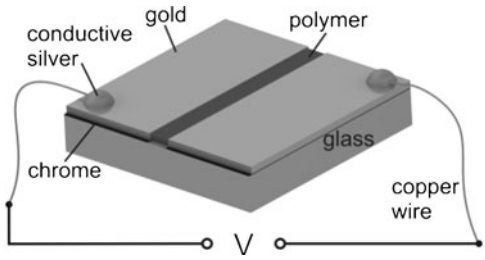

Fig. 5 Schematic of electrodes on a glass substrate. The thickness of the chrome and gold layer $(5 + 50\,\text{nm})$ and the gap between the electrodes $(10\,\mu\text{m})$ are not true to scale. The size of the arrangement (sample size) is about $6 \times 6 \times 1\,\text{mm}^3$. The electric field is homogeneous between the electrodes. Reprinted with permission from [33]. Copyright 2009 American Chemical Society

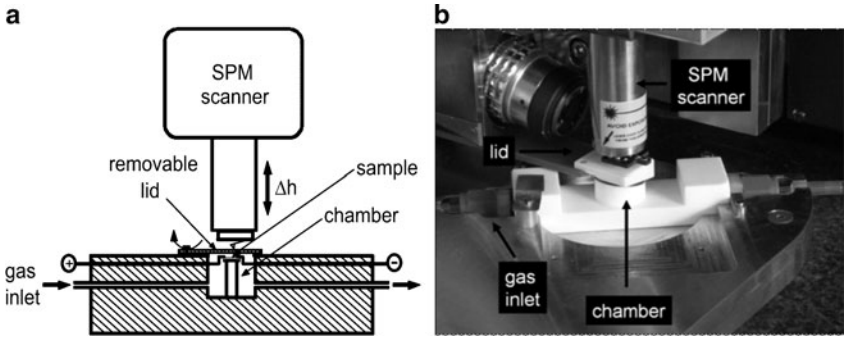

Fig. 6 (**a**) Schematic and (**b**) photograph of the quasi in situ SFM setup. Adapted with permission from Soft Matter [9]. Copyright 2006 Royal Society of Chemistry

in order to fix the table during the experiment. The air bearing table holds a reactor chamber module made of machinable ceramics. The top opening of the reactor chamber can be closed by a moveable lid.

The sample treatment is executed as follows: The sample is located inside the chamber. The SFM scanner is retracted by about 8 mm from the sample. Then the chamber is closed by the lid. In order to anneal the sample successfully, we perform the treatment in a hermetically sealed reactor chamber. The sample is exposed to chloroform vapor while a voltage is applied across the electrodes on the glass substrate. The gas flow rate through the system is controlled by mass flow controllers and additionally checked by a flow meter installed at the outlet of the chamber. After a certain annealing time, the solvent is removed with a flow of pure argon while the voltage is still applied in order to quench the structure in the presence of the electric field. Subsequently the lid is opened, the voltage is switched off, and the SFM scanner is moved towards the sample. This procedure is repeated several times. The accomplishable position stability as a key performance feature of the quasi in situ SFM amounts to almost the same value as reported in [32] (low pressure plasma treatments). The increase in lateral drift is only about 23 nm per process step. The

technical details will be published elsewhere. The SFM tip can easily and reliably be repositioned on a specific sample spot. The scan area $(3 \times 3\,\mu m^2)$ was kept constant during the experiment. In a first post-processing step the remaining lateral offsets between successive SFM images were corrected by maximization of the cross correlation between the images. To reduce nonlinear image distortions the images were then subsequently registered following the method described in [35]. After registration, a smaller detail of each SFM image was cut out to provide a series of images taken at exactly the same spot of the sample (see later for an example). For further details on the experimental setup, refer to [34].

Figure 7a displays a SFM phase image of a spin-coated $S_{47}H_{10}M_{43}{}^{82}$ film that has a disordered surface structure. The ordering effect of the simultaneous solvent vapor annealing and application of a voltage between the electrodes is shown in Fig. 7b. After 6.5 h of treatment the stripe pattern appears highly ordered parallel to the electric field vector. Importantly, during the swelling of the film, the polar middle PHEMA block remains anchored to the substrate. This preserves the self-assembled stripe pattern of the two major PS and PMMA blocks (Fig. 7c).

3.1 Quasi In Situ Imaging

In order to elucidate the mechanism of microdomain alignment, we used the newly developed quasi in situ SFM. Due to the high electric field strength and the sharp SFM tip it is impossible to perform in situ scanning in the presence of the electric field. The electric field would produce SFM artifacts due to additional electrostatic forces between tip and sample. Moreover, the applied voltage can easily damage the piezoelectric scanner by flashovers. Performing ex situ sample treatments with the aim of imaging the same spot on the sample prior to and after annealing would require time-consuming repositioning protocols. This might not be feasible because of rather abrupt changes in the structure during the snapshot treatment in the electric field [36]. With the experimental setup used here we managed to overcome these problems [9].

Our approach is validated by comparison of the treatment time when the sample is treated continuously and step-wise for snapshot imaging. Since in both cases the complete orientation of the stripe pattern along the electric field vector is achieved within 6–7 h, we concluded that the quasi in situ treatment has no significant effect on the mechanism of the microdomain alignment and ordering.

In Fig. 8, the evolution of the initially disordered structure (Fig. 8a) into a highly ordered, defect-free lamellar array (Fig. 8i) is shown as a function of the treatment time. The most representative defects at different time-scales of the structure evolution were identified and quantitatively analyzed. Ring-like defects (tori defects), as well as defect configurations with interrupted continuity of a lamella domain (open-end defects) dominate at the early stage of the orientation process, while only classical topological defects (disclinations and dislocations) are observed at the late stages of the long-range ordering, in agreement with recent observations [37].

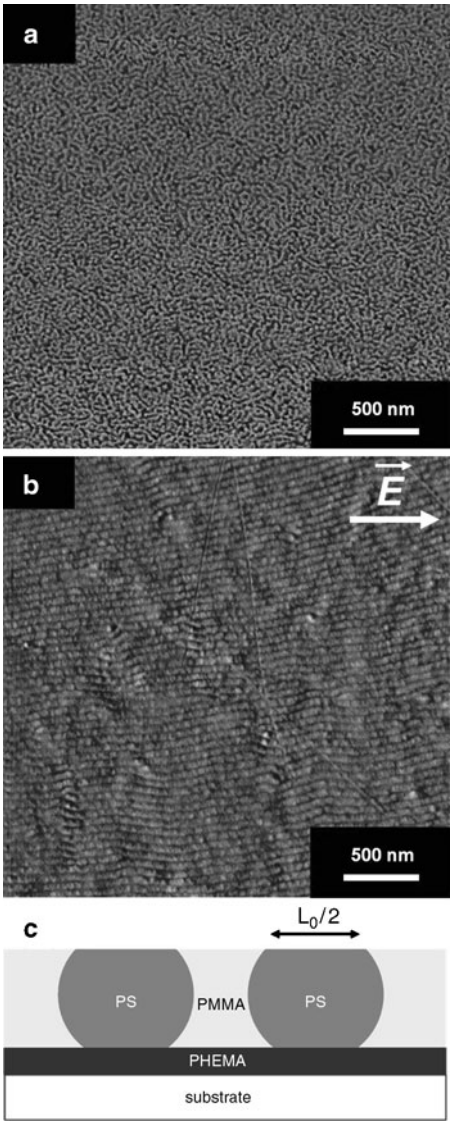

Fig. 7 SFM phase ($\Delta\varphi = 0$–$20°$) images of a 39-nm thick $S_{47}H_{10}M_{43}{}^{82}$ film: (**a**) after spin coating and (**b**) after annealing for 6.5 h in saturated toluene vapor at 15 V/μm. The *arrow* in (**b**) indicate the direction of the electric field vector. (**c**) Microphase-separated structure in an ultrathin ABC block copolymer film with the short middle block selectively anchored to the substrate (adapted from [17]). Reprinted with permission from ACS [33]. Copyright 2009 American Chemical Society

In SFM phase images, the tori are represented by the harder PMMA phase, which thus appears brighter than the PS phase.

Snapshot imaging of the same spot revealed that the lamella alignment proceeds via creation, opening, and joining of tori structures (Fig. 8a–i). When the initially disordered pattern in Fig. 8a is subjected to a 30-min treatment, the tori defects become clearly visible (Fig. 8b). During the next treatment steps, the tori break and open (Fig. 8c–f), and finally merge into straight lamellae (Fig. 8g–i). On the one hand, merged tori form lamellae with the orientation parallel to the electric field

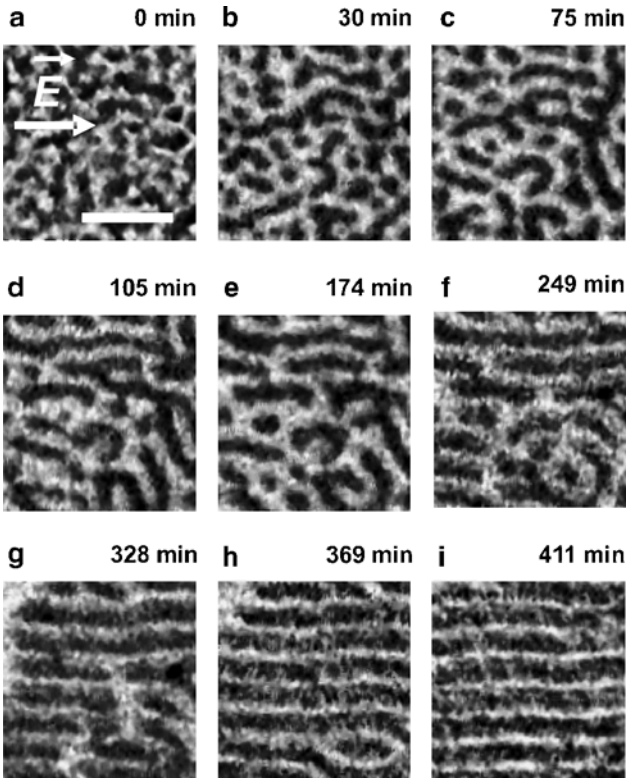

Fig. 8 (**a–i**) Crops $(150 \times 150\,\mathrm{nm}^2)$ from registered SFM phase images illustrating the transition from the disordered structure (**a**) to highly ordered striped pattern (**i**). The *arrow* in (**a**) indicate the direction of the electric field vector. *Scale bar:* 500 nm. The film was annealed in saturated chloroform vapor under an electric field of $15\,\mathrm{V}/\mu\mathrm{m}$ in the quasi in situ SFM chamber. The PMMA phase appears brighter in the images than the PS phase. The raw data were acquired by scanning areas of $3 \times 3\,\mu\mathrm{m}^2$, with 1024×1024 pixels, using TappingMode imaging. Reprinted with permission from ACS [33]. Copyright 2009 American Chemical Society

vector, while on the other hand the merging of tori connects neighboring lamellae that are already oriented along the electric field via bridges (necks) (see for example Fig. 8g). Such bridges allow chain transport in the direction orthogonal to the PS–PMMA interface without crossing it. This kind of point defect was observed in the lyotropic lamellar liquid crystal phase [38, 39], and very recently in cylinder-forming block copolymer films with sufficient chain mobility [37]. After further annealing, the bridges between ordered lamella are annihilated (Fig. 8h).

At the late stage of lamella orientation, classical topological defects (dislocations and disclinations) dominate [40, 41] (Fig. 8h and Fig. 9), and their movement and annihilation can be followed in Fig. 8h–i and Fig. 9. The latter presents an example of the apparent topological defect interactions and their transformations. Displayed are two dislocations of PMMA, which have an attractive interaction due to their opposite core sign. Therefore, in the next annealing step the dislocation is shifted

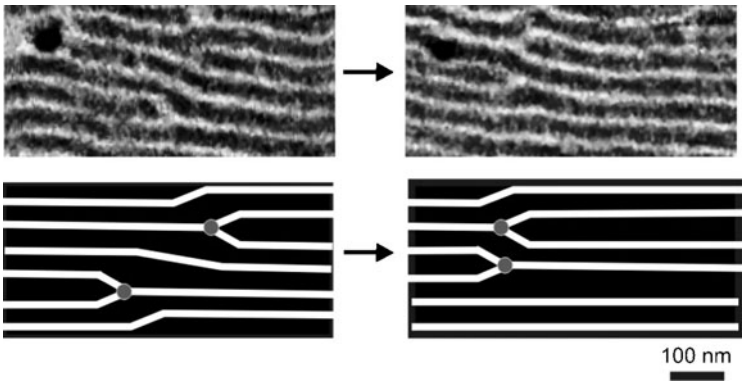

Fig. 9 Details from quasi in situ SFM images showing the interaction of a (−)- and (+)-dislocation of PMMA under an electric field of 15 V/μm. The *lower images* illustrate the movement of the defects visible in the *upper images*. The propagation velocity amounts to 192 ± 5 nm/h. Reprinted with permission from ACS [33]. Copyright 2009 American Chemical Society

one lamella up. The fact that the defects, after the applied snapshot treatment, behave and interact in agreement with what is known about typical defects in block copolymers and in other kinds of soft and solid matter [42, 43] is an additional confirmation that the step-wise annealing does not affect the ordering mechanism.

Important quantitative information regarding the alignment process was gained through detailed analysis of the defect density and of the structure order parameter. Figure 10 shows the defect density of tori and of the open-end defects as a function of time. The data was collected from $3 \times 3\,\mu m^2$ SFM images. After short-term annealing of about 5 min, a similar density of tori and of open-end defects (ca. 60 defects/μm^2) was measured. With further treatment, the number of open-end defects decreased exponentially until they vanished after ∼370 min of the film treatment. In contrast, new tori defects were formed after further annealing, with the density reaching its maximum value of about 110 defects/μm^2 after about 80 min of film treatment. With further annealing and corresponding ordering, the number of tori constantly decreased, and after ∼410 min all tori were annihilated.

The orientational order parameter P_2 was calculated according to (2) and (3) and plotted as a function of time in Fig. 10. The plot shows an almost linear dependence and reaches a constant value of $P_2 = -0.21$ after approximately 320 min of film treatment. Comparison of the time-evolution of the defect density with the evolution of P_2, suggests that open-end defects are quickly annihilated during the alignment process, whereas tori defects are generated to support the orientation process during its early stage. We note that open-end defects are generated as a result of the fast freezing of the structure during sample preparation by spin-coating, and that they are energetically highly unfavorable due to the high local curvature of the interface. As a consequence, in the course of annealing, their density is always smaller than the density of the tori.

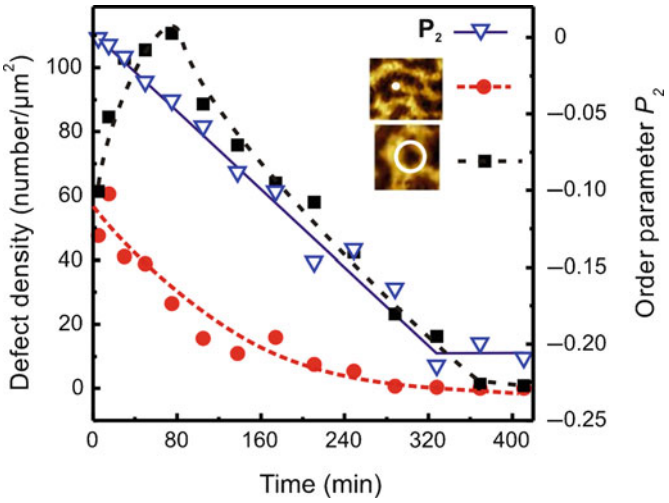

Fig. 10 Time evolution of the defect density (*left-hand axis*) and of the orientational order parameter P_2 (*right-hand axis*) during combined treatment with an electric field and solvent annealing. The *lines* are drawn as guides to the eye. The data was collected from $3 \times 3\,\mu m^2$ SFM images. Reprinted with permission from ACS [33]. Copyright 2009 American Chemical Society

The creation of the tori has the advantage that the polymer chains are able to diffuse along the A–B–C interface. If an electric field is applied, breaking of the tori along the electric field vector is favorable. In order to form a perfectly aligned structure, no translational movement of the center of mass of the tori is required. Simply breaking and merging the tori is sufficient. Thus, such a ring-like structure is an ideal transition state during the reorientation process. Interestingly, similar ring-like defects were previously found in dynamic density functional theory simulations and transmission electron microscopy images of bulk PS-*b*-PHEMA-*b*-PMMA samples oriented from a concentrated solution under an electric field [44, 45]. In addition, the creation of tori was also described in the smectic phase of liquid crystals [46] and in the cylinder phase of block copolymers [37, 47] as a transient excited state.

Finally, we analyzed the velocities of the topological defects during annealing at zero electric field and in the presence of an electric field. Figure 11a, b shows two examples of the propagation of dislocations after annealing in chloroform vapor at zero electric field and subsequent quenching with argon. The defect velocities (v) were calculated via the changes in the *xy*-positions of the white points (marked in the images), and amount to $15 \pm 5\,nm/h$. We note that the displayed dislocations are not surrounded by other defects and therefore any interaction forces can be excluded. When similar isolated defects are subjected to an electric field with a strength of $15\,V/\mu m$ (Fig. 11c–d), a distinct increase in defect velocity is detected. The dislocations in Fig. 11c–d propagate at a velocity of $93 \pm 5\,nm/h$. For comparison, we evaluated the propagation velocity of two dislocations with an opposite sign under an applied electric field of $15\,V/\mu m$ (Fig. 9). Here, the two defects are found to

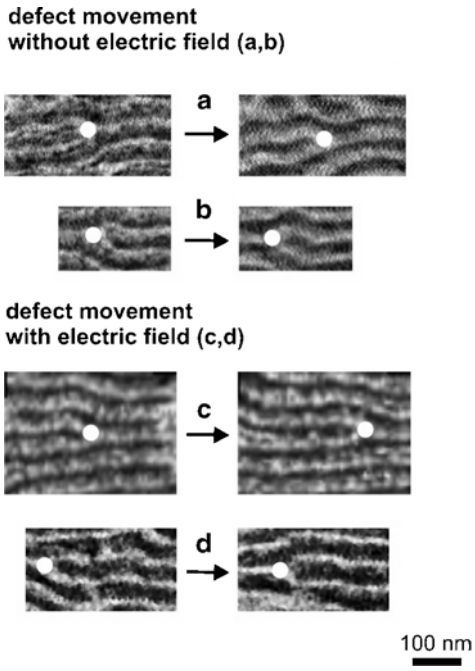

Fig. 11 Propagation of classical defects at zero electric field (**a**, **b**), and at an electric field strength of $15\,\mathrm{V}/\mu\mathrm{m}$ (**c**, **d**). The velocities were calculated via the change in the xy-positions of the *white points* and amount to $15 \pm 5\,\mathrm{nm}/\mathrm{h}$ (**a**, **b**) and $93 \pm 5\,\mathrm{nm}/\mathrm{h}$ (**c**, **d**). Reprinted with permission from ACS [33]. Copyright 2009 American Chemical Society

approach one another with an average velocity of $192 \pm 5\,\mathrm{nm}/\mathrm{h}$. In this case, the velocity of a dislocation in the vicinity of another dislocation with an opposite sign, and thus with an attractive interaction, is about twice as high as the defect velocity of an isolated dislocation.

4 Reversible Tuning of the Domain Spacings

We will now turn to the bulk behavior of block copolymers. In this respect, we will concentrate on the phase behavior of the systems under high electric fields. First, we describe a procedure that allows tuning of the morphology and size of the nanoscopic patterns. In the past, this was typically achieved by changing the molecular weights or the block ratios of the polymers used. However, this only allows control of the characteristic spacing on a coarse scale and precise adjustment of the spacing is impossible. The addition of homopolymer corresponding to one or both of the polymer blocks or the addition of a nonselective solvent have successfully been used to fine-tune block copolymer nanostructures [48–51]. However, exact adjustment to within a percent or so of the characteristic spacing seems barely possible. Moreover, this approach is not reversible.

We have studied three different lamellar polystyrene-*block*-polyisoprene (SI) diblock copolymers (see Table 1) with molecular weights of around 50 kg/mol using

Table 1 Composition and molecular weight of the studied polystyrene-*block*-polyisoprene (SI) copolymers

Polymer	Isoprene volume fraction (%)	Molecular weight (kg/mol)
SI^{51}	48	51
SI^{48}	45	48
SI^{47}	39	47

SAXS at the ID2 beamline at the European Synchrotron Radiation Facility (ESRF, Grenoble, France). The static dielectric constants of the PS and polyisoprene (PI) are 2.4 and 2.1, respectively. The polymers were dissolved in toluene or tetrahydrofuran (THF) with concentrations of 50–57 wt%. The experiments were performed at room temperature in a home-built capacitor with electrode spacing of 1 mm (see Fig. 12). A direct current voltage of up to 10 kV was applied across the electrodes and resulted in a homogeneous electric field, pointing perpendicular to the direction of the X-ray beam, with a maximum strength of 10 kV/mm. The diameter of the X-ray beam was 100 µm. The photon energy was set to 12.5 keV. SAXS patterns were recorded with a 2D camera located at a distance of 10 m from the sample within an evacuated flight tube. The charge-coupled device (CCD) detector can monitor up to 300 frames (1024 × 256 pixels) at a rate of 22 frames/s. The highest resolution of the camera is 2048 × 2048 pixels. Before data analysis, background scattering was subtracted from the data and corrections were made for spatial distortions and for the detector efficiency.

To exclude effects that might arise from the reorientation process itself, all samples were prealigned; therefore most of the lamellae were oriented along the electric field lines. Figure 13a shows the scattering patterns for different electric field strengths. We observed highly anisotropic SAXS patterns at higher electric fields. The position of the first-order Bragg peak is different for lamellae aligned in the field direction and for those perpendicular to the field direction. Figure 13b shows the effect of the electric field strength on the lamellar spacing calculated from the position of the first-order Bragg peak for the lamellae aligned in the field direction (filled circles) and the lamellae aligned perpendicular to the field (open circles). The lamellar distance for the lamellae oriented along the field lines decreases rapidly

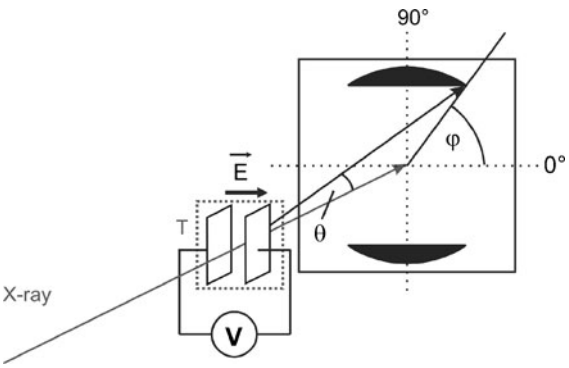

Fig. 12 Experimental setup for the in situ SAXS measurements. Depending on the type of experiments the capacitor, represented by two electrodes, can be temperature-controlled. The X-ray beam penetrates the sample perpendicular to the electric field vector

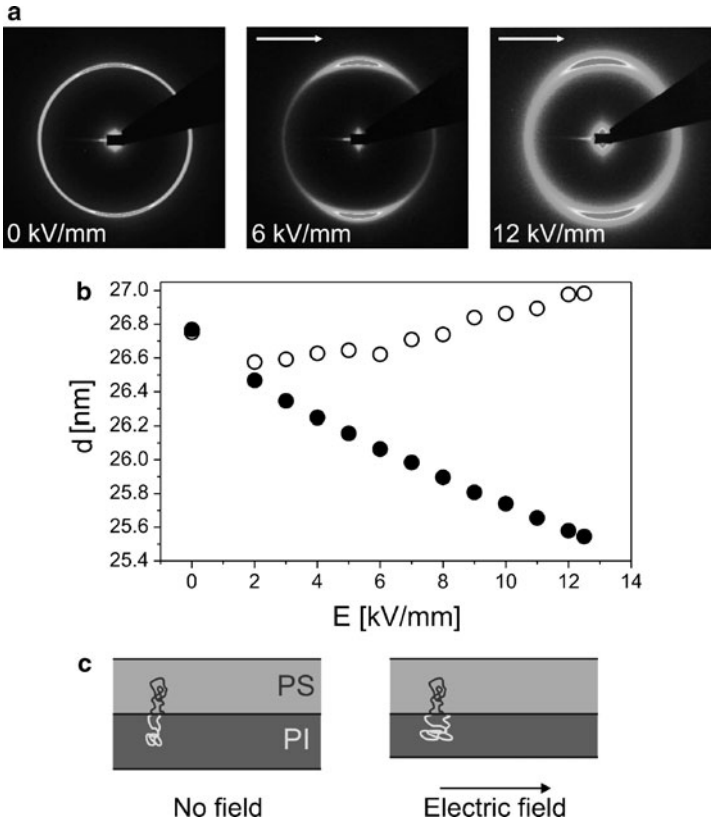

Fig. 13 Effect of an electric field on the lamellar distance of a block copolymer solution. (**a**) 2D scattering pattern of a 50 wt% solution of SI[51] dissolved in THF for different electric field strengths. (**b**) Dependence of the lamellar distance *d* of parallel (*filled circles*) and perpendicular (*open circles*) aligned lamellae, with respect to the electric field lines, on the electric field strength for the same solution. (**c**) Proposed chain stretching effect for lamellae aligned parallel to the field lines. Adapted with permission from Nature Materials [57]. Copyright (2008) Nature Publishing Group

with increasing electric field strength, whereas the lamellar distance for the lamellae oriented perpendicular to the field increases only slightly. This behavior could be explained by stretching of the polymer chains. The only theoretical prediction of chain stretching of block copolymers under the influence of an electric field was described by Gurovich [52, 53]. His results, based on self-consistent field theory calculations, indicate that the electric field polarizes the monomers, interacts with the induced polar moments, and eventually orients them. In consequence, chains are elongated parallel or perpendicular to an applied field depending on the anisotropic polarizability of the monomers.

The equilibrium microphase structures of block copolymers result from a competition between entropic and enthalpic contributions to the free energy. The former accounts for the entropic losses due to stretching or compression of the

polymer chains. The latter accounts for the interfacial energy ($F_{\text{interfacial}}$), which depends on the segregation power. Whereas the interfacial energy favors large lamellar spacings, the entropic stretching prefers smaller ones where the chain is in its most probable conformation [54]. The interfacial energy of a phase-separated block copolymer solution can be estimated by considering the polymer concentration, polymer composition, interaction parameter of the blocks with each other, and the interaction parameter between the blocks and the solvent [55]. It is given as:

$$\frac{1}{k_B T} F_{\text{interfacial}} = \chi_{AB} f_A f_B + \chi_{AS} f_A f_S + \chi_{BS} f_B f_S, \tag{4}$$

where k_B is Boltzmann's constant, T is the temperature, χ is the interaction parameter and f is the volume fraction of A-block, B-block and solvent. For a 50 wt% solution of SI[51] in THF, $F_{\text{interfacial}} = 245.58\,\text{J/mol}$, corresponding to a lamellar distance of 26.7 nm that was determined experimentally. For a 57 wt% solution, we can determine $F_{\text{interfacial}} = 251.74\,\text{J/mol}$, corresponding to a lamellar distance of 27.8 nm. It was shown earlier that the lamellar distance is proportional to the concentration of polymer solution in the concentration range 35–70 wt% [12]. Therefore, for the relatively small changes observed here (namely about 6% change in lamellar spacing, corresponding to concentrations of 50 and 57 wt%), we can use a linear approximation for the relationship between lamellar distance and interfacial energy. Hence, we can estimate the reduction of the interfacial energy due to the electric field. For 50 wt% solution of SI[51] in THF, we observed a decrease of the lamellar distance from 26.7 nm without field to 25.6 nm under an electric field of 12 kV/mm, corresponding to $F_{\text{interfacial}} = 245.58\,\text{J/mol}$ and $F_{\text{interfacial}} = 239.35\,\text{J/mol}$ respectively. Thus, the interfacial energy is reduced by 6.23 J/mol owing to the electric field.

If a lamella is aligned parallel to the field direction (Fig. 13c), we expect the following effect: the chains will be stretched along the field direction, that is, parallel to the phase boundary. Therefore, to a small extent, the electric field counteracts the stretching induced by the microphase separation. In consequence, the chain conformation entropy increases and the lamellar distance decreases. On the other hand, if the lamellae are oriented perpendicular to the electric field direction, the chain stretching induced by the electric field acts perpendicular to the lamellar plane and therefore adds to the stretching already induced by the microphase separation. In consequence, the lamellar spacing increases and the conformational entropy decreases further. Owing to the associated entropic penalty, this effect is indeed expected to be weaker than in the other direction, in agreement with the experimental observation (Fig. 13b). Such a chain stretching is associated with a reorientation of the monomeric units of the polymer chain. For the overall process to be energetically favorable, the decrease in the electric energy associated with the monomer reorientation has to compensate the energetic penalty for the chain stretching. The electric energy could be decreased by two different effects: anisotropic polarizability of the polymer and reorientation of permanent dipole moments of the chain monomers. Owing to its symmetry and rotational freedom, we do not expect the phenyl side

group to have a net influence on the chain orientation. Hence, we expect a stronger response of the PI chains because of the high polarizability and dipole moment of the 1,4-polyisoprene backbone C = C double bonds [56].

We next consider the gain in electric energy that compensates the energetic penalty for the resulting chain stretching. We observe a decrease of the lamella thickness by 1.1 nm due to the electric field. The length of one PI monomer is 6.8 Å [58]. As the monomers can be reoriented from two different orientations perpendicular to the electric field lines (in-plane and out-of-plane with respect to the interface), we can estimate that four PI monomers have to change their orientation from perpendicular to parallel to the field lines to cause the observed decrease in the lamellae thickness. The change of electric energy associated with this reorientation is given by the gain in polarizability. Per PI chain, we have:

$$w = \frac{1}{2} n \alpha E^2 \tag{5}$$

where w is the electric energy and α is the difference in polarizability of the PI monomer in the directions parallel and perpendicular to the backbone. It amounts to $2.42 \times 10^{-40}\,\mathrm{cm}^2/\mathrm{V}$ [59]. With our effective experimental electric field of $E_{\mathrm{effective}} = \mathrm{E}/\varepsilon = 2.28 \times 10^6/\mathrm{Vm}$ and the four monomers calculated above, we get $w = 0.0015\,\mathrm{J/mol}$. If the chains are stretched because of different polarizabilities along and perpendicular to the backbone of the chain as described by Gurovich, the gain in energy from reorientation is about three orders of magnitude too small to solely induce the observed effect. However, when considering the electric energy due to reorientation of the permanent dipole moment of the PI monomers, it is adequate to account for our experimental observations. For this, we calculate per PI chain:

$$w = n\, p_{\mathrm{parallel}} \times E. \tag{6}$$

With $p_{\mathrm{parallel}} = 10 \times 10^{-31}\,\mathrm{cm}$, we get $w = 5.49\,\mathrm{J/mol}$, which is in the right order of magnitude and would yield a sufficient driving force for the observed effect [56].

To assess the influence of incompatibility, composition, and different solvents we quantify the relative change in the lamellar distance as follows:

$$\Delta d = \frac{d_{\mathrm{perpendicular}} - d_{\mathrm{parallel}}}{d_{\mathrm{without\ field}}}. \tag{7}$$

For all solutions, we find a linear dependence of Δd on the electric field strength. However, we observe a different behavior for different degrees of phase separation, for different solvents, and for different compositions. Comparing 50 wt% SI[51] and 57 wt% SI[51] solutions in THF (Fig. 14a), the chain stretching effect is stronger for systems with a lower concentration, that is, a lower degree of phase separation. As mentioned above, the lamellar distance is determined by the balancing of the interfacial energy and the entropic energy. The degree of phase separation has an influence only on the interfacial energy, that is, a lower degree of phase separation leads to a lower interfacial energy. Thus, as the electrical energy of the field is the same, the entropic energy has a stronger influence at lower concentrations and the relative change is higher for solutions with lower interfacial energy.

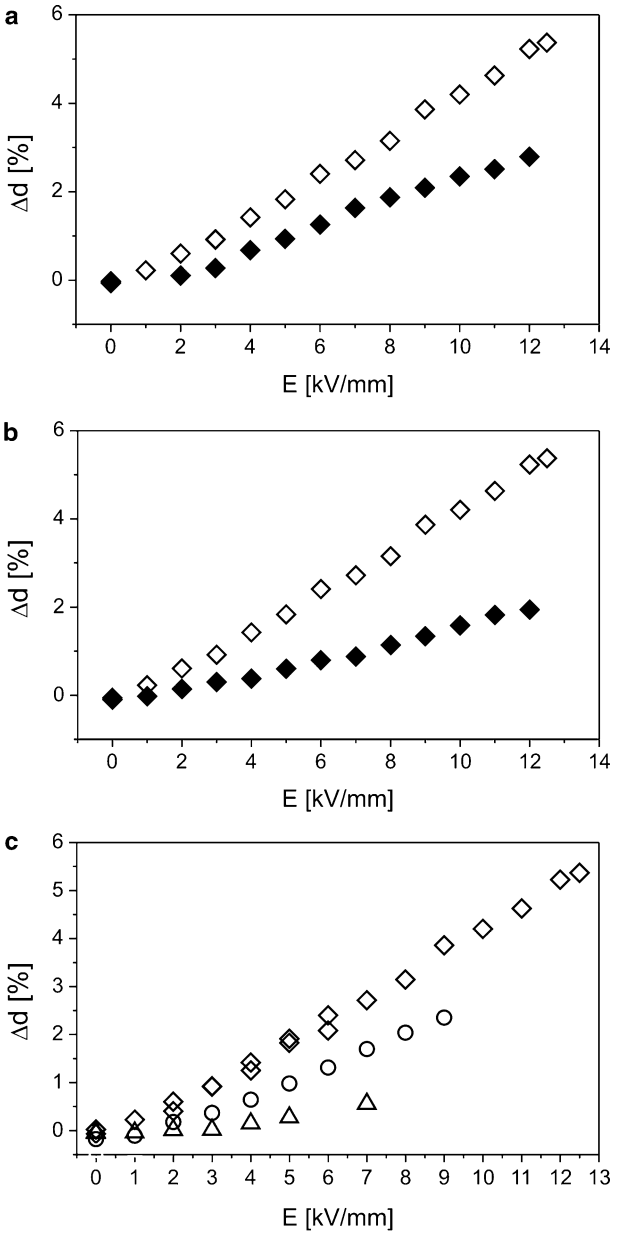

Fig. 14 Dependence of the relative change in the lamellar distance $\Delta d = (d_{\text{perpendicular}} - d_{\text{parallel}})/d_0$ on the electric field strength E. (**a**) Dependence on the degree of phase separation: 50 wt% (*open diamonds*) and 57 wt% (*filled diamonds*) SI[51] in THF. (**b**) Dependence on the solvent type: 50 wt% SI[51] in THF (*open diamonds*) and 50 wt% SI[51] in toluene (*filled diamonds*). (**c**) Dependence on the composition: SI[51] (PI volume fraction 48%) (*diamonds*), SI[48] (PI volume fraction 45%) (*circles*), and SI[47] (PI volume fraction 39%) (*triangles*); all 50 wt% solutions in THF. Adapted with permission from Nature Materials [57]. Copyright (2008) Nature Publishing Group

Furthermore, we also show that the solvent has an influence by comparing the copolymer SI[51] dissolved in toluene and in THF (Fig. 14b). The THF solution is more strongly influenced by the electric field than the toluene solution. Both THF and toluene are good solvents for PI ($\chi_{\text{PI-toluene}} = \chi_{\text{PI-THF}} = 0.40$) and PS; however, the solubility of PS is slightly higher in THF than in toluene ($\chi_{\text{PS-toluene}} = 0.44$, $\chi_{\text{PS-THF}} = 0.32$) [60]. Thus, the interfacial energy is lower for the THF solutions. Because the same arguments as noted above can be applied to this case, the THF solutions are more affected.

In addition, we also find a significant influence of the block copolymer composition on the magnitude of the chain stretching effect. This is illustrated in Fig. 14c, where we compare three different block copolymers with varying PI content (all 50 wt% solutions in THF) but nearly the same molecular weight. As mentioned above, we expect that the effect is mainly induced by the stretching of the PI chains. Indeed, the polymer systems with a higher PI content show a stronger response to the electric field.

As the change in the characteristic spacing of the microdomain structure can be highly useful with respect to possible technological applications, it is of great interest to quantify the kinetics and the reversibility of this process. Therefore, we followed the time evolution of the lamellar distance on application of the electric field. To be able to monitor the time dependence of this process, we used the lowest possible resolution of the CCD detector that allows images with the highest possible time resolution to be taken, that is, 45 ms per image. Figure 15a shows a plot of the time dependence of the lamellar distance for lamellae oriented in the field direction when the electric field is switched on. As soon as the electric field is applied, the copolymer structure responds and the periodicity of the lamellae decreases immediately. This process is faster than the time resolution of the detector, that is, the process has a time constant considerably smaller than 45 ms. To assure that the process is reversible, we followed the relaxation of the domain spacing after the applied field was switched off. Figure 15b shows the time evolution of the lamellar distance of the aligned lamellae when the field strength is decreased (owing to the high voltage applied, it takes several seconds for the capacitor to unload). The domain size closely follows the decreasing electric field strength.

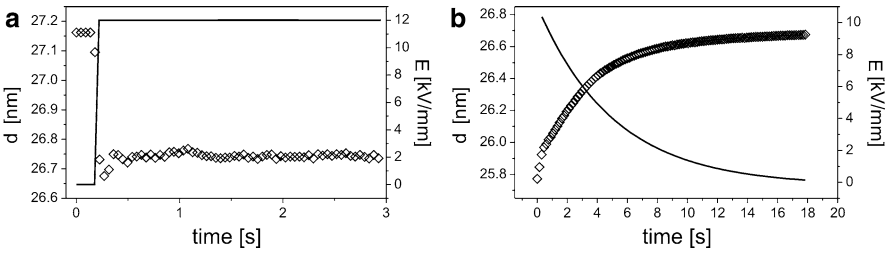

Fig. 15 Time dependence of the lamellar distance *d* of aligned lamellae (*diamonds*). (**a**) Time dependence with increasing electric field strength (*E; solid line*) for a 50 wt% solution of SI[51] dissolved in toluene. (**b**) Time dependence with decreasing electric field strength for the same solution. Adapted with permission from Nature [57]. Copyright (2008) Nature Publishing Group

This very rapid response of the concentrated solutions suggests a reasonable kinetic behavior in the melt. However, for future applications, there is also the possibility of quickly quenching the solutions under an applied electric field. This would freeze the structure at any desired microdomain spacing.

5 Influence of a High Electric Field on the Order–Disorder Transition

After reading Sect. 4, one may anticipate that sufficiently high electric fields not only deform the polymer coils in solution, but also have a strong impact on the phase behavior at the order–disorder transition (ODT). Earlier experiments by Debye and Kleboth in 1965 showed that the phase behavior of binary mixtures can be influenced by external electric fields. They found that a moderate electric field lowers the critical point of a mixture of low molecular weight components [61]. In 1993, Wirtz et al. proved the same for polymer solutions of homopolymers [62]. However, the behavior of block copolymer systems in melt and solution is still under debate because different theoretical approaches predict opposite effects of an electric field on different binary systems (polymer–solvent or polymer–polymer). On one hand, the electric field favors mixing and reduces the order–disorder transition temperature (T_{ODT}) [63, 64]. On the other hand, the electric field should suppress composition fluctuations and weaken the phase transition, thus causing T_{ODT} to shift to higher temperatures [65]. So far, theory only agrees that the observed effect should increase with increasing electric field strength [52, 62, 66–69]. However, in the past, it was anticipated that experimentally accessible electric fields would not be of sufficient strength to induce a measurable effect [63].

Next, we present experimental evidence for the electric-field-induced decrease of T_{ODT} in a block copolymer. Because of the high melt viscosities, temperatures close to the decomposition temperature and extremely high electric field strengths are required to achieve a measurable effect. In recent studies, we have demonstrated that concentrated block copolymer solutions in a neutral solvent act like a melt, thereby effectively circumventing the above-mentioned limitations [31, 57, 70].

For the experiments, a lamella-forming SI copolymer consisting of 46 wt% PS and 54 wt% PI with a total number-average molecular weight of 108 kg/mol and a polydispersity ($M_{\mathrm{w}}/M_{\mathrm{n}}$) of 1.05 was used. The polymer was dissolved in toluene at a concentration of 32.5 wt%. The temperature-controlled experiments were performed in a home-built cubic capacitor designed for square ($2 \times 2\,\mathrm{mm}^2$) glass tubes, which fit between the electrode spacing of 2 mm. The whole capacitor is filled with insulating oil, which is also used to heat the sample. The oil temperature can be adjusted by an external temperature control system to within ± 0.05 K. The X-ray beam penetrates the sample in the center of the capacitor through two small tubes with diamond windows to reduce the background scattering from the oil.

A direct current voltage of up to 20 kV was applied across the electrodes, resulting in a homogeneous electric field pointing perpendicular to the direction of the

X-ray beam, with a maximum strength of 10 kV/mm. The basic layout of the setup is shown in Fig. 12. Synchrotron SAXS measurements were performed at the ID2 beamline at the European Synchrotron Radiation Facility (ESRF, Grenoble, France). The diameter of the X-ray beam was 150 µm. The photon energy was set to 12.5 keV. SAXS patterns were recorded with a 2D camera located at a distance of 5 m from the sample within an evacuated flight tube. An image intensified CCD detector was used, which can handle the full X-ray flux. The CCD detector is capable of acquiring continuously high resolution images of 2048×2048 pixels every 5 s. Prior to data analysis, background scattering was subtracted from the data and corrections were made for spatial distortions and for the detector efficiency.

In order to determine T_{ODT}, the solution of SI was filled into the glass tube and sealed to avoid solvent evaporation. As the volume of the glass tube is small compared to the volume of the surrounding oil, the oil temperature in the capacitor cube was taken as the actual temperature of the sample. Next, we applied a constant heating rate of $1.25°\mathrm{C/min}$ starting below T_{ODT} at 45°C. At 62°C, above T_{ODT}, the temperature was kept constant for a few minutes in order to equilibrate the system. Subsequently, the cooling cycle was started with a rate of $-1.25°\mathrm{C/min}$ until 45°C was reached. Again, we kept the temperature constant, followed by the application of an electric field of 3 kV/mm. With the electric field we oriented the lamellae parallel to the electric field vector as reported earlier [12]. After complete orientation, we applied a different electric field strength and proceeded with the next heating and cooling cycle [31, 70]. Notice that we always oriented and equilibrated the sample at 3 kV/mm and 45°C before each cycle to have the same starting conditions. To avoid systematic errors, we used a random sequence of electric field strengths. In addition, we repeated the measurements for different electric field strengths to ensure reproducibility.

To define general criteria for T_{ODT} we looked at changes in the patterns of the 2D SAXS images. The 2D scattering patterns show typical corrugated peaks for oriented lamellae as long as the system is in the phase-separated regime (see Fig. 16a). Heating the sample above T_{ODT} results in an isotropic intensity distribution. The azimuthal scattering reflects this behavior, as can be seen in Fig. 16b. For oriented lamellae parallel to the electric field vector, the maximum intensity can be found at $\varphi = 0°$ and $\varphi = 180°$, whereas for an isotropic disordered state a uniform distribution is obtained. Therefore, we propose the orientational order parameter P_2 as a good indicator for the ODT. It is calculated according to (2) and (3). As an additional indicator for the ODT, the characteristics of the 1D scattering profile can be used [71]. Besides a narrow first-order peak, additional peaks of higher orders are visible below T_{ODT}. Above T_{ODT}, all higher order peaks vanish and a broad first-order peak remains, which arises from the correlation hole scattering and does not change during further heating (see Fig. 17).

During the heating and cooling cycles, we took SAXS images every 5 s to document the evolution of the system. In Fig. 16a we show four exemplary 2D SAXS patterns around the ODT during a heating cycle. The electric field strength was set to 3 kV/mm. A significant difference between the scattering patterns is clearly observed. While heating the polymer solution, the scattering becomes more

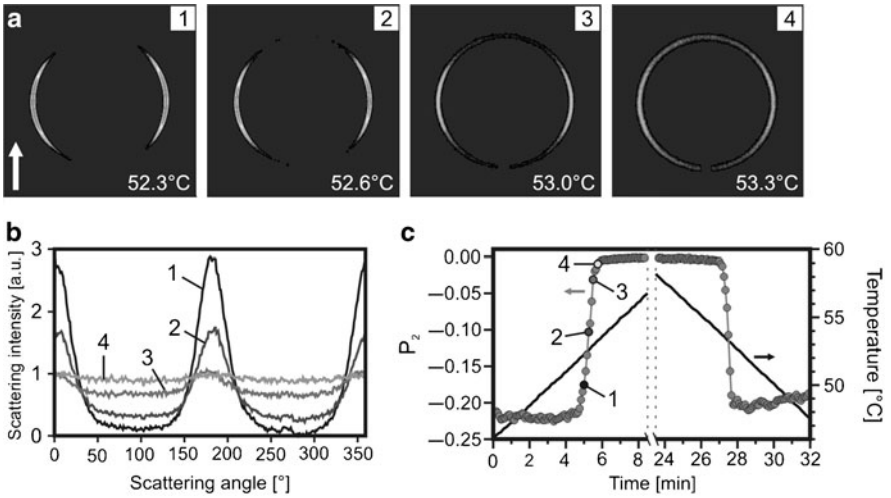

Fig. 16 (**a**) 2D-SAXS images of a 32.5 wt% solution of SI in toluene under an electric field of 3 kV/mm at different temperatures. The *arrow* in the first image indicates the direction of the electric field vector. (**b**) Azimuthal scattering intensity after background subtraction and normalization. The *curves* correspond to the sequence of images in (**a**). (**c**) Order parameter P_2 (*filled circles*) and temperature (*solid line*) as functions of time. *Numbers 1–4* correspond to scattering patterns shown in (**a**) and (**b**). Adapted with permission from Macromolecules [72]. Copyright 2009 American Chemical Society

and more isotropic, i.e., the degree of order decreases until a completely uniform intensity distribution is found. Fig. 16b shows the corresponding azimuthal distribution of the scattering intensity. The time dependence of P_2 and the corresponding temperature of the sample are shown in Fig. 16c. Starting with $P_2 = -0.22$, the order parameter increases during the heating cycle and reaches ~ 0 at 53.3°C, which we determine as ${T_{\mathrm{ODT}}}^{\mathrm{h}}$ (3 kV/mm) according to the conditions defined above. The points corresponding to the SAXS pattern in Fig. 16a, b are marked in Fig. 16c. P_2 remains constant until the temperature falls below ${T_{\mathrm{ODT}}}^{\mathrm{c}}$ (3 kV/mm) during the cooling cycle. We can verify the T_{ODT} by analyzing the 1D SAXS profile for the appearance of higher order peaks and the correlation hole scattering. Figure 17 presents a series of measurements starting at 52.0°C. The higher order peaks vanish prior to the transition, while the azimuthal scattering distribution at 53.0°C is still slightly anisotropic. Reaching 53.3°C, the shape of the first-order peak does not change anymore and the azimuthal scattering intensity distribution becomes isotropic.

By performing the described analysis for every heating and cooling cycle for different electric field strengths, in random order to exclude any possible effects of the sample history, we derived the dependence of T_{ODT} on the electric field strength, which is shown in Fig. 18. We find a clear decrease of the T_{ODT} with increasing electric field strength for the heating cycles. During cooling, the transition always occurs at the same temperature, independently of the applied field. One would

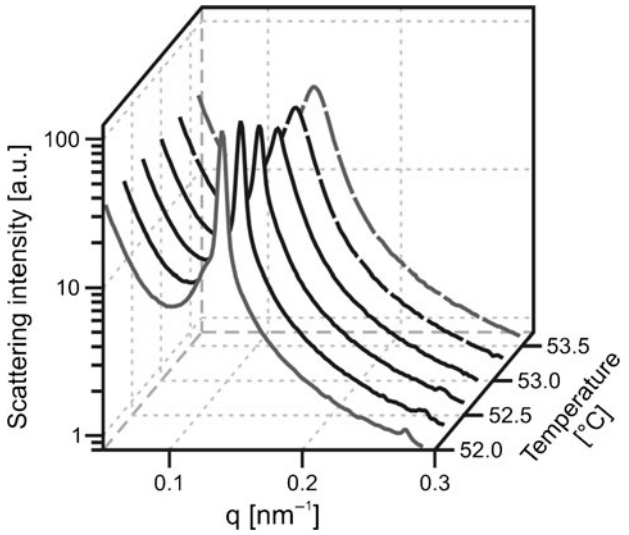

Fig. 17 Time evolution of the SAXS spectra of a 32.5 wt% solution of SI in toluene exposed to an electric field of 3 kV/mm during heating cycle. The order–disorder temperature (T_{ODT}) was 53.3°C. The *dashed lines* correspond to temperature above the T_{ODT} and the *solid lines* to temperatures below T_{ODT}. Data in *black* correspond to the pattern shown in Fig. 16. Reprinted with permission from Macromolecules [72]. Copyright 2009 American Chemical Society

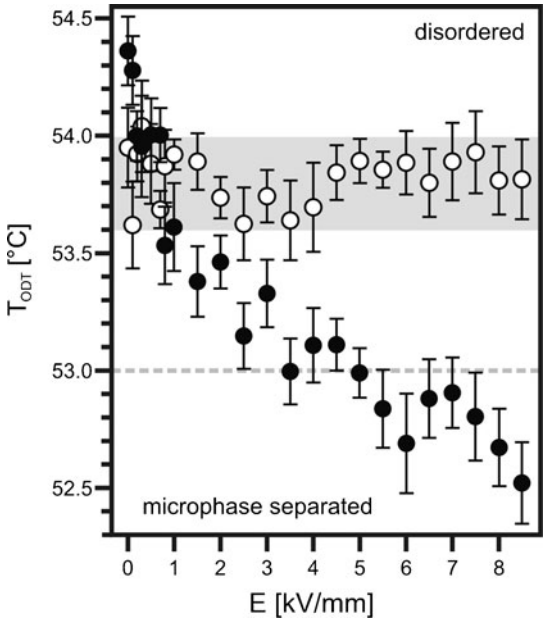

Fig. 18 Order–disorder transition temperature (T_{ODT}) as a function of the electric field strength E of a 32.5 wt% solution of SI in toluene. The temperatures have been obtained during cooling (*open circles*) and heating cycles (*solid circles*) of the solution. The *dashed line* at 53.0°C refers to the constant temperature experiment in Fig. 19. Reprinted with permission from Macromolecules [72]. Copyright 2009 American Chemical Society

expect the same influence for both heating and cooling cycles. This discrepancy can be explained as follows: As we pre-align the lamellae in the microphase-separated regime, the system exhibits well-ordered and large domains. Therefore, the electric field can act on these domains and induce their melting during the heating process. In the case of cooling of the system, a kinetic effect comes into play. As long as the temperature is above $T_{\mathrm{ODT}}{}^{\mathrm{c}} = 53.8 \pm 0.2°\mathrm{C}$ the system is disordered, i.e., there are no lamellar domains for the electric field to act on. As soon as the system starts to microphase separate, very small domains are generated that are too small to couple effectively to the electric field [23]. Because the cooling rate is too large, the temperature of the system is already below $T_{\mathrm{ODT}}{}^{\mathrm{h}}$ before the electric field can act on the growing domains and suppresses the microphase separation. Hence, the system remains microphase-separated. Therefore, this behavior depends strongly on the chosen cooling rate and follows $T_{\mathrm{ODT}}{}^{\mathrm{h}}$ dependence only for very small cooling rates.

To verify this assumption, we changed the procedure in order to exclude kinetic effects. We heated the system to 10 K above T_{ODT} without an electric field until it was completely disordered. In the disordered state we applied an electric field of 7 kV/mm. Cooling very slowly down to 53.0°C with a rate lower than $-0.1°\mathrm{C/min}$ allowed the sample to remain in the disordered state. The corresponding SAXS spectra are shown in Fig. 19. Switching off the electric field at the same temperature resulted in microphase separation of the sample. The influence of the electric field could be considered as crossing the horizontal line of transition in the phase diagram. This transition is fully reversible because switching the electric field on and off toggles disordering and microphase separation of the sample.

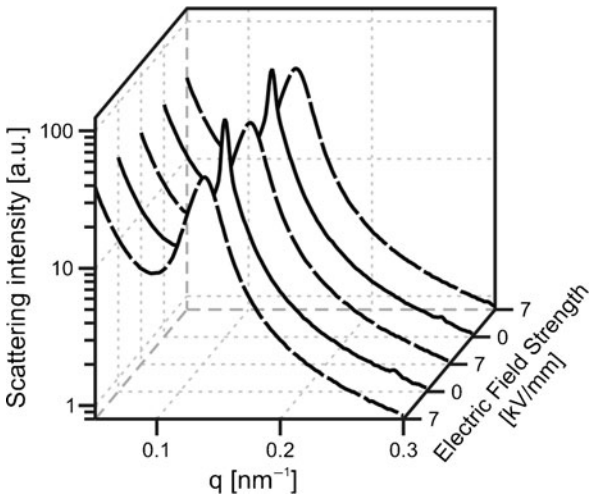

Fig. 19 SAXS spectra of a 32.5 wt% solution of SI in toluene at a constant temperature of 53.0°C. The electric field strength was switched between 7 kV/mm (disordered, *dashed lines*) and 0 kV/mm (microphase separated, *solid lines*). Reprinted with permission from Macromolecules [72]. Copyright 2009 American Chemical Society

Further decreasing the temperature with an applied field of 7 kV/mm again induces microphase separation. This behavior confirms the general result that the electric field lowers the T_{ODT}, as found during the heating cycle.

6 Conclusion

In conclusion, we have given an overview on the parameters governing the electric-field-induced orientation of block copolymer microdomains. A new method for determination of the threshold field strengths for thin films has been presented. In addition, we have demonstrated the power of quasi in situ SFM imaging to reveal typical intermediate structures during thin film orientation, and identified the creation of ring-like defects as an important step during microdomain alignment.

When turning to bulk samples, we have presented first experimental results on the influence of high electric fields ($E > 5\,\mathrm{kV/mm}$) on the microdomain structures. On one hand, chain deformation was shown to be the reason for the change in domain spacing at sufficiently high electric fields, which allows tuning the microdomain spacing on the order of a few nanometers. On the other hand, large field strengths also show an effect on the T_{ODT}. For fields of about 8.5 kV/mm we find a decrease in the T_{ODT} of more than 1.5 K. This could be used to tailor samples by locally melting specific spots with spatially confined electric fields.

All the above-described effects show the high potential of the application of electric fields to block copolymer systems and also encourage the design of additional experiments aiming to find novel effects that might broaden the range of potential applications for block copolymer-based systems.

Acknowledgments The authors thank D. Andelman, P. Bösecke, E. di Cola, F. Fischer, H. Hänsel, M. Hund, S. Hüttner, G. Krausch, H. Krejtschi, V. Kuntermann, C. Liedel, A. Mihut, T. Narayanan, C. W. Pester, S. Rehse, M. Ruppel, K. A. Schindler, F. Schubert, G. J. A. Sevink, S. Stepanov, M. Sztucki, L. Tsarkova, Y. Tsori, V. Urban, T. M. Weiss, H. Zettl, and A. V. Zvelindovsky for support of this work. We are grateful to the ESRF for provision of synchrotron beam time. This work was carried out in the framework of the Sonderforschungsbereich 481 (TP A2) funded by the German Science Foundation (DFG). AB acknowledges financial support by the Lichtenberg-Program of the VolkswagenStiftung.

References

1. Angelescu DE et al (2005) Shear-induced alignment in thin films of spherical nanodomains. Adv Mater 17(15):1878
2. Albalak RJ, Thomas EL (1993) Microphase separation of block copolymer solutions in a flow field. J Polym Sci B Polym Phys 31(1):37–46
3. Hashimoto T et al (1999) The effect of temperature gradient on the microdomain orientation of diblock copolymers undergoing an order-disorder transition. Macromolecules 32(3):952–954
4. Kim SH et al (2004) Highly oriented and ordered arrays from block copolymers via solvent evaporation. Adv Mater 16(3):226

5. Yoon J, Lee W, Thomas EL (2006) Highly oriented thin-film microdomain patterns of ultra-high molecular weight block copolymers via directional solidification of a solvent. Adv Mater 18(20):2691
6. Segalman RA, Yokoyama H, Kramer EJ (2001) Graphoepitaxy of spherical domain block copolymer films. Adv Mater 13:1152
7. Morkved TL et al (1996) Local control of microdomain orientation in diblock copolymer thin films with electric fields. Science 273:931
8. Thurn-Albrecht T et al (2000) Ultrahigh-density nanowire arrays grown in self-assembled diblock copolymer templates. Science 290(5499):2126–2129
9. Olszowka V et al (2006) Large scale alignment of a lamellar block copolymer thin film via electric fields: a time-resolved SFM study. Soft Matter 2(12):1089–1094
10. Xu T, Wang J, Russell TP (2007) Electric field alignment of diblock copolymer thin films. In: Zvelindovsky AV (ed) Nanostructured soft matter: experiment, theory, simulation and perspectives. Springer, Berlin, pp 171–198
11. Böker A et al (2006) The influence of incompatibility and dielectric contrast on the electric field-induced orientation of lamellar block copolymers. Polymer 47(3):849–857
12. Böker A et al (2003) Electric field induced alignment of concentrated block copolymer solutions. Macromolecules 36(21):8078–8087
13. Thurn-Albrecht T et al (2000) Overcoming interfacial interactions with electric fields. Macromolecules 33:3250–3253
14. Xu T, Hawker CJ, Russell TP (2003) Interfacial energy effects on the electric field alignment of symmetric diblock copolymers. Macromolecules 36(16):6178–6182
15. Tsori Y, Andelman D (2002) Thin film diblock copolymers in electric field: transition from perpendicular to parallel lamellae. Macromolecules 35(13):5161–5170
16. Pereira GG, Williams DRM (1999) Diblock copolymer melts in electric fields: the transition from parallel to perpendicular alignment using a capacitor analogy. Macromolecules 32(24):8115–8120
17. Böker A, Müller AHE, Krausch G (2001) Nanoscopic surface patterns from functional ABC triblock copolymers. Macromolecules 34(21):7477–7488
18. Brandrup J, Immergut EH (1998) Polymer handbook, 4th edn. Wiley, New York
19. Olszowka V, Tsarkova L, Böker A (2009) 3-Dimensional control over lamella orientation and order in thick block copolymer films. Soft Matter 5(4):812–819
20. Olszowka V, Kuntermann V, Böker A (2008) Control of orientational order in block copolymer thin films by electric fields: a combinatorial approach. Macromolecules 41:5515–5518
21. Rockford L et al (1999) Polymers on nanoperiodic, heterogeneous surfaces. Phys Rev Lett 82(12):2602–2605
22. Kim SO et al (2003) Epitaxial self-assembly of block copolymers on lithographically defined nanopatterned substrates. Nature 424(6947):411–414
23. Amundson K et al (1991) Effect of an electric field on block copolymer microstructure. Macromolecules 24(24):6546–6548
24. Landau LD, Lifshitz EM (1960) Electrodynamics of continuous media. Pergamonn, Oxford
25. Chen ZR et al (1997) Pathways to macroscale order in nanostructured block copolymers. Science 277(5330):1248–1253
26. Balsara NP, Hammouda B (1994) Shear effects on solvated block-copolymer lamellae – polystyrene-polyisoprene in dioctyl phthalate. Phys Rev Lett 72(3):360–363
27. Winey KI et al (1993) Morphology of a lamellar diblock copolymer aligned perpendicular to the sample plane – transmission electron-microscopy and small-angle X-ray-scattering. Macromolecules 26(16):4373–4375
28. Polis DL et al (1999) Shear-induced lamellar rotation observed in a diblock copolymer by in situ small-angle X-ray scattering. Macromolecules 32(14):4668–4676
29. Wiesner U (1997) Lamellar diblock copolymers under large amplitude oscillatory shear flow: order and dynamics. Macromol Chem Phys 198:3319–3352
30. Böker A et al (2002) Microscopic mechanisms of electric-field-induced alignment of block copolymer microdomains. Phys Rev Lett 89(13):135502

31. Schmidt K et al (2005) Influence of initial order on the microscopic mechanism of electric field induced alignment of block copolymer microdomains. Langmuir 21(25):11974–11980
32. Hund M, Herold H (2007) Design of a scanning probe microscope with advanced sample treatment capabilities: an atomic force microscope combined with a miniaturized inductively coupled plasma source. Rev Sci Instrum 78(6):063703
33. Olszowka V et al (2009) Electric field alignment of a block copolymer nanopattern: direct observation of the microscopic mechanism. ACS Nano 3(5):1091–1096
34. Hund M, Herold H (2006) Rastersondenmikroskop. German Patent No. 10 2004 043 191 B4 (24 May 2006); US Patent Application No. US 20080229812 A1 (25 Sep 2008)
35. Scherdel S et al (2006) Non-linear registration of scanning probe microscopy images. Nanotechnology 17(3):881–887
36. Tsarkova L, Knoll A, Magerle R (2006) Rapid transitions between defect configurations in a block copolymer melt. Nano Lett 6:1574–1577
37. Horvat A et al (2008) Specific features of defect structure and dynamics in cylinder phase of block copolymers. ACS Nano 2(6):1143–1152
38. Constantin D, Oswald P (2000) Diffusion coefficients in a lamellar lyotropic phase: evidence for defects connecting the surfactant structure. Phys Rev Lett 85(20):4297–4300
39. Hubbard PL, McGrath KM, Callaghan PT (2005) A study of anisotropic water self-diffusion and defects in the lamellar mesophase. Langmuir 21(10):4340–4346
40. Trebin HR (1982) The topology of nonuniform media in condensed matter physics. Adv Phys 31(3):195–254
41. Mermin ND (1979) Topological theory of defects in ordered media. Rev Mod Phys 51(3): 591–648
42. Hahm J et al (1998) Defect evolution in ultrathin films of polystyrene-block-polymethylmethacrylate diblock copolymers observed by atomic force microscopy. J Chem Phys 109(23):10111–10114
43. Hahm J, Sibener SJ (2001) Time-resolved atomic force microscopy imaging studies of asymmetric PS-b-PMMA ultrathin films: dislocation and disclination transformations, defect mobility, and evolution of nanoscale morphology. J Chem Phys 114(10):4730–4740
44. Zvelindovsky AV, Sevink GJA (2003) Microscopic mechanisms of electric-field-induced alignment of block copolymer microdomains. Comment. Phys Rev Lett 90(4):049601
45. Böker A, Abetz V, Krausch G (2003) Microscopic mechanisms of electric-field-induced alignment of block copolymer microdomains. Reply. Phys Rev Lett 90(4):049602
46. Choi MC et al (2004) Ordered patterns of liquid crystal toroidal defects by microchannel confinement. Proc Natl Acad Sci USA 101(50):17340–17344
47. Tsarkova L et al (2006) Defect evolution in block copolymer thin films via temporal phase transitions. Langmuir 22(19):8089–8095
48. Winey KI, Thomas EL, Fetters LJ (1991) Swelling a lamellar diblock copolymer with homopolymer – influences of homopolymer concentration and molecular-weight. Macromolecules 24(23):6182–6188
49. Winey KI, Thomas EL, Fetters LJ (1991) Ordered morphologies in binary blends of diblock copolymer and homopolymer and characterization of their intermaterial dividing surfaces. J Chem Phys 95(12):9367–9375
50. Tanaka H, Hasegawa H, Hashimoto T (1991) Ordered structure in mixtures of a block copolymer and homopolymers.1. Solubilization of low-molecular-weight homopolymers. Macromolecules 24(1):240–251
51. Jeong UY et al (2003) Precise control of nanopore size in thin film using mixtures of asymmetric block copolymer and homopolymer. Macromolecules 36(26):10126–10129
52. Gurovich E (1994) On microphase separation of block-copolymers in an electric-field – 4 universal classes. Macromolecules 27(25):7339–7362
53. Gurovich E (1995) Why does an electric-field align structures in copolymers? Phys Rev Lett 74(3):482–485
54. Matsen MW, Bates FS (1997) Block copolymer microstructures in the intermediate-segregation regime. J Chem Phys 106(6):2436–2448

55. de Gennes PG (1991) Scaling concepts in polymer physics, 4th edn. Cornell University Press, Cornell, p 324
56. Adachi K, Kotaka T (1993) Dielectric normal-mode relaxation. Prog Polym Sci 18(3):585–622
57. Schmidt K et al (2008) Reversible tuning of a block copolymer nanostructure via electric fields. Nat Mater 3(7):142–145
58. Lodge TP, McLeish TCB (2000) Self-concentrations and effective glass transition temperatures in polymer blends. Macromolecules 33(14):5278–5284
59. Furukawa J et al (1969) Stiffness of molecular chain of synthetic rubber. J Appl Polym Sci 13(12):2527
60. Huang CI et al (1998) Quantifying the "neutrality" of good solvents for block copolymers: poly(styrene-b-isoprene) in toluene, benzene, and THF. Macromolecules 31(26):9384–9386
61. Debye P, Kleboth K (1965) Electrical field effect on the critical opalescence. J Chem Phys 42(9):3155–3162
62. Wirtz D, Fuller GG (1993) Phase transitions induced by electric fields in near-critical polymer solutions. Phys Rev Lett 71(14):2236–2239
63. Amundson K et al (1994) Alignment of lamellar block-copolymer microstructure in an electric-field. 2. Mechanisms of alignment. Macromolecules 27(22):6559–6570
64. Lin C-Y, Schick M, Andelman D (2005) Structural changes of diblock copolymer melts due to an external electric field: a self-consistent-field theory study. Macromolecules 38(13):5766–5773
65. Gunkel I et al (2007) Fluctuation effects of the microphase separation of diblock-cpolymers in the presence of an electric field. Macromolecules 40(6):2186–2191
66. Onuki A (1995) Electric-field effects in fluids near the critical-point. Europhys Lett 29(8):611–616
67. Orzechowski K (1999) Electric field effect on the upper critical solution temperature. Chem Phys 240:275–281
68. Reich S, Gordon JM (1979) Electric field dependence of lower critical phase separation behavior in polymer-polymer mixtures. J Polym Sci B Polym Phys 17(3):371–378
69. Tsori Y (2004) Demixing in simple fluids induced by electric field gradients. Nature 430:544–547
70. Schmidt K et al (2007) Scaling behavior of the reorientation kinetics of block copolymers exposed to electric fields. Soft Matter 3(4):448–453
71. Sakamoto N, Hashimoto T (1995) Order-disorder transition of low molecular weight polystyrene-block-polyisoprene. 1. SAXS analysis of two chracteristic temperatures. Macromolecules 28(20):6825–6834
72. Schoberth HG et al (2009) Shifting the order-disorder transition temperature of block copolymer systems with electric fields. Macromolecules 42(10):3433–3436

Adv Polym Sci (2010) 227: 33–73
DOI:10.1007/12_2010_54

Published online: 25 March 2010

Nanopattern Evolution in Block Copolymer Films: Experiment, Simulations and Challenges

Larisa Tsarkova, G.J. Agur Sevink, and Georg Krausch

Abstract The present contribution reviews novel insights into block copolymer phase behavior and nanostructure formation in confined geometries. We focus on state-of-the-art experimental and theoretical progress in this area, with an emphasis on characterization methods and techniques that provide a quantitative framework for fundamental analysis. We discuss and compare basic system parameters that are readily controlled in simulations and in experiments, and present comparative studies of increasing degree of complexity concerning the phase behavior and ordering dynamics of cylinder- and lamella-forming block copolymers in thin films.

Keywords Nanostructures · Block copolymers · Thin films · Computer simulations · Scanning force microscopy

Contents

L. Tsarkova (✉)
Universität Bayreuth, Physikalische Chemie II, 95440 Bayreuth, Germany
e-mail: larisa.tsarkova@uni-bayreuth.de

G.J.A. Sevink
Leiden University, Leiden Institute of Chemistry, PO Box 9502, 2300 RA Leiden, The Netherlands
e-mail: a.sevink@chem.leidenuniv.nl

G. Krausch
Johannes Gutenberg Universität Mainz, Mainz
e-mail: krausch@uni-mainz.de

Abbreviations

a_0	Bulk domain spacing
BCC	Body-centered cubic
$C_{\parallel}$	Parallel-oriented cylinder
$C_{\perp}$	Perpendicular-oriented cylinder
DDFT	Dynamic density functional theory
DSCFT	Dynamic self-consistent field theory
GISAXS	Grazing incidence small angle X-ray scattering
h	Film thickness
L	Lamella
MC	Monte Carlo
ODT	Order–disorder transition
P2VP	Poly(2-vinyl pyridine)
PB	Polybutadiene
PL	Hexagonally perforated lamella phase
PS	Polystyrene
SAXS	Small angle X-ray scattering
SB	Polystyrene-*block*-polybutadiene diblock copolymer
SBS	Polystyrene-*block*-polybutadiene triblock copolymer
SCFT	Self-consistent field theory
SCMF	Particle-based SCFT
SE	Spectroscopic ellipsometry
SFM	Scanning force microscopy
SV	Polystyrene-*block*-poly(2-vinyl pyridine) diblock copolymer
SVT	Polystyrene-*block*-poly(2-vinylpyridine)-*block*-poly(*tert*-butylmethacrylate) triblock copolymer
TEM	Transmission electron microscopy
ϕ	Polymer volume fraction

1 Introduction

Thin block copolymer films have been the subject of intensive research over the last few decades, using both experimental and theoretical means. This interest is primarily due to the high potential of block copolymers in (nano)technological applications (see [1–5] for comprehensive reviews) and stems from their intrinsic ability to phase-separate and (self-)assemble into uniform microdomains with tunable dimensions, as well as on the unlimited number of pathways for introducing nanostructure functionality. Applications of block copolymer thin films in nanotechnology range from masks for nanolithography [6, 7], templates for controlled arrangement of nanoparticles [8, 9] and fabrication of nanoporous films [10], photonic band-gap materials [3, 9], high-density information storage media [11, 12], and many other more intricate yet fascinating applications.

The recent success in control and optimization of block copolymer patterns as well as block copolymer-based hybrid structures has been enabled by significant advances in thin film modeling and characterization. In particular, the rather recent developments of realistic models and atomic imaging techniques has been key to the determination of fundamentals underlying structure formation and ordering in block-copolymer thin films [13–22]. Surface fields effects (i.e., modification of the interfacial interactions at the surfaces of the film) as well as constraints caused by the confinement (i.e., control over the substrate topography and/or film thickness) have proved to be effective in manipulating phase behavior (microphase separation and structure orientation) both at the film surface and in the interior of the film. Control of the above parameters is often referred to as the "bottom-up" approach, in order to emphasize the fundamental role of the confined geometry on structure formation.

Uniform orientation and long-range lateral order of the microdomains with low or even vanishing densities of defects are a prerequisite for applications in nanotechnology. The standard experimental routine, consisting of equilibration of block copolymers under elevated temperature or in a solvent vapor, has had limited success in this respect, despite considerable research efforts. Several alternative strategies utilizing external stimuli were developed to overcome this functional limitation of block copolymer patterns [19, 21, 23, 24]. Variation of the solvent quality and of the velocity of the solvent evaporation during preparation, for example, provide rather flexible means of controlling the resulting structures and their orientation relative to the film plane, but are prone to many undefined variables. Theoretical studies have guided experimentalists into the rationalization of microdomain ordering mechanisms upon application of external electric fields [25, 26], through utilization of graphoepitaxy (chemically or topographically patterned surfaces) [23, 27, 28], or by quenching thick films at temperatures close to the order–disorder transition (ODT) temperature [29].

The present paper focuses on recent progress in experimental, theoretical, and experimental-simulational comparative studies of nanostructure formation in confined geometries that have led to the disclosure of novel fundamental insights. We review in particular the detailed results for the phase behavior and ordering

dynamics in thin films of cylinder- and lamella-forming block copolymers. The emphasis lies on the characterization methods and techniques that provide quantitative information for analytical and simulational methodology. This new understanding is further used to analyze particular experimental conditions, which have to be varied in order to target specific applications of nanopatterns. Along with mapping phase behavior of swollen and molten block copolymers in thin films, we focus on issues that are seldom discussed in the literature: molecular architecture effects, including complex ABC terpolymers; collective defect dynamics; swelling under confinement; analysis of the microdomain dimensions and of structure in the interior of the films.

1.1 Block Copolymers

Block copolymers consist of two or more covalently bounded immiscible components (blocks) and belong to the class of ordered fluids that display crystal-like order on a mesoscopic length scale and fluid-like order at a microscopic scale. The mesoscopic structure formation in such systems is governed by competing interactions. The incompatibility of the monomers of different blocks provides the short range repulsion, which drives the phase segregation of the blocks into microdomains with mesoscopic length scales of 10–100 nm (microphase separation). A macroscopic phase separation is prohibited due to the covalent bond between the blocks.

In mean field theory, two parameters control the phase behavior of diblock copolymers: the volume fraction of the A block f_A, and the combined interaction parameter $\chi_{AB}N$, where χ_{AB} is the Flory–Huggins parameter that quantifies the interaction between the A and B monomers and N is the polymerization index [30]. The block copolymer composition determines the microphase morphology to a great extent. For example, comparable volume fractions of block copolymer components result in lamella structure. Increasing the degree of compositional asymmetry leads to the gyroid, cylindrical, and finally, spherical phases [31].

If there are no strong specific interactions between A and B monomers like hydrogen bonding or charges, the interaction parameter χ_{AB} is usually a positive value and is small compared to unity. Positive values of χ_{AB} indicate a net enthalpic repulsion of the monomers. If $\chi_{AB}N$ is large enough, the system minimizes the non-favorable contacts between A and B monomers by microphase separation (strong segregation). The induced order incorporates some loss of translational and configurational entropy. χ_{AB} is inversely proportional to the temperature of the system. Therefore, mixing of the blocks is typically enhanced at elevated temperatures. When the temperature of the system increases (χ_{AB} decreases), the entropic factors eventually dominate and the system becomes disordered. This process is called ODT. Since the enthalpic and entropic contributions scale as χ_{AB} and N^{-1}, respectively, the product $\chi_{AB}N$ controls the phase state of the polymer [31].

1.2 Physics of Block Copolymers in Thin Films

A block copolymer in a confined environment exhibits certain properties that can be characterized as thin film behavior. This behavior is primarily dictated by the enhanced role of surface/interfacial energetics, as well as by the interplay between the characteristic block copolymer spacings and the film thickness.

1.2.1 Surface Fields

Surface fields are defined as differences in the surface/interfacial energies between A and B blocks of the copolymer at the film surfaces. They determine to a great extent the film composition near the surfaces, i.e., the wetting conditions. The interfacial energetics and related wetting conditions for lamella-forming systems are explicitly delivered in the review by Fasolka et al. [32]. *Symmetric wetting* occurs when the same block is located at both interfaces. Alternatively, block copolymer films with different blocks at each surface, termed antisymmetric films in the case of lamella systems, exhibit *asymmetric wetting* conditions.

1.2.2 Surface Relief Structures

Preferential attraction of one of the blocks to the surface brakes the symmetry of the structure and results in layering of microdomains parallel to the surface plane through the entire film thickness. The energetically favored film thicknesses are then quantinized with the characteristic structure period in the bulk through the formation of surface relief structures, also called terrace formation. These structures were established initially for lamella systems [37–39] and later for cylinder- [40–43] and sphere-forming block copolymers.

Experimentally, nucleation and subsequent growth of surface relief structures have been investigated as a function of surface fields [44–46], molecular architecture [37], film thickness [39, 47, 48], and annealing conditions [37–40, 49]. A more detailed summary of the experimental studies can be found in recent reviews [15, 19, 50, 51]; theoretical work on this issue is summarized in [41, 42].

The spontaneous development of the macroscopic topographic features in spin-coated samples, or in samples prepared by a gradient combinatorial approach [52, 53], has been fruitfully used for the analysis of thickness-dependent morphological behavior by constructing phase diagrams of surface structures [43, 49, 53, 54].

An interesting, but little-exploited, strategy is to use a regular thickness gradient created by patterned substrates in order to achieve complex sequenced microphase-separated structures within macroscopic topographic patterns [55, 56].

1.2.3 Deviations from the Bulk Morphology

The intrinsic 3D interfacial curvature in compositionally asymmetric block copolymers provides extra degrees of freedom for the phase behavior in hexagonally structured microdomains. It is now well established that confinement of a cylinder-forming block copolymer to a thickness other than the characteristic structure dimension in bulk, together with surface fields, can cause the microstructure to deviate from that of the corresponding bulk material. Surface structures in Fig. 1 are examples of simulated [57–59] and experimentally observed morphologies [40, 49, 60–62] that are formed in thin films of bulk cylinder-forming block copolymers.

ABC terblock copolymers in confined geometries exhibit a higher versatility and complexity of phase behavior than do binary block copolymers, and this has only been partly explored so far [4, 18, 63].

With advanced knowledge of the underlying physics, the structure formation in block copolymer films can be guided to achieve the most desirable large-domain ordered surface patterns: striped patterns can be produced by aligning the lying cylinder phase or the up-standing lamella phase; dot-like patterns originate from the up-standing hexagonally ordered cylinders or body-centered cubic (BCC) sphere phases, as well as from the perforated lamella phase [21]. Complex gyroid structures have a narrow stability range, and are produced by ABC terblock copolymers [18].

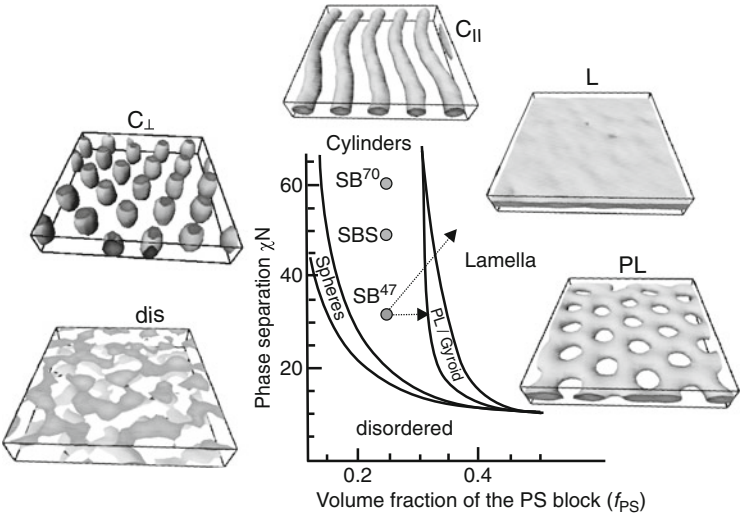

Fig. 1 Phase diagram of self-assembled structures in AB diblock copolymer melt, predicted by self-consistent mean field theory [31] and confirmed experimentally [33]. The MesoDyn simulations [34, 35] demonstrate morphologies that are predicted theoretically and observed experimentally in thin films of cylinder-forming block copolymers under surface fields or thickness constraints: *dis* disordered phase with no distinct morphology, $C_{\perp}$ perpendicular-oriented and $C_{\parallel}$ parallel-oriented cylinders, *L* lamella, *PS* polystyrene, *PL* hexagonally perforated lamella phase. *Dots* with related labels within the areal of the cylinder phase indicate the bulk parameters of the model AB and ABA block copolymers discussed in this work (Table 1). Reprinted from [36], with permission. Copyright 2008 American Chemical Society

2 Modeling with Computer Simulations

During the last two decades, block copolymer self-assembly in 1D confinement has been studied in great detail by a number of analytical and computational methods. In spite of the peculiarities of these methods (i.e., benefits and limitations), all of them apply some form of averaging over degrees of freedom in order to remain computationally tractable and all provide a coarse-grained description of phenomena in the mesoscopic regime (1–1000 nm). The purpose of this review is to list the fundamental insights obtained during a decade of collaboration between our computational and experimental groups using a very successful synergetic approach that enabled us to unravel several generic and essentially dynamical aspects of structure formation in cylinder-forming block copolymer thin films. It is not our intention to provide a complete overview of all theoretical efforts in this field or to give an extensive introduction into dynamic density functional theory (DDFT), the theory used in this review. For these aspects, the interested reader is referred to several existing reviews (e.g., [5, 15, 64]) and to the collected work on thin films of the Leiden group, in which the computational results are discussed in detail in relation to other experimental and theoretical findings. Here, we only briefly sketch the main directions in modeling structure formation in thin block copolymer films and emphasize the specific benefits of DDFT.

Before setting our modeling approach in context, we will focus on some general aspects of thin block copolymer film modeling. The majority of modeling studies so far have considered either coarse-grained particle-based Monte-Carlo (MC) computer simulations or field-based numerical calculations. Despite their relative success, a generic drawback of particle-based methods is that they, except in rare instances, are less capable of equilibrating sufficiently large systems of block polymers at realistic densities to extract meaningful information about structure and thermodynamics. For this reason, the parameter space in these studies is often rather limited. Few studies have used particle-based models that include a realistic kinetic description, e.g., dissipative particle dynamics (see, for instance, Kong et al. [65]).

Field-based models use a free energy that is either phenomenological or stems from an underlying coarse-grained molecular description, like in self-consistent field theory (SCFT) or DDFT [34, 35, 66]. These models overcome some of the drawbacks by further averaging and are clearly advantageous at melt densities and high molecular weights. The molecular field strategy in mean-field SCFT and DDFT involves a number of steps: (1) representation of the block copolymer by a suitable particle-based model, leading to a reduction of the degrees of freedom to particle coordinates; (2) conversion to a field theory by replacing the variables in the partition function from particle coordinates to one or more fluctuating potential fields; (3) discretization on a computational grid; and (4) sampling with the proper statistical weights.

A hybrid method, particle-based SCFT (SCMF) [67], was formulated as an alternative to mean-field SCFT and was applied to complex phenomena such as solvent evaporation in thin polymer films and reconstruction of chemically patterned substrates.

MC and mean-field SCFT were compared for thin films of lamellae-forming diblock copolymers [68]. The results showed an underestimation of the segregation of neutral solvent in SCFT and increasing discrepancy between SCFT and MC with decreasing chain length and temperature. The effect of composition fluctuations, which becomes particularly important for short chains and close to ODT, in lamellae-forming system has been studied using a field-theoretic approach that goes beyond the mean-field approximation [69] and particle-based simulations [70]. The influence of confinement close to ODT was also considered using alternative field models [71–73]. Other research directions used or adapted these methodologies to explore the effect of additional constraints, aimed at structure tailoring and defect-reduction, or optimized the (bulk) phase properties given desired thin film structures. Among the first directions were chemical linking of one block to the substrate [74] and chemical patterning of and/or introducing roughness to the confining surfaces [27, 45, 67, 75–86]. The second direction explores alternative molecular architectures, for instance ABC or dendrites, or mixtures of simple/cheap (di)block copolymers [6, 87–90]. The mechanical properties of such systems was also considered [91, 92].

In this review we describe on the theoretical results obtained for AB diblock or ABA triblock copolymer melts confined between two flat, homogeneous hard surfaces in the regime where fluctuations can be neglected (sufficiently long chains well below the ODT). Most studies in this field focused on the phase behavior of lamellae-forming symmetric diblock copolymers in confinement. Two general mechanisms were identified [13, 93–97]. For a commensurate film thickness (i.e., a film thickness that matches the discrete length scale set by the natural domain distances), the difference in surface-block interaction (the surface field) determines whether lamellae orient perpendicular (vanishing) or parallel (above a threshold) to the confining surface. Incommensurate film thicknesses give rise to stability of perpendicular lamellae. Confinement was therefore found only to affect the orientation of the (bulk) lamellar structure. In particular, mixed lamellar phases were found to be metastable by SCFT [13]. Only in the case of dissimilar block–surface interactions (i.e., different surface fields at each of the confining surfaces), were stable non-lamellar or hybrid structures identified in very thin films by SCFT [98]. Several studies considered defect dynamics and layer hopping in lamellae-forming systems [99–101].

Although these mechanisms are clearly general, the situation is considerably different for asymmetric AB or ABA block copolymers. First, confinement-induced chain deformations have been shown to lead to a stabilization of non-bulk morphologies in very thin films and parts of thicker films, even for similar interactions [62]. Second, microphase separation in these systems naturally gives rise to a matrix and a minority phase. Structure evolution and defect dynamics is clearly affected by these topological constraints and therefore very specific. The anticipated equivalence to lamella-forming systems is therefore partially lost. For these and other reasons, the thin film phase behavior of systems that form bicontinuous phases, cylinders, or spheres in bulk has attracted considerably less theoretical attention, despite their relevance in nanotechnology. Most studies on sphere-forming systems have focused

on packing of spherical domains in thin films, in particular on obtaining neat structures on a larger scale, and on the nature of the transition from a hexagonal structure in very thin (2D) films to the 3D (BCC) bulk lattice on increasing the film thickness [48, 102–106]. Only very recently were confinement-induced deviations from the bulk (sphere) structure studied using DDFT [107]. In cylinder-forming systems, our detailed DDFT studies for SB and SBS block copolymers are complemented by static phenomenological and mean-field SCFT calculations as well as by particle-based MC simulations (see [64, 97, 108–110]). In combination, they provide a complete and general picture of the fundamental phenomena, reviewed here, of cylinder-forming block copolymers in thin films.

The often-employed mean-field SCFT is a static theory, based on determining free energy minima or saddle points using mathematical techniques. SCFT is very well suited for determining equilibrium phase behavior (away from ODT). It is increasingly recognized, however, that experimentally accessed soft matter structures are often only metastable, even after very long equilibration, and that the understanding of dynamic pathways is therefore crucial for further development of soft matter material science. Although DDFT and SCFT share the free energy expression, the dynamic model in DDFT minimizes this free energy following collective diffusive dynamics, where the gradient of the chemical potential acts as a driving force. DDFT is therefore able to relate directly to the dynamic pathways and saddle points that are relevant in experimental systems, in a computationally efficient way. Despite the fact that some physical phenomena, like fluctuations, viscoelastic and hydrodynamic effects as well as chain entanglements, are not properly captured in this model, the work reviewed here shows that these contributions do not play a major role in these thin film systems. In addition, we note that the presence of neutral solvent in the experimental system was only considered as an effective scaling of the interaction parameters [62]. In particular, the (quasi)equilibrium and dynamic behavior was captured computationally in great detail (Sect. 4.5). We conclude that the theoretical approach provides a decisive understanding of the experimental results as it illustrates detailed microscopic mechanisms and allows for more extensive variations of the system parameters than one could achieve in experiments. Figure 2 compares the sample dimensions of the experiment with that of the computational simulation. In experiments, a typical film surface area available for the optical microscopy or scanning force microscopy (SFM) measurements is about a centimeter

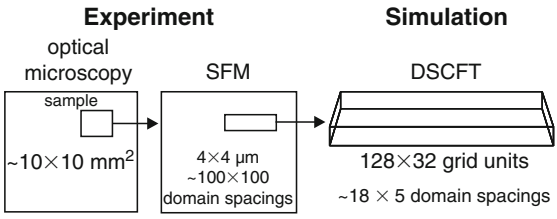

Fig. 2 Comparison of typical lateral scales that are covered in experimental measurements (optical microscopy and SFM) and in a simulation box. DSCFT is sometimes used as an acronym for DDFT. Reprinted from [41], with permission. Copyright 2007 American Chemical Society

square with an averaged terrace size of several micrometer square. Typically, in block copolymer films, each terrace accommodates in the lateral direction up to several hundred microdomains.

3 Characterization Techniques

The experimental studies on phase behavior and pattern formation reviewed here have been done on substrate-supported films of cylinder-forming polystyrene-*block*-polybutadiene diblock (SB) [36, 43, 51, 111–114] and triblock (SBS) [49, 62, 115–117] copolymers (Table 1), lamella-forming polystyrene-*block*-poly(2-vinyl pyridine) diblock copolymers (SV) [118, 119] and ABC block terpolymers of various compositions [53, 63, 120–131]. In simulation studies, a spring and bid model of ABA Gaussian chains has been used (see Sect. 2) [36, 42, 58, 59].

We present a brief summary of the original experimental approaches that allowed advances in the characterization and understanding of dynamic and equilibrium behavior on block copolymers under confinement.

3.1 Scanning Force Microscopy of Polymer Surfaces

The advent of advanced SFM methods facilitated surface studies of soft materials without causing damage to the sample. Typical problems in imaging polymeric samples with TappingMode concern the quantitative reproducibility of height and phase images, the distinction between real surface topography and indentation, and even the frequently occurring contrast inversion of height and phase images. These problems have been quantitatively addressed in [132]. In particular, the "real" surface topography can be distinguished quantitatively from the lateral differences in tip indentation. This approach allowed detection of a 10-nm-thick PB layer covering the true surface of SBS films [132].

Of particular importance are in situ SFM measurements, which allow real-time data collection during structure evolution [111, 112, 117, 133–135]. Both concentrated block copolymer solutions [117, 136, 137] and block copolymer melts [111, 112] have been imaged in situ to access the microdomain dynamics. Figure 3

Table 1 Copolymers of polystyrene and polybutadiene blocks

		Molecular weight		
Label	Structure	(kg/mol)	f_{PS} (wt%)	a_0 (nm)
SB^{47}	$S_{13}B_{34}$	47.3	26.1	30
SBS	$S_{14}B_{73}S_{15}$	102.0	26.0	40
SB^{70}	$S_{26}B_{70}$	96	24.5	64

f_{PS} refers to the fraction of PS in the copolymer, and a_0 to the bulk domain distance

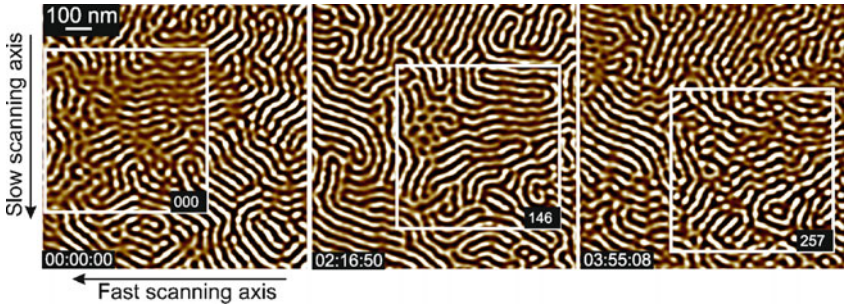

Fig. 3 Fourier filtered tapping mode SFM phase images of the surface structures in a fluid SB^{47} film at 105°C. The scale is 5° and bright corresponds to PS microdomains below an ≈10-nm-thick PB layer [132]. The images are frames from a SFM movie [111, 112] (the corresponding frame numbers and the elapsed time are shown). *White squares* highlight the same sample area that has been cut out for the movie. The *arrows* by the left image indicate the fast scanning axis, along which the tip moves with the velocity of 20 µm/s, and the slow scanning axis, along which the image is completed within ≈46 s. Reprinted from [111], with permission. Copyright 2006 American Chemical Society

shows the first frame, an intermediate frame, and the last frame from the sequence of continuously scanned SFM images. During the long term in situ measurements, the scanning area (highlighted by white squares) steadily moves due to thermal drift. We noted considerable changes to the surface structures with annealing time, making identification of the moving sample area of interest in snap-shot imaging experiments extremely difficult or even impossible. In Sect. 4.5 we describe original approaches towards the quantitative evaluation of dynamic SFM measurements [111, 112, 117, 136, 137].

Further challenge in SFM characterization of block copolymer structures is related to the precise measurements of the lateral dimensions. This analysis is possible when an SFM instrument meets the tight limits on axis orthogonality, flatness of the x,y plane, linearity, accuracy, and repeatability of the produced images. Recently, a home-built software has been used for the digital analysis of SFM Metrology images to evaluate confinement effects on the lateral dimensions of the microdomains [113]. Figure 4a presents a typical phase image of the cylinder structures aligned parallel to the film plane. Between two neighboring terraces, the film thickness increases gradually. The results of the analytical procedure are shown in Fig. 4b where characteristic distances between the cylinders are plotted as a function of the local thickness of the film (Sect. 4.4) [113, 138].

3.2 High Resolution Volume Imaging

Traditionally, SFM is limited to surface studies and sheds little light on the inner structure of the material. The nanotomography approach was suggested as a way

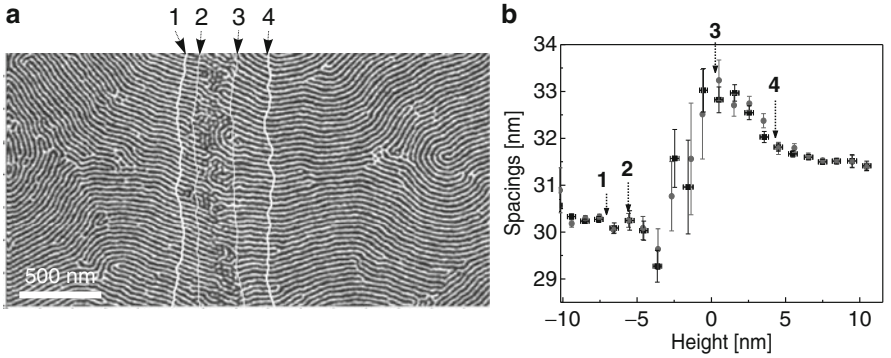

Fig. 4 (**a**) SFM phase image (3×1.5 μm) of the surface structures in SB^{47} films annealed in vacuum at 120°C. The *white contour lines* are taken from the height image (not shown) and mark the borders between the flat regions, as well as the transition region between the indicated terraces. (**b**) Spacings of cylindrical microdomains as a function of the local film thickness

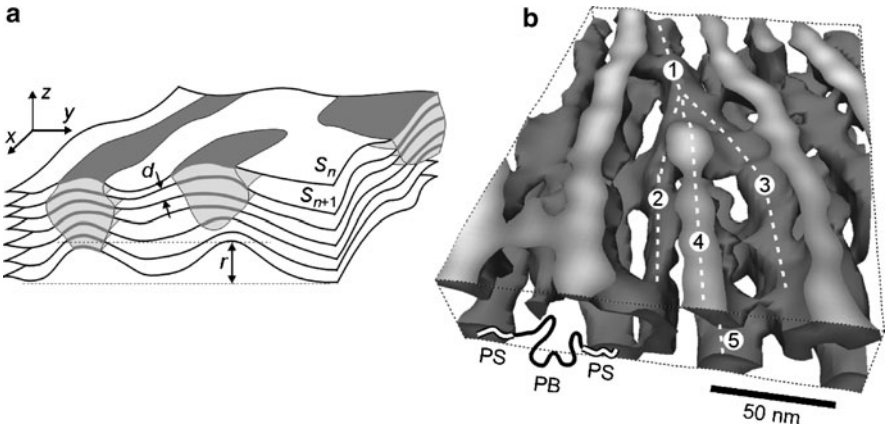

Fig. 5 (**a**) Illustration of the principle of volume reconstruction from a series of scanning probe microscopy images. (**b**) 3D image of the isosurface enclosing the volume with normalized TappingMode phase reconstructed from a series of phase and topography images. An SBS molecule bridging two PS cylindrical microdomains is sketched. Reprinted from [116], with permission. Copyright 2002 by the American Physical Society

to overcome the limitations of 2D imaging [115, 116, 139–141]. A key feature of nanotomography is that both the surface properties under study as well as the actual (and changing) shape of the surface are measured with SFM after each erosion step, and as a result a 3D nanostructure is reconstructed (Fig. 5).

The potential of the nanotomographic approach is supported by advances in automation of SFM imaging. State-of-the-art SFMs have general limits in performing harsh sample treatments because their design concept is focused on in situ scanning in a closed environment (liquid/heating cells). Aggressive treatments like plasma

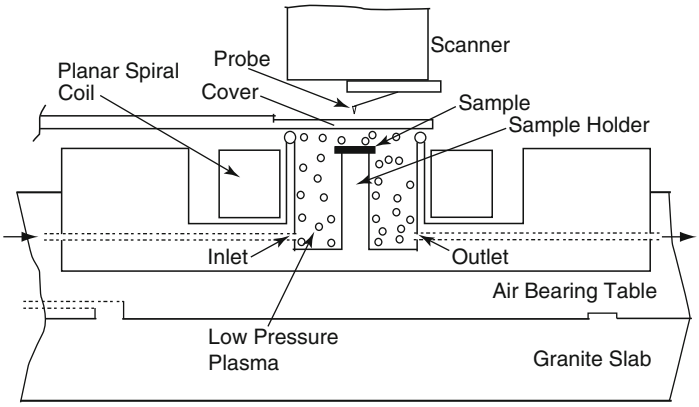

Fig. 6 Side view of the quasi in situ SFM prototype. The sample treatment and the scanning probe microscopic examination are temporally and spatially separated from each other. The probe is not affected by the sample treatment process, and a specific sample spot can be examined without readjustment. Reprinted from [142], with permission. Copyright 2007 American Institute of Physics

etching or etching in aggressive liquids typically require removing the sample from the microscope. Recently, a new SFM-based setup with quasi in situ sample treatment capability has been developed [142] (Fig. 6). Its capabilities have been demonstrated by successive plasma etching and imaging of lamella polymer films, which gives access to depth-profiling with high lateral and normal resolution [143]. The new development concerns the possibility of repositioning the SFM tip on a specific sample spot after successive treatments performed inside the SFM.

3.3 Annealing Under Controlled Conditions

Phase separation in block copolymer films has been shown to be sensitive to the solvent selectivity and its concentration in the film [49, 51, 114, 120, 123]. We emphasize the importance of a well-controlled atmosphere of solvent vapor for the annealing process since even slight changes in the solvent concentration or in the temperature of the system may induce structural phase transitions.

One of the easy and effective approaches for quantifying the polymer volume fraction within films in situ is to use in situ spectroscopic ellipsometry (SE) [49, 118, 119, 144]. The measurements should be performed in a thermostated cell (Fig. 7) with full control over the solvent vapor atmosphere p/p_0, where p_0 is the solvent vapor pressure at saturation and p is the actual pressure, which can be adjusted by a combination of the saturated vapor flow and dry nitrogen flow [118, 119], or by the difference between the temperature T_1 of the polymer sample and the temperature T_2 of the solvent vapor [49, 114, 144].

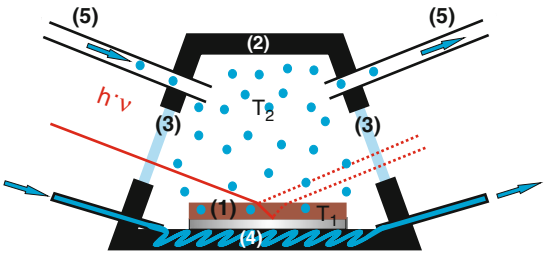

Fig. 7 Schematic of the annealing chamber: (1) substrate-supported polymer film; (2) sealed stainless steel chamber; (3) glass windows, which are perpendicular to the incident light; (4) temperature control of the substrate (T_1); (5) input and output for the temperature- and flow-controlled solvent vapor (T_2). Reprinted from [114], with permission. Copyright 2009 American Chemical Society

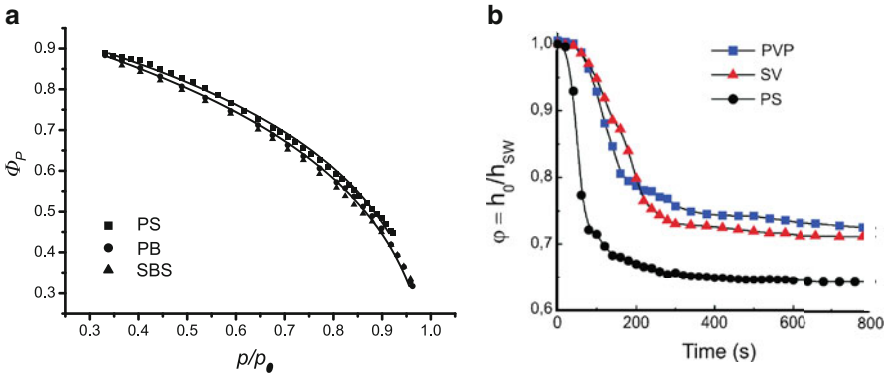

Fig. 8 Polymer volume fraction $\phi = h_0/h_{sw}$, where h_0 is the thickness of the polymer film after spin-coating and h_{sw} is the thickness of a swollen film, measured by in situ spectroscopic ellipsometry as a function of (**a**) the relative solvent vapor pressure for thin films of homopolymers PS, PB, and SBS block copolymer. Reprinted from [49], with permission. Copyright 2004 American Institute of Physics. (**b**) Polymer volume fraction as a function of the swelling time for PS-*b*-P2VP (SV) block copolymer and for homopolymers PS and P2VP at $p/p_0 = 1.0$ [118]. The equilibrium degree of swelling indicates that toluene is a selective solvent for the PS block, and that SV block copolymer shows asymmetric swelling under toluene vapor. Reproduced by permission of The Royal Society of Chemistry (RSC) [118]

Figure 8a displays ϕ_{pol} as a function of the relative chloroform vapor pressure p/p_0 in films of PS and PB homopolymers, and in films of SBS block copolymer [49]. It shows that chloroform is a good solvent for both homopolymers, exhibiting only a small selectivity to PB. Figure 8b displays kinetic measurements of the swelling behavior of a symmetric SV block copolymer and of respective homopolymers at controlled toluene vapor [118]. The comparison of the equilibrium degree of swelling suggests that toluene is a selective solvent for the PS block. Moreover, the swelling behavior of the symmetric SV block copolymer is dictated by the P2VP component. Thus, the relative affinity of a solvent towards the block copolymer components can be accessed by well-controlled swelling experiments [144].

4 Block Copolymer Self-Assembly Under Confinement

The presence of external selective surfaces and confinement, in particular to dimensions comparable with the characteristic structure size, can considerably alter the microphase separation and stabilize non-bulk morphologies. Confinement effects on the surface and bulk film structures have been systematically analyzed in elegant experiments by Knoll et al. [49, 62] on thin films of concentrated solutions of SBS in chloroform. DDFT-based calculations on cylinder-forming ABA chains revealed stunning agreement in the sequence of stabilized morphologies between the calculated and the measured phase diagrams [43, 49, 57, 58, 62, 145]. As an example, Fig. 9 shows a comparison of the experimental results (upper panel) and the calculations (lower panel) for a given strength of the surface field [62]. A rich morphological variety is observed as the film thickness increases from left to right: a featureless wetting layer for the smallest thickness; dot-like pattern of vertically oriented cylinders $C_{\perp}$; striped pattern of parallel-oriented cylinders $C_{\parallel}$; hexagonally perforated lamella phase (PL), etc. The phase transitions occur at well-defined film thicknesses, highlighted by white contour lines, which are calculated from the SFM height images and represent borders of equal film thickness.

These results represent solid evidence for a general mechanism governing the phase behavior at surfaces and in thin films of modulated phases: The interplay

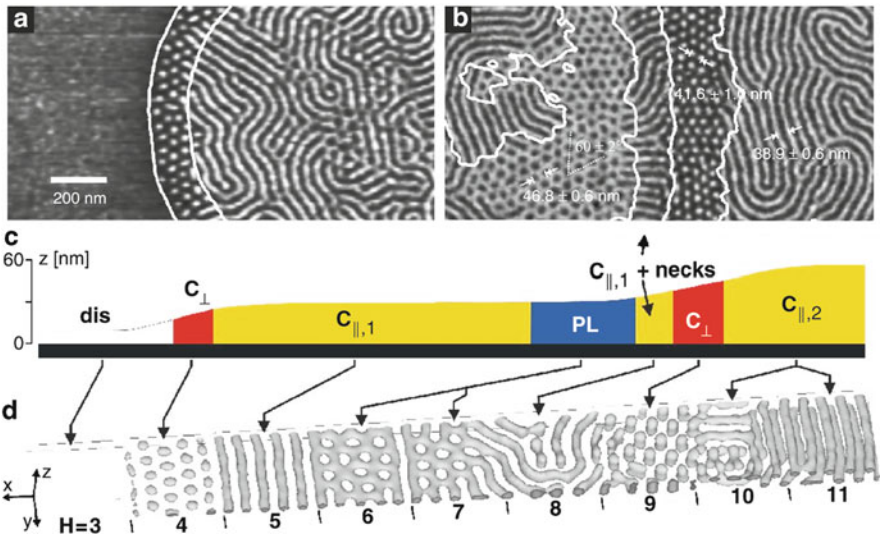

Fig. 9 (**a, b**) TappingMode SFM phase images of thin SBS films on Si substrates after annealing in chloroform vapor. The surface is covered with an approximately 10-nm-thick PB layer. *Bright* (*dark*) corresponds to PS (PB) microdomains in the top PB layer. *Contour lines* from the corresponding height images are superimposed. (**c**) Height profile of the thin film shown in (**a, b**). (**d**) Computer simulation of a block copolymer film in one large simulation box with increasing film thickness (from *left to right*). The isodensity surface of the density distribution of the A component ρ_A is shown for $\rho_A = 0$. Reprinted from [62], with permission. Copyright 2002 by the American Physical Society

between the strength of the surface field and the deformability of the bulk structure determines the system response, either via reorientation or via phase transitions and surface reconstructions. The stability regions of the different phases are modulated by the film thickness via interference and confinement effects.

4.1 Surface-Induced Phases in Melts

4.1.1 Simulations

We have used a slightly adapted version of the 3D DDFT implementation that was commercialized in the late nineties of last century as the MESODYN code. The adaptation was required to include asymmetric surface interactions. In general terms, all non-ideal chain interactions are included via a mean field and the strength of interaction between A and B components or blocks in the coarse-grained molecular chain representation is characterized by the interaction parameter ϵ_{AB}. This parameter is directly related to the conventional Flory-Huggins parameter χ and was determined based on a detailed mapping procedure [58]. Interfaces are treated as hard walls with reflecting boundary conditions, and proper constraints on the density. The interaction between chain components and interfaces (labeled by M) is characterized by corresponding mean field. As only the difference between the interactions of each component with the interfaces is relevant, we worked with effective interaction parameters $\epsilon_M = \epsilon_{AM} - \epsilon_{BM}$ which characterize the strength of each surface field. By setting $\epsilon_{BM} = 0$, a positive ϵ_M parameter corresponds to a repulsion between component A and the interface.

Variation of the preferential interaction of the block copolymer components with the substrate has proved to be an important tool for tuning the phase separation near the surfaces. The results of calculations in Fig. 10 quantify the effects of the surface fields in a solvent-free-cylinder-layer thick film. The variation of ϵ_{M} at constant

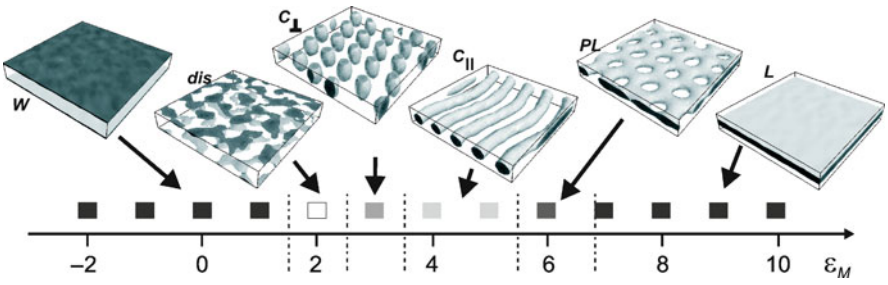

Fig. 10 Simulation results for a cylinder-forming $A_3B_{12}A_3$ ($\epsilon_{\mathrm{AB}} = 6.5$) in thin films (thickness $= 6nm = a_0$) with varied strength of the symmetric surface field ϵ_M. The isodensity profiles ($\rho_{\mathrm{A}} = 0.45$) are shown for indicated simulation parameters. Reprinted from [58], with permission. Copyright 2004 American Institute of Physics

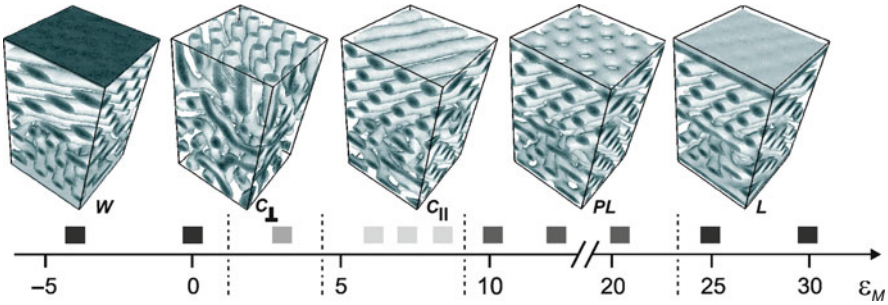

Fig. 11 Effect of the strength of the surface field ϵ_M on the phase separation in the interior of the film and at interfaces. Simulation results for a cylinder-forming $A_3B_{12}A_3$ ($\epsilon_{AB} = 6.5$) in thick films (thickness $= 54nm = 9a_0$) with surfaces at $z = 0$ and at indicated values of symmetric surface field ϵ_M. The isodensity profiles ($\rho_A = 0.45$) are shown for indicated simulation parameters. Reprinted from [58], with permission. Copyright 2004 American Institute of Physics [58]

film thickness induces structures ranging from the non-bulk lamella (at $\epsilon_M = 7$) and perforated lamella (at $\epsilon_M = 6$) to a disordered phase (at $\epsilon_M = 2$) with no well-defined microdomain structure, but with the two components A and B being still slightly segregated [58].

These and other results provide examples of an intriguing surface effect – deviations from the bulk microdomain structure in the vicinity of the interface – which has been called "surface reconstruction" owing to its analogy to the reconstruction in crystal surfaces. The effect is especially pronounced in films of relatively large thickness with nine microdomain layers ($h = 54$ nm) (Fig. 11). The main difference between the thin films of Fig. 10 and these thicker films is that in the vicinity of one film interface the influence of the other one is negligible. In the interior of the film in most cases the hexagonally ordered cylinders remain aligned parallel to the film plane. Depending on the strength of the surface field, considerable rearrangements of microdomains near the interfaces occur.

The calculated phase behavior for asymmetric surface fields, where the interactions between the components and the top (ϵ_{M1}) and bottom (ϵ_{M2}) interface may vary freely, is even much richer (see Fig. 12 for two layers of structure) than for the symmetric case. A particular feature is the appearance of hybrid structures, which are either a coexistence of different surface reconstructions close to each of the interfaces or interconnected structures. Nevertheless, the general features of Fig. 12 can still be explained in terms of surface field and confinement effects, noting that each of the surface fields now supports its own surface reconstruction, which may interconnect for combinations of perpendicular and parallel structures. As in the symmetric case, this behavior is modulated by the film thickness via interference and confinement effects in a very complicated manner.

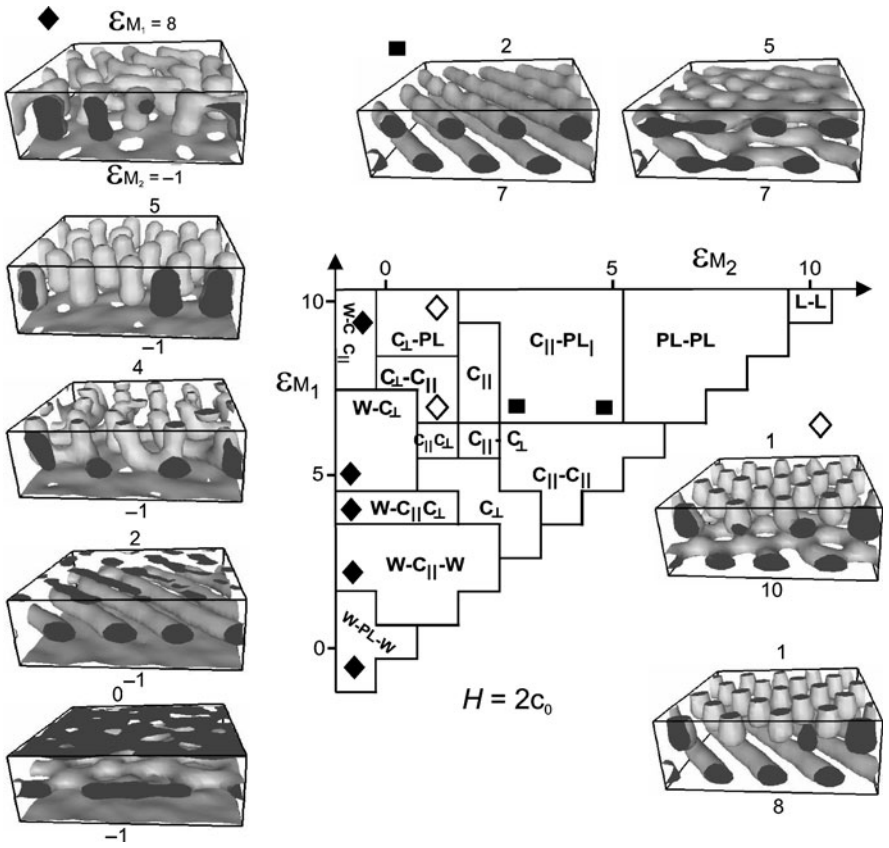

Fig. 12 Diagram of structures for varying interaction of the compounds with the top (ϵ_{M1}) and bottom (ϵ_{M2}) interface. *Symbols* denote the structures that are shown as *insets*. Isodensity profiles for $\rho_A = 0.45$ are shown, and the thickness h is twice the bulk domain distance a_0 (c_0 in [59]). Reprinted from [59], with permission. Copyright 2004 American Institute of Physics

4.1.2 Experiment

Various experimental routes towards surface modification have been utilized in order to control the microphase separation in thin films, as well as to achieve large-area patterns with desirable orientation relative to the film plane [2, 19, 21, 51].

In [43], the phase behavior and interlayer period of cylindrical domains have been tuned by varying the interactions with the substrate and by varying the related wetting conditions. Thin films of SB^{47} (Table 1) have been equilibrated by thermal annealing on two chemically different substrates and used as models of symmetric and asymmetric wetting. As seen from the experimentally established phase diagram in Fig. 13, on a neutral substrate (carbon-coated silicon) under asymmetric wetting conditions, cylinders are aligned parallel to the surface ($C_{||}$) both at the

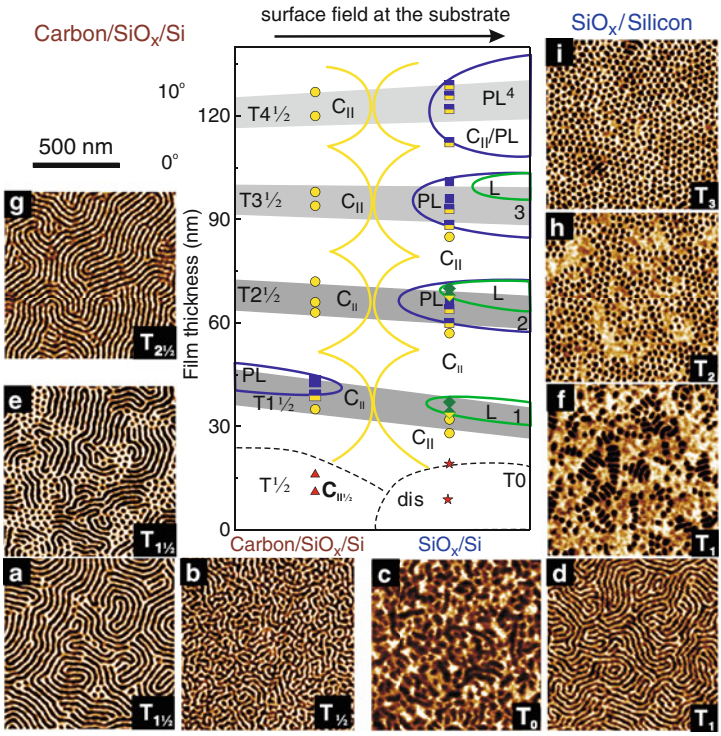

Fig. 13 Phase diagram of the surface structures on a weakly interacting surface (carbon coating) and under strong surface field with a preference for the majority component (silicon oxide). *Gray* areas mark the borders of the preferred film thickness (data taken from Fig. 14). The SFM phase images ($1 \times 1\,\mu m$) present examples of the surface structures on carbon-coated (*left*) and silicon oxide (*right*) substrates at the indicated film thickness. *Symbols* indicate the following morphologies: *circles* the $C_{\|}$ cylinder phase (**a**,**d**,**g**); *squares* the PL phase (**i**); *half-filled squares* coexisting $C_{\|}$/PL structures (**e**); *diamonds* the lamella (L) phase; *half-filled diamonds* coexisting $C_{\|}$/L patches (**f**) or coexisting PL/L microdomains (**h**); *triangles* half-cylinder structures $C_{1/2}$ (**b**); *stars* the disordered phase (**c**) [43]. *Black curves* schematically contour the phase boundaries and are drawn as a guide for the eye in line with the DDFT simulations [58]. Adopted from [43], with permission. Copyright 2006 American Chemical Society

favored (natural) and at the transition thicknesses. A half-cylinder phase $C_{1/2}$ forms in ultrathin films (with h below a_o, Fig. 13b) and probably also forms as a bottom layer in thicker films.

For a strong surface field and symmetric wetting conditions, a perforated lamella (PL) phase typically develops in up to four layers of structures, with an exception for the first layer of structures at the favored film thickness. For one layer and all transition regions between terraces a $C_{\|}$ phase was found.

The comparison of the surface structures on two substrates suggests strong surface effects on the microphase separation. For lamella systems, the degree of interfacial segregation has been shown to be proportional to the surface potential [146]. The same line of argument can be used to explain the surface field effects

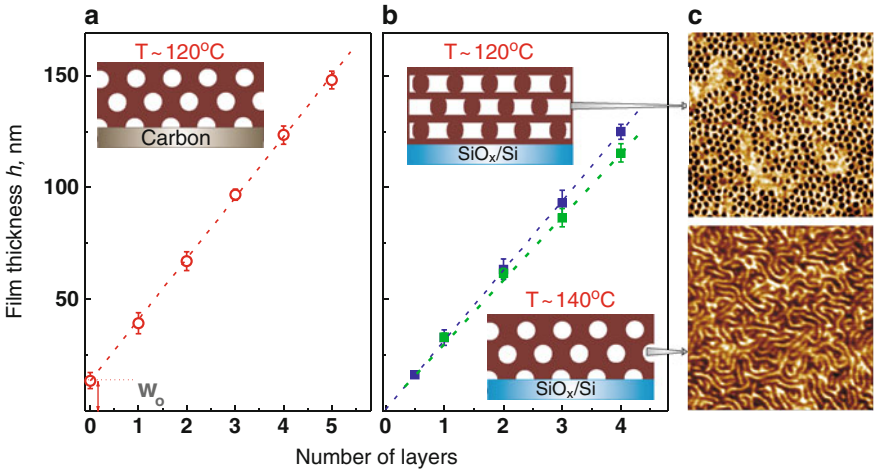

Fig. 14 Averaged terrace heights plotted versus the number of layers on (**a**) carbon-coated substrate (*circles*) at 120°C and on (**b**) silicon oxide substrate at 120°C (*blue squares*) and at 140°C (*green squares*). The *straight lines* are linear fits with the slopes corresponding to the mean interlayer distance: $c_{ca} = 27.4 \pm 0.2$ nm and $c_{si} = 31.1 \pm 0.2$ nm on the carbon-coated and silicon oxide substrates, respectively, at 120°C. The intercept on the carbon coating indicates a wetting layer of 13.4 ± 0.5 nm, which supports the upper layers. Increasing the annealing temperature to 140°C results in the phase transition from PL to the bulk cylinder morphology (**c**). The sketches introduce the tentative structure throughout the film and the related wetting conditions: symmetric wetting of the silicon substrate and the free surface by the PB (*dark*) component, and asymmetric wetting conditions on the carbon coating

in the cylinder phase: the strongly interacting silicon oxide surface affects the enthalpic interactions of the adsorbed monomers and thus increases the incompatibility of the block copolymer components, which in turn initiates phase transitions to non-bulk morphologies.

An important insight regarding the bottom-up assisted self-assembly of microdomains is provided by analysis of the equilibrium terrace heights. Figure 14 summarizes the effect of wetting and segregation conditions on the structure formation in block copolymer melts. The linear fits at 120°C for the two substrates differ in the slope and in the offset value at the thickness axis. We note that on increasing the annealing temperature to 140°C, the morphological transition to the bulk cylinder phase (SFM images in Fig. 14c) and the related decrease in the slope of the linear fit (Fig. 14b) were observed [138].

The interlayer period on the silicon substrate (Fig. 14b) strongly suggests that under a certain strength of the surface fields, the substrate-induced phase transition to non-bulk morphology propagates through the entire film thickness (in contrast to the simulation results in Fig. 11). Direct experimental evidence on the propagation range of the surface-induced reconstructions can be provided by in-depth profiling of block copolymer materials (see Sect. 3.2). Here, we emphasize that recent success in utilizing chemically and topogaphically patterned substrates confirms the efficiency of the bottom-up self-assembly approach [2].

4.2 Phase Diagrams of Surface Structures in Swollen Films

The equilibration of block copolymer films by exposure to solvent vapor is an alternative to the thermal annealing procedure. The resulting structures are extremely sensitive to the solvent evaporation rate [147–150] and exhibit structural polymorphism in the presence of selective solvents [122, 150–157]. Solvent-assisted fabrication of non-equilibrium highly ordered block copolymer patterns is a rapidly developing experimental approach that is very promising in terms of fundamental understanding and practical applications. Here, we focus on the equilibrium behavior of block copolymer films swollen with a non-selective solvent [49, 51]. A non-selective solvent in a swollen film acts as a plasticizer and effectively lowers the glass-transition temperature of the glassy components. As a result, the chain mobility is considerably enhanced without a significant increase in the processing temperature.

As established by Knoll et al. [49, 62], exposing thin films to well-controlled vapor pressure with a subsequent fast quench provides reproducible phase behavior under variation of the film thickness and of the polymer volume fraction (Fig. 15). At favored film thicknesses, cylinders orient parallel to the film plane, whereas a perpendicular orientation dominates at intermediate film thicknesses. In films thinner than 1.5 nm domain spacings and at high polymer concentration, the cylindrical

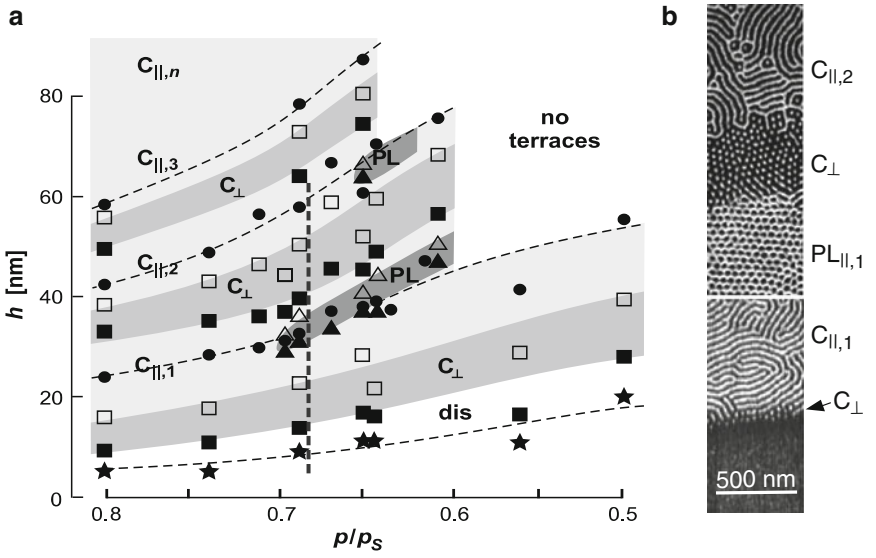

Fig. 15 (**a**) Phase diagram of the surface structures in SBS films (see Table 1) versus the partial chloroform vapor pressure. Horizontal *dashed lines* represent the energetically favored terrace thickness. Data are given for equilibrium film thickness of lying cylinders (*circles*), disordered structures (*stars*), and for upper and lower bounds (*open* and *closed symbols*, respectively) of upstanding cylinders (*squares*), and the perforated lamella phase (*triangles*). Reprinted from [62], with permission. Copyright 2002 by the American Physical Society. (**b**) Phase SFM images representing the indicated surface structures along the vertical *dashed line* in (**a**)

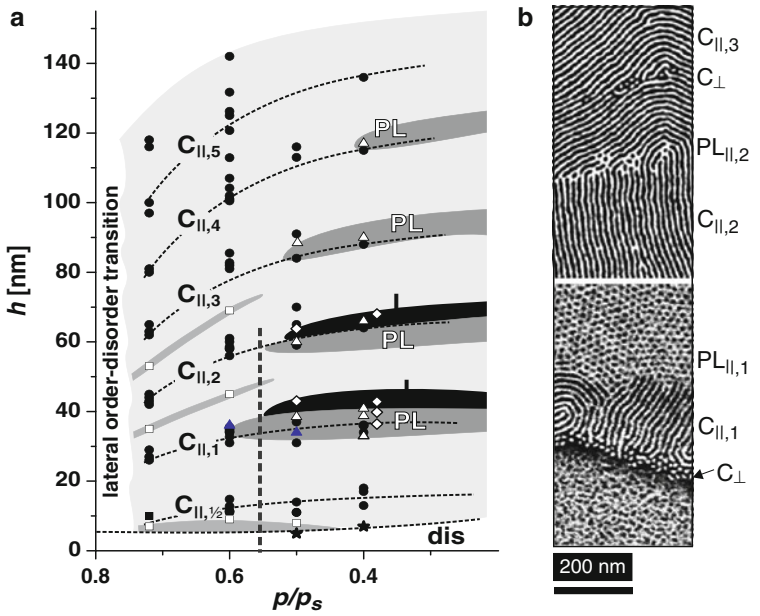

Fig. 16 (**a**) Phase diagram of the surface structures in SB^{47} films (see Table 1) versus the partial chloroform vapor pressure. Horizontal *dashed lines* represent the energetically favored thickness of the terraces. Data are given for equilibrium film thickness of lying cylinders (*circles*), disordered structures (*stars*), up-standing cylinders (*squares*), the perforated lamella (*triangles*), and lamella (*diamonds*) phases. (**b**) Phase SFM images representing the indicated surface structures along the vertical *dashed line* in (**a**)

microdomains reconstruct to the PL structure. These experimental results are in excellent agreement with model calculations based on the DDFT [58, 59, 62]. We have used the same experimental approach to study concentrated solutions of SB^{47} diblock copolymer in thin films. A comparison of the phase diagrams of surface structures in Figs. 15 and 16 suggests that the general phase behavior of SBS triblock copolymer is very similar to that of SB^{47} diblock copolymer. In particular, the same sequence of structures with increasing film thickness is observed (Figs. 15b and 16b), including deviations from the bulk structure, such as the PL and a wetting layer in ultrathin films. This confirms the universality of the reported phenomena. However, the phase diagrams differ in details, such as the position of the phase boundaries, the structure of the steps between the terraces, and the stabilization of the lamella phase and of vertically oriented cylinders. The established difference is presumably the consequence of the molecular architecture effects, which originate from the larger molecular weight of the middle majority block and from the possible loops- versus-tails chain arrangement in the microphase domains of ABA triblock copolymers. We note that in a recent theoretical study on the phase behavior of sphere-forming di- and triblock copolymers, a stabilization of vertically oriented cylinder phase (a deviation from the bulk morphology) has been reported for ABA systems [107].

4.3 *Confinement Effects on the Microphase Separation and Polymer–Solvent Interactions in Swollen Films*

The current trend towards miniaturization of functional systems and devices has driven the study of confinement effects (finite film thickness and the nature of the binding interfaces) on the fundamental physical properties of soft materials. Rapid developments of novel sensor and lab-on-chip technologies, and of polymer-based stimuli-responsive materials, raise the question of changes in solvent–polymer interactions under confinement.

Both, organo- and water-soluble polymers have been subjected to studies of their swelling dynamics, the distribution of the solvent within thin films, and the diffusion of the solvent. Furthermore, the distribution of the electron density along the depth of dried films has been studied using different experimental techniques including SE [158], optical reflectometry, X-ray or neutron reflectivity [159, 160], grazing incidence small angle X-ray scattering (GISAXS) [161], quartz crystal microbalance [162], and other complementary techniques.

In contrast to swollen homopolymer films, only a limited number of studies on thin films of block copolymers have been reported in which the degree of the film swelling has been directly accessed. In situ SE has been used to evaluate the polymer–solvent interaction parameters [144], to construct phase diagrams of surface structures [49, 51], and to control the mechanism of lamella reorientation in thick swollen films [118, 163, 164]. Spectroscopic reflectometry combined with real-time GISAXS has been used to follow structural instabilities in swollen lamella films [165]. Recently, it was demonstrated that swelling of diblock copolymer films in organic selective and non-selective solvents follows the same physical behavior as in thin films of homopolymers [119].

Up to now, published results contain non-consistent or even contradicting information concerning the influence of confinement on solvent absorption and distribution in a swollen film. In particular, the correlation between the absolute solvent uptake and the film thickness, as well as the effect of substrate interactions on the distribution of the solvent within the film, remain unclear. Here, we address solvent-assisted self-assembly of block copolymers, and present recent studies on the response of the microphase-separated patterns towards solvent uptake under controlled variation of the the film thickness, interfacial interactions, and of the solvent concentration in the atmosphere [114, 166]. This research brings novel insights into the degrees of freedom that govern self-assembly of soft matter in a confined geometry and indicates new approaches towards fabrication and functioning of nanostructured materials.

In our experiments, the quench from a swollen to a glassy state has been achieved within tens of seconds, and has been shown not to alter the phase separation in a swollen state[49]. Figure 17 compares surface structures in SB^{47} films that have been exposed to a relative vapor pressure p/p_0 of 72% and of 80%. With an increase of the solvent concentration, the in-plane order of the microdomains

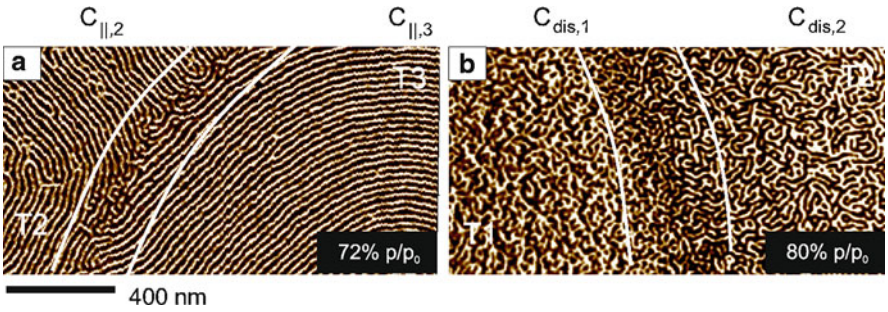

Fig. 17 SFM phase images (scale 10°) of SB^{47} films swollen with chlorofrom at (**a**) $p/p_0 = 72\%$ showing lying cylinders with a high degree of a long-range order, and (**b**) at $p/p_0 = 80\%$ showing a phase-separated pattern with a low long-range order (a disordered cylinder phase) [114]. White lines are guides for the eye and mark the borders of the areas with a constant film thickness

is dramatically reduced, indicating that the system is close to the ODT. In this segregation regime, the interface between two blocks is subjected to strong composition fluctuations [114, 166].

The increase of the solvent concentration in SB^{47} films on raising the partial pressure of chloroform vapor, and the related loss of long-range order, can be explained in terms of the so-called "dilution approximation" for the bulk block copolymer phases [167, 168]. The above results clearly demonstrate the high sensitivity of the polymer–polymer interactions towards solvent content. Therefore, the microphase-separated structures in swollen block copolymer films can be used as a qualitative measure of the degree of swelling of the films [49, 166].

Along with the surface interactions, the chain conformation that is imposed by the confined geometry and by the film preparation strongly affects the swelling behavior of polymer films [119, 169–171].

Figure 18a,b displays SFM images of SV films that have been prepared from chloroform and from toluene solutions, respectively. The mixed pattern of featureless areas and round-shaped stripes in Fig. 18a can be identified as in-plane lamella and perpendicular-oriented lamellae, respectively. The microstructure prepared from toluene solutions (Fig. 18b) is attributed to P2VP micelles surrounded by the PS shell. The micelle morphology is a result of the SV self-assembly in a selective solvent [119]. We have made use of this morphological difference to study the microstructure response to solvent uptake by block copolymer films.

Figure 18c displays swelling kinetics of two SV films with the same initial thickness but different microphase-separated structures. The curves show up to 10% larger swelling (smaller ϕ_{pol}) of SV films with the initial bulk lamella morphology as compared to the films with the non-bulk micelle phase [119].

This difference is probably associated with the chain expansion and/or contraction relative to the interface between the blocks within the particular morphology. In analogy to solid inorganic materials whose solubility increases under external pressure and to colloid systems where the capillary pressure leads to an increase in the solubility (Ostwald ripening effect), one would intuitively expect larger swelling of

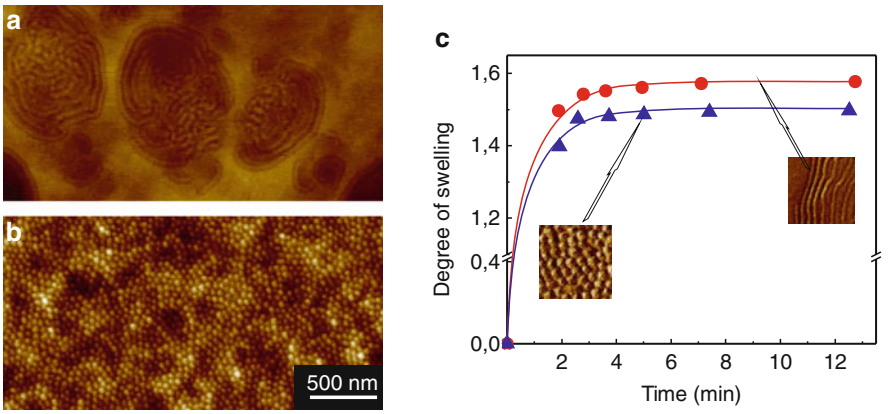

Fig. 18 SFM height images (scale 20 nm) of representative surface structures in SV films after spin-coating from chloroform solution (**a**), and from toluene solution (**b**). (**c**) Comparison of the swelling kinetics of ≈ 400-nm-thick SV films with starting micelle (*triangles*) and lamella (*circles*) morphologies

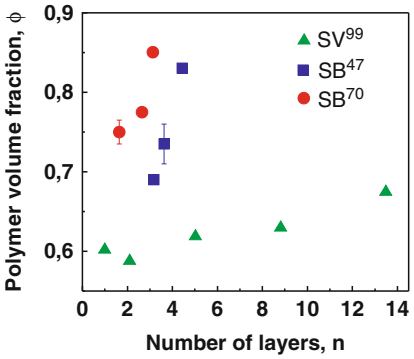

Fig. 19 Polymer volume fraction $\phi = h_{\mathrm{dry}}/h_{\mathrm{sw}}$ in swollen films of two PS-*b*-PB diblock copolymers (SB^{47} (*circles*) and SB^{70} (*squares*)) that have been equilibrated at $p/p_0 = 50\%$ of the partial chloroform (non-selective solvent) vapor pressure [114], and of SV films (*triangles*) equilibrated under $p/p_0 = 80\%$ of toluene (selective solvent) [119] versus the number of layers (film thickness normalized by the respective structure dimension in bulk)

the polymer chains that form non-bulk structures due to their stronger perturbation. However, we observed the opposite effect, which has to be considered in computer simulations and analytical theories on molecular conformations of block polymer chains in microdomain space.

Figure 19 summarizes the effect of confinement on the macroscopic swelling of the studied block copolymer systems. The systems differ in the molecular weight and composition of the studied block copolymers, in the solvent quality, and in the experimental conditions (which control the solvent atmosphere; see Sect. 3). At a constant vapor pressure, the equilibrium ϕ_{pol} for each polymer becomes smaller

as the film thickness decreases. The decrease of the solvent uptake by relatively thick SV film excludes a substantial contribution of an excess solvent layer at the polymer–substrate interface to an enhanced swelling of ultrathin films.

The established thickness-dependent degree of swelling discloses newly observed nanoscale effects of confinement on the chain conformations and on the polymer–solvent interactions in thin films. In particular, an easy and effective approach towards multilevel control over lamella orientation and order in thick diblock copolymer films has been demonstrated. The novel finding concerns the reorientation of lamella domains relative to the substrate upon equilibration under selective solvent [118]. The lamellar orientation perpendicular to the film plane on long-term selective solvent annealing was detected only in a narrow window of film thickness (between 19 and 22 characteristic lamella spacings in bulk L_0), and was confirmed by combined SFM, GISAXS, and TEM measurements (Fig. 20). Otherwise, lamellae were perfectly aligned parallel to the film plane due to surface field effects. The reorientation of lamella domains is attributed to the thickness-dependent degree of swelling when the concentration fluctuations in the interior of the film due to chain stretching overcome the suppression by the surface fields, which decline in strength

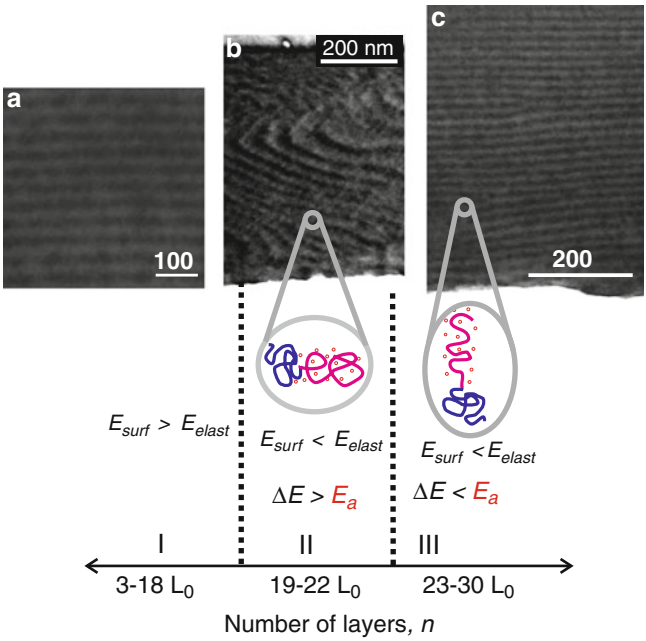

Fig. 20 Cross-sectional TEM images of equilibrated SV films within the respective thicknesses regions (**a**, **b**, **c**). The *dark regions* represent the stained P2VP microdomains. Schematic presents a qualitative analysis of the two contributions to the total free energy density of the system, E_{surf} and E_{elast}. E_{elast}. E_a is the activation energy for the reorientation of lying lamella to upstanding lamella [118]. L_0, lamella spacing in bulk. The sketches indicate that the chain conformation in regions II and III

with increasing distance from the boundary surfaces. We note that the combination of multiple fields based on solvent annealing and electric field yields an excellent control over the 3D orientation and order of lamellar microdomains [118].

4.4 Scaling of Cylinder Spacings in Thin Films

For an in-depth understanding of the self-assembly process in block copolymer films, a quantitative measure of the characteristic distances and their dependence on relevant physical parameters (temperature, chain length, etc.) is essential. In bulk, such measurements have typically been done by small angle X-ray scattering (SAXS) and the results are broadly in line with the theoretical predictions [172]. In thin films, however, the situation is considerably more difficult because conventional scattering experiments are barely possible due to the insufficient amount of material. In lamellar-forming block copolymers, neutron reflection experiments have successfully been used to determine the characteristic lamellar spacing in thin films [173, 174]. We present here quantitative experiments on characteristic lengths for compositionally asymmetrical block copolymers. The algorithm to quantify the characteristic lateral spacings in thin films of cylinder block copolymers is described in [113].

The results of the analytical procedure are shown in Fig. 21 where characteristic distances between the cylinders are plotted as a function of the local thickness of the film. Quite strikingly, we observed a systematic variation of the lateral spacing between the cylinders as the film thickness increases from n to $n+1$ layers of cylinders. Moreover, the characteristic spacings in the lower terrace was systematically

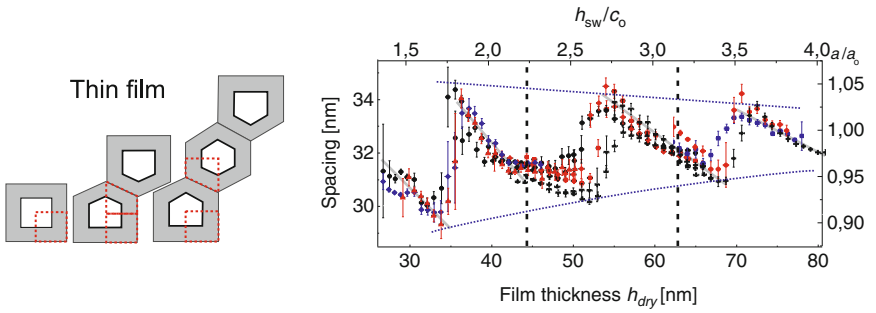

Fig. 21 Absolute microdomain spacings and reduced spacings versus the thickness h_{dry} of quenched films. Different symbols correspond to different measurements and experiments. The vertical *dashed lines* indicate the energetically favored film thicknesses at terraces. The straight *gray lines* emphasize different slopes of spacing relaxation on accommodation of the next layer of cylinders. Two *dotted lines* follow the minimum and maximum deviations of the macrodomain spacings from a_o, where a_o is the spacing in the bulk. (*Left*) Unit cells in thin films used for the strong-segregation theory calculation in [113]. The *dotted lines* denote the actual calculated geometries. Reprinted from [113], with permission. Copyright 2007 American Chemical Society

0.5–1 nm smaller than that in the neighboring higher terrace (Figs. 21 and 4). The differences in the lateral spacings in the adjacent terraces vanish in the fourth layer [113]. The effect is clearly measurable and points to 1D stretching of a unit cell in thin block copolymer films.

The digital spacing analysis and its applications present a novel type of quantitative characterization of thin structured films. In particular, changes to the cylinder spacings in thermally annealed films with the variation of the annealing temperature suggested stronger segregation under confinement relative to the bulk melt at the same temperature [51, 138]. Also, accumulation of spacings data during the development of a dewetting rim can be used for quantitative analysis of stress distribution within the moving front, which may bring insights into the rheological properties of polymer films on a mesoscale [51].

4.5 Microdomain Dynamics

The growing number of applications of nanopatterns in technology is a strong incentive to develop an improved understanding of ordering dynamics with the aim of controlling the resulting nanopatterned surfaces. The high degree of order relative to the film surfaces, as well as long-range in-plane order of the film, are imperative to applications of nanopatterned surfaces [2, 3, 19].

Common, though for many applications undesired, features in block copolymer nanostructures are point and line defects, grain boundaries, metastable phases, as well as distortions in microdomains orientation. The key role of the generation and annihilation of topological defects was emphasized in the studies on structural phase transitions, long range alignment, and reorientation of microdomains under shear and under electric fields. However, all these studies relied on indirect experimental evidence from scattering and other spatially averaging techniques.

In this section, we review our research on structural defects and their short- to long-term dynamics in block copolymer films using in situ SFM measurements at elevated temperatures, and DDFT-based simulations. The strength of our approach is that structures visualized with SFM 2D are directly compared with computational structures that provide access to the structure away from the surface of imaging, in the interior of the film. We focus on specific defects in the cylinder phase that are kinetically trapped in thermal equilibrium during the lateral ordering of lying microdomains. While topological defects in polymer thin films resemble those commonly observed in other forms of ordered matter, block copolymers exhibit morphological and dynamic properties that are specific to their polymeric nature [175–180].

4.5.1 Classification of Characteristic Defects

We distinguish between classical, modified, specific, and grain boundary defect configurations. Figure 22 presents examples of simulated and measured classical

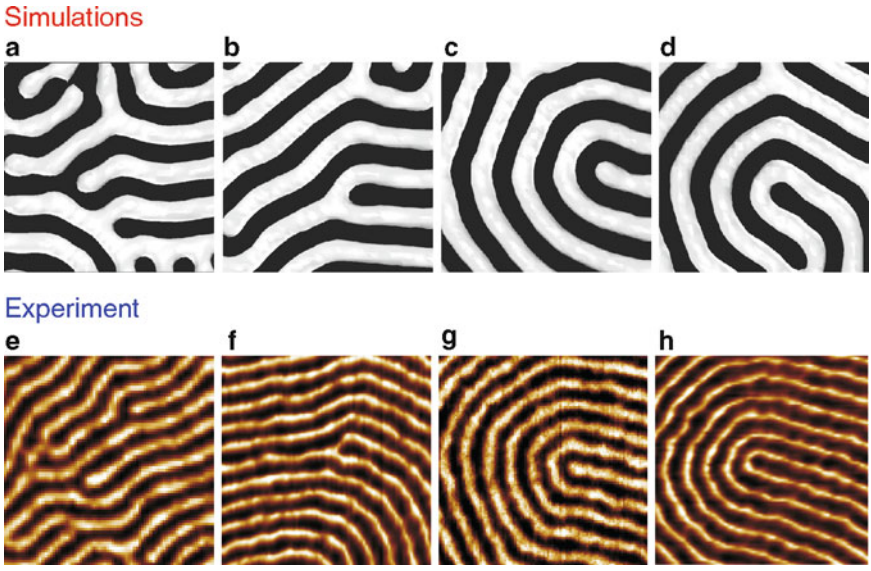

Fig. 22 Simulated images (*upper panel*) and SFM phase images (300×300 nm) (*lower panel*) presenting classical topological defect configurations in lying cylinders: (**a, e**) cyl-dislocation; (**b, f**) m-dislocation; (**c, g**) $+1/2$ cyl-disclination; and (**d, h**) $+1/2$ m-disclination. SB films were annealed under 70% of the saturated vapor pressure of chloroform. Reprinted from [36], with permission. Copyright 2008 American Chemical Society

defects in triblock and diblock copolymers. Purely topological arguments are sufficient to describe defects in films with upstanding lamella, since a topological defect always implies the abruption of one component. In contrast, in cylindrical phases the major dark-colored matrix (PB phase) is always interconnected, but the 2D representation of topological defects conceals this important property.

In order to account for the real 3D structure of cylindrical microdomains, we denote the configurations in Fig. 22a, e and c, g as cylinder-phase defects (cyl-dislocation and $+1/2$ cyl-disclination), and the configurations in Fig. 22b,f and d,h as matrix defects (m-dislocation and m-disclination). In our systems, cyl-dislocations generally develop during the early stages of film annealing when the overall defect density is high. In well-equilibrated films, cyl-dislocations are less frequent as compared to m-dislocations.

Modified Classical Defects

The rich phase behavior of cylinder-forming block copolymers is reflected in the modification of classical defects by incorporation of elements of non-bulk structures such as $+1/2$ disclination with incorporated PL ring (Fig. 23a, d) or white dot (b, e); and $-1/2$ disclination with incorporated PL domain (Fig. 23c, f). Defects Fig. 23a and b are topologically equivalent, but functionally different. Their

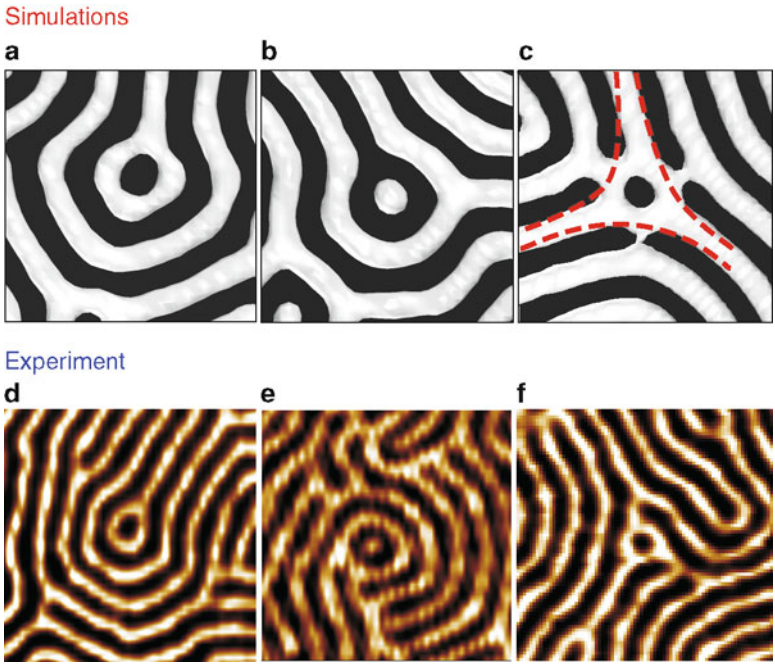

Fig. 23 Simulated images (*upper panel*) and SFM phase images (300×300 nm) (*lower panel*) presenting specific defect configurations: $+1/2$ disclination (**a, d**) and $-1/2$ disclination (**c, f**) with incorporated PL fragment; (**b, e**) $+1/2$ dot-disclination. SB films were annealed under 50% of the saturated vapor pressure of chloroform. Reprinted from [36], with permission. Copyright 2008 American Chemical Society

temporal stability and role in the overall structure evolution are discussed in detail in [36]. In particular, the PL phase lacks the axial symmetry; therefore it effectively compensates large disorientations of cylinder grains.

Specific Defects

Figure 24 presents specific neck defects, which can be viewed as a closely interacting pair of m-dislocations (Fig. 24a and related sketch). Such necks provide connectivity of the minority phase and thereby facilitate material transport without crossing the PS–PB interface. Interestingly, in DDFT simulations neck defects are not seen in the ordered cylinder phase. This fact probably indicates a small energy difference between the neck defect and the defect-free cylinders. Considering the experimental conditions when the necks between cylinders form, we conclude that their origin is driven by local concentration fluctuations.

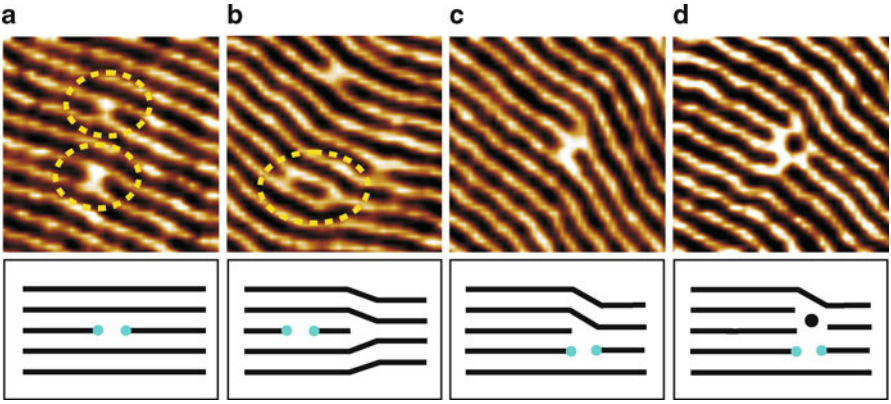

Fig. 24 SFM phase images of surface structures in SB films, which were equilibrated under 70% of the chloroform-saturated atmosphere, showing specific neck defects (**a**) highlighted by *dashed circles*; interaction of neck-defects with m-dislocations (**b, c**), and with a single PL ring (**d**). Reprinted from [36], with permission. Copyright 2008 American Chemical Society

Detailed analysis of defect configurations in the cylinder phase and of their evolution allowed us to conclude that representative defect configurations provide connectivity of the minority phase in the form of dislocations with a closed cylinder end or of classical disclinations with incorporated alternative, non-bulk structures with planar symmetry. Further, block copolymers show a strong correlation between the defect structure and chain mobility on both short- and long-term time scales.

We note that earlier research focused on the similarities of defect interaction and their motion in block copolymers and thermotropic nematics or smectics [181, 182]. Thermotropic liquid crystals, however, are one-component homogeneous systems and are characterized by a non-conserved orientational order parameter. In contrast, in block copolymers the local concentration difference between two components is essentially conserved. In this respect, the microphase-separated structures in block copolymers are anticipated to have close similarities to lyotropic systems, which are composed of a polar medium (water) and a non-polar medium (surfactant structure). The phases of the lyotropic systems (such as lamella, cylinder, or micellar phases) are determined by the surfactant concentration. Similarly to lyotropic phases, the morphology in block copolymers is ascertained by the volume fraction of the components and their interaction. Therefore, in lyotropic systems and in block copolymers, the dynamics and annihilation of structural defects require a change in the local concentration difference between components as well as a change in the orientational order. Consequently, if single defect transformations could be monitored in real time and space, block copolymers could be considered as suitable model systems for studying transport mechanisms and phase transitions in 2D fluid materials such as membranes [183], lyotropic liquid crystals [184], and microemulsions [185].

4.5.2 Phase Transitions and Defect Evolution in Dynamic SFM Measurements and DDFT Simulations

Using the calculational method based on DDFT, deviations from the cylinder bulk morphology have been identified as surface reconstructions [58, 62]. The constructed structure or phase diagrams allowed surface field and confinement effects to be distinguished [57–59, 107, 145, 186]. The comparative analysis of defect types and dynamics disclosed annihilation pathways via temporal phase transitions [36, 111]. Further, a quantitative analysis of defect motion led to an estimate of the interfacial energy between the cylinder and the PL phases [117]. A DDFT-based model was effectively used to simulate a block copolymer film with a free surface and to study the dynamics of terrace development [41, 42]. We showed how our computational method and an advanced dynamic SFM can be exploited in a synergetic fashion to extend the information about the elementary steps in structural transitions at the mesoscopic level. In particular, the experiments validate the dynamic DDFT method, and the DDFT calculations rationalize the characterization of the film surface in the interior of the film [187].

In situ dynamic measurements and DDFT simulations to non-bulk PL and lamella morphologies (Figs. 25 and 26) demonstrate that annihilation of topological

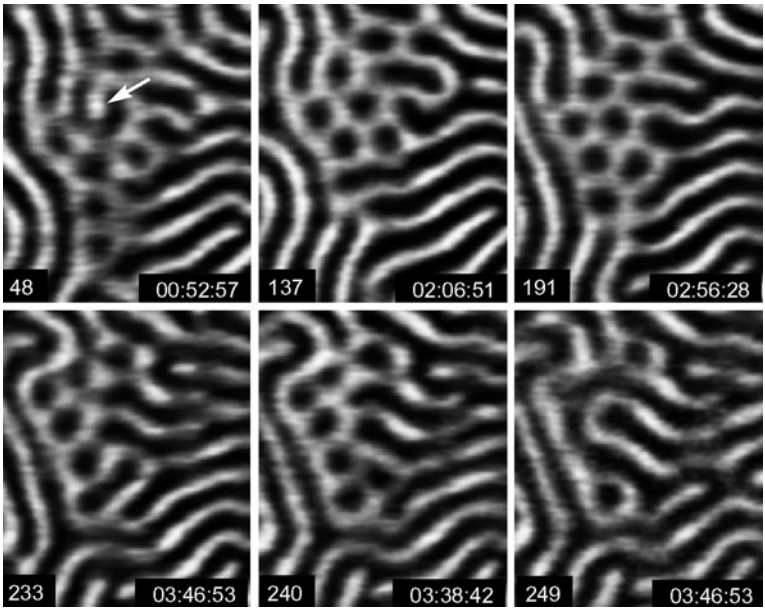

Fig. 25 SFM phase images showing the transient PL phase at the boundary between the cylinder grains. In *Frame 48*, an array of PL rings is aligned along the grain boundary and grouped around a "horse-shoe" defect (*arrow*). In *Frame 249* the transient phase is annihilated into the +1/2 disclination. The total evolution of the PL phase is about 4 h. The frame number and the elapsed time of the measurement are shown. Reprinted from [111], with permission. Copyright 2006 American Chemical Society

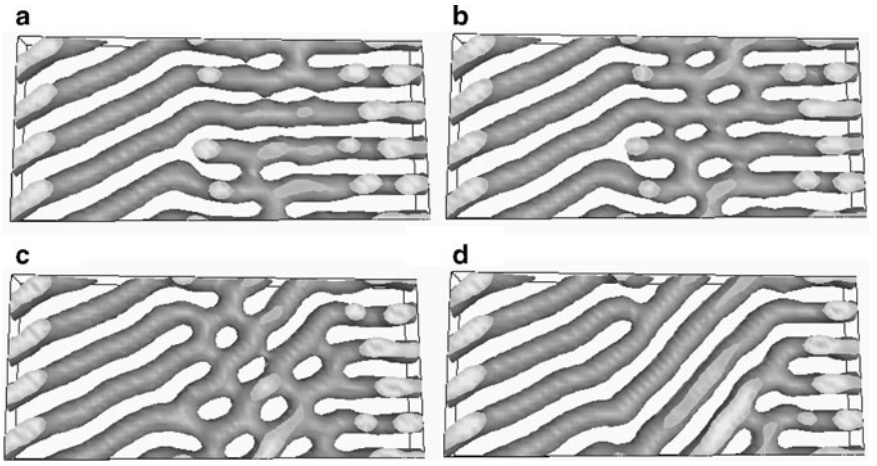

Fig. 26 Snapshots of DDFT calculations, modeling a thin supported film of $A_3B_{12}A_3$ cylinder-forming block copolymer in a $128 \times 32 \times 26$ bit volume. Crops of the middle layer, visualizing the reorientation of cylinders via the transient PL phase are shown after (**a**) 56,000, (**b**) 57,200, (**c**) 58,400, and (**d**) 59,600 time steps. The thin film morphology is shown by the isodensity surface of A component for a threshold value of $\epsilon_A = 0.33$. Reprinted from [111], with permission. Copyright 2006 American Chemical Society

defects in the cylinder phase in many instances proceeds via local temporal phase transitions. The low interfacial tension of $\sim 2.5\,\mu Nm^{-1}$ between the cylinder and the PL phases probably accounts for the energetically favorable pathway of structural rearrangements via phase transitions [117].

4.5.3 Evaluation of the Dynamic SFM Measurements

The high temporal resolution of SFM imaging uncovered elementary dynamic processes of structural rearrangements. We observed short-term interfacial undulations [111], fast repetitive transitions between distinct defect configurations [112], their spatio-temporal correlations on a length scale of several microdomains [112], and unexpected defect annihilation pathways via formation of temporal excited states [51, 111].

To analyze the temporal evolution of the microdomain oscillations between certain defect configurations, we associate the configurational energy of defects 1–2 and A–F in Fig. 27a with the number of open ends in the structures, and in Fig. 27b plot their temporal evolution. The thick gray curves highlight the periods of prevailing appearance of configurations with one open end and with two open ends. Within each of these periods there are short-time transitions into other configuration. The similarity of the averaging curves suggests that the events at the two neighboring sites are correlated on the scale of at least several domain spacings and

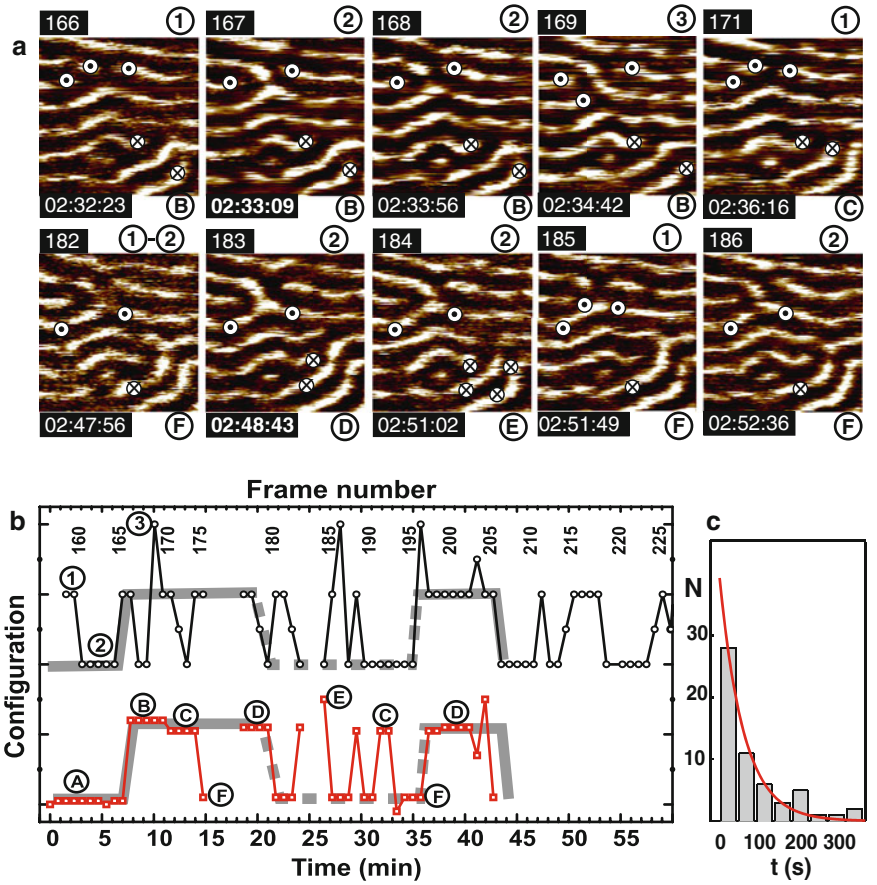

Fig. 27 (**a**) Crops (250 × 250 nm) from selected frames of the SFM movie showing the oscillations between distinct defect configurations. *Circled dot* and *crossed circle* mark the open ends of the cylinders. The structure marked with the *circled dot* fluctuates mainly between the configuration with three "open ends" (1) and the configuration with two "open ends" (2). The structure marked with the *crossed circle* fluctuates between configurations with one (*A*, *F*) or two "open ends" (*B*, *C*, *D*). (**b**) Temporal evolution of the defect configurations displayed in Fig. 27a. The configurations are sorted and grouped along the configuration coordinate according to their number of "open ends". The *gray curves* suggest correlations of defect dynamics. (**c**) Histogram of the time between two successive transitions shown in (**b**). Reproduced with permission from [112]. Copyright 2006 American Chemical Society

on a time scale of seconds. Moreover, we estimated the relaxation times involved and proposed possible molecular mechanisms that could account for these dynamics (Fig. 27c) [112]. Comparison of typical transition time with characteristic diffusion coefficients suggests that the motion proceeds via correlated movement of clusters of chains.

An original approach to the reduction and visualization of large sets of temporal evolution data has been recently presented [136]. Microdomains are reduced to thin smooth lines with colored branching points and visualized with a tool for protein visualization.

4.6 Structural Polymorphism of ABC Terpolymers

When a chemical variety of a linear block copolymer is increased to three different components, an intricate diversity of structures becomes possible [188, 189]. This is due to considerable increase in the number of involved polymer–polymer and polymer–surfaces interaction parameters. The studies on thin film behavior of ABC terpolymers are rare, even though they may potentially be more versatile than binary block copolymer morphologies due to the increased complexity.

Both theoretical [186, 190–192] and experimental [63, 123, 124, 128, 193] studies have demonstrated that interaction of the middle B block with a substrate plays a decisive role in the lamella structure orientation and order in thin films.

In the case of non-symmetrical volume composition, Elbs et al. facilitated different phases in polystyrene-*block*-poly(2-vinylpyridine)-*block*-poly(*tert*-butylmethacrylate) (SVT) films by exposing them to different solvent vapors (Fig. 28). Further studies indicated a large morphology dependence on the annealing vapor and drying conditions [4]. Rehse et al. demonstrated the presence of

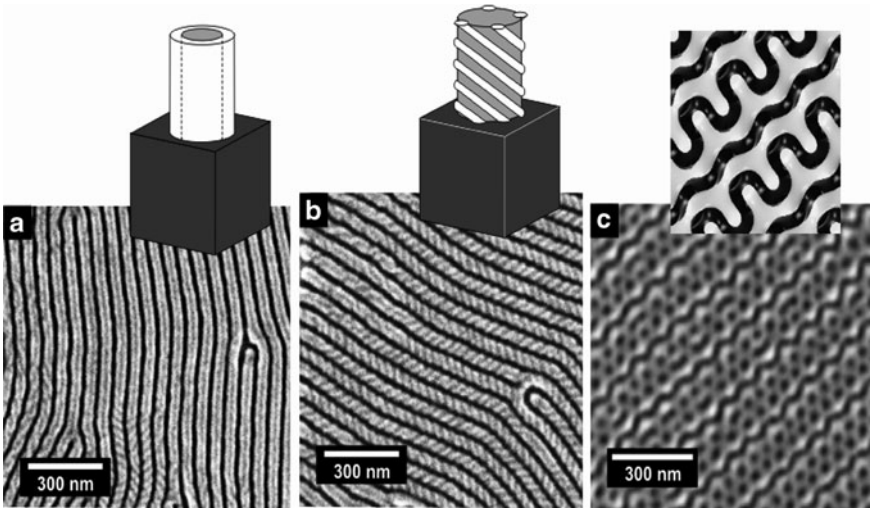

Fig. 28 SEM images of about 60 nm thick films of SVT block terpolymers along with expected structural elements of the thin-film structure. (**a**) Core–shell cylinders; (**b**) helices wound around a cylindrical core; (**c**) (112) plane of an ideal double gyroid structure. Copyright (2002) Wiley. Used with permission from [18]

non-bulk surface-reconstruction morphologies using ABC terpolymers of different compositions [126–128]. Ludwigs et al. systematically studied the phase behavior of SVT thin films [53, 63, 129, 130] and could match these results to DDFT calculations [186]. These studies demonstrated that confined systems are very sensitive to small changes in the energetic interaction between the different components, leading to a wide variety of possible surface reconstructed morphologies. Amongst other morphologies, a stable and highly ordered PL phase has been found, which could find use in membrane applications [63, 131]. The high order of the PL phase over macroscopically large areas was presumably caused by the bicontinuous nature of the morphology. Studies by other groups have been recently reviewed in [4].

5 Perspectives and Challenges

With advanced physical characterization techniques and theoretical analyses, the scientific understanding of the structure, dynamics, and thin film behavior of both compositionally simple and complex block copolymer architectures is rapidly expanding. The interest is supported, above all, by their growing importance in nanotechnology. The development is possible due to conjugation of new synthetic capabilities, processing methods, and self-assembly paradigms. Currently, attention is shifting towards new structural motifs for designing systems capable of hierarchical self-assembly into complex, well ordered, functional mesostructures.

Recent remarkable progress in polymerization techniques allows the preparation of well-defined tailor-made macromolecules, with precise control over the molecular weight, structure, architecture, and placement of functional groups [194]. A comprehensive review by Granick et al. [195] describes recommended synthetic directions and approaches, including the creation of organo-polymeric composites (light-emitting devices) and bio-related hybrid materials.

Increasing the structural complexity and functionality of new block copolymer materials while introducing additional hierarchy into self-assembly inevitably implies more complex dynamic routes for achieving the desired order on mesoscopic and macrososcopic scales. A detailed comparison between morphological studies and theoretical predictions will develop better understanding and control over the structure of functionalized block copolymers and will allow the tailoring of optical, mechanical, conducting, and other functional properties.

However, with the expanding spectrum of complexity and functionality of new polymer-based hybrid materials, no general routes and recipes for processing polymer-assisted materials should be expected. The effort to establish new approaches for guiding self-assembly of complex functional materials is the key to further technological application.

Acknowledgements This research has been supported by the DPG (Sonderforschungsbereich 481, TP B7/A9). The authors acknowledge the valuable contribution of R. Magerle, A.V. Zvelindovsky, A. Knoll, S. Ludwigs, A. Horvat, N. Rehse, H. Elbs, K. Lyakhova, J. Gensel, and M. Hund.

References

1. Park C, Yoon J, Thomas EL (2003) Polymer 44:6725
2. Li M, Coenjarts CA, Ober CK (2005) In: Abetz V (ed) Block copolymers II. Advances in polymer science, vol 190. Springer, Heidelberg, pp 183–226
3. Nie Z, Kumacheva E (2008) Nat Mater 7(4):277
4. van Zoelen W, ten Brinke G (2009) Soft Matter 5(8):1568
5. Hamley IW (2009) Prog Polym Sci 34(11):1161
6. Tang C, Lennon EM, Fredrickson GH, Kramer EJ, Hawker CJ (2008) Science 322(5900):429
7. Guo LJ (2007) Adv Mater 19(4):495
8. Haryono A, Binder WH (2006) Small 2(5):600
9. Hashimoto T, Fukunaga K (2007) In: Zvelindovsky AV (ed) Nanostructured soft matter: experiment, theory, simulation and perspectives. Springer, Heidelberg, pp 45–97
10. Hillmyer MA (2005) In: Block copolymers II. Advances in polymer science, vol 190. pp 137–181
11. Cheng JY, Ross CA, Chan VZH, Thomas EL, Lammertink RGH, Vancso GJ (2001) Adv Mater 13:1174
12. Thurn-Albrecht T, Schotter J, Kastle GA, Emley N, Shibauchi T, Krusin-Elbaum L, Guarini K, Black CT, Tuominen MT, Russell TP (2000) Science 290:2126
13. Matsen MW (1997) J Chem Phys 106:7781
14. Matsen MW (1998) Curr Opin Colloid Interface Sci 3:40
15. Fasolka MJ, Mayes AM (2001) Annu Rev Mater Res 31:323
16. Hamley IW (1998) The physics of block copolymers. Oxford University Press, Oxford
17. Hamley IW (2004) Developments in block copolymer science and technology. Wiley, Hoboken, pp 1–29
18. Krausch G, Magerle R (2002) Adv Mater 14:1579
19. Segalman RA (2005) Mater Sci Eng R Rep 48:191
20. Trawick M, Angelescu D, Chaikin P, Register R (2005) Nanolithography and patterning techniques in microelectronics. Woodhead Publishing, Cambridge, pp 1–38
21. Darling SB (2007) Prog Polym Sci 32:1152
22. Farrell RA, Fitzgerald TG, Borah D, Holmes JD, Morris MA (2009) Int J Mol Sci 10(9):3671
23. Cheng JY, Ross CA, Smith HI, Thomas EL (2006) Adv Mater 18:2505
24. Bita I, Yang JKW, Jung YS, Ross CA, Thomas EL, Berggren KK (2008) Science 321(5891):939
25. Böker A (2007) In: Zvelindovsky AV (ed) Nanostructured soft matter:experiment, theory, simulation and perspectives. Springer, Heidelberg, pp 199–229
26. Xu T, Wang J, Russel TP (2007) In: Zvelindovsky (ed) Nanostructured soft matter: experiment, theory, simulation and perspectives. Springer, Heidelberg, pp 171–198
27. Daoulas KC, Müller M, Stoykovich MP, Kang H, de Pablo JJ, Nealey PF (2008) Langmuir 24:1284
28. Ruiz R, Kang H, Detcheverry FA, Dobisz E, Kercher DS, Albrecht TR, de Pablo JJ, Nealey PF (2008) Science 321:936
29. Khanna V, Cochran EW, Hexemer A, Stein GE, Fredrickson GH, Kramer EJ, Li X, Wang J, Hahn SF (2006) Macromolecules 39(26):9346
30. Bates FS, Fredrickson GH (1990) Annu Rev Phys Chem 41:525
31. Matsen MW, Bates FS (1996) Macromolecules 29(4):1091
32. Fasolka MJ, Banerjee P, Mayes AM, Pickett G, Balazs AC (2000) Macromolecules 33:5702
33. Khandpur AK, Förster S, Bates FS, Hamley IW, Ryan AJ, Bras W, Almdal K, Mortensen K (1995) Macromolecules 28:8796
34. van Vlimmeren B, Maurits N, Zvelindovsky A, Sevink G, Fraaije J (1999) Macromolecules 32:646
35. Sevink GJA, Zvelindovsky AV, van Vlimmeren BAC, Maurits NM, Fraaije JGEM (1999) J Chem Phys 110(4):2250

36. Horvat A, Knoll A, Sevink GJA, Zvelindovsky AV, Krekhov A, Tsarkova L (2008) ACS Nano 2:1143
37. Liu Y, Zhao W, Zheng X, King A, Singh A, Rafailovich MH, Sokolov J, Dai KH, Kramer EJ (1994) Macromolecules 27:4000
38. Maaloum M, Ausserre D, Chatenay D, Coulon G, Gallot Y (1992) Phys Rev Lett 68:1575
39. Menelle A, Russell TP, Anastasiadis SH, Satija SK, Majkrzak CF (1992) Phys Rev Lett 68:67
40. Kim HC, Russell TP (2001) J Polym Sci B Polym Phys 39:663
41. Horvat A, Knoll A, Krausch G, Tsarkova L, Lyakhova KS, Sevink GJA, Zvelindovsky AV, Magerle R (2007) Macromolecules 40:6930
42. Lyakhova KS, Horvat A, Zvelindovsky AV, Sevink GJA (2006) Langmuir 22:5848
43. Tsarkova L, Knoll A, Krausch G, Magerle R (2006) Macromolecules 39:3608
44. Peters RD, Yang XM, Nealey PF (2002) Macromolecules 35:1822
45. Heier J, Kramer EJ, Groenewold J, Fredrickson GH (2000) Macromolecules 33:6060
46. Heier J, Sivaniah E, Kramer EJ (1999) Macromolecules 32:9007
47. Carvalho BL, Thomas EL (1994) Phys Rev Lett 73:3321
48. Yokoyama H, Mates TE, Kramer EJ (2000) Macromolecules 33:1888
49. Knoll A, Magerle R, Krausch G (2004) J Chem Phys 120:1105
50. Green PF, Limary R (2001) Adv Colloid Interface Sci 94:53
51. Tsarkova L (2007) In: Zvelindovsky AV (ed) Nanostructured soft matter:experiment, theory, simulation and perspectives. Springer, Heidelberg, pp 231–266
52. Smith AP, Douglas JF, Meredith JC, Amis EJ, Karim A (2001) Phys Rev Lett 87:015503
53. Ludwigs S, Schmidt K, Stafford CM, Amis EJ, Fasolka MJ, Karim A, Magerle R, Krausch G (2005) Macromolecules 38:1850
54. van Zoelen W, Polushkin E, ten Brinke G (2008) Macromolecules 41(2):8807
55. Bosworth JK, Black CT, Obert CK (2009) ACS Nano 3(7):1761
56. Park SM, Berry BC, Dobisz E, Kim HC (2009) Soft Matter 5:957
57. Huinink HP, van Dijk MA, Brokken-Zijp JCM, Sevink GJA (2001) Macromolecules 34:5325
58. Horvat A, Lyakhova KS, Sevink GJA, Zvelindovsky AV, Magerle R (2004) J Chem Phys 120:1117
59. Lyakhova KS, Sevink GJA, Zvelindovsky AV, Horvat A, Magerle R (2004) J Chem Phys 120:1127
60. Henkee CS, Thomas EL, Fetters LJ (1988) J Mater Sci 23:1685
61. Radzilowski LH, Carvalho BL, Thomas EL (1996) J Polym Sci B 34:3081
62. Knoll A, Horvat A, Lyakhova KS, Krausch G, Sevink GJA, Zvelindovsky AV, Magerle R (2002) Phys Rev Lett 89:035501/1
63. Ludwigs S, Böker A, Voronov A, Rehse N, Magerle R, Krausch G (2003) Nat Mater 2(11):744
64. Wang Q (2007) In: Zvelindovsky AV (ed) Nanostructured soft matter: experiment, theory, simulation and perspectives. Springer, Heidelberg, pp 498–528
65. Kong Y, Manke CW, Madden W, Schlijper A (1994) Int J Thermophys 15:1093
66. Fredrickson GH, Ganesan V, Drolet F (2002) Macromolecules 35:16
67. Daoulas KC, Müller M, de Pablo JJ, Nealey PF, Smith G (2006) Soft Matter 2:573
68. Wang Q, Nealey PF, de Pablo JJ (2002) Macromolecules 35:9563
69. Alexander-Katz A, Fredrickson G (2007) Macromolecules 40:4075
70. Nie Z, Su Z, Sun Z, Shi T, An L (2005) Macromol Theory Simul 14(8):463
71. Milner S, Morse D (1996) Phys Rev E 54:3793
72. Miao B, Yan D, Han C, Shi AC (2006) J Chem Phys 124:144902
73. Tsori Y, Andelman D (2001) Eur Phys J E 5(5):605
74. Matsen MW, Griffiths G (2009) Eur Phys J E 29:219
75. Nath SK, Nealey PF, de Pablo JJ (1999) J Chem Phys 110(15):7483
76. Tsori Y, Andelman D (2001) Macromolecules 34:2719
77. Tsori Y, Andelman D (2001) Europhys Lett 53:722
78. Tsori Y, Andelman D (2001) J Chem Phys 115:1970
79. Kim SO, Solak HH, Stoykovich MP, Ferrier NJ, de Pablo JJ, Nealey PF (2003) Nature 424:411

80. Tsori Y, Andelman D (2003) Macromolecules 36(22):8560
81. Tsori Y, Andelman D (2003) Interface Sci 11(2):259
82. Wang Q (2004) Macrom Theor Sim 14:96
83. Tsori Y, Sivaniah E, Andelman D, Hashimoto T (2005) Macromolecules 38:7193
84. Edwards EW, Stoykovich MP, Müller M, Solak HH, de Pablo JJ, Nealey PF (2005) J Polym Sci B 43:3444
85. Kim S, Kim BH, Meng D, Shin DO, Koo CM, Solak H, Wang Q (2007) Adv Mater 19:3271
86. Stoykovich M, Kang H, Daoulas KC, Liu G, Liu CC, de Pablo J., Müller M, Nealy PF (2007) ACS Nano 1:168
87. Koneripalli N, Levicky R, Bates FS, Matsen MW, Satija SK, Ankner J, Kaiser H (1998) Macromolecules 31(11):3498
88. Lee W, Elliott R, Mezzenga R, Fredrickson G (2009) Macromolecules 42:849
89. Hur SM, Garcia-Cervera C, Kramer E, Fredrickson G (2009) Macromolecules 42:5861
90. Tang C, Bang J, Stein G, Fredrickson GH, Hawker CJ, Kramer EJ, Sprung M, Wang J (2002) Macromolecules 35:9391
91. Ruokolainen J, Fredrickson GH, Kramer EJ, Ryu CY, Hahn SF, Magonov S (2002) Macromolecules 35:9391
92. Ryu CY, Ruokolainen J, Fredrickson GH, Kramer EJ, Hahn SF (2002) Macromolecules 35(6):2157
93. Pickett G, Balazs A (1997) Macromolecules 30:3097
94. Fasolka MJ, Harris DJ, Mayes AM (1997) Phys Rev Lett 79(16):3018
95. Geisinger T, Müller M, Binder K (1999) J Chem Phys 111(11):5241
96. Wang Q, Yan Q, Nealey PF, de Pablo JJ (2000) J Chem Phys 112(1):450
97. Meng D, Wang Q (2007) J Chem Phys 126:234902
98. Fasolka MJ, Banerjee P, Mayes AM, Pickett G, Balazs AC (2000) Macromolecules 33(15):5702
99. Tsori Y, Andelman D, Schick M (2000) Phys Rev E 61(3):2848
100. Boss A, Sides S, Katsov K, Garcia-Cervera C, Fredrickson G (2006) J Polym Sci B Polym Phys 44:2495
101. Croll A, Matsen M, Shi AC, Dalnoki-Veress K (2008) Eur Phys J E 27:407
102. Stein GE, Kramer EJ, Li X, Wang J (2007) Macromolecules 40:2453
103. Yokoyama H, Kramer EJ, Rafailovich MH, Sokolov J, Schwarz SA (1998) Macromolecules 31:8826
104. Segalman AR, Hexemer A, Kramer JE (2003) Phys Rev Lett 91(19):196101
105. Stein GE, Kramer EJ, Li X, Wang J (2007) Phys Rev Lett 98:086101
106. Stein GE, Cochran EW, Katsov K, Fredrickson GH, Kramer EJ, Li X, Wang J (2007) Phys Rev Lett 98:158302
107. Sevink GJA, Zvelindovsky AV (2009) Macromolecules. doi:10.1021/ma9014438
108. Wang Q, Nealey PF, de Pablo JJ (2001) Macromolecules 34(10):3458
109. Hammond MR, Sides SW, Fredrickson GH, Kramer EJ, Ruokolainen J, Hahn SF (2003) Macromolecules 36:8712
110. Khanna V, Cochran EW, Hexemer A, Stein GE, Fredrickson GH, Kramer EJ, Li X, Wang J, Hahn SF (2006) Macromolecules 39(26):9346
111. Tsarkova L, Horvat A, Krausch G, Sevink GIA, Zvelindovsky AV, Magerle R (2006) Langmuir 22:8089
112. Tsarkova L, Knoll A, Magerle R (2006) Nano Lett 6:2817
113. Knoll A, Tsarkova L, Krausch G (2007) Nano Lett 7:843
114. Zettl U, Knoll A, Tsarkova L (2009) Langmuir doi: 10.1021/la903922y
115. Konrad M, Knoll A, Krausch G, Magerle R (2000) Macromolecules 33:5518
116. Magerle R (2000) Phys Rev Lett 85(13):2749
117. Knoll A, Horvat A, Lyakhova KS, Krausch G, Sevink GJA, Zvelindovsky AV, Magerle R (2004) Nat Mater 3:886
118. Olszowka V, Tsarkova L, Böker A (2009) Soft Matter 5:812
119. Gensel J, Liedel C, Schoberth HG, Tsarkova L (2009) Soft Matter 5:2534

120. Elbs H, Fukunaga K, Stadler R, Sauer G, Magerle R, Krausch G (1999) Macromolecules 32(4):1204
121. Elbs H, Abetz V, Hadziioannou G, Drummer C, Krausch G (2001) Macromolecules 34(23):7917
122. Elbs H, Drummer C, Abetz V, Krausch G (2002) Macromolecules 35:5570
123. Fukunaga K, Elbs H, Magerle R, Krausch G (2000) Macromolecules 33(3):947
124. Fukunaga K, Hashimoto T, Elbs H, Krausch G (2002) Macromolecules 35(11):4406
125. Fukunaga K, Hashimoto T, Elbs H, Krausch G (2003) Macromolecules 36:2852
126. Rehse N, Knoll A, Magerle R, Krausch G (2001) Polym Mater Sci Eng 84:316
127. Rehse N, Knoll A, Konrad M, Magerle R, Krausch G (2001) Phys Rev Lett 87:035505
128. Rehse N, Knoll A, Magerle R, Krausch G (2003) Macromolecules 36(9):3261
129. Ludwigs S, Böker A, Abetz V, Müller AHE, Krausch G (2003) Polymer 44(22):6815
130. Ludwigs S, Schmidt K, Krausch G (2005) Macromolecules 38(6):2376
131. Sperschneider A, Schacher F, Gawenda M, Tsarkova L, Müeller AHE, Ulbricht M, Krausch G, Këhler J (2007) Small 3:1056
132. Knoll A, Magerle R, Krausch G (2001) Macromolecules 34:4159
133. Reiter G, Castelein G, Sommer JU, Röttele A, Thurn-Albrecht T (2001) Phys Rev Lett 87(22):226101
134. Yufa NA, Li J, Sibener SJ (2009) Macromolecules 42(7):2667
135. Hobbs JK, Mullin N, Weber CHM, Farrance OE, Vasilev C (2009) Mater Today 12(7–8):26
136. Scherdel S, Schoberth HG, Magerle R (2007) J Chem Phys 27(1):14903
137. Rehse S, Mecke K, Magerle R (2008) Phys Rev E 77:051805
138. Tsarkova, unpublished
139. Dietz C, Zerson M, Riesch C, Gigler AM, Stark RW, Rehse N, Magerle R (2008) Appl Phys Lett 92(14):143107
140. Rehse N, Marr S, Scherdel S, Magerle R (2005) Adv Mater 17(18):2203
141. Magerle R (2002) Lect Notes Phys 600:93
142. Hund M, Herold H (2007) Rev Sci Instrum 78(6):063703
143. Max E, Hund M, Tsarkova L (2008) PMSE Preprints 99:689–690
144. Elbs H, Krausch G (2004) Polymer 45(23):7935
145. Huinink HP, Brokken-Zijp JCM, van Dijk MA, Sevink GJA (2000) J Chem Phys 112:2452
146. Mansky P, Russell TP, Hawker CJ, Mays J, Cook DC, Satija SK (1997) Phys Rev Lett 79:237
147. Kim S, Misner M, Xu T, Kimura M, Russell T (2004) Adv Mater 16(3):226
148. Zhang Q, Tsui OKC, Du B, Zhang F, Tang T, He T (2000) Macromolecules 33(26):9561
149. Kim G, Libera M (1998) Macromolecules 31:2569
150. Turturro A, Gattiglia E, Vacca P, Viola GT (1995) Polymer 36:3987
151. Alexandridis P, Spontak RJ (1999) Curr Opin Colloid Interface Sci 4:130
152. Park S, Kim B, Xu J, Hofmann T, Ocko BM, Russell TP (2009) Macromolecules 42(4):1278
153. Xu T, Stevens J, Villa J, Goldbach JT, Guarini KW, Black CT, Hawker CJ, Russell TP (2003) Adv Funct Mater 13:698
154. To T, Wang H, Djurisic AB, Xie MH, Chan WK, Xie Z, Wu C, Tong SY (2004) Thin Solid Films 467:59
155. Huang H, Hu Z, Chen Y, Zhang F, Gong Y, He T, Wu C (2004) Macromolecules 37:6523
156. Harant AW, Bowman CN (2005) J Vac Sci Technol B 23:1615
157. Tokarev I, Krenek R, Burkov Y, Schmeisser D, Sidorenko A, Minko S, Stamm M (2005) Macromolecules 38:507
158. Tang Y, Lu JR, Lewis AL, Vick TA, Stratford PW (2002) Macromolecules 35(10):3955
159. Vogt BD, Soles CL, Jones RL, Wang CY, Lin EK, Wu Wl, Satija SK, Goldfarb DL, Angelopoulos M (2004) Langmuir 20(13):5285
160. Mukherjee M, Singh A, Daillant J, Menelle A, Cousin F (2007) Macromolecules 40(4):1073
161. Wang W, Troll K, Kaune G, Metwalli E, Ruderer M, Skrabania K, Laschewsky A, Roth SV, Papadakis CM, Müeller-Buschbaum P (2008) Macromolecules 41(9):3209
162. Vogt BD, Soles CL, Lee HJ, Lin EK, Wu W (2005) Polymer 46(5):1635
163. Olszowka V, Hund M, Kuntermann V, Scherdel S, Tsarkova L, Böker A (2009) ACS Nano 3(5):1091–1096

164. Olszowka V, Hund M, Kuntermann V, Scherdel S, Tsarkova L, Böker A, Krausch G (2006) Soft Matter 2:1089
165. Papadakis CM, Di Z, Posselt D, Smilgies DM (2008) Langmuir 24(24):13815
166. Tsarkova L (2010) Prog Colloid Polym Sci, in press
167. Helfand E, Tagami Y (1972) J Chem Phys 56(7):3592
168. Fredrickson GH, Leibler L (1989) Macromolecules 22(3):1238
169. Mondal MH, Mukherjee M, Kawashima K, Nishida K, Kanaya T (2009) Macromolecules 42(3):732
170. Barbero DR, Steiner U (2009) Phys Rev Lett 102(24):248303
171. Perlich J, Koerstgens V, Metwalli E, Schulz L, Georgii R, Müeller-Buschbaum P (2009) Macromolecules 42(1):337
172. Fredrickson GH, Bates FS (1996) Annu Rev Mater Sci 26:501
173. Koneripalli N, Levicky R, Bates FS (1996) Langmuir 12:6681
174. Lambooy P, Russell TP, Kellogg GJ, Mayers AM, Gallagher PD, Satija SK (1994) Phys Rev Lett 72:2899
175. Hamersky MW, Hillmyer MA, Tirrell M, Bates FS, Lodge TP, von Meerwall ED (1998) Macromolecules 31:5363
176. Yokoyama H, Kramer EJ (1998) Macromolecules 31:7871
177. Yokoyama H, Kramer EJ, Fredrickson GH (2000) Macromolecules 33:2249
178. Yokoyama H, Kramer EJ (2000) Macromolecules 33:954
179. Cavicchi KA, Lodge TP (2003) J Polym Sci B Polym Phys 41:715
180. Cavicchi KA, Lodge TP (2004) Macromolecules 37:6004
181. Harrison C, Adamson DH, Cheng Z, Sebastian JM, Sethuraman S, Huse DA, Register RA, Chaikin PM (2000) Science 290:1558
182. Harrison C, Cheng Z, Sethuraman S, Huse DA, Chaikin PM, Vega DA, Sebastian JM, Register RA, Adamson DH (2002) Phys Rev E 66:01170671
183. Müller M, Katsov K, Schick M (2003) J Polym Sci B 41(13):1441
184. Constantin D, Oswald P (2000) Phys Rev Lett 85(20):4297
185. Matsen MW (1998) J Chem Phys 110:4658
186. Ludwigs S, Krausch G, Magerle R, Zvelindovsky A, Sevink G (2005) Macromolecules 38(5):1859
187. Sevink GJA, Fraaije JGEM (2008) Macromolecules 1:53
188. Brinkmann S, Stadler R, Thomas EL (1998) Macromolecules 31(19):6566
189. Stadler R, Auschta C, Beckmann J, Krappe U, Voigt-Martin I, Leibler L (1995) Macromolecules 28(9):3080
190. Chen HY, Fredrickson GH (2002) J Chem Phys 116(3):1137
191. Chen P, Liang H (2006) J Phys Chem B 110(37):18212
192. Huang Y, Liu H, Hu Y (2006) Macromol Theory Simul 15(2):117
193. Fukunaga K, Elbs H, Krausch G (2000) Langmuir 16(7):3474
194. Kulbaba K, Manners I (2002) Polym News 27:43
195. Granick S et al (2003) J Polym Sci B 41:2755

Adv Polym Sci (2010) 227: 75–99
DOI:10.1007/12_2009_22

Published online: 6 November 2009

Controlled Wrinkling as a Novel Method for the Fabrication of Patterned Surfaces

Alexandra Schweikart, Anne Horn, Alexander Böker, and Andreas Fery

Abstract This contribution reviews recent findings on nonlithographic approaches for topographical structuring of polymeric surfaces and application of the resulting surfaces for creating hierarchical structures. External mechanical fields are used to induce a so-called buckling instability, which causes the formation of wrinkles with well-defined wavelength. We introduce the theoretical foundations of the phenomenon. The universality of the principle and the range of wavelengths between fractions of a micrometer and hundreds of microns that can be achieved are discussed. In the following we focus on the application of these surfaces as templates for the deposition of colloidal particles such as artificial particles (polystyrene beads, gold-nanoparticles or polymeric core-shell particles) and bionanoparticles (tobacco mosaic virus). We demonstrate how patterns can be transferred from the supporting wrinkled surfaces onto a broad variety of flat surfaces like glass or silicon wafers by stamping, where the complex colloidal patterns are accessible for studying their optical, electronic or other physical properties.

Keywords wrinkling · Thin-film · Elastomeric polymer · Polydimethylsiloxane · Patterns · Deformation · Surfaces · Self-assembly · Polyelectrolyte multilayer films · Thin-films · Polymer brushes · Colloidal crystallization · Mechanical-properties · Assembled monolayers · Buckling instability · Elastomeric polymer · Tobacco-mosaic-virus · Soft lithography · Arrays

Contents

A. Schweikart, A. Horn, A. Böker, and A. Fery (✉)
Physical Chemistry Department II, University of Bayreuth, 95440 Bayreuth, Germany
e-mail: andreas.fery@uni-bayreuth.de

1 Introduction

Periodically patterned surfaces are used as functional building blocks in many devices; periodic patterning can also cause special surface properties. Spatial periodicity causes unique optical, electronic or acoustic properties due to wave interference phenomena. Thus optical elements like lenses, grids, or bandgap materials based on periodically micro-structured surfaces are feasible. Many applications in modern micro fluidics, microelectronics, or combinatorial chemistry for sensing, analysis, or synthesis require array-type structures as building blocks. Periodic patterns can serve as templates for the assembly of more complex hierarchical structures like 3-D colloidal crystals [1–7]. In particular, biological examples show that periodicity can cause special hydrodynamic or aerodynamic properties, like reduction of turbulent drag/hydrodynamic friction [8–10] as found with sharkskin or dragonfly wings. Patterning is essential for special wetting/self-cleaning properties like the celebrated lotus effect [11–13].

Consequently a huge variety of approaches for the fabrication of such structures has been developed in the past. A recent review on various patterning approaches can be found [14]. So far, strategies are generally divided into bottom-up and top-down approaches. In the first approach, structure formation is achieved by using (typically molecular scale) building blocks that tend to self-assemble; prominent examples are amphiphilic lipids, surfactants, block-copolymers, or colloidal particles. In the second, originally homogenous materials are shaped by means of invasive techniques like lithography. Both approaches have their specific benefits and drawbacks. While bottom-up approaches allow reaching small periodicities, they are more vulnerable to defects and limited in the degree of pattern control. They also require the synthesis of tailor-made compounds if certain periodicities are desired. Top-down approaches are unparalleled in terms of versatility and fidelity, but they face intrinsic limits concerning lateral periodicities that can be reached and typically are rather expensive. Both approaches face serious difficulties for upscaling to macroscopic dimensions. In this review we focus on a novel approach for surface patterning based on controlled wrinkling, which belongs to neither of the two categories. Interestingly, it allows creating topographical surface patterns with periodicities between few 100 nm and many tens of microns and has few restrictions in terms of upscaling.

2 Theoretical Foundations of Wrinkling

Wrinkles are encountered in many everyday life situations. If a thin membrane is exposed to a compressive in-plane strain, the system responds at low deformations by a so-called buckling instability. The membrane bends out of plane and a wrinkle develops, as can be frequently observed for cloth, skin, or paper. In spite of its mundane character, wrinkling has only recently found applications as a method for topographical patterning. This is mainly due to the fact that the buckling process underlying wrinkle formation is highly nonlinear in nature and, therefore, reproducibility is often low and wrinkle formation suffers in many situations from defects. The fact that has fascinated painters for ages (that a piece of cloth will never wrinkle in precisely the same fashion) is undesirable for patterning, where control and uniformity are desired. Recent developments have introduced experimental solutions under which this restriction is greatly diminished. Wrinkle periodicity becomes highly uniform and controllable by external parameters. Topographically structured surfaces such as those shown in Fig. 1 become accessible. The approach to "tame" wrinkles is to use membranes that are not freely suspended but attached to an elastomeric substrate, as schematically depicted in Fig. 2 [15–20].

In the situation depicted in Fig. 2, the film on the elastomeric substrate undergoes a buckling transition in order to relieve stress upon compression. In contrast

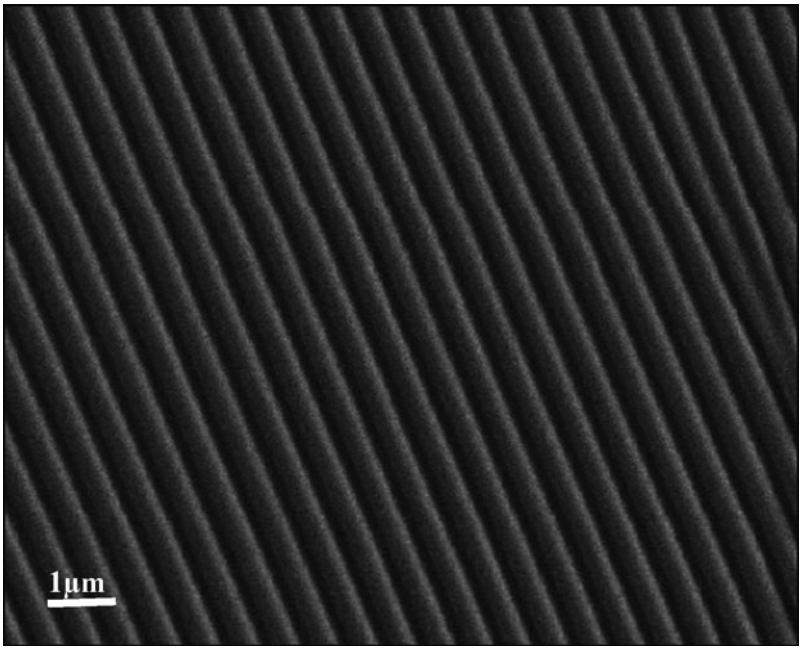

Fig. 1 SEM image of sub-micron periodicity wrinkles created by plasma oxidation of strained polydimethylsiloxane and subsequent stress release

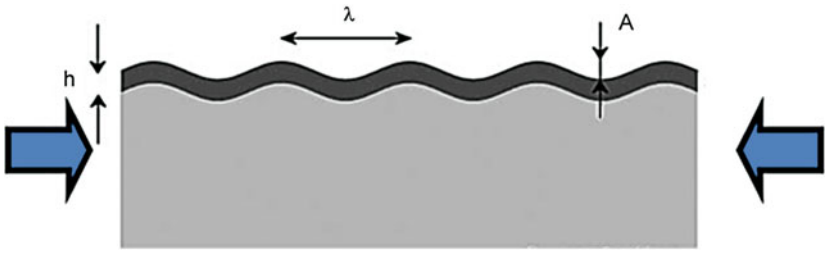

Fig. 2 Schematic depiction of wrinkle formation of a hard film in adhesive contact with a softer elastomeric substrate. The wavelength λ is mainly determined by film thickness h and elastic properties of film and substrate. The amplitude A can be controlled by the strain

to a free membrane, however, the wavelength of wrinkles is influenced by the fact that the film is coupled to the elastomer. While the minimal elastic energy conformation of the film is a single fold, this situation is highly unfavorable for the elastomeric substrate for which out-of-plane deformations are linked to an energy penalty. As a consequence, a well-defined wavelength, which minimizes elastic deformations of film and substrate, develops. This phenomenon is of broad interest and has motivated recent theoretical studies of the mechanics and kinetics of the wrinkle-formation [15, 19–30]. Mechanical buckling instability of thin coatings deposited on soft polymeric substrates has been described by Volynskii and coworkers [20] who considered the stability of a surface layer to follow buckling theories of Biot [31, 32] and Euler [33]. For the dominant wavelength λ, the following expression is given where h is the thickness of the coating, E and v are the Young's Modulus and Poisson's Ratio of substrate (s) and film (f):

$$\lambda = 2\pi h \left[\frac{\left(1 - v_S^2\right) E_f}{3\left(1 - v_f^2\right) E_S} \right]^{1/3}. \tag{1}$$

In the situation of uniaxial strain, this equation predicts the direct proportionality between the wavelength λ and the thickness of the coating, and an increase in λ with the decrease in substrate rigidity (described by the Young's Modulus E_s). The critical buckling stress in the coating σ is [20]

$$\sigma = \left[\frac{9 E_f {E_s}^2}{64\left(1 - {\nu_f}^2\right)\left(1 - {\nu_s}^2\right)^2} \right]^{1/3}. \tag{2}$$

Neglecting the Poisson's coefficient, the buckling strain is

$$\varepsilon = \left[\frac{9 {E_s}^2}{64 {E_f}^2} \right]^{1/3}. \tag{3}$$

Sridhar and coworkers studied the kinetics of a compressed film on a viscous substrate [30]. They performed linear-stability analysis to determine the onset and maximally unstable mode of this mechanical instability as a function of misfit strain, viscous layer thickness, and viscosity.

3 Experimental Approaches to Wrinkle Formation

The theoretical concept explained above is rather universal. It has few restrictions in terms of materials used for wrinkle formation. The main requirement is that the Young's modulus of the film is large as compared to the substrate elastomer. In addition, if micron- and sub-micron wavelengths are desired, the film thickness should be controllable on the nanoscale. In most of the work, polydimethylsiloxane (PDMS) was used as elastomeric substrate. Experimentally, both transient wrinkles, which only exist when macroscopic strains are applied, and "permanent" wrinkles, which remain in the absence of macroscopic strains, can be produced. Both cases are illustrated in Figs. 3 and 4 for the simplest situation of a uniaxial deformation.

In Fig. 3 the sheet is macroscopically stretched as indicated by the arrows. As a consequence, transversal contraction takes place perpendicular to the stretching direction. Wrinkles will appear in the macroscopically stretched state and – provided the system is linearly elastic and no plastic deformations occur – disappear upon relaxation [22].

In Fig. 4 the film was wrinkle-free in the macroscopically stretched state (e.g., it could be prepared on a stretched substrate, as in some of the cases explained below). Now wrinkles are formed as the macroscopic tension is relaxed and remain

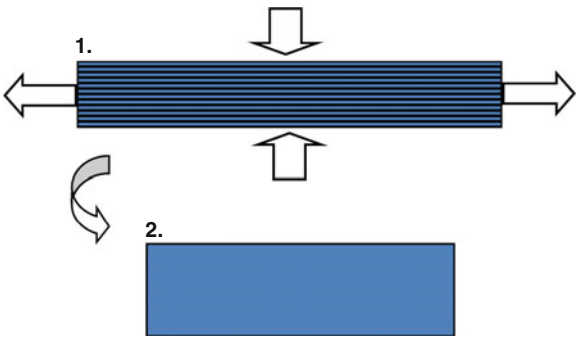

Fig. 3 A typical situation in which wrinkles occur in the presence of a macroscopic stress is schematically depicted: A thin sheet is exposed to a uniaxial macroscopic deformation (**1**). As a consequence, the sheet is compressed in the direction perpendicular to the elongation axis and the reacts by a buckling instability. Wrinkles are formed, which however relax as the macroscopic strain is released (**2**), unless plastic deformations occur in the macroscopically stressed state

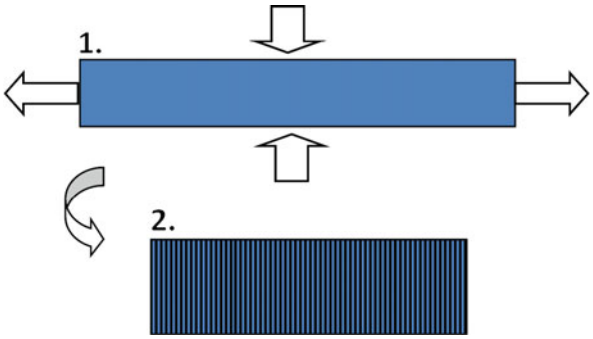

Fig. 4 In order to obtain wrinkles that are stable in the absence of macroscopic stresses, a macroscopic substrate of large thickness has to be modified in stressed state as explained below. While the substrate does not react to compressive strains by wrinkling (**1**), the thin membrane that was created in the stressed state wrinkles when the substrate is relaxed (**2**). While the system is still under tension microscopically, no macroscopic stress is necessary to maintain the wrinkle structure and long-term stable wrinkles can be created

permanent. In fact, on a microscopic level, the system is not tension-free and long term-relaxation might take place.

Recent experiments were carried out for more complex strain situations. Biaxial or multiaxial strain on films which were deposited on compliant substrates has been described by Chen [24] and coworkers as well as by Lin [28] and coworkers. Films that are prepatterned with a circular depression (representing a multiaxial or circular strain) showed herringbone buckling patterns. This type of buckling instability was found to be the most suitable buckling mode to reduce the overall in-plane stress in the film in all directions. In the case of biaxial mechanical stretching, Lin and coworkers found consistent structures. They presented perfect herringbone buckling patterns if the biaxial strain is released sequentially in the *x*- and *y*-directions.

A possibility for the formation of more complex patterns is the use of prepatterned substrates as presented by several authors by either masking the surface partially to avoid the formation of a hard layer in the masked regions [19] or topographical prepatterning, where a relief structure is modified in order to wrinkle [15–17, 34]. Periodic porous structures have been reported to undergo pattern transformation due to buckling instabilities when external forces are applied. This results in more complex hierarchical structures [35–37].

We have recently introduced embossing as a possibility to generate circular wrinkled patters [38]. Here, the substrate is uniform, but in the embossing process, stresses vary locally. Thus, complex patterns like those depicted in Fig. 5 are feasible.

For the hard film, a variety of realizations like metal films, inorganic layers, or polymeric layers have been demonstrated. Figure 6 provides an overview of the range of achievable wavelengths for the various approaches, which will be discussed in detail below.

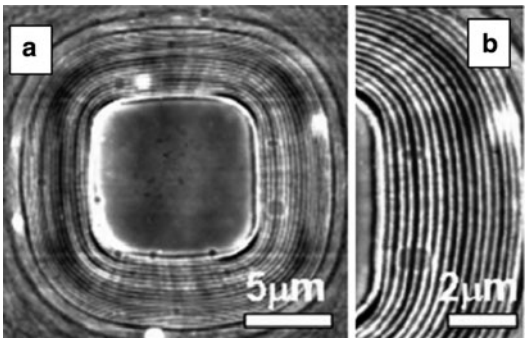

Fig. 5 AFM images of wrinkled substrates embossed by 10 µm (**a**) overview, (**b**) magnified detail-sized pillar patterns. *Height scales* $\Delta Z = 150$ nm [38]

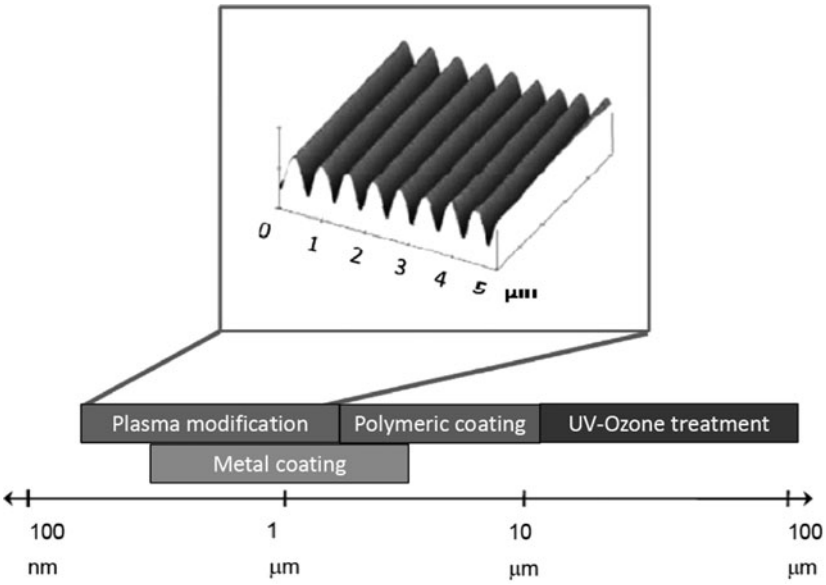

Fig. 6 Overview of the wavelength ranges that can be routinely achieved using the various modification techniques of PDMS surfaces. The *inset* displays a 3-D AFM height-image of a plasma-modified surfaces

3.1 Evaporation/Sputtering and Thin Metal Films

Historically, wrinkles on PDMS were first observed upon metal evaporation. Martin and coworkers reported wrinkle formation by evaporation of aluminum onto PDMS [39], which was first not followed further. The potential of metal evaporation onto PDMS for structuring purposes was recognized only 17 years later by Bowden [15]. In these experiments, the metal was coated onto thermally expanded PDMS. Returning the sample to room temperature causes thermal shrinkage of the PDMS and consequently wrinkling of the top layer. Chen and coworkers have theoretically shown that the herringbone-type pattern observed under these conditions

constitutes a minimum energy conformation of the system [24]. Huck and coworker used a gold coating instead of aluminum and – more importantly – demonstrated that more complex wrinkle patterns can be achieved by using PDMS which is patterned in its mechanical properties [19]: They exposed the PDMS prior to metal evaporation to UV light through a mask. This is well known to generate surface radicals which recombine to form various types of networks [40] and increase the Young's modulus of the topmost layer of PDMS [19] in the illuminated area relative to the nonilluminated areas. This influences the wrinkle wavelengths and patterning thus provides a means of gaining control over more complex wrinkle geometries. Volynskii and coworkers showed similar effects as Bowden for gold and platinum coatings of poly(ethylene terephthalate) [20]. Recently, Khang and coworkers identified mechanical buckling of Si-membranes coupled to PDMS substrates to serve as so-called "stretchable electronics" in organic transistors or photovoltaic [41, 42].

3.2 Plasma Oxidation and Thin Silica Layers

A significant number of papers take advantage of the fact that oxidation of PDMS (either by exposure to UV-ozone or to oxygen plasma) can create a stiff silica-like material [17, 40, 43]. During the oxidation process, up to 50% of PDMS in the topmost layer is converted into silica [40]. Oxygen plasma treatment was first applied by Bowden and coworkers [16] to create such a surface layer and use a thermal shrinkage process to create wrinkles. They found patterns with wavelengths between fractions of a micron and 10 μm. They also reported the appearance of cracks which arise due to the brittle nature of the silica material.

These patterns were found to be locally ordered but macroscopically disordered. Genzer and coworkers presented the first effort to align the wrinkles by the use of a custom-built stretch-apparatus [44, 45]. In this experimental setup a clamped PDMS slab was uniaxially stretched to a length of 30–50% relative to its original length. PDMS, that was subsequently oxidized in this prestrained state, formed periodic wrinkles perpendicular to the applied direction of stretching once the strain was released. Given the case that strain is well controlled and homogenous, wrinkle patterns are highly regular as shown in Fig. 7. Detailed investigations concerning the effect of the strain-removal rate on the buckle morphology was done by Efimenko and coworkers [46]. They reported the development of structural defects (junctions marked with arrow in Fig. 7) which decrease dramatically with decreasing velocity of stain-removal from the specimen. During the relaxation process cracks form parallel to the strain [47]. Since SiO_2 is rather brittle, it can crack as the strain is released because of lateral elongation of the rubber (PDMS). Contrary to expectations, more cracks develop if the strain is released slowly compared to releasing the strain instantaneously.

For the case of uniaxial strain and the surface oxidation mechanism, quantitative evaluations of wavelength and amplitude reported by us [48] and also by Chiche and

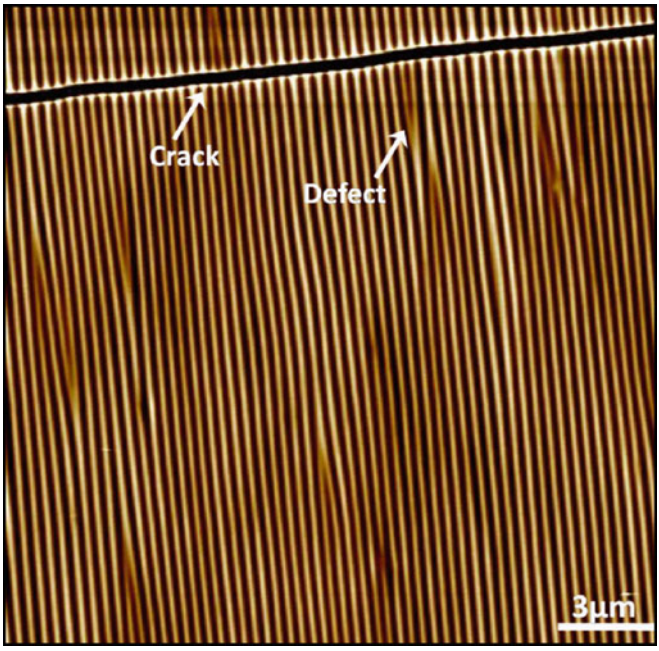

Fig. 7 Atomic force microscopy image illustrating defect structures in wrinkled surfaces prepared by plasma treatment of stretched PDMS and subsequent relaxation

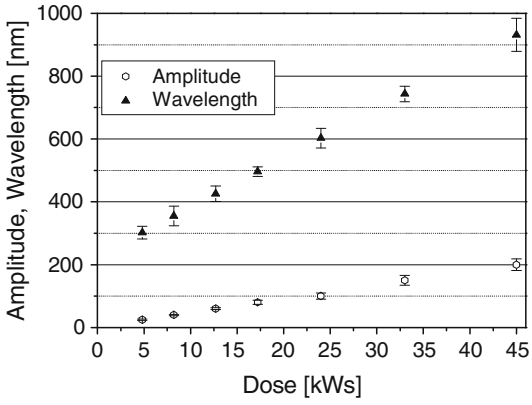

Fig. 8 Increase of wavelength (filled triangles) and amplitude (open circles) of the wrinkles with increasing plasma dose (oxygen plasma exposure time multiplied by plasma power). The values were evaluated by quantitative FFT-analysis applied to AFM height-images

coworkers [49] indicate that a single "dose" parameter (oxygen plasma exposure time multiplied by plasma power) characterizes the surface conversion of PDMS, as shown in Fig. 8.

The amplitude of the wrinkling pattern in particular was quantitatively evaluated for the first time by [50, 51] and follows the equation

$$A = h\left[\frac{\varepsilon}{\varepsilon_c} - 1\right]^{1/2}. \tag{4}$$

where ε_c is the threshold value for buckling and has to be exceeded for obtaining a wrinkled pattern [50, 52].

3.3 Polymeric Films and Coatings

Different approaches to obtain wrinkles in thin polymer sheets were presented by Harrison and Stafford [53, 54]. Thin polyethylene (PE) sheets were first spin-coated onto silicon wafers and subsequently transferred to a relatively thick slab of PDMS by releasing the film in water. This technique takes advantage of the tunable film thickness by the spin-coating process (spin velocity, concentration of polymer solution) as well as the water-insoluble nature of PE. Wrinkles were induced by either compressing the PDMS-PE-bilayer setup [54] or depositing the PE-sheet onto a prestrained PDMS slab and releasing the strain afterwards [53].

Polyelectrolyte multilayer offer an interesting alternative to classic spin-cast polymeric films, since their thickness can be controlled on the nanometer scale and they allow the achieving of a broad range of elastic constants. The layer-by-layer deposition, in which polyanions and polycations are deposited on charged substrates by alternating adsorption from aqueous solution, was introduced by Decher and coworkers [55–57]. Depending on the type of polyelectrolyte used for the layer-buildup, elastic constants can vary greatly [58], but especially multilayer-films that show a linear thickness increase as a function of deposition steps are promising candidates for wrinkle formation, as their Young's modulus is typically large as compared to PDMS and at the same time their thickness can be controlled precisely. Several groups used wrinkling as a means for estimating the Young's modulus of multilayer of various composition including gold-nanoparticle-containing multilayer [59]. This so-called "strain induced elastic buckling instability for mechanical measurements" (SIEBIMM) was developed by Stafford and coworkers [54]. Rearrangement of (1) can be used to solve the elastic modulus E_f of thin films on top of a compliant substrate:

$$E_f = \frac{3E_s\left(1-\nu_f^2\right)}{\left(1-\nu_s^2\right)}\left(\frac{\lambda}{2\pi h}\right)^3. \tag{5}$$

This solution predicts the film's properties depending on the buckling wavelength λ and the material properties of the substrate E_s. The solution is reported to be valid in the limit of low strain ($\varepsilon \ll 10\%$), $E_{f/}E_s \gg 1$, the substrate being much thicker than the film and the amplitude of the wrinkles is much smaller than their wavelength. Other examples of systems investigated by SIEBIMM are protein films

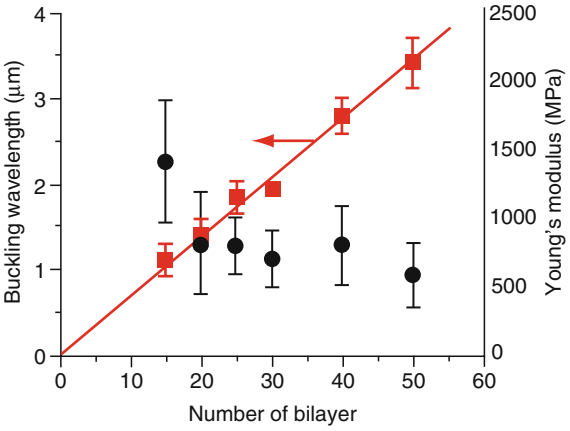

Fig. 9 Buckling wavelength (filled squares, *left axis*) and estimated Young's modulus based on film thickness measurements and the observed wavelength as well as elastic properties of the substrate (filled circles, *right axis*) for $(NDR/Au\text{-}NP)_n$ films for different number of assembly cycles n [59]

based on silk fibroins [60], polymer-brush films [61], ion-irradiated PS surfaces [62], and composites of polyelectrolyte multilayers and encapsulated nanoparticles [63]. Figure 9 displays the thickness dependency of multilayer formed from Nitrodiazoresin (NDR) and gold nanoparticles [59]. The buckling wavelength is found to depend linearly on the film thickness and the elastic modulus of the multilayer film can be estimated from the data. At low film thicknesses, Young's moduli deviate from the values found at higher film thickness because the PDMS has to be plasma modified in order to render it hydrophilic. Thus, at low film thickness, the silica layer influences the wavelength, while at larger film thicknesses, the effective modulus approaches a value characteristic of the polyelectrolyte multilayer.

We used SIEBIMM to explore the influence of linear charge density and state of hydration on the ealstic properties of polyelectrolyte multilayers [64]. Multilayers were prepared from polystyrenesulfonate (PSS) and various statistical random copolymers made from diallyldimethyl-ammoniumchlorid (DADMAC) and *N*-methyl-*N*-vinylacetamid (NMVA) monomers [65]. While the DADMAC and NMVA monomers are comparable concerning their hydrophilicity, DADMAC is charged while NMVA is uncharged. Thus variation of the DADMAC-content allows for controlling the linear charge density of the polycation. Figure 10 displays the elastic constants obtained for multilayers using polycations of 100, 89, and 75% DADMAC content as a function of humidity at room temperature. The results clearly indicate that the elastic modulus (and consequently the wrinkle wavelength at fixed film thickness) strongly depends on humidity and that water acts as a plasticizer for the multilayers. Variation of linear charge density also allows fine-tuning elastic constants and wavelengths.

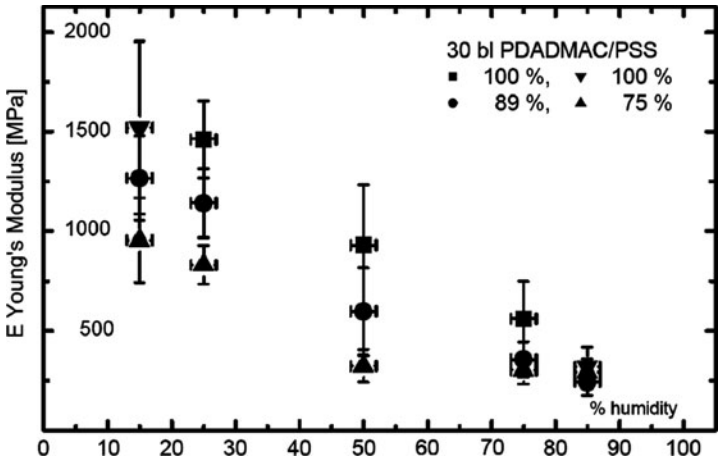

Fig. 10 Young's modulus for multilayer of PSS/(DADMAC/NMVA) random copolymers as a function of ambient humidity at room temperature. The DADMAC-content of the copolymer is varied between 75 and 100% (75%: filled triangles, 89%: filled circles, 100%: filled squares and filled inverted triangles), indicating a clear dependency of the mechanical properties of the multilayer on the linear charge density. In all cases, a plasticizing effect of water is evident

4 Wrinkling as Strategy for Building Lithography-Free Hierarchical Structures

A variety of interesting applications takes advantage of the periodic nature provided by highly ordered wrinkling patterns, which were used as building blocks for hierarchical structures. This includes the utilization of wrinkled substrates as micro fluidic sieves [46] or diffraction gratings [16, 53]. Several authors have described laser diffraction measurements for determining the dominant wavelength of a wrinkling pattern as a suitable method [54, 57, 66, 67]. Utilizing tunable wrinkled surfaces as optical phase gratings is therefore a promising direction. Bowden and coworkers introduced optical gratings created by tunable buckled surfaces [16]. They reported the angular displacement of the first order diffraction spot to increase linearly with increasing compressive strain. As mentioned in the theoretical description of the wrinkle formation, it is proven that compressive strain mainly affects the amplitude of wrinkles. This dependency had also been confirmed later by Harrison and coworkers [53]. They sent coherent light through a wrinkled surface and observed a local phase shift that was imparted with a magnitude proportional to the wrinkled amplitude. The diffraction pattern from a coherent beam normal to a transparent surface with a sinusoidal topography can be calculated in the Fraunhofer limit. Wrinkled substrates were used as templates for guiding cell proliferation [68, 69] and for patterned assembly of colloidal particles [70]. We focus in the following on the latter aspect and show how wrinkles can be used as templates for particle assembly on the micron and sub-micron scale.

4.1 Template-Assisted Self-Assembly of Colloidal Particles by Wrinkled Surfaces

Ordered arrays made from colloidal particles have various applications such as optical bandgap materials, triggering the epitactic growth of 3-D crystals [1–7]. If the assembled colloidal particles are of nanoscale dimensions, they can serve as optical, electronic functional units, sensors, or for data storage. The preparation of defect-free alignments of colloidal particles, however, remains challenging. Much research has been directed towards investigating templates and procedures to guide the self assembly into either topographically [1, 71–80] or chemically [75, 81–83] structured surfaces. Such template-assisted assembly reduces the number of defects and allows defining the regions in which colloids are assembled. Conventionally, lithography is used to fabricate periodically structured surfaces. Downsizing the features' structure requires electron-beam lithographic techniques and includes environmentally harmful etching steps. There is no doubt that mass production and upscaling is unfavorable. Different authors predicted that controlled wrinkling provides an alternative solution to structure templates which can be used in a template-assisted self-assembly (TASA) process.

We demonstrated how ordered lines of colloidal polystyrene particles can be achieved by a simple dip coating process [70]. We used wrinkles produced via a stretch retraction process of a glassy polyelectrolyte multilayer film mounted on a PDMS substrate. Here, the template was dipped into a colloidal particle suspension with the orientation of the wrinkle's grooves with the withdrawing direction of dipping as the sketch in Fig. 11 indicates.

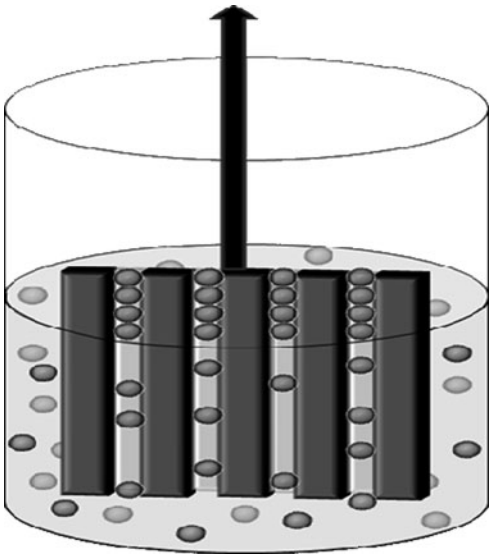

Fig. 11 Template-assisted deposition of particles on wrinkled films. For successful assembly, the surface charge of the particles has to be of like sign as the surface charge of the wrinkled film to avoid adhesion of the particles towards the film surface

Successful assembly requires matching features of the template, meaning that wavelength and height have to be of the same dimensions. Additionally, adhesion of particles and surface must be avoided by weak repulsive forces. In this context, polyelectrolyte multilayer-wrinkles are particularly useful, as the wettability of the multilayer is determined by the part of the layer adjacent to the film/solution or film/air interface respectively, while the elastic properties are determined by the total film [84]. Thus, elastic constants can be adjusted largely independent from wettability properties.

We used polyelectrolyte multilayer formed from polyallylamine hydrochloride (PAH) and PSS successfully for templating deposition of colloidal particles, as displayed in Fig. 12. The wavelength of the wrinkles was adjusted by the number of polyelectrolyte deposition cycles and, accordingly, single lines of particles or double lines, as well as other geometries, could be achieved [70].

An interesting aspect of the use of polyelectrolyte multilayer for this structuring approach is the fact that the mobility of polyelectrolytes in the multilayer critically depends on humidity. As the wrinkle structure is still under tension microscopically, plasticizing due to humidity increase (as evident from Fig. 10) allows for relaxing these internal tensions. The wrinkles smoothen as a consequence. Thus a removable template is available and quantitative studies on the relaxation processes are currently on the way. Figure 13 displays a scheme of the total process: In the first step, the multilayer is plastically deformed, relaxation wrinkles are created, and the thin polymer layer is strained (depicted by the red color). Particles can be aligned on those wrinkles in the second step. In the final step the whole sample can be annealed, resulting in a relaxation process of the wrinkles, which does not destroy the order of the particles, as their mobility is negligible.

Recently we were able to expand this approach to the fabrication of patterned arrays of bionanoparticles [85]. The tobacco mosaic virus (TMV) is particularly

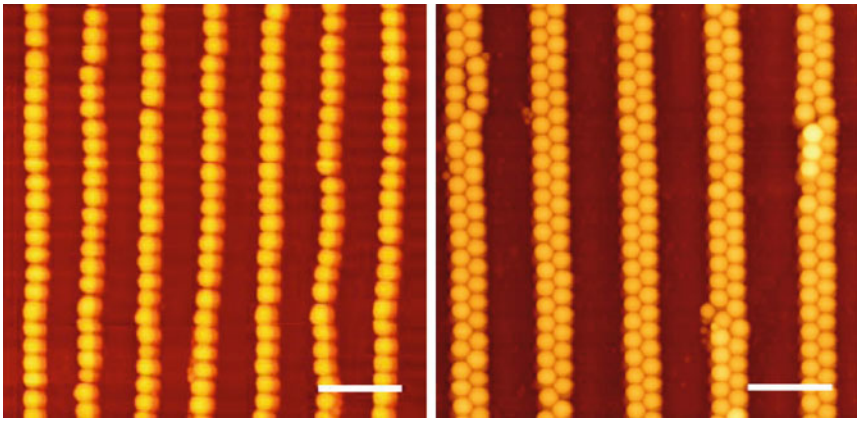

Fig. 12 AFM images of selective deposition of 380 nm-sized colloidal particles on $(\text{PAH–PSS})_n$ wrinkled films with different number of bilayer: $n = 30$ (*left*), 40 (*right*). *Scale bars* = 2 µm; *height scales* $\Delta Z = 910$ nm (*left*), 860 nm (*right*) [70]

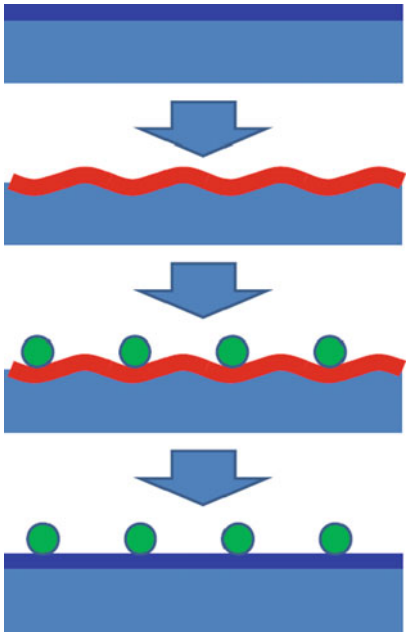

Fig. 13 Scheme of the proposed application of polyelectrolyte multilayer as removable templates. First wrinkles are formed by plastic deformation of the multilayer. The particles are deposited while the multilayer is in a glassy state and subsequently the multilayer is annealed

suited for this approach, since it is highly anisotropic in shape. The virus is 300 nm long and 18 nm in width. As a biological nanoparticle, it is not only of exceptional monodispersity, but also offers a well-defined chemical composition down to molecular dimensions. Wrinkles generated by plasma oxidation of PDMS have periodicities in the range of and below the length of the TMV and are thus ideally suited for guiding patterning of the virus. It turns out that viruses can even by aligned on these substrates by means of a spin-coating process. Figure 14 displays an AFM image (left) of TMVs on a wrinkled surface that were assembled using this process. The inset displays a cross-section of the image, in which the topographical features of the virus particles can be investigated. We frequently find that viruses form not only single lines (marked by a full arrow) but also double lines formed by two parallel virus particles, which can be distinguished by a larger width (marked by broken arrow). An alternative technique for studying the patterning of the virus particles is scanning electron microscopy, which does not provide topographical information but is particularly suited for studying larger areas due to the pronounced contrast between virus particles and template (Fig. 14 right).

The efficiency of the alignment process depends critically on concentration and rotation frequency in the spin-coating process. The impact of both parameters can be quantified using scanning electron microscopy. The occupancy of the grooves can be quantified by normalizing the total length of virus-filled grooves by the total length of grooves of the sample. In a similar fashion, a virus deviator parameter can be determined that normalizes the total length of viruses that do not follow the

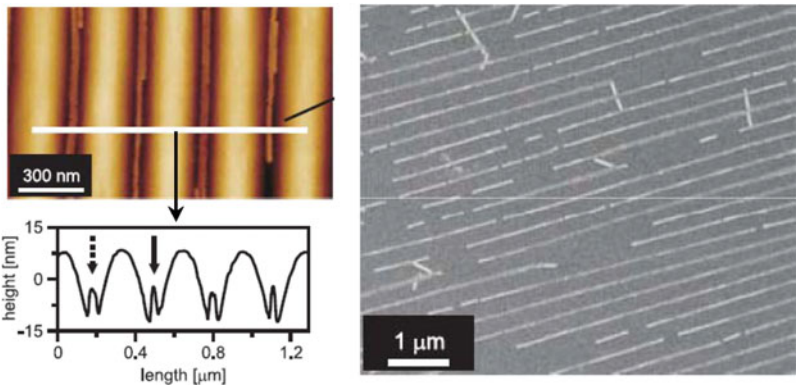

Fig. 14 AFM height-image of selective deposition of TMV virus particles onto wrinkles created by plasma oxidation of PDMS and corresponding height profile showing single (*full arrow*) and multiple adsorption (*broken arrow*) of the virus in the grooves (*left*). SEM image of TMVs aligned in the grooves showing lines of viruses over several micrometers (*right*) [85]

template pattern by the total length of viruses which follow the pattern. Taking the sample areas into account as well, we define

$$\Omega = \frac{1}{A_{\text{tot}}} \sum_{k=1}^{4} A_k \frac{V_k}{W_k} \tag{6}$$

and

$$\Phi = \frac{1}{A_{\text{tot}}} \sum_{k=1}^{4} A_k \frac{\text{O}_k}{\text{f}_k V_k + \text{O}_k} \tag{7}$$

for the occupancy parameter Ω and the deviator parameter Φ. Figure 15 shows a graphical summary of optimum conditions and the dependency on both parameters: concentration and spin speed.

TMVs offer exciting perspectives for further chemical processing as they are not only monodisperse in size but also offer a well defined surface chemistry down to molecular scale. This has already been used by several groups for further chemical modification of TMVs like metallization and mineralization [86–92]. In particular, metal wires could be created by controlled metallization of the viruses. This line of research is currently being pursued.

Another possible application using the hierarchical nature of the wrinkles has been discussed by Efimenko and coworkers [46]. They treated a mechanically stretched PDMS sheet with UV-ozone in order to create a stiff surface layer. A detailed analysis with AFM and profilometry of the wrinkles after releasing the strain showed that the wrinkling patterns are hierarchical themselves. They observed up to five "generations" of different wavelengths with different periodicities. These features made so structured surfaces valuable candidates for separate colloidal particles of different sizes by acting as a micro fluidic sieve. A suspension

of particles of different sizes (large silica particles (10 μm) and small polystyrene particles (67 nm)) was pumped past the wrinkled surface with a constant flow rate perpendicular to the to the buckles' orientation. Smaller particles seemed to align themselves in smaller grooves and bigger particles resided predominantly in the grooves of wrinkles with larger periodicity. Lines of particles could be observed that were separated according to their size. Recently, Chung and coworkers investigated wrinkled substrates to serve as nanochannels for protein preconcentration [93].

4.2 *Pattern Transfer from Wrinkled to Planar Surfaces by Stamping*

In many cases, transfer of patterns from wrinkled surfaces to planar substrates is desirable, since PDMS has poor optical properties and particles are not as accessible to characterization techniques or to further modifications when they are "buried" in the wrinkles. Here, stamping approaches that build up on the so-called micro contact-printing technique (μCP) [94–96] provide a convenient pathway for pattern transfer. μCP uses the relief patterns on a structured PDMS stamp to form patterns of self-assembled monolayer of inks onto the surface of a substrate through mechanical contact. Structured stamps were traditionally fabricated by molding PDMS against a prestructured silicone master which was fabricated by photolithography [96]. If this silicone master is structured on the sub-micron scale, expensive electron beam lithography has to be implemented [97, 98].

We have recently discussed the application of wrinkled PDMS serving as a stamp for μCP and showed that flat surfaces can be chemically structured by mechanical contact of polyelectrolyte-covered wrinkles [48]. The transfer of the structure was enhanced by chemical modification of the substrate with polyelectrolyte multilayer, as shown schematically in Fig. 16.

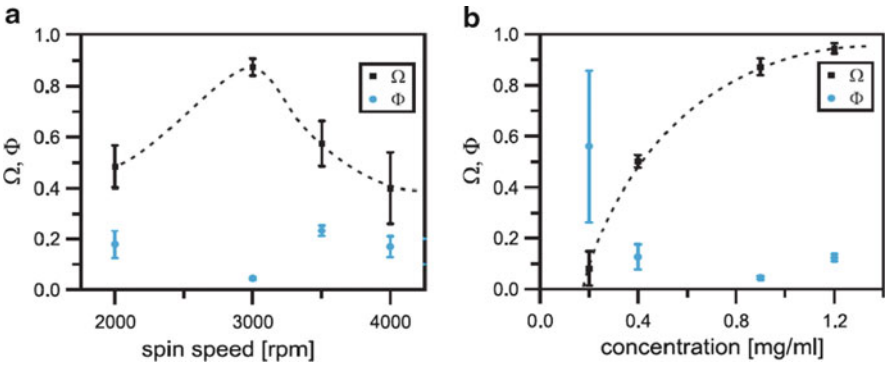

Fig. 15 Occupancy parameter (**Ω**) and deviation parameter (**Φ**) as a function of spin speed (**a**) and concentration (**b**) of TMV solution for spin-assisted assembly of TMV particles on wrinkled surfaces [85]

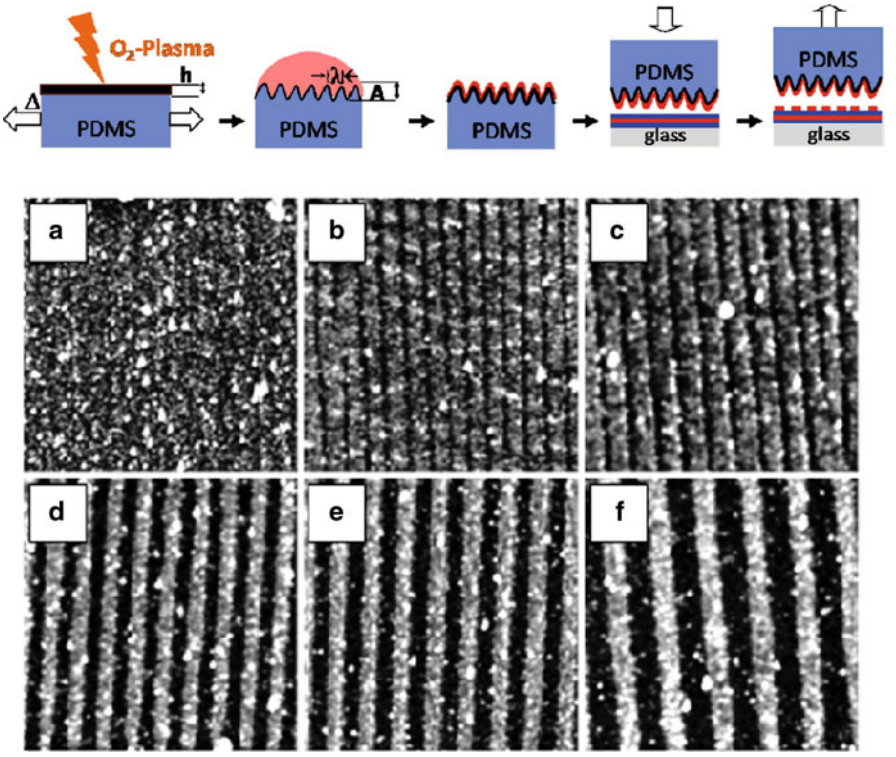

Fig. 16 *Top*: Summary of the μCP process using wrinkled stamps. *Bottom*: AFM height-images $5 \times 5\,\mu m$ (*height scale* $\Delta Z = 15\,nm$) of surfaces, which are patterned via μCP by the use of wrinkled stamps with different periodicities and heights. With increasing features of the stamp, the stripes of the pattern broaden and separate. (**a**) A/λ: 25/302 nm, (**b**) A/λ: 40/355 nm, (**c**) A/λ: 60/426 nm, (**d**) A/λ: 100/603 nm, (**e**) A/λ: 150/743 nm, (**f**) A/λ: 200/931 nm) [48]

The patterns obtained were reported to be highly regular, having periodicities below 1 μm as can be seen in Fig. 16a–f. The striped pattern represents the negative of the wrinkled stamp with different wavelengths and amplitudes.

Stamping can also be used to transfer colloidal particles from wrinkled substrates to planar substrates. We have explored this possibility, especially for the case of TMV assemblies in wrinkles. After TMVs were assembled in the wrinkles as described above, the PDMS structures were brought in direct contact with hydrophilic surfaces like silicon wafer or glass substrates, while microscopic amounts of water were still present on the PDMS structure. Under these conditions, capillary forces can cause transfer of the TMVs from the PDMS wrinkles onto the substrate. Subsequently, the surfaces were investigated using imaging AFM and SEM. Figure 17 displays an AFM image, in which the transferred TMVs can be clearly distinguished in the topography. The periodicity of the TMV stripes corresponds to the wrinkle periodicity and the height of the TMVs is within the accuracy of the AFM measurement, in agreement with the expected value for lines consisting of single TMV particles.

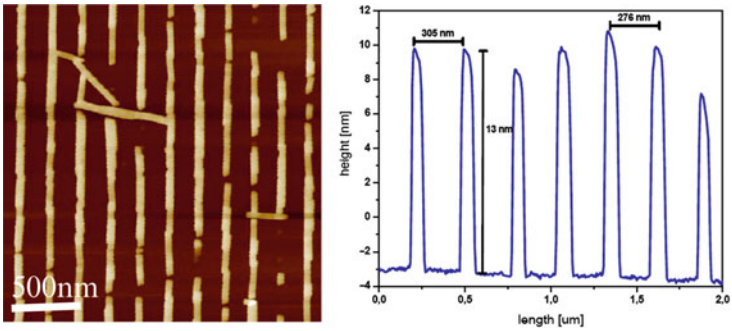

Fig. 17 *Left*: AFM-image of TMV particles after transfer onto a silicon wafer surface. *Right*: A cross-section perpendicular to the stripe direction, indicating that the periodicity of the wrinkle-template was preserved in the stamping process. In addition, the height of the TMV particles is compatible with the assumption that individual particles were transferred in the stamping process

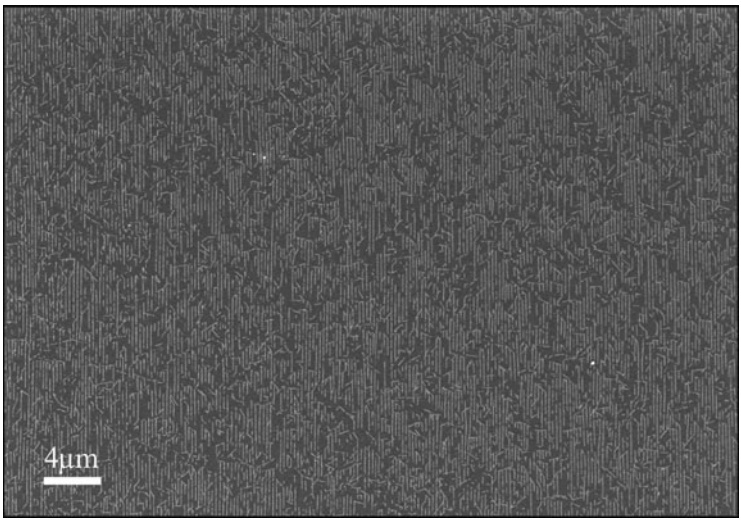

Fig. 18 Scanning electron microscopy image indicating that long-range order is preserved in the stamping process and those mesoscale dimensions can be approached using stamping

Scanning electron microscopy was used, to investigate the long range order of transferred patterns. As evident from Fig. 18, which displays an electron microscopy image of an arbitrarily selected region of the wafer after the stamping process, the transfer process is not limited to micron-range, but rather allows accessing mesoscale dimensions. Thus, properties linked to nanoscale anisotropy of the particles like anisotropic electronic or optical properties could be preserved in the resulting structures. These aspects will be investigated in future work in detail.

Another interesting aspect of the stamping transfer is the fact that the same substrate can be stamped multiple times, creating cross-patterns.

5 Conclusions

In conclusion, we have summarized a novel approach for using external mechanical fields for creating topographically and chemically structured polymeric surfaces. The underlying process in structure formation is a controlled buckling instability of a thin elastic layer which is in adhesive contact with an elastic substrate. We reviewed the theoretical background of the process as well as the materials and methods that are available. In particular, it turns out that, depending on the film composition and thickness, periodic patterns with wavelengths between 150 nm and hundreds of microns are feasible. While it is common in our and others' work to use PDMS as elastomeric substrate, a rich choice of materials for the film is available including metallic-, inorganic insulator- (e.g., silica), and polymeric layers of different composition. We discuss the range of wavelengths for which the different film types are most useful.

In the following, we introduce the buildup of more complex surface patterns by TASA of colloidal particles on the wrinkled surfaces. We find that the process is rather versatile and can be applied to various particle types like silica particles, gold particles, polystyrene particles, and bionanoparticles like TMV particles. For the latter, we find that even spin-coating of wrinkled substrates results in large range ordering of TMV particles.

Finally, we show that patterns can be transferred from wrinkled surfaces onto flat substrates like silicon wafers or glass substrates. We show two examples, which are both based on a stamping process. Stamping is feasible because the wrinkled surfaces are compliant: they can be used as stamps for micro-contact printing, enabling stamping of patterns with sub-micron periodicity. Although we demonstrated printing only for synthetic polyelectrolyte and proteins, we expect that stamping of low molecular species forming self-assembled monolayer should be possible. Classical micro-contact printing is a high-print process – transfer occurs from the elevated regions of the wrinkled surfaces which are brought in contact with the substrate. We demonstrate in the second example that low-print transfer of materials from the "valleys" of the wrinkled surfaces onto flat substrates is also possible. We find that transfer of ordered particles like TMVs is possible for mesoscale areas, preserving periodicity and order of the particles.

Wrinkling offers several advantages as compared to state of the art methods for microstructuring of surfaces. Since the structure formation process is based on macroscopic strains, upscaling is particularly simple. Requirements in terms of instrumentation are also moderate and a large choice of materials for the film-part of the wrinkled surface is available. TASA allows using wrinkled surfaces for creating structures of larger complexity and hybrid structures. Finally, the stamping approaches eliminate the restriction that the patterned substrate is limited to elastomers (or other materials of low elastic modulus). Drawbacks of the approach are mainly in the intrinsic vulnerability to defects, which are energetically favorable. Thus defect-free patterns are most likely only achievable by using additional constraints. Still, for many applications like surface patterning for controlling optical, electronic, wetting, or friction properties, defects can be tolerated.

Acknowledgments We gratefully acknowledge financial support from German science foundation within SFB 481, "Complex Macromolecular and Hybrid Systems in Internal and External Fields" and within project Fe 600/4–1 "Structure–mechanical property relations of polyelectrolyte multilayer and free-standing membranes." A.H. and A.B. acknowledge support by the Lichtenberg-Program of the Volkswagen Stiftung.

References

1. Hoogenboom JP, Retif C, de Bres E, de Boer MV, van Langen-Suurling AK, Romijn J, van Blaaderen A (2004) Template-induced growth of close-packed and non-close-packed colloidal crystals during solvent evaporation. Nano Lett 4:205–208
2. Hoogenboom JP, van Langen-Suurling AK, Romijn J, van Blaaderen A (2003) Hard-sphere crystals with hcp and non-close-packed structure grown by colloidal epitaxy. Phys Rev Lett 90:1–4
3. Hoogenboom JP, van Langen-Suurling AK, Romijn J, van Blaaderen A (2004) Epitaxial growth of a colloidal hard-sphere hcp crystal and the effects of epitaxial mismatch on crystal structure. Phys Rev E 69:051602–051617
4. Hynninen AP, Thijssen JHJ, Vermolen ECM, Dijkstra M, Van Blaaderen A (2007) Self-assembly route for photonic crystals with a bandgap in the visible region. Nat Mater 6:202–205
5. van Blaaderen A (2004) Colloids under external control. MRS Bull 29:85–90
6. van Blaaderen A, Hoogenboom JP, Vossen DLJ, Yethiraj A, van der Horst A, Visscher K, Dogterom M (2003) Colloidal epitaxy: playing with the boundary conditions of colloidal crystallization. Faraday Discuss 123:107–119
7. Vossen DLJ, Fific D, Penninkhof J, van Dillen T, Polman A, van Blaaderen A (2005) Combined optical tweezers/ion beam technique to tune colloidal masks for nanolithography. Nano Lett 5:1175–1179
8. Bechert DW, Bruse M, Hage W (2000) Experiments with three-dimensional riblets as an idealized model of shark skin. Exp Fluids 28:403–412
9. Reif WE (1985) Morphology and hydrodynamic effects of the scales of fast swimming sharks. Fortschr Zool 30:483–485
10. Wainwright SA, Vosburgh F, Hebrank JH (1978) Shark skin – function in locomotion. Science 202:747–749
11. Barthlott W, Neinhuis C (1997) Purity of the sacred lotus, or escape from contamination in biological surfaces. Planta 202:1–8
12. Furstner R, Barthlott W, Neinhuis C, Walzel P (2005) Wetting and self-cleaning properties of artificial superhydrophobic surfaces. Langmuir 21:956–961
13. Neinhuis C, Barthlott W (1997) Characterization and distribution of water-repellent, self-cleaning plant surfaces. Ann Bot 79:667–677
14. del Campo A, Arzt E (2008) Fabrication approaches for generating complex micro- and nanopatterns on polymeric surfaces. Chem Rev 108:911–945
15. Bowden N, Brittain S, Evans AG, Hutchinson JW, Whitesides GM (1998) Spontaneous formation of ordered structures in thin films of metals supported on an elastomeric polymer. Nature 393:146–149
16. Bowden N, Huck WTS, Paul KE, Whitesides GM (1999) The controlled formation of ordered, sinusoidal structures by plasma oxidation of an elastomeric polymer. Appl Phys Lett 75: 2557–2559
17. Chua DBH, Ng HT, Li SFY (2000) Spontaneous formation of complex and ordered structures on oxygen-plasma-treated elastomeric polydimethylsiloxane. Appl Phys Lett 76:721–723
18. Genzer J, Groenewold J (2006) Soft matter with hard skin: from skin wrinkles to templating and material characterization. Soft Matter 2:310–323
19. Huck WTS, Bowden N, Onck P, Pardoen T, Hutchinson JW, Whitesides GM (2000) Ordering of spontaneously formed buckles on planar surfaces. Langmuir 16:3497–3501

20. Volynskii AL, Bazhenov S, Lebedeva OV, Bakeev NF (2000) Mechanical buckling instability of thin coatings deposited on soft polymer substrates. J Mater Sci 35:547–554
21. Bandyopadhyay D, Sharma A, Shankar V (2008) Instabilities and pattern miniaturization in confined and free elastic-viscous bilayers. J Chem Phys 128:154909–154912
22. Cerda E, Mahadevan L (2003) Geometry and physics of wrinkling. Phys Rev Lett 90:1–4
23. Cerda E, Ravi-Chandar K, Mahadevan L (2002) Thin films – wrinkling of an elastic sheet under tension. Nature 419:579–580
24. Chen X, Hutchinson JW (2004) Herringbone buckling patterns of compressed thin films on compliant substrates. J Appl Mech 71:597–603
25. Groenewold J (2001) Wrinkling of plates coupled with soft elastic media. Physica A 298: 32–45
26. Huang ZY, Hong W, Suo Z (2004) Evolution of wrinkles in hard films on soft substrates. Phys Rev E 70:030601–030604
27. Im SH, Huang R (2008) Wrinkle patterns of anisotropic crystal films on viscoelastic substrates. J Mech Phys Solids 56:3315–3330
28. Lin PC, Yang S (2007) Spontaneous formation of one-dimensional ripples in transit to highly ordered two-dimensional herringbone structures through sequential and unequal biaxial mechanical stretching. Appl Phys Lett 90:241903
29. Mei HX, Huang R, Chung JY, Stafford CM, Yu HH (2007) Buckling modes of elastic thin films on elastic substrates. Appl Phys Lett 90:151902–151903
30. Sridhar N, Srolovitz DJ, Suo Z (2001) Kinetics of buckling of a compressed film on a viscous substrate. Appl Phys Lett 78:2482–2484
31. Biot MA (1937) Bending of an infinite beam on an elastic foundation. J Appl Mech 4:A-1
32. Biot MA (1965) Mechanics of incremental deformation. Wiley, New York
33. Landau LD, Lifshitz EM (1965) Theorie of elasticity. Butterworth-Heinemann, Moscow
34. Yoo PJ, Lee HH (2008) Complex pattern formation by adhesion-controlled anisotropic wrinkling. Langmuir 24:6897–6902
35. Singamaneni S, Bertoldi K, Chang S, Jang JH, Thomas EL, Boyce MC, Tsukruk VV (2009) Instabilities and pattern transformation in periodic, porous elastoplastic solid coatings. Appl Mater Interfaces 1:42–47
36. Singamaneni S, Bertoldi K, Chang S, Jang JH, Young SL, Thomas EL, Boyce MC, Tsukruk VV (2009) Bifurcated mechanical behavior of deformed periodic porous solids. Adv Funct Mater 19:1426–1436
37. Zhang Y, Matsumoto EA, Peter A, Lin PC, Kamien RD, Yang S (2008) One-step nanoscale assembly of complex structures via harnessing of elastic instability. Nano Lett 8:1192–1196
38. Lu C, Möhwald H, Fery A (2008) Large-scale regioselective formation of well-defined wrinkles of multilayered films via embossing. Chem Mater 20:7052–7059
39. Martin GC, Su TT, Loh IH, Balizer E, Kowel ST, Kornreich P (1982) The metallization of silicone polymers in the rubbery and the glassy state. J Appl Phys 53:797–799
40. Efimenko K, Wallace WE, Genzer J (2002) Surface modification of Sylgard-184 poly(dimethyl siloxane) networks by ultraviolet and ultraviolet/ozone treatment. J Colloid Interface Sci 254:306–315
41. Khang DY, Jiang HQ, Huang Y, Rogers JA (2006) A stretchable form of single-crystal silicon for high-performance electronics on rubber substrates. Science 311:208–212
42. Khang DY, Rogers JA, Lee HH (2009) Mechanical buckling: mechanics, metrology, and stretchable electronics. Adv Funct Mater 19:1526–1536
43. Ouyang M, Yuan C, Muisener RJ, Boulares A, Koberstein JT (2000) Conversion of some siloxane polymers to silicon oxide by UV/ozone photochemical processes. Chem Mater 12:1591–1596
44. Genzer J, Efimenko K (2000) Creating long-lived superhydrophobic polymer surfaces through mechanically assembled monolayers. Science 290:2130–2133
45. Efimenko K, Genzer J (2001) How to prepare tunable planar molecular chemical gradients. Adv Mater 13:1560–1563
46. Efimenko K, Rackaitis M, Manias E, Vaziri A, Mahadevan L, Genzer J (2005) Nested self-similar wrinkling patterns in skins. Nat Mater 4:293–297

47. Lin CB, Lin CC, Lee S, Chou YT (2008) The effect of dislocations on crack propagation in wrinkled gold film deposited on polydimethylsiloxane. J Appl Phys 104:016106.1-016106.3
48. Pretzl M, Schweikart A, Hanske C, Chiche A, Zettl U, Horn A, Boker A, Fery A (2008) A lithography-free pathway for chemical microstructuring of macromolecules from aqueous solution based on wrinkling. Langmuir 24:12748–12753
49. Chiche A, Stafford CM, Cabral JT (2008) Complex micropatterning of periodic structures on elastomeric surfaces. Soft Matter 4:2360–2364
50. Huang R (2005) Kinetic wrinkling of an elastic film on a viscoelastic substrate. J Mech Phys Solids 53:63–89
51. Jiang HQ, Khang DY, Song JZ, Sun YG, Huang YG, Rogers JA (2007) Finite deformation mechanics in buckled thin films on compliant supports. Proc Nat Acad Sci USA 104: 15607–15612
52. Huang ZY, Hong W, Suo Z (2005) Nonlinear analyses of wrinkles in a film bonded to a compliant substrate. J Mech Phys Solids 53:2101–2118
53. Harrison C, Stafford CM, Zhang WH, Karim A (2004) Sinusoidal phase grating created by a tunably buckled surface. Appl Phys Lett 85:4016–4018
54. Stafford CM, Harrison C, Beers KL, Karim A, Amis EJ, Vanlandingham MR, Kim HC, Volksen W, Miller RD, Simonyi EE (2004) A buckling-based metrology for measuring the elastic moduli of polymeric thin films. Nat Mater 3:545–550
55. Bertrand P, Jonas A, Laschewsky A, Legras R (2000) Ultrathin polymer coatings by complexation of polyelectrolytes at interfaces: suitable materials, structure and properties. Macromol Rapid Commun 21:319–348
56. Decher G (1997) Fuzzy nanoassemblies: toward layered polymeric multicomposites. Science 277:1232–1237
57. Decher G, Hong JD, Schmitt J (1992) Buildup of ultrathin multilayer films by a self-assembly process. 3. Consecutively alternating adsorption of anionic and cationic polyelectrolytes on charged surfaces. Thin Solid Films 210:831–835
58. Picart C, Bernard S, Sengupta K, Dubreuil F, Fery A (2007) Measuring mechanical properties of polyelectrolyte multilayer thin films: novel methods based on AFM and optical techniques. Colloids Surf A Physicochem Eng Asp 303:30–36
59. Lu C, Donch I, Nolte M, Fery A (2006) Au nanoparticle-based multilayer ultrathin films with covalently linked nanostructures: spraying layer-by-layer assembly and mechanical property characterization. Chem Mater 18:6204–6210
60. Jiang CY, Wang XY, Gunawidjaja R, Lin YH, Gupta MK, Kaplan DL, Naik RR, Tsukruk VV (2007) Mechanical properties of robust ultrathin silk fibroin films. Adv Funct Mater 17: 2229–2237
61. Huang H, Chung JY, Nolte AJ, Stafford CM (2007) Characterizing polymer brushes via surface wrinkling. Chem Mater 19:6555–6560
62. Karade Y, Pihan SA, Brunger WH, Dietzel A, Berger R, Graf K (2009) Determination of cross-link density in ion-irradiated polystyrene surfaces from rippling. Langmuir 25:3108–3114
63. Jiang C, Singamaneni S, Merrick E, Tsukruk VV (2006) Complex buckling instability patterns of nanomembranes with encapsulated gold nanoparticle arrays. Nano Lett 6:2254–2259
64. Dönch I (2008) Mechanische eigenschaften von polyelektolyt-multilagen bei verschiedenen ladungsdichten und hydratationszuständen. Potsdam, Germany
65. Blockcopolymers were a gift from Laschewsky and Ott FIfAPR. Golm, Germany
66. Nolte AJ, Cohen RE, Rubner MF (2006) A two-plate buckling technique for thin film modulus measurements: applications to polyelectrolyte multilayers. Macromolecules 39:4841–4847
67. Nolte AJ, Rubner MF, Cohen RE (2005) Determining the Young's modulus of polyelectrolyte multilayer films via stress-induced mechanical buckling instabilities. Macromolecules 38:5367–5370
68. Jiang XY, Takayama S, Qian XP, Ostuni E, Wu HK, Bowden N, LeDuc P, Ingber DE, Whitesides GM (2002) Controlling mammalian cell spreading and cytoskeletal arrangement with conveniently fabricated continuous wavy features on poly(dimethylsiloxane). Langmuir 18:3273–3280

69. Uttayarat P, Toworfe GK, Dietrich F, Lelkes PI, Composto RJ (2005) Topographic guidance of endothelial cells on silicone surfaces with micro- to nanogrooves: orientation of actin filaments and focal adhesions. J Biomed Mater Res 75A:668–680
70. Lu CH, Mohwald H, Fery A (2007) A lithography-free method for directed colloidal crystal assembly based on wrinkling. Soft Matter 3:1530–1536
71. Allard M, Sargent EH, Lewis PC, Kumacheva E (2004) Colloidal crystals grown on patterned surfaces. Adv Mater 16:1360–1364
72. Cui Y, Bjork MT, Liddle JA, Sonnichsen C, Boussert B, Alivisatos AP (2004) Integration of colloidal nanocrystals into lithographically patterned devices. Nano Lett 4:1093–1098
73. Dziomkina NV, Vancso GJ (2005) Colloidal crystal assembly on topologically patterned templates. Soft Matter 1:265–279
74. Juillerat F, Solak HH, Bowen P, Hofmann H (2005) Fabrication of large-area ordered arrays of nanoparticles on patterned substrates. Nanotechnology 16:1311–1316
75. Maury P, Escalante M, Reinhoudt DN, Huskens J (2005) Directed assembly of nanoparticles onto polymer-imprinted or chemically patterned templates fabricated by nanoimprint lithography. Adv Mater 17:2718–2723
76. Ozin GA, Yang SM (2001) The race for the photonic chip: colloidal crystal assembly in silicon wafers. Adv Funct Mater 11:95–104
77. vanBlaaderen A, Ruel R, Wiltzius P (1997) Template-directed colloidal crystallization. Nature 385:321–324
78. Varghese B, Cheong FC, Sindhu S, Yu T, Lim CT, Valiyaveettil S, Sow CH (2006) Size selective assembly of colloidal particles on a template by directed self-assembly technique. Langmuir 22:8248–8252
79. Winkleman A, Gates BD, McCarty LS, Whitesides GM (2005) Directed self-assembly of spherical particles on patterned electrodes by an applied electric field. Adv Mater 17: 1507–1511
80. Xia DY, Brueck SRJ (2004) A facile approach to directed assembly of patterns of nanoparticles using interference lithography and spin coating. Nano Lett 4:1295–1299
81. Aizenberg J, Braun PV, Wiltzius P (2000) Patterned colloidal deposition controlled by electrostatic and capillary forces. Phys Rev Lett 84:2997–3000
82. Chen KM, Jiang XP, Kimerling LC, Hammond PT (2000) Selective self-organization of colloids on patterned polyelectrolyte templates. Langmuir 16:7825–7834
83. Jonas U, del Campo A, Kruger C, Glasser G, Boos D (2002) Colloidal assemblies on patterned silane layers. Proc Natl Acad Sci USA 99:5034–5039
84. Decher G, Schlenoff JB (2003) Multilayer thin films. Wiley, Weinheim
85. Horn A, Schoberth HG, Hiltl S, Chiche A, Wang Q, Schweikart A, Fery A, Böker A (2009) Nanostructured wrinkled surfaces for templating bionanoparticles. Faraday Discuss. 143:143–150
86. Knez M, Sumser MP, Bittner AM, Wege C, Jeske H, Hoffmann DM, Kuhnke K, Kern K (2004) Binding the tobacco mosaic virus to inorganic surfaces. Langmuir 20:441–447
87. Kuncicky DM, Naik RR, Velev OD (2006) Rapid deposition and long-range alignment of nanocoatings and arrays of electrically conductive wires from tobacco mosaic virus. Small 2:1462–1466
88. Radloff C, Vaia RA, Brunton J, Bouwer GT, Ward VK (2005) Metal nanoshell assembly on a virus bioscaffold. Nano Lett 5:1187–1191
89. Royston E, Lee SY, Culver JN, Harris MT (2006) Characterization of silica-coated tobacco mosaic virus. J Colloid Interface Sci 298:706–712
90. Soto CM, Blum AS, Wilson CD, Lazorcik J, Kim M, Gnade B, Ratna BR (2004) Separation and recovery of intact gold-virus complex by agarose electrophoresis and electroelution: application to the purification of cowpea mosaic virus and colloidal gold complex. Electrophoresis 25:2901–2906
91. Wargacki SP, Pate B, Vaia RA (2008) Fabrication of 2D ordered films of tobacco mosaic virus (TMV): processing morphology correlations for convective assembly. Langmuir 24: 5439–5444

92. Yoo PJ, Nam KT, Belcher AM, Hammond PT (2008) Solvent-assisted patterning of polyelectrolyte multilayers and selective deposition of virus assemblies. Nano Lett 8:1081–1089
93. Chung S, Lee JH, Moon MW, Han J, Kamm RD (2008) Non-lithographic wrinkle nanochannels for protein preconcentration. Adv Mater 20:3011–3016
94. Kumar A, Whitesides GM (1994) Patterned condensation figures as optical diffraction gratings. Science 263:60–62
95. Whitesides GM, Ostuni E, Takayama S, Jiang XY, Ingber DE (2001) Soft lithography in biology and biochemistry. Annu Rev Biomed Eng 3:335–373
96. Xia YN, Whitesides GM (1998) Soft lithography. Angew Chem Int Ed 37:551–575
97. Pompe T, Fery A, Herminghaus S, Kriele A, Lorenz H, Kotthaus JP (1999) Submicron contact printing on silicon using stamp pads. Langmuir 15:2398–2401
98. Xia YN, Rogers JA, Paul KE, Whitesides GM (1999) Unconventional methods for fabricating and patterning nanostructures. Chem Rev 99:1823–1848

Adv Polym Sci (2010) 227: 101–143
DOI:10.1007/12_2009_37

Published online: 16 March 2010

Layered Systems Under Shear Flow

Daniel Svenšek and Helmut R. Brand

Abstract We discuss and review a generalization of the usual hydrodynamic description of smectic *A* liquid crystals motivated by the experimentally observed shear-induced destabilization and reorientation of smectic *A* like systems. We include both the smectic layering (via the layer displacement u and the layer normal $\hat{p}$) and the director $\hat{n}$ of the underlying nematic order in our macroscopic hydrodynamic description and allow both directions to differ in non equilibrium situations. In a homeotropically aligned sample the nematic director couples to an applied simple shear, whereas the smectic layering stays unchanged. This difference leads to a finite (but usually small) angle between $\hat{n}$ and $\hat{p}$, which we find to be equivalent to an effective dilatation of the layers. This effective dilatation leads, above a certain threshold, to an undulation instability of the layers with a wave vector parallel to the vorticity direction of the shear flow. We include the couplings of the velocity field with the order parameters for orientational and positional order and show how the order parameters interact with the undulation instability. We explore the influence of the magnitude of various material parameters on the instability. Comparing our results to available experimental results and molecular dynamic simulations, we find good qualitative agreement for the first instability. In addition, we discuss pathways to higher instabilities leading to the formation of onions (multilamellar vesicles) via cylindrical structures and/or the break-up of layers via large amplitude undulations.

D. Svenšek
Theoretische Physik III, Universität Bayreuth, 95440 Bayreuth, Germany, and Department of Physics, Faculty of Mathematics and Physics, University of Ljubljana, Jadranska 19, SI-1111 Ljubljana, Slovenia
e-mail: daniel.svensek@fmf.uni-lj.si

H.R. Brand (✉)
Theoretische Physik III, Universität Bayreuth, 95440 Bayreuth, Germany
e-mail: brand@uni-bayreuth.de

Keywords Block copolymers · Director · Hydrodynamics · Layer normal · Layered systems · Liquid crystals · Macroscopic behavior · Multilamellar vesicles · Onions · Shear flow · Smectic A · Smectic cylinders · Undulations

Contents

1 Introduction

When many complex fluids are submitted to an applied shear flow, they show interesting coupling phenomena between their internal structure and the flow field. For layered systems of smectic *A* type (including block copolymers, lyotropic systems, and side-chain liquid crystalline polymers) this coupling can induce a reorientation of the layers. Experiments on a large number of systems which differ significantly in their microscopic details nevertheless show striking similarities in their macroscopic behavior under shear. The systems under investigation include block copolymers [1–9], low molecular weight (LMW) liquid crystals [10–12], lyotropic lamellar phases (both LMW [13–21] and polymeric [22]), and liquid crystalline side-chain polymers [23–25]. The experiments performed make either use of steady shear (typically for the low viscosity systems, e.g., in a Couette cell) or large amplitude oscillatory shear (LAOS, often in the highly viscous polymeric systems, e.g., in a cone–plate or plate–plate geometry). Due to these experimental differences a direct comparison between the different systems is not always straightforward. The most common features of all these experiments can be summarized as follows. Starting with an aligned sample where the layers are parallel to the planes of constant velocity ("parallel" orientation), the layering is stable up to a certain critical shear rate [2, 5, 11–13, 17, 22]. At higher shear rates two different situations prevail. Depending on the system either multi-lamellar vesicles [13, 19–22] ("onions", typically in lyotropic systems) or layers perpendicular to the vorticity direction [1–5, 11, 12, 24] ("perpendicular" orientation, typically in solvent free systems) are

observed. In a number of systems a third regime is observed at even higher shear rates with a parallel orientation [5, 13]. If the starting point is rather a randomly distributed lamellar phase, the first regime is not observed [1, 4, 19, 26]. This last point illustrates that experiments on layered liquids depend on the pre-history of the sample. In our further discussion we will concentrate on systems showing a well aligned parallel orientation before shear is applied.

The experimental similarities between different systems suggest that the theoretical description of these reorientations can be constructed, at least to some extent, from a common basis independent of the actual system. (On the other hand, a description including the differences between the systems under investigation must refer more closely to their microscopic details. In particular single molecule effects are expected to influence significantly the phenomena observed for polymers and block-copolymers). When looking for a macroscopic description, the well established standard smectic A hydrodynamics [27–30] might appear as a good starting point for such a theoretical approach. However, using the usual set of hydrodynamic equations of the smectic A phase [28–30] the observed change of orientation cannot be explained, because in these models each layer is assumed to be a two dimensional isotropic fluid. Or to put it differently: no destabilizing mechanism for well aligned parallel layers is present in the standard smectic A hydrodynamics.

In the framework of irreversible thermodynamics (compare, for example, [31, 32]) the macroscopic variables of a system can be divided into those due to conservation laws (here mass density ρ, momentum density $g = \rho v$ with the velocity field v and energy density ε) and those reflecting a spontaneously broken continuous symmetry (here the layer displacement u characterizes the broken translational symmetry parallel to the layer normal). For a smectic A liquid crystal the director $\hat{n}$ of the underlying nematic order is assumed to be parallel to the layer normal $\hat{p}$. So far, only in the vicinity of a nematic–smectic A phase transition has a finite angle between $\hat{n}$ and $\hat{p}$ been shown to be of physical interest [33].

Smectic A liquid crystals are known to be rather sensitive to dilatations of the layers. As shown in [34, 35], a relative dilatation of less than 10^{-4} parallel to the layer normal suffices to cause an undulation instability of the smectic layers. Above this very small, but finite, critical dilatation the liquid crystal develops undulations of the layers to reduce the strain locally. Later on Oswald and Ben-Abraham considered dilated smectic A under shear [36]. When a shear flow is applied (with a parallel orientation of the layers), the onset for undulations is unchanged only if the wave vector of the undulations points in the vorticity direction (a similar situation was later considered in [37]). Whenever this wave vector has a component in the flow direction, the onset of the undulation instability is increased by a portion proportional to the applied shear rate.

Over the last decade several explanations have been proposed for specific systems. In [38] the effect of shear flow on layer fluctuations in lamellar phases has been considered. The authors found that the lifetime of thermal fluctuations is significantly influenced by the shear flow and concluded that this can give rise to a destabilization of the layers. In [39], Williams and MacKintosh calculated the effect of the tangential strain on each layer in a sheared block copolymer. By minimization

of the free energy of the system they found a tilt of the polymer chains and a tendency of the layers to reduce their thickness. They interpreted this tendency as a dilatation and found an undulation instability by similar arguments as those given in [34, 35]. About a decade ago Zilman and Granek [40] considered short wavelength fluctuations. In their model these fluctuations are suppressed for energetic reasons leading to an undulation instability of the layers. More recently Marlow and Olmsted investigated the importance of the entropic Helfrich interactions [41] for lyotropic systems and found the possibility of an undulational instability for non-permeable or only slowly permeating membranes.

Throughout this chapter we focus on the extended hydrodynamic description for smectic A-type systems presented in [42, 43]. We discuss the possibility of an undulation instability of the layers under shear flow keeping the layer thickness and the total number of layers constant. In contrast to previous approaches, Auernhammer et al. derived the set of macroscopic dynamic equations within the framework of irreversible thermodynamics (which allows the inclusion of dissipative as well as reversible effects) and performed a linear stability analysis of these equations. The key point in this model is to take into account both the layer displacement u and the director field $\hat{n}$. The director $\hat{n}$ is coupled elastically to the layer normal $\hat{p} = \frac{\nabla(z-u)}{|\nabla(z-u)|}$ in such a way that $\hat{n}$ and $\hat{p}$ are parallel in equilibrium; z is the coordinate perpendicular to the plates.

This chapter is organized as follows. After a review of the model presenting the macroscopic equations in Sect. 2.1 and their implementation in Sect. 2.2, we extend the basic model in the following sections. Especially we include the cross coupling to the velocity field and the moduli of the nematic and smectic order parameters. It turns out that the coupling terms to the velocity are important since they can change the critical parameters significantly. We find that the moduli of the order parameters also show undulations and, thus, regions with a reduced order parameter can be identified. The comparison of the different levels of approximations shows that the basic model is contained in this more general analysis as a special case. We also compare our results to experiments and molecular dynamic simulations and show that an oscillatory instability is extremely unlikely to occur. In the last two sections we discuss higher instabilities leading to the formation of onions (multilamellar vesicles, MLVs) via cylindrical structures and/or the break-up of layers due to large amplitude undulations, pathways that have also been suggested in scattering experiments, in particular in Richtering's group.

2 Model and Technique

In this and the next section we will draw heavily on [43] and we will also make use of our older work [42].

2.1 Physical Idea of the Model

In a smectic *A* liquid crystal one can easily define two directions: the normal to the layers $\hat{p}$ and an average over the molecular axes, the director, $\hat{n}$. In the standard formulation of smectic *A* hydrodynamics these two directions are parallel by construction. Only in the vicinity of phase transitions (either the nematic–smectic *A* or smectic *A*–smectic C^*) has it been shown that director fluctuations are of physical interest [33, 44, 45]. Nevertheless $\hat{n}$ and $\hat{p}$ differ significantly in their interaction with an applied shear flow.

We consider a situation as show in Fig. 1. A well aligned smectic *A* liquid crystal is placed between two parallel and laterally infinite plates. The upper plate (located at $z = d/2$) moves with a constant velocity $v_u = d\dot{\gamma}\hat{e}_x/2$ to the right and the lower plate (at $-d/2$) moves with the same velocity in the opposite direction ($v_l = -d\dot{\gamma}\hat{e}_x/2$). Thus the sample is submitted to an average shear given by $(v_u - v_l)/d = \dot{\gamma}$. As mentioned above, a three dimensional stack of parallel fluid layers cannot couple directly to an applied shear flow. Neither does the layer normal: it stays unchanged as long as the flow direction lies within the layers. In contrast, it is

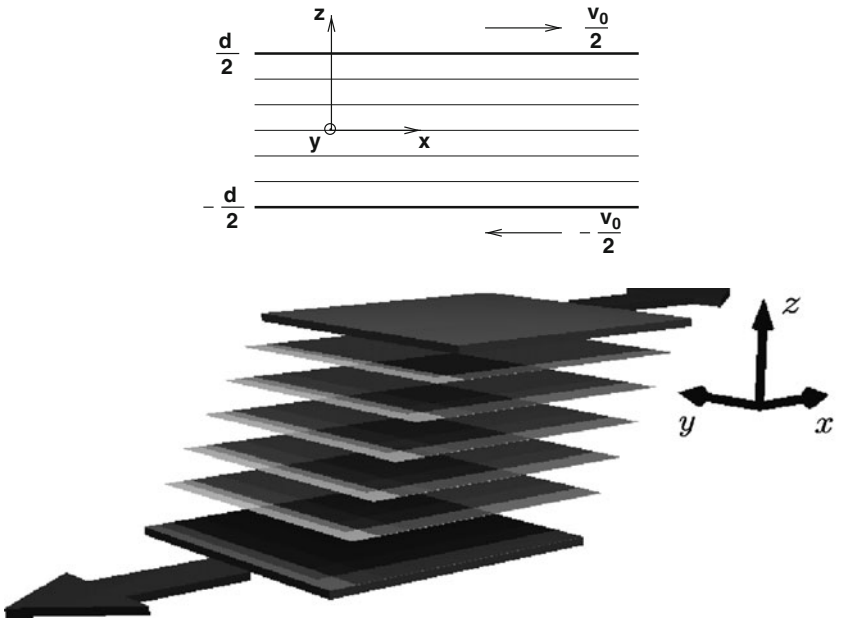

Fig. 1 At the level of the approximation we use in this chapter, all experimental shear geometries are equivalent to a simple steady shear. We choose our system of coordinates such that the normal to the plates points along the *z*-axis and the plates are located at $z = \pm\frac{d}{2}$. Between two parallel plates we assume a defect-free well aligned lamellar phase. The upper plate moves with the velocity $\frac{v_0}{2}$ in positive *x* direction, the lower plate moves with the same velocity in negative *x* direction. The *y*-direction points into the *xz*-plane. We call the plane of the plates (*xy*-plane) the shear plane, the *x*-direction the flow direction, and the *y*-direction the vorticity direction

well known from nematodynamics that the director experiences a torque in a shear flow. This torque leads – in the simplest case – to a flow aligning behavior of the director. The key assumption in the model of [42] is that this torque is still present in a smectic *A* liquid crystal and acts only on the director $\hat{n}$ and not on the layer normal $\hat{p}$. An energetic coupling between $\hat{n}$ and $\hat{p}$ ensures that both directions are parallel in equilibrium.

Submitted to a shear flow the layer normal will stay unchanged, but the director will tilt in the direction of the flow until the torques due to the flow and due to the coupling to the layer normal balance one another. For any given shear rate a finite, but usually small, angle θ between $\hat{n}$ and $\hat{p}$ will result. This finite angle has important consequences for the layers: Since the preferred thickness of the layers is proportional to the projection of the director on the layer normal, a finite angle between those two directions is equivalent to an effective dilatation of approximately $\theta^2/2$ (see Fig. 2). If we assume a constant total sample thickness and exclude effects of defects, the system can accommodate this constraint by layer rotations. A global rotation of the layers is not possible, but they can rotate locally (as in the case of dilated smectic *A* liquid crystals [34, 35]). This local rotation of the layers leads to undulations as shown in Fig. 3. These undulation are a compromise between the effective dilatation (which is not favorable for the system) and the curvature of the layers due to the undulations (which costs energy). In the static case of dilated smectic *A* liquid crystals no direction is preferred, but Oswald and Ben-Abraham [36] have shown that this symmetry is broken if an additional shear is applied to the system. In this case the standard formulation of smectic *A* hydrodynamics predicts that the wave vector of the undulations will point along the neutral direction of the shear (vorticity direction). In this chapter we will assume that this result of Oswald and Ben-Abraham also holds in the case of our extended formulation of smectic *A* hydrodynamics (see Fig. 3).

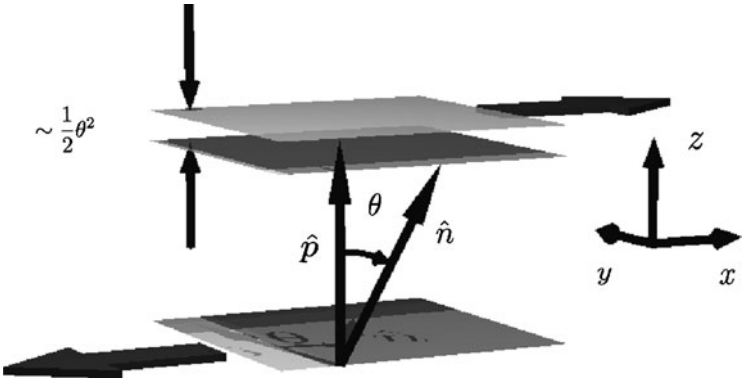

Fig. 2 A finite angle θ between $\hat{n}$ and $\hat{p}$ leads to a tendency of the layers to reduce their thickness. Assuming a constant number of layers in the sample, this tendency is equivalent to an effective dilatation of the layers. For small angles between $\hat{n}$ and $\hat{p}$ the relative effective dilatation is given by $\theta^2/2$

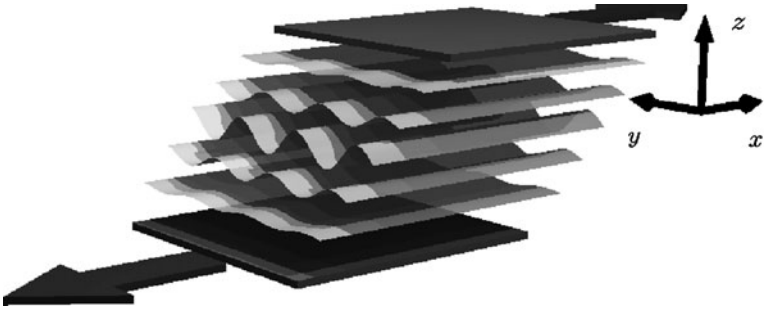

Fig. 3 Above a certain threshold the effective dilatation due to the director tilt will lead to buckling of the layers. Note the difference in directions: the director is tilted in the flow direction, whereas the wave vector points along the *y*-axis. This configuration cancels the direct coupling between the flow and the buckling

2.2 Implementation of the Model

To generate the macroscopic hydrodynamic equations we follow the procedure given by the framework of irreversible thermodynamics [31]. This method has successfully been applied in many cases to derive the macroscopic hydrodynamic equations of complex fluids (see, e.g., [28, 30, 42, 46, 47]). The advantage of this method is its systematic way of deducing the governing equations. Once the set of variables is given, the macroscopic hydrodynamic equations follow by applying basic symmetry arguments and thermodynamic considerations.

Let us briefly review the essential ingredients to this procedure (for more details of the method see [30] and for our model [42]). For a given system the hydrodynamic variables can be split up into two categories: variables reflecting conserved quantities (e.g., the linear momentum density, the mass density, etc.) and variables due to spontaneously broken continuous symmetries (e.g., the nematic director or the layer displacements of the smectic layers). Additionally, in some cases non-hydrodynamic variables (e.g., the strength of the order parameter [48]) can show slow dynamics which can be described within this framework (see, e.g., [30, 47]).

Using all these variables the relations, which form the starting point for the further calculations, can be constructed. These relations are: the energy density ε, the dissipation function R, the Gibbs-relation and the Gibbs–Duhem relation. To illustrate the idea of our model we split up ε and R into several parts according to the different origin of the variables:

- Conserved quantities (index *cons*)
- Symmetry variables (index *sym*)
- The modulus of the order parameter (index *ord*)

In the spirit of our model, two order parameters play a role: the nematic tensorial order parameter Q_{ij} and the smectic A complex order parameter Φ. For practical reason we use the director $\hat{n}$ and the modulus $S^{(n)}$ in the uniaxial nematic case

$[Q_{ij} = \frac{3}{2}S^{(n)}(n_i n_j - \frac{1}{3}\delta_{ij})]$ and the layer displacement u and the modulus $S^{(s)}$ in the smectic A case $[\varphi = S^{(s)}\exp\{\mathrm{i}q_0(z-u)\}]$. Here, as in the rest of the chapter, we refer to the system of coordinates defined in Sect. 2.1. We note that u is only a good variable if we consider small deformations of the layers. For large layer deformations the phase $\varphi = z - u$ is the appropriate variable [49, 50]. In our further discussion, we will concentrate on the parts due to symmetry variables and the order parameters, while for terms already present in the isotropic fluid see, e.g., [30, 31].

Let us first consider the energy density. The conventions of notation introduced by the following equations are summarized in Table 1:

$$\varepsilon = \varepsilon_{\mathrm{cons}} + \varepsilon_{\mathrm{sym}} + \varepsilon_{\mathrm{ord}}^{(n)} + \varepsilon_{\mathrm{ord}}^{(s)} \tag{1}$$

$\varepsilon_{\mathrm{cons}}$, which is identical to the isotropic fluid, is discussed elsewhere [30, 31]. The symmetry part reads

$$\begin{aligned}\varepsilon_{\mathrm{sym}} = {} & \frac{1}{2}K_1(\nabla\cdot\hat{n})^2 + \frac{1}{2}K_2\left[\hat{n}\cdot(\nabla\times\hat{n})\right]^2 + \frac{1}{2}K_3\left[\hat{n}\times(\nabla\times\hat{n})\right]^2 + \frac{1}{2}K\left(\nabla_\perp^2 u\right)^2 \\ & + \frac{1}{2}B_0\left[\nabla_z u + (1-n_z) - \frac{1}{2}\left(\nabla_\perp u\right)^2\right]^2 + \frac{1}{2}B_1\left(\hat{n}\times\hat{p}\right)^2\end{aligned} \tag{2}$$

In (2) the spirit of the model becomes clear. We combine the properties of a nematic liquid crystal (the first two lines) with these of a smectic A (the third and fourth lines) and couple both parts (the last lines) in such a way that $\hat{n}$ and $\hat{p}$ are parallel

Table 1 Summary of the notation. In these definitions we use the transverse Kronecker symbol $\delta_{ij}^{\perp} = \delta_{ij} - n_i n_j$. Due to the thermodynamic stability of the systems the following combinations of constants must be positive: B_0, B_1, K, L_0, $L_\perp^{(n,s)}$, $L_\parallel$, and $M_0^2 - KL_\parallel$. For the last relation we used the equivalence of K and K_1

Symbol	Explicit form	Comment
K	K	Bending modulus of layers
B_0	B_0	Compressibility of layers
B_1	B_1	Coupling between the director and the layer normal
$L_0^{(n,s)}$	$L_0^{(n,s)}$	Variations of the order parameter (nematic and smectic, respectively)
$L_{1,ij}^{(n)}$	$L_\perp^{(n)}\delta_{ij}^{\perp} + L_\parallel^{(n)} n_i n_j$	Gradients terms of the order parameter (nematic)
M_{ijk}	$M_0(\delta_{ij}^{\perp} n_k + \delta_{ik}^{\perp} n_j)$	Cross-coupling between the director and order parameter (nematic)
$L_{1,ij}^{(s)}$	$L_\perp^{(s)}(\delta_{ij} - p_i p_j) + L_\parallel^{(s)} p_i p_j$	Gradients terms of the order parameter (smectic)

in equilibrium. As discussed earlier [42], ε_{sym} simplifies considerably by dropping higher order terms and assuming a small angle between $\hat{n}$ and $\hat{p}$. Splay deformations of the director are generally considered as higher order corrections to dilatations of the smectic layers. Twist deformations are forbidden in standard smectic A hydrodynamics and must be small as long as the angle between $\hat{n}$ and $\hat{p}$ is small. Additionally, the difference between the splay deformation of the director field $K_1/2\ (\nabla\cdot\hat{n})^2$ and bending of the layers $K/2\ \left(\nabla_\perp^2 u\right)^2$ is negligible. Consequently we combine splay and bend in a single term with a single elastic constant which we call K': $K_1/2\ (\nabla\cdot\hat{n})^2 + K/2\ \left(\nabla_\perp^2 u\right)^2 \approx K'/2\ \left(\nabla_\perp^2 u\right)^2$. In the following we drop the prime and call the new elastic constant K. The approximated version of ε_{sym} is now given by

$$\begin{aligned}\varepsilon_{\text{sym}} = &\frac{1}{2}K\left(\nabla_\perp^2 u\right)^2 \\ &+\frac{1}{2}B_0\left[\nabla_z u + (1-n_z) - \frac{1}{2}\left(\nabla_\perp u\right)^2\right]^2 + \frac{1}{2}B_1\left(\hat{n}\times\hat{p}\right)^2\end{aligned} \tag{3}$$

In our model the moduli of the nematic and smectic order parameters play similar roles, so we will deal with both. Since we consider a situation beyond the phase transition regime, the equilibrium value of the order parameter is non-zero ($S_0^{(n,s)}$, for both nematic and smectic) and only its variations $s^{(n,s)}$ can enter the energy density ($S^{(n,s)} = S_0^{(n,s)} + s^{(n,s)}$):

$$\begin{aligned}\varepsilon_{\text{ord}}^{(n)} = &\frac{1}{2}L_0\left(s^{(n)}\right)^2 + \frac{1}{2}L_{1,ij}^{(n)}\left(\nabla_i s^{(n)}\right)\left(\nabla_j s^{(n)}\right) \\ &+ M_{ijk}\nabla_j n_i \nabla_k s^{(n)}\end{aligned} \tag{4}$$

$$\varepsilon_{\text{ord}}^{(s)} = \frac{1}{2}L_0\left(s^{(s)}\right)^2 + \frac{1}{2}L_{1,ij}^{(s)}\left(\nabla_i s^{(s)}\right)\left(\nabla_j s^{(s)}\right) \tag{5}$$

By a similar construction we write down the dissipation function as (see Table 2 for a list of the thermodynamic variables and their conjugates)

Table 2 Variables and their conjugates, i.e., the corresponding thermodynamic forces

Name	Variable	Conjugate
Mass density	ρ	μ
Momentum density	g	v
Nematic director	$\hat{n}$	h
Smectic layer displacement	u	Ψ
Variation of the modulus of the order parameter (either nematic or smectic)	$s^{(n,s)}$	$\Xi^{(n,s)}$

$$R = R_{\rm cons} + R_{\rm sym} + R_{\rm ord} \tag{6}$$

$$R_{\rm cons} = \frac{1}{2}\nu_{ijkl}\left(\nabla_j v_i\right)\left(\nabla_l v_k\right) + R_0 \tag{7}$$

$$R_{\rm sym} = \frac{1}{2\gamma_1} h_i \delta_{ij}^{\perp} h_j + \lambda_p \Psi^2 \tag{8}$$

$$R_{\rm ord} = \frac{1}{2}\alpha^{(n)}\,\Xi^{(n)2} + \frac{1}{2}\alpha^{(s)}\,\Xi^{(s)2} \tag{9}$$

where R_0 summarizes further terms due to conservations laws, which do not enter our further calculation, and (after [46])

$$\begin{aligned}\nu_{ijkl} = {} & \nu_2(\delta_{jl}\delta_{ik} + \delta_{il}\delta_{jk}) \\ & + 2(\nu_1 + \nu_2 - 2\nu_3) n_i n_j n_k n_l \\ & + (\nu_3 - \nu_2)(n_j n_l \delta_{ik} + n_j n_k \delta_{il} \\ & \qquad + n_i n_k \delta_{jl} + n_i n_l \delta_{jk}) \\ & + (\nu_4 - \nu_2)\delta_{ij}\delta_{kl} \\ & + (\nu_5 - \nu_4 + \nu_2)(\delta_{ij} n_k n_l + \delta_{kl} n_i n_j)\end{aligned} \tag{10}$$

As mentioned in Sect. 2.1, we consider a shear induced smectic C like situation (but with a small tilt angle, i.e., a weak biaxiality). We neglect this weak biaxiality in the viscosity tensor and use it in the uniaxial formulation given above (with the director $\hat{n}$ as the preferred direction). This assumption is justified by the fact that the results presented in this chapter do not change significantly if we use $\hat{p}$ instead of $\hat{n}$ in the viscosity tensor.

Throughout our calculations we will not assume any restriction on the viscosity constants except the usual requirements due to thermodynamic stability (see, e.g., [30]). Later on we will impose the incompressibility of the fluid by assuming a constant mass density ρ of the fluid. We emphasize that this procedure does not require any further assumption about the material parameters.

The set of basic equations is completed by the Gibbs–Duhem (the local formulation of the second law of thermodynamics) and the Gibbs relation (which connects the pressure P with the other thermodynamic quantities), which we will use in the following form:

$$\begin{aligned}\mathrm{d}\varepsilon = {} & \mathrm{d}\varepsilon_0 + v\mathrm{d}g + \varphi_{ij}\mathrm{d}\nabla_j n_i + h_i'\mathrm{d}n_i + \psi_i \mathrm{d}\nabla_i u \\ & + \Xi'^{(n)}\mathrm{d}s^{(n)} + \Xi_i''^{(n)}\mathrm{d}\nabla_i s^{(n)} \\ & + \Xi'^{(s)}\mathrm{d}s^{(s)} + \Xi_i''^{(s)}\mathrm{d}\nabla_i s^{(s)}\end{aligned} \tag{11}$$

$$P = -\varepsilon + \mu\rho + T\sigma + v \cdot g \tag{12}$$

The newly defined quantities in (11) are connected to the thermodynamic forces (Table 2) by the following relations:

$$h_i = h_i' - \nabla_j \varphi_{ij} = \frac{\delta\varepsilon}{\delta n_i} \tag{13}$$

$$\Psi = -\nabla_i \psi_i = \frac{\delta\varepsilon}{\delta u} \tag{14}$$

$$\Xi^{(n,s)} = \Xi'^{(n,s)} - \nabla_i \Xi_i''^{(n,s)} = \frac{\delta\varepsilon}{\delta s^{(n,s)}} \tag{15}$$

Following the standard procedure within the framework of irreversible thermodynamics we find the following set of macroscopic hydrodynamic equations [30, 31, 42, 47]:

$$\begin{aligned} &\frac{\partial}{\partial t} u + v_j \nabla_j u \\ &\quad = v_z - \lambda_p \Psi \end{aligned} \tag{16}$$

$$\begin{aligned} &\frac{\partial}{\partial t} n_i + v_j \nabla_j n_i \\ &\quad = \frac{1}{2}\left[(\lambda - 1)\delta_{ij}^{\perp} n_k + (\lambda + 1)\delta_{ik}^{\perp} n_j\right] \nabla_j v_k \\ &\qquad - \frac{1}{\gamma_1} \delta_{ik}^{\perp} h_k \end{aligned} \tag{17}$$

$$0 = \nabla_i v_i \tag{18}$$

$$\begin{aligned} &\rho\left(\frac{\partial}{\partial t} v_i + v_j \nabla_j v_i\right) \\ &\quad = -\nabla_j \Big\{ \psi_j (\nabla_i u + \delta_{i3}) + \beta_{ij}^{(n,s)} \Xi^{(n,s)} \\ &\qquad - \frac{1}{2}\left[(\lambda - 1)\delta_{jk}^{\perp} n_i + (\lambda + 1)\delta_{ik}^{\perp} n_j\right] h_k \\ &\qquad + \nu_{ijkl} \nabla_l v_k \Big\} \\ &\qquad - \nabla_i P \end{aligned} \tag{19}$$

$$\begin{aligned} &\frac{\partial}{\partial t} s^{(n,s)} + v_j \nabla_j s^{(n,s)} \\ &\quad = -\beta_{ij}^{(n,s)} \nabla_j v_i - \alpha^{(n,s)} \Xi^{(n,s)} \end{aligned} \tag{20}$$

For the reversible parts of the equations some coupling constants have been introduced: the flow-alignment tensor

$$\lambda_{ijk} = \frac{1}{2}\left[(\lambda-1)\delta^{\perp}_{ij}n_k + (\lambda+1)\delta^{\perp}_{ik}n_j\right] \tag{21}$$

with the flow-alignment parameter λ (and using $\delta^{\perp}_{ij} = \delta_{ij} - n_i n_j$) and the coupling between flow and order parameter

$$\beta^{(n)}_{ij} = \beta^{(n)}_{\perp}\delta^{\perp}_{ij} + \beta^{(n)}_{\parallel} n_i n_j \tag{22}$$

$$\beta^{(s)}_{ij} = \beta^{(s)}_{\perp}(\delta_{ij} - p_i p_j) + \beta^{(s)}_{\parallel} p_i p_j \tag{23}$$

Furthermore, there is a reversible coupling between the layer displacement and the velocity field in (16). But its coupling constant has to be unity due to the Gallilei invariance of the equations. As mentioned above, the use of u is limited to small layer deformations.

The transverse Kronecker symbols $\delta^{\perp}_{ij}$ in (17) and (21) guarantee the normalization of $\hat{n}$. This implies that only two of the (17) are independent. For the following calculations it turned out to be useful to guarantee the normalization of the director by introducing two angular variables θ and ϕ to describe the director:

$$n_x = \sin\theta\cos\phi \tag{24}$$

$$n_y = \sin\theta\sin\phi \tag{25}$$

$$n_z = \cos\theta \tag{26}$$

Consequently, (17) has to be replaced using angular variables. Denoting the right hand side of (17) with Y_i, this can be done the following way:

$$\frac{\partial}{\partial t}\theta + v_j\nabla_j\theta = Y_x\cos\theta\cos\phi + Y_y\cos\theta\sin\phi - Y_z\sin\theta \tag{27}$$

$$\frac{\partial}{\partial t}\phi + v_j\nabla_j\phi = -Y_x\frac{\sin\phi}{\sin\theta} + Y_y\frac{\cos\phi}{\sin\theta} \tag{28}$$

In the same way, we guarantee the normalization of $\hat{p}$ by using

$$p_x = 0 \tag{29}$$

$$p_y = -\nabla_y u \tag{30}$$

$$p_z = \sqrt{1-p_y^2} \tag{31}$$

The different ways of normalizing $\hat{n}$ and $\hat{p}$ arise from the fact that $\hat{p}$ is parallel to $\hat{e}_z$ in zeroth order, whereas $\hat{n}$ encloses a finite angle with $\hat{e}_z$ for any given shear rate.

The set of macroscopic hydrodynamic equations we now deal with, (16), (18)–(20), (27), and (28), follows directly from the initial input in the energy density and the dissipation function without any further assumptions.

To solve these equations we need suitable boundary conditions. In the following we will assume that the boundaries have no orienting effect on the director (the homeotropic alignment of the director is only due to the layering and the coupling between the layer normal $\hat{p}$ and the director $\hat{n}$). Any variation of the layer displacement must vanish at the boundaries:

$$u\left(\pm\frac{1}{2}d\right) = 0 \tag{32}$$

For the velocity field the situation is a little more complex: We assume no-slip boundary conditions, i.e., the velocity of the fluid and the velocity of the plate are the same at the surface of the plate. It is convenient to split the velocity field in to two parts: the shear field v_0 which satisfies the governing equations and the no-slip boundary condition and the correction v_1 to this shear field. The boundary condition for v_1 now reads

$$v_1\left(\pm\frac{1}{2}d\right) = 0 \tag{33}$$

Making use of the following considerations this condition can be simplified. Due to (16) the z-component of v_1 is suppressed by a factor of λ_p (which is typically extremely small [29, 36]). Making use of the results of [36] we can assume that v_1 depends only on y and z and thus conclude [with (18)] that the y-component of v_1 is also suppressed by λ_p. For this reason one can assume that $v_{1,y}$ and $v_{1,z}$ are negligible and the only relevant boundary condition for the velocity field is

$$v_{1,x} = 0 \tag{34}$$

The validity of this assumption is nicely illustrated by our results. Figure 7 shows that v_y and v_z are indeed suppressed by λ_p.

2.3 Technique of Solution

The aim now is twofold: finding a spatially homogeneous solution of the governing equations (for a given shear rate) and investigating the stability of this solution. In this section we will describe the general procedure and give the results in Sect. 3.

We write the solution as the vector $X = (\theta, \phi, u, v_x, v_y, v_z, P, s^{(n,s)})$ consisting of the angular variables of the director, the layer displacement, the velocity field, the pressure, and the modulus of the (nematic or smectic) order parameter. For a spatially homogeneous situation the equations simplify significantly and the desired solution X_0 can directly be found (see Sect. 3.1). To determine the region of stability of X_0 we perform a linear stability analysis, i.e., we add a small perturbation X_1 to

Table 3 If the symmetry under inversion of z is given for one component of X_1, the symmetry of all other components follows directly from the linearized set of equations. Here we give the z-symmetry of all components assuming that u is an even function of z

Quantity	z-Symmetry	Quantity	z-Symmetry
u	Even	v_x	Even
θ	Odd	v_y	Odd
ϕ	Even	v_z	Even
P	Odd	$s^{(n,s)}$	Odd

the homogeneous solutions X_0: $X = X_0 + X_1$ (with $X_1 \ll X_0$) and linearize the governing equations in the small perturbations. In short, the solution of the equation $\mathsf{L} X_1 = \frac{\partial}{\partial t} X_1$ is analyzed. Here L denotes the operator for the linearized set of the governing equations. The ansatz for the unknown quantities must fulfill the boundary conditions [see the discussion following (32)] and follow the symmetry scheme given by Table 3. Assuming an exponential time dependence and harmonic spatial dependence of X_1:

$$X_{1,i} \sim \exp\left[(\mathrm{i}\omega + \frac{1}{\tau})t\right] \begin{Bmatrix}\cos(qy)\\ \sin(qy)\end{Bmatrix} \begin{Bmatrix}\cos(q_z z)\\ \sin(q_z z)\end{Bmatrix} \tag{35}$$

fulfills all requirements (with an oscillation rate ω, a growth rate $1/\tau$, and a wave vector $q = q\hat{e}_y + q_z\hat{e}_z$). In this ansatz we made use of the results by Oswald and Ben-Abraham [36], who have shown that in standard dilated smectic A under shear the first instability will set in with a wave vector along the neutral direction of the flow ($q \cdot \hat{e}_x = 0$). After inserting the above ansatz in the linearized set of (partial differential) equations, a set of coupled linear equations is obtained to determine $1/\tau$ and ω.

From the standard smectic A hydrodynamics it is known that shear does not destabilize the layers. Since our extended formulation of the smectic A hydrodynamics is equivalent to the standard smectic A hydrodynamics for vanishing external fields (e.g., shear rate), we assume that the layers are stable for low enough shear rates, i.e., $1/\tau < 0$ for small shear rates. So $1/\tau = 0$ marks the set of external parameters (shear rate) and material parameters above which X_1 grows. Typically we hold the material parameters fixed and the only external parameter is the shear rate. The solvability condition of the corresponding set of linear equations gives a relation between the shear rate [and tilt angle θ_0, which is directly connected to the shear rate, see (38) below], ω and the wave vector q. For every given q a specific shear rate (and tilt angle θ_0) can be determined which separates the stable region (below) from the unstable region (above). This defines the so-called curve of marginal stability (or neutral curve) $\theta_0(q)$. If, for any given set of external parameters, the tilt angle θ_0 lies above the curve of marginal stability for at least one value of q, the spatial homogeneous state is unstable and undulations grow. The smallest shear rate (tilt angle) for which undulations can grow is called the critical shear rate (tilt angle). Technically

speaking, we solve $\mathbb{L} X = i\omega X$ – in many cases we can set $\omega = 0$, see below. We point out that this linear analysis is only valid at the point where the first instability sets in. Without further investigations no prediction of the spatial structure of the developing instability can be made. Also the nature of the bifurcation (backward or forward) must be determined by further investigations.

For practical reasons we used dimensionless units in our numerical calculations. The invariance of the governing equations under rescaling time, length, and mass allows us to choose three parameters in these equations to be equal to unity. We will set

$$B_1 = 1, \quad \gamma_1 = 1, \quad \text{and} \quad \frac{d}{\pi} = q_z = 1 \tag{36}$$

and measure all other quantities in the units defined by this choice. Nevertheless we will keep these quantities explicitly in our analytical work.

To extract concrete predictions for experimental parameters from our calculations is a non-trivial task, because neither the energetic constant B_1 nor the rotational viscosity γ_1 are used for the hydrodynamic description of the smectic *A* phase (but play an important role in our model). Therefore, we rely here on measurements in the vicinity of the nematic–smectic *A* phase transition. Measurements on LMW liquid crystals made by Litster [33] in the vicinity of the nematic–smectic *A* transition indicate that B_1 is approximately one order of magnitude less than B_0. As for γ_1 we could not find any measurements which would allow an estimate of its value in the smectic *A* phase. In the nematic phase γ_1 increases drastically towards the nematic–smectic *A* transition (see, e.g., [51]). Numerical simulations on a molecular scale are also a promising approach to determine these constants [52].

Due to the complexity of the full set of governing equations, we will start our analysis with a minimal set of variables (θ, ϕ, and u) and suppress the coupling to the other variables (see Sect. 3.2.1). Step by step the other variables will be taken into account. The general picture of the instability will turn out to be already present in the minimal model, but many interesting details will be added throughout the next sections. In comparison to our earlier work [42], we now use the way of normalizing $\hat{n}$ and $\hat{p}$ derived above. This will lead to some small differences in the results but leaves the general picture unchanged. First we assume a stationary instability (i.e., we let $\omega = 0$); later on we discuss the possibility for an oscillatory instability and have a look at some special features of the system (Sects. 3.3 and 3.4).

3 Results and Discussion

3.1 Spatially Homogeneous State

Looking for a spatially homogeneous solution, the governing equations simplify significantly. A linear shear profile

$$v_0 = \dot{\gamma} z \hat{e}_x \tag{37}$$

is a solution to (18) and u stays unchanged in this regime. The only variables which have a zeroth order correction for all shear rates are the tilt angle θ and the modulus of the nematic order parameters $s^{(n)}$:

$$\left(\frac{\lambda+1}{2}-\lambda\sin^2(\theta_0)\right)\dot{\gamma} = \frac{B_1}{\gamma_1}\sin(\theta_0)\cos(\theta_0) + \frac{B_0}{\gamma_1}\sin(\theta_0)(1-\cos(\theta_0)) \tag{38}$$

$$\alpha^{(n)}L_0 s_0^{(n)} = (\beta_\parallel^{(n)}-\beta_\perp^{(n)})\sin(\theta_0)\cos(\theta_0)\dot{\gamma} \tag{39}$$

Equation (39) shows that nematic degrees of freedom couple to simple shear, but not the smectic degrees of freedom; the modulus of the nematic order parameter has a non-vanishing spatially homogeneous correction (see (39)), whereas the smectic order parameter stays unchanged. The reason for this difference lies in the fact that $\beta_{ij}^{(n)}$ and $\beta_{ij}^{(s)}$ include $\hat{n}$ and $\hat{p}$, respectively, which coupled differently to the flow field (see (22) and (23)). Equation (38) gives a well defined relation between the shear rate $\dot{\gamma}$ and the director tilt angle θ_0, which we will use to eliminate $\dot{\gamma}$ from our further calculations. To lowest order θ_0 depends linearly on $\dot{\gamma}$:

$$\theta_0 = \dot{\gamma}\frac{\gamma_1}{B_1}\,\frac{\lambda+1}{2}+O(\theta_0^3) \tag{40}$$

We are not aware of any experimental data, which would allow a direct comparison with these results. We stress, however, that molecular dynamics simulations by Soddemann et al. [53] are in very good agreement with (38) and (40).

In contrast to the director tilt the lowest order correction to the nematic order parameter is quadratic in the shear rate (tilt angle):

$$s_0^{(n)} = \frac{2}{\lambda+1}\,\frac{B_1}{\gamma_1}\,\frac{\beta_\parallel^{(n)}-\beta_\perp^{(n)}}{\alpha^{(n)}L_0}\theta_0^2+O(\theta_0^4) \tag{41}$$

In the following we consider perturbations around the spatially homogeneous state given above.

3.2 Stationary Instability

3.2.1 Minimal Set of Variables

Let us first consider the effect of our modifications regarding the normalization of $\hat{n}$ and $\hat{p}$ in comparison to our earlier results [42]. For this purpose we consider only

a minimal set of variables: the director (characterized by the two angles θ and ϕ) and the layer displacement u. We neglect all couplings of these variables to other quantities describing the system, namely the velocity field and the moduli of the nematic and smectic order parameters. Within these approximations the equations to solve are

$$\begin{aligned} 0 = A_\theta \Big\{ & 2\dot{\gamma}\lambda \sin(\theta_0)\cos(\theta_0) \\ & + \frac{B_0}{\gamma_1}\left[\sin^2(\theta_0) - \cos^2(\theta_0) + \cos(\theta_0)\right] \\ & - \frac{B_1}{\gamma_1}\left[\sin^2(\theta_0) - \cos^2(\theta_0)\right] \Big\} \\ & - A_u \ \frac{B_0}{\gamma_1}\sin(\theta_0) q_z \end{aligned} \tag{42}$$

$$0 = A_\phi \ \frac{1}{2}\dot{\gamma}(\lambda + 1) - A_u \ \frac{B_1}{\gamma_1} q \tag{43}$$

$$\begin{aligned} 0 = & A_\theta \ \lambda_p B_0 \sin(\theta_0) q_z \\ & + A_\phi \ \lambda_p B_1 q \sin(\theta_0)\cos(\theta_0) \\ & - A_u \ \lambda_p \Big[- B_0 q^2 (1 - \cos(\theta_0)) \\ & \qquad + B_1 q^2 \cos^2(\theta_0) + K q^4 + B_0 q_z^2 \Big] \end{aligned} \tag{44}$$

Here we inserted an ansatz of the type (35) and denoted the linear amplitudes of θ, ϕ, and u by A_θ, A_ϕ, and A_u, respectively. One can solve these equations either by expanding them in a power series of θ_0 (expecting to get a closed result for the critical values) or numerically. It turns out that one has to take into account terms (at least) up to order ${\theta_0}^5$ in (42)–(44) to get physically meaningful (but rather long and complicated) analytical results. For this reason the closed expressions have no advantage over the purely numerical solutions and we do not give the analytical approximations explicitly. A comparison with the results of [42] will be given in the Appendix. We will present and discuss our findings using the minimal set of variables in Sect. 3.2.2 in direct comparison to the results of the full set of equations.

3.2.2 Coupling to the Velocity Field

In the previous section we have shown that a minimal set of variables supports our picture of the physical mechanism. But neglecting the coupling between velocity field and nematic director and vice versa is a rather crude approximation since it is well known, that this coupling plays an important role in nematohydrodynamics [29, 30]. So the natural next step is to include this coupling and to perform a linear

stability analysis of (16)–(18), (27) and (28). In this case the standard procedures leads to a system of seven coupled linear differential equations. Following the discussion after (32) these equations can be solved by an ansatz of the type given in (35). This reduces the system of equations to seven coupled linear equations which are easily solved using standard numerical tools (such as singular value decomposition and inverse iteration to find the eigenvectors). Due to the complexity of the equations we used Maple to determine the final set of linear equations. The key ingredients of this Maple script are given in [54].

Figure 4 gives a comparison of typical neutral curves for the minimal model and calculations including the velocity field. The overall shape of the neutral curve is not changed due to the coupling to the velocity field but a shift of the critical values (especially in the critical tilt angle) is already visible. The inset shows the relative amplitudes of the linear solutions at onset on a logarithmic scale. For θ, ϕ, and u the left bars correspond to the minimal model and the right bars to the extended version. Note that amplitudes with a different sign are shown with a different line style in the histograms (see figure caption for details).

Let us have a closer look at the differences between the minimal and the extended set of equations and follow these differences along some paths in the parameter space. As mentioned in Sect. 2.3, we can omit some of the physical parameters by using dimensionless parameters. In Figs. 5–9 we show the dependence of the critical values of the tilt angle and wave vector on the dimensionless parameters (as defined

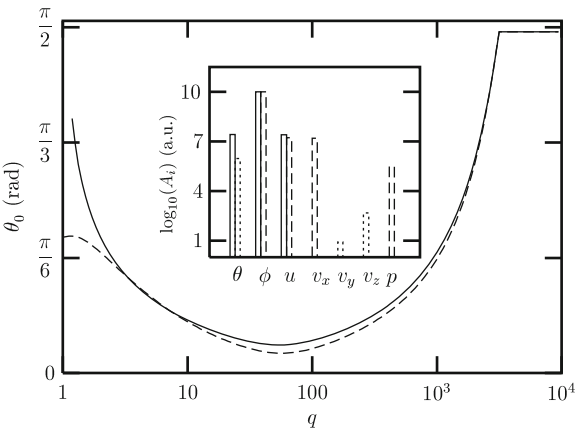

Fig. 4 A typical picture for the comparison of the neutral curves using the minimal set of variables (*solid line*) and including the velocity fields (*dashed line*). The overall behavior does not change but the critical values are altered due to the coupling with the velocity field. For this plot we used (in the dimensionless units discussed in Sect. 2.3) $B_0 = 10$, $K = 10^{-6}$, $\lambda = 1.1$, $\nu_1 = \nu_2 = \nu_3 = \nu_4 = \nu_5 = 0.1$, and $\lambda_p = 10^{-6}$. The *inset* shows the linear amplitudes A_i (where i stands for θ, ϕ, etc.) at onset. Since the logarithm of the amplitudes is shown, amplitudes with different sign are shown with a different line style. Using the minimal set (*left bars*) all amplitudes have the same sign (*solid lines*). Including the velocity field (*right bars*) some amplitudes are positive (*dashed lines*), others negative (*dotted lines*). Note that we use in this and all following plots the dimensionless units defined by (36)

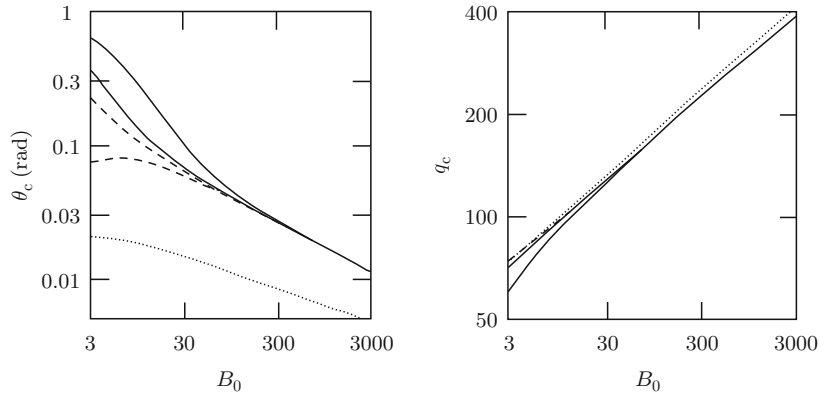

Fig. 5 A significant difference between the various approaches is only visible for $B_0 \lesssim 100$. At higher values of B_0 the number of free variables plays no noticeable role and the critical values follow a master curve. The *solid lines* show results including the velocity field, the *dashed lines* correspond to the minimal set of variables. At low B_0 in the upper curves we used $\lambda = 2$

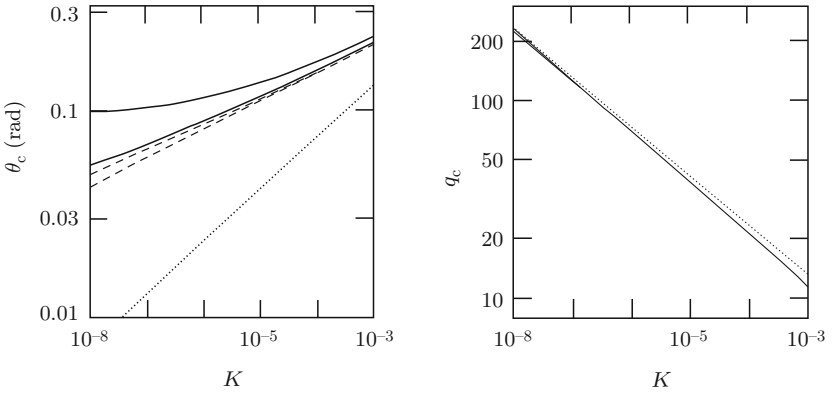

Fig. 6 Plotting the critical values as a function of the bending modulus K shows a convergence of the curves, which is nevertheless not as pronounced as in the case of Fig. 5. The influence of λ on the critical tilt angle is significant ($\lambda = 2$ in the upper curves and $\lambda = 1.1$ in the lower ones). Again the *solid lines* show results including the velocity field, the *dashed lines* correspond to the minimal set of variables, and the *dotted lines* depict the outcome of the first approach. Note that the wave vectors of the minimal set and of the calculations including the velocity field are indistinguishable within the resolution of the plot

in (36)). For all these figures we used the same basic set of parameters: $B_0 = 10$, $K = 10^{-6}$, $\lambda = 1.1$, $\nu_1 = \nu_2 = \nu_3 = \nu_4 = \nu_5 = 0.1$, and $\lambda_p = 10^{-6}$. These values are estimates for a typical thermotropic LMW liquid crystal, where we made use of the results of [33, 51] (as far as B_1 and γ_1 are concerned, see also the last paragraph in Sect. 3.2.1). For flow alignment parameters in the range $1 \lesssim \lambda \lesssim 3$ the critical values vary strongly with λ (see Fig. 9). Therefore we discuss in addition the situation for $\lambda = 2$ to indicate the range of possible values.

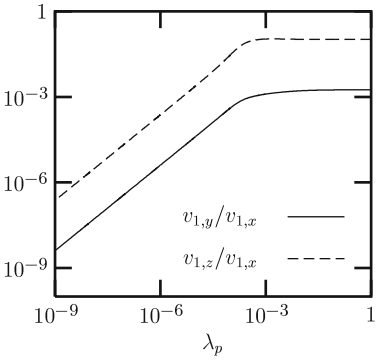

Fig. 7 In all our calculations $v_{1,x}$ is the dominating component of v_1. This graph demonstrates that the other components are suppressed by λ_p (making them almost negligible)

Considering the critical values as a function of the compression modulus B_0 results in a rather simple situation (Fig. 5). For small values of B_0 a significant influence of the coupling between the director and velocity field is apparent, which also shows a strong dependence on λ. For large B_0 all these differences vanish and only a single curve is obtained. At this point a comparison to dilated smectic *A* is instructive. It is well known [34, 35] that in dilated smectic the critical wave vector and the critical dilatation show a power law behavior as a function of B_0 with exponents $1/4$ and $-1/2$, respectively. In the limit of large B_0 we found the same exponents already in our earlier analysis [42]. If we fit power laws to our results for $B_0 > 10^2$ we find the exponents equal to ≈ 0.235 and ≈ -0.37 for q_c and θ_c, respectively (note that the dilatation in our model is $\approx \frac{1}{2}\theta_c^2$). So both approaches (the minimal set of variables and the calculations including the velocity field) show, despite all similarities to the standard model of smectic *A* and to our earlier analysis, differences in the details of the instability.

A similar, but less pronounced, situation is apparent, when plotting the critical values as a function of the bending modulus (see Fig. 6). The curves tend to converge for large *K*, but there remains a difference between the minimal set of variables and the calculations including the the velocity field. Fitting the *K*-dependence with power laws (here for $K > 10^{-4}$) only the critical wave number exhibits an exponent close to the values expected from dilated smectic *A* (≈ -0.26 vs $-\frac{1}{4}$). This illustrates the fact that shearing a lamellar system is similar to dilating it but not equivalent.

In contrast to the cases discussed above, the permeation constant λ_p has no strong influence on the critical values. For dimensionless values $\lambda_p < 10^{-6}$ the critical values do not change at all with λ_p. For large values variations within a factor of two are possible. The permeation constant is known to be very small. In our dimensionless units we expect it be of the order of $< 10^{-9}$ for LMW thermotropic liquid crystals and neglect its influence on the critical values for this reason. In Sect. 2.2 we have emphasized that the *y*- and *z*-components of the velocity field are suppressed via λ_p. These qualitative arguments are clearly confirmed by our numerical results. In all our calculations $v_{1,x}$ is the dominating component of v_1 and the ratio $v_{1,y}/v_{1,x}$

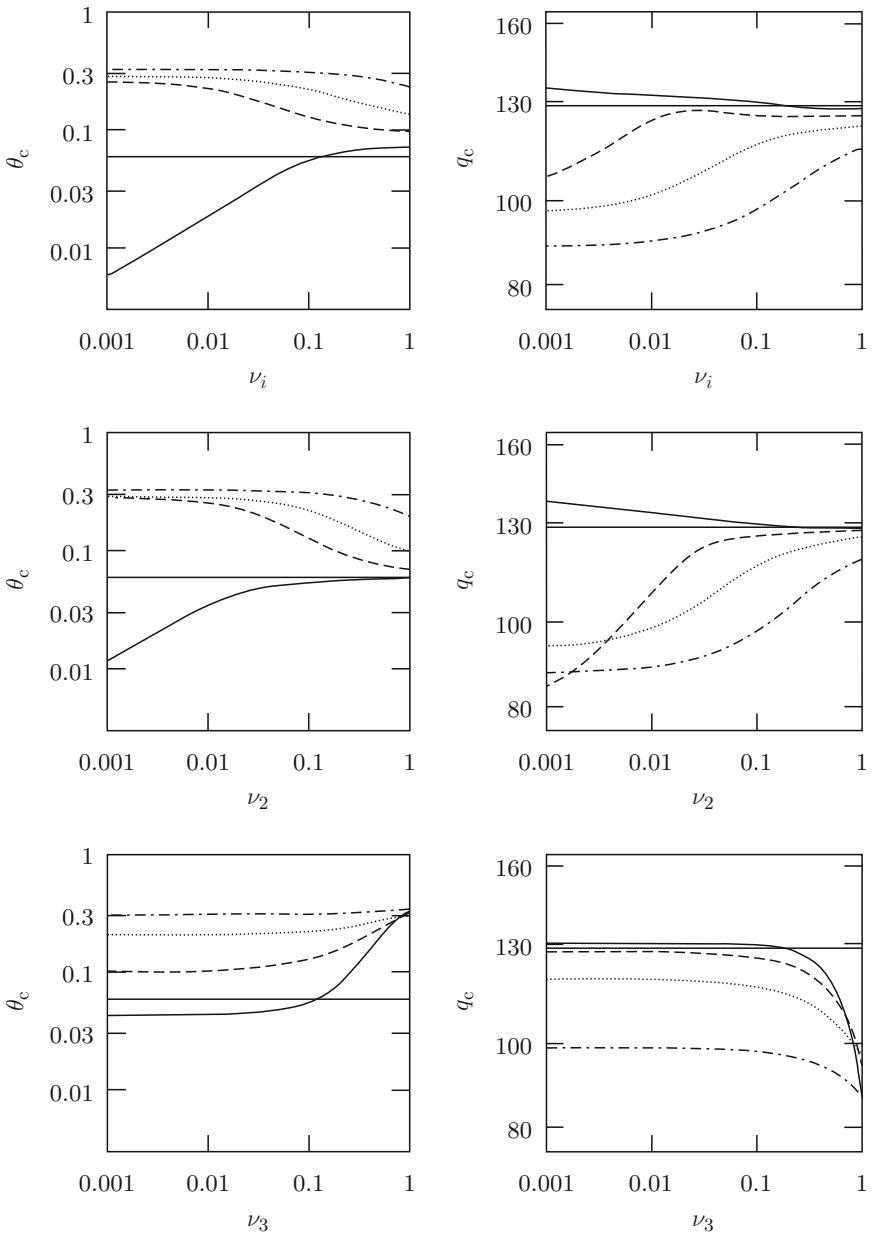

Fig. 8 Only the viscosities ν_2 and ν_3 can influence the critical parameters significantly. The upper row depicts the dependence on a isotropic variation of the viscosity. In the middle and lower row we present the variation with ν_2 and ν_3 setting the other viscosities to $\nu_i = 0.1$. Here the *thick solid lines* represent the minimal set of variables. For the full set of variables we have chosen four different values of λ: the *solid curves* with $\lambda = 0.7$, the *dashed curves* with $\lambda = 1.3$, the *dotted curves* with $\lambda = 2$ and the *dot-dashed curves* with $\lambda = 3.5$. Note the similarities between the curves for small (*solid*) and large λ (*dot-dashed*) in the upper and middle row. In these regimes ν_2 is the dominating viscosity

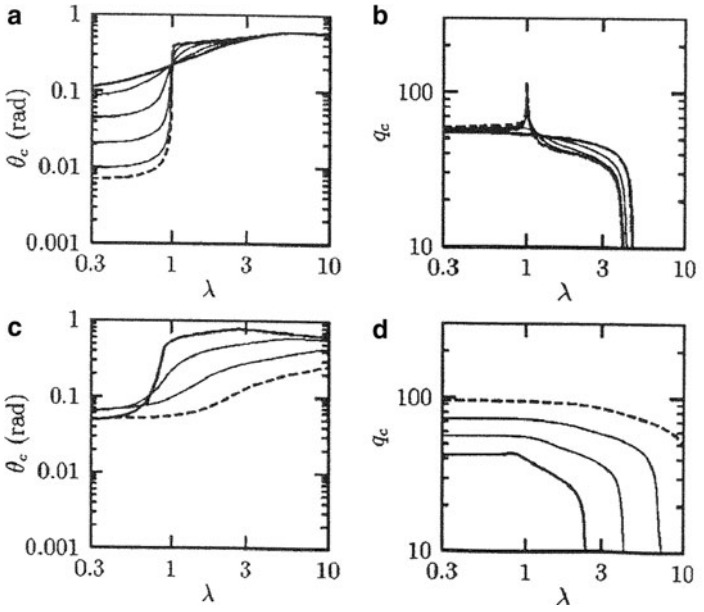

Fig. 9 Critical values as functions of the flow alignment parameter λ for various viscosities (**a**, **b**) and compressibilities (**c**, **d**). In the upper row we plot this dependence for a set of (isotropic) viscosities ranging from $\nu_i = 1$ (*thick solid line*,) down to $\nu_i = 10^{-3}$ (*thick dashed line*,). The lower row illustrates the behavior for varying layer compressibility B_0 with $B_0 \approx 3$ for the *thick solid curve* and $B_0 = 100$ for the *thick dashed curve*. In all plots the *thin solid lines* give the behavior for some intermediate values. For an interpretation of this behavior see the text

is of the order of λ_p over the whole range of physical relevant values of λ_p (see Fig. 7). This fact nicely supports our argument that we can neglect the boundary condition for $v_{1,y}$, because $v_{1,y}$ vanishes anyway.

Out of the five viscosities, only two (ν_2 and ν_3) show a significant influence on the critical values. In Fig. 8 we present the dependence of θ_c and q_c on an assumed isotropic viscosity (upper row) and on these two viscosity coefficients (middle and lower row). Since the flow alignment parameter λ has a remarkable influence on these curves we have chosen four different values of λ in this figure, namely $\lambda = 0.7$, $\lambda = 1.1$, $\lambda = 2$, and $\lambda = 3.5$. The curves for $\lambda \lesssim 1$ and $\lambda \gtrsim 3$ for an isotropic viscosity tensor are very similar to the corresponding curves where only ν_2 is varied. In this parameter range the coefficient ν_2 dominates the behavior. Note that the influence of ν_3 on the critical values is already much smaller than that of ν_2. We left out the equivalent graphs for the other viscosity coefficients, because they have almost no effect on the critical values. For further comments on the influence of an anisotropic viscosity tensor see also Sect. 3.4.

All the parameters we have discussed up to now caused variations in the critical values that did not select specific values of the considered parameter. In this aspect the situation is completely different in the case of the flow alignment parameter λ. As shown in Fig. 9 there is a clear change in behavior for $\lambda \approx 1$ and $\lambda \approx 3$. The

critical tilt angle is increased for values of λ in this interval and the critical wave vector tends to rise only at the boundaries of the interval and is reduced in between. Figure 9 illustrates how this structure depends on the viscosities (assuming all five viscosities to be equal) and on the elastic constants of the layers. In the first row we follow this behavior for viscosities varying from $\nu_i = 1$ down to $\nu_i = 10^{-3}$. Clearly, the influence of λ is more pronounced the lower the viscosities are. Both elastic constants of the layers, the compressibility B_0 and the bending modulus K (in our dimensionless units $B_1 = 1$), have in general a similar influence on the shape of the graphs: the smaller the elastic constants, the more pronounced the structure becomes. For this reason we just give the plot for B_0 (second row in Fig. 9) and omit the plot for K.

These dependencies on the system parameters give some important hints for an interpretation of Fig. 9. The currents and quasi-currents for the velocity field and the director consist of two parts (see (17) and (18)): a diagonal one (coupling, e.g., the components of v among each other) and an off-diagonal one (coupling the director to the velocity field). The former is proportional to the elastic constants or to the viscosity tensor whereas the latter is a function of the flow alignment parameter. So reducing either the elastic constants or the viscosities increases the portion of the cross-coupling terms in theses equations, i.e., the observed tendencies are exactly what one would expect. The next step in the interpretation of the shape of the curves is to have a closer look at the structure of the cross-coupling term. The flow alignment tensor $\lambda_{ijk} = \frac{1}{2}\left[(\lambda-1)\delta^{\perp}_{ij}n_k + (\lambda+1)\delta^{\perp}_{ik}n_j\right]$ obviously changes its behavior for $\lambda = 1$: the first part changes its sign. Note that we are in a region of the parameter space where λ_{ijk} is a dominating term (since either the viscosities or the elastic constants are small). Additionally, $\delta^{\perp}_{ij}n_k$ contains up to the third power of one director component. For this reason we expect that – in the linearized set of equations – some coupling terms change their sign for $\lambda = 1$ others for $\lambda = 3$. For example, the ϕ-component of the director is coupled to the x and z components of the velocity field by the terms $(\lambda-1)/2\,\partial_y v_x$ and $(\lambda-1)/2\,\cot(\theta_0)\partial_y v_z$. Similarly the reversible part of the coupling of v_y to ϕ vanishes for $\lambda = 3$. The monitored structure in the plots cannot be attributed to one single cross-coupling term, but the given examples demonstrate that something should happen in this parameter range.

3.2.3 Including the Order Parameters

In the preceding paragraphs we investigated undulations assuming a constant modulus of the order parameter $S^{(n,s)} = S_0^{(n,s)} + s_0^{(n,s)}$. In general one would expect that the undulations in the other observable quantities should couple to some extent to the order parameter. In the formulation of the free energy (see Sect. 2.2) we have assumed that $S^{(n,s)}$ varies only slightly around $S_0^{(n,s)}$ and thus only the lowest order terms in $s^{(n,s)}$ contribute to the free energy. For the spatially homogeneous state we had (see (39) and (41)) a correction to the nematic $S^{(n)}$ proportional to the square of the shear rate ($\theta_0 \sim \dot{\gamma}$ for low $\dot{\gamma}$):

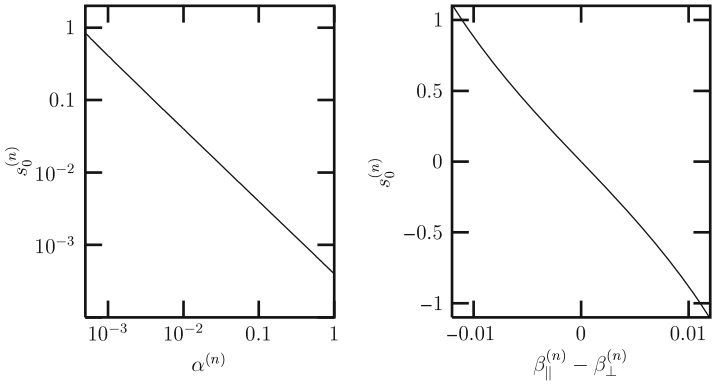

Fig. 10 Evaluating (41) and (45) at onset gives an important restriction on the range of possible parameter values (here the cases of $\alpha^{(n)}$ and $\beta_\parallel^{(n)} - \beta_\perp^{(n)}$). Note that the critical θ_0 is a function of the material parameters

$$s_0^{(n)} = -\frac{2}{\lambda+1}\frac{B_1}{\gamma_1}\frac{\beta_\parallel^{(n)} - \beta_\perp^{(n)}}{\alpha^{(n)} L_0}\theta_0^2 + O(\theta_0^4)$$

As a consequence $s_0^{(n)}$ must be small compared to $S_0^{(n,s)}$ (which is by construction limited to the range $0 \le S_0^{(n,s)} \le 1$). Thus a reasonable restriction is

$$|s_0^{(n)}| \lesssim 0.5 \tag{45}$$

As shown in Fig. 10, evaluating this relation at the onset of the instability reduces significantly the physically reasonable range for some parameters. This restriction applies only for the nematic material parameters and, in general, nothing can be said about the corresponding smectic parameters. We will, however, take the smectic parameters in the same range as the nematic ones. If not indicated otherwise we used $L_0^{(n,s)} = 0.1$, $L_\perp^{(n,s)} = 0.01$, $L_\parallel^{(n,s)} - L_\perp^{(n,s)} = 0.005$, $M_0 = 10^{-4}$, $\beta_\perp^{(n,s)} = 0.01$, $\beta_\parallel^{(n,s)} - \beta_\perp^{(n,s)} = 0.005$, $\alpha^{(n,s)} = 0.001$ for the plots of this section (along with parameter set specified in the previous section).

The ansatz for $s_1^{(n,s)}$ following (35) reads

$$s_1^{(n,s)} = A_s^{(n,s)} \exp\left[\left(\mathrm{i}\omega + \frac{1}{\tau}\right)t\right] \sin(q_z z)\cos(qy). \tag{46}$$

The modulations of $S^{(n,s)}$ in the linear analysis are maximum at the boundaries and in phase with the layer displacement u. The sign of the amplitude $A_s^{(n,s)}$ depends on the coupling to the velocity field (only the anisotropic part $\beta_\parallel^{(n)} - \beta_\perp^{(n)}$ is relevant) and on the coupling to the director undulations (via M_{ijk}, only for the nematic

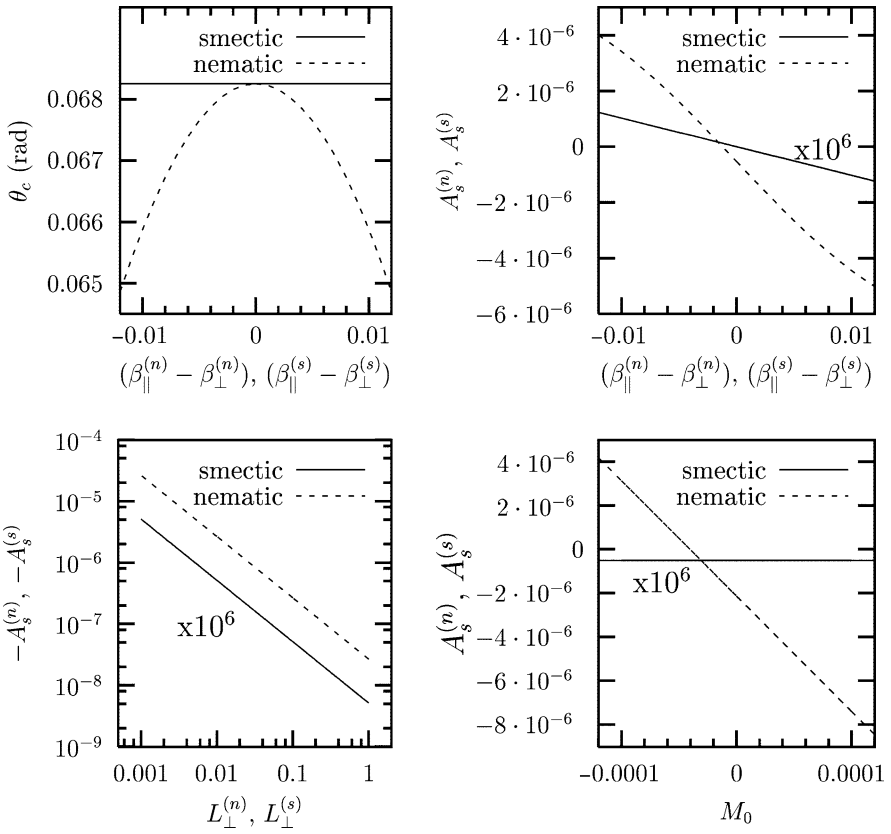

Fig. 11 Out of the material parameters connected with the order parameter, only $\beta_\parallel^{(n,s)} - \beta_\perp^{(n,s)}$ has a measurable effect on the critical values. Some more parameters can influence the amplitudes of the order parameter undulation, namely $L_\perp^{(n,s)}$ and M_0 (the latter is only present in the case of the nematic order parameter). All amplitudes have been normalized such that $A_\phi = 1$. Note that the smectic $A_s^{(s)}$ has been multiplied by 10^6 in the right column. For a better comparison we used a log–log scale in the lower left plot and changed the sign of $A_s^{(s)}$ in this plot

amplitudes $A_s^{(n)}$). If one assumes that shear reduces (and does not increase) the modulus of the order parameter, the nematic $\beta_\parallel^{(n)} - \beta_\perp^{(n)}$ is positive (39) and (41); once again nothing can be said about the smectic $\beta_\parallel^{(s)} - \beta_\perp^{(s)}$.

In general the critical values are not at all or only very slightly influenced by the coupling to the modulus of the order parameter (see Fig. 11). Figure 11 summarizes the parameters with the largest influence on $A_s^{(n,s)}$. In almost all investigated cases the modulation of the nematic order is much larger than in the smectic order. Whether the order is reduced or increased in regions where the layers are compressed depends in the phenomenological constants $\beta_\parallel^{(n,s)} - \beta_\perp^{(n,s)}$ and M_0 which have not been measured up to now.

The above results reveal some interesting features. As shown in Table 3, the modulations of the order parameter change sign under inversion of the z-axis. Considering the boundary condition (i.e., taking our ansatz) this leads to the fact that the effect on the modulus of the order parameters is maximum at the boundaries. So the linear analysis predicts that the regions where the order parameter is influenced most by the undulations are close to the boundaries. Since the probability for the formation of defects is higher in places where the order parameter is lower, we have identified areas where the creation of defects is facilitated. But our analysis does not allow one to predict the structure of the defects. Nevertheless this effect gives a possible way to reorient the parallel layers. Interestingly, experiments in block copolymers by Laurer et al. [3] show a defect structure close to the boundaries which is consistent with this picture.

3.3 Oscillatory Instability

All our arguments in the previous sections were based on the assumption that the undulations set in as a stationary instability. That is, that the oscillation rate ω in our ansatz (35) vanishes at onset. In this section we will discuss the situation for non-zero ω and find that our previous assumption was justified. In our linear analysis enters now (for the first time in this chapter) the mass density of the system, which we will choose to be equal to unity $\rho = 1$.

The search for a possible oscillatory instability is slightly different from the procedure used in the stationary case. The solvability condition of the linearized set of equations determines both the neutral curve and the frequency along this curve. When searching for such a solution we scanned approximately the same parameter space as used for Figs. 5–7. Since the frequency tends to zero when the oscillatory neutral curve gets close to the stationary one, we concentrated on the frequency range $0 \leq \omega \leq 2$ and checked in some cases for higher frequencies.

It turned out that only in cases when the director field is very weakly coupled to the layering a neutral curve for an oscillatory instability is possible. This weak coupling manifests itself in small B_1 and γ_1, which is in our set of dimensionless variables equivalent to large B_0 and ν_i. Oscillatory neutral curves were only found for $B_0 \gtrsim 100$ or $\nu_i \gtrsim 1$. In all investigated cases an oscillatory neutral curve is either absent or lies above the neutral curve for a stationary instability. When an oscillatory neutral curve is possible, it ends in the points where it meets the stationary neutral curve (see Fig. 12). The corresponding frequency approaches zero in the end points of the oscillatory neutral curve. If we ignore for the moment the stationary neutral curve and consider only the oscillatory instability, the corresponding critical values are found to be rather close to the stationary one and approach each other the weaker the coupling between the director and the layers becomes. To summarize, an oscillatory instability was not found to be possible in all investigated cases and seems to be extremely unlikely to occur.

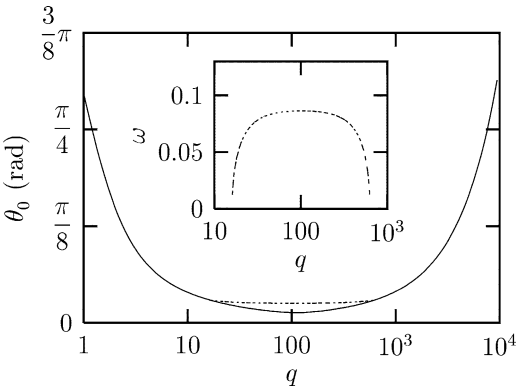

Fig. 12 In most parts of the scanned parameter space no possibility for an oscillatory instability was found. If the director field is only very weakly coupled to the layering (in this plot we used $B_0 = 200$ and $\nu_i = 0.4$) a neutral curve for an oscillatory instability (*dashed line*) appears above the stationary neutral curve (*solid line*). Note that the critical wave vectors are close to each other for both oscillatory and stationary instability. The *inset* shows the frequency along the neutral curve

3.4 Anisotropic Viscosity

In Fig. 8 we have illustrated that a small viscosity coefficient ν_2 facilitates the onset of undulations. In this section we will have a closer look at the effect of an anisotropic viscosity tensor and ask whether undulations can be caused only due to viscosity effects without any coupling to the director field (i.e., we consider standard smectic *A* hydrodynamics in *this* section).

Let us start our considerations by looking at the spatially homogeneous state. In a sample with parallel alignment the apparent viscosity is ν_3, which can easily be seen from the force on the upper boundary:

$$F_{\parallel} = \hat{e}_z \cdot \underline{\sigma} = \dot{\gamma} \nu_3 \hat{e}_x \tag{47}$$

Similarly the viscosity of a perpendicular alignment is given by ν_2:

$$F_{\perp} = \hat{e}_z \cdot \underline{\sigma} = \dot{\gamma} \nu_2 \hat{e}_x \tag{48}$$

For $\nu_2 < \nu_3$ a simple shear flow in a perpendicular alignment causes less dissipation than in a parallel alignment. The next step is to study the stability of these alignments in the linear regime. Following the standard procedure (as described above) we find a solvability condition of the linearized equations which does not depend on the shear rate $\dot{\gamma}$:

$$\begin{aligned} 0 = & \left\{ q^2 + \lambda_p \left[\nu_3 \left(q^2 - q_z^2 \right)^2 + 2 \left(\nu_2 + \nu_3 \right) q^2 q_z^2 \right] \right\} \times \\ & \times \left(B_0 q_z^2 + K q^4 \right) \left(\nu_2 q^2 + \nu_3 q_z^2 \right) \end{aligned} \tag{49}$$

Consequently, a parallel alignment of smectic layers is linearly stable against undulations even if the perpendicular alignment might be more preferable due to some thermodynamic considerations. As we have shown in Fig. 8, this rigorous result of standard smectic *A* hydrodynamics is weakened in our extended formulation of smectic *A* hydrodynamics. When the director can show independent dynamics, an appropriate anisotropy of the viscosity tensor can indeed reduce the threshold values of an undulation instability.

4 Comparison to Experiments and Simulations

In the previous sections we have shown that the inclusion of the director of the underlying nematic order in the description of a smectic *A* like system leads to some important new features. In general, the behavior of the director under external fields differs from the behavior of the layer normal. In this chapter we have only discussed the effect of a velocity gradient, but the effects presented here seem to be of a more general nature and can also be applied to other fields. The key results of our theoretical treatment are a tilt of the director, which is proportional to the shear rate, and an undulation instability which sets in above a threshold value of the tilt angle (or equivalently the shear rate).

Both predictions are in agreement with experimental observations. For side-chain liquid crystalline polymers Noirez [25] observed a shear dependence of the layer thickness. In the parallel orientation the layer thickness is reduced by several percent with increasing shear. To our knowledge, two groups have investigated the evolution of a parallel alignment to the vesicle state for lyotropic systems (see Müller et al. [17] and Zipfel et al. [55]). In both papers the authors argue that cylindrical structures (with an axis along the flow direction) are observable as intermediates. These observed cylindrical intermediates are very close to the undulations proposed by our theoretical treatment.

For an approximate quantitative comparison of our theoretical results with the experiments on lyotropic liquid crystals we make a number of assumptions about the material parameters. As we have shown in Sect. 3.2 the different approaches cause only small variations in the critical wave number. For this estimate it suffices to use the critical wave number obtained in our earlier work [42]. For lyotropics it is known [56, 57], that the elastic constants can be expressed as

$$K = \frac{\kappa}{l} \tag{50}$$

and

$$B = \frac{9}{64}\pi^2 \frac{(k_\mathrm{B}T)^2}{\kappa} \frac{l}{(l-\delta)^4}, \tag{51}$$

where $\kappa = \alpha_\kappa k_B T$ is the bending modulus of a single bilayer, l is the repeat distance, δ is the membrane thickness, k_B is the Boltzmann constant, T is temperature, and α_κ is a dimensionless number of order of unity. With this relations we can estimate the critical wave vector for a sample of thickness d using [42]:

$$q_c^2 \approx \frac{3\pi^2}{8\alpha_\kappa d} \frac{l}{(l-\delta)^2} \tag{52}$$

The parameters of the experiment by Zipfel et al. [55] are: $d = 1$ mm, $\delta = 2.65$ nm, $l = 6.3$ nm, and $\alpha_\kappa = 1.8$ [55, 58]. On this basis we estimate the critical wave length to be of the order of

$$\lambda_c \approx 6.4\,\mu\text{m} \tag{53}$$

Zipfel et al. [55] observed a vesicle radius of 3 μm, which is clearly compatible with our calculation. We note that this estimate assumes that the experiments are done in the hydrodynamic regime.

In Sect. 3.2.3 we have pointed out that the effect on the order parameter is maximum close to the boundaries of the layer. In a reoriented sample Laurer et al. [3] have identified defects near the boundary of the sample which are in accordance with the predicted influence on the order parameter.

The mechanism we have proposed here is somewhat similar to a shear induced smectic-*C* like situation. Consequently, undulations should also be observed near the smectic-*A*–smectic-*C* transitions. Indeed, Johnson and Saupe [59] and later Kumar [60] report such undulations just below the transition temperature. In the same spirit Ribotta and Durand [61] report a compression induced smectic-*C* like situation.

Molecular dynamic simulations recently made by Soddemann et al. [52, 53] offer a very precise insight into the behavior of the layered systems under shear. As we will briefly discuss now, a direct comparison of these simulations to the analytic theory presented above shows very good agreement between both approaches [53]. In Fig. 13 we have plotted the strain rate, $\dot{\gamma}$, as a function of the tilt angle, θ_0.

Clearly flow aligning behavior of the director is present and θ_0 increases linearly with the tilt angle, θ_0. Above a threshold in the strain rate, $\dot{\gamma} \approx 0.011$, undulations in vorticity direction set in. In Fig. 14 the results of simulations for $\dot{\gamma} = 0.015$ are shown. In Fig. 15 we have plotted the undulation amplitude obtained as a function of the shear rate. The dashed line indicates a square root behavior corresponding to a forward bifurcation near the onset of undulations. This is, indeed, what is expected, when a weakly nonlinear analysis based on the underlying macroscopic equations is performed [54]. In Fig. 16 we have plotted an example for the dynamic behavior obtained from molecular dynamics simulations. It shows the time evolution after a step-type start for two shear rates below the onset of undulations. The two solid lines correspond to a fit to the data using the solutions of the averaged linearized form of (27). The shear approaches its stationary value for small tilt angle (implied by the use of the linearized equation) with a characteristic time scale $\tau = \gamma_1/B_1$.

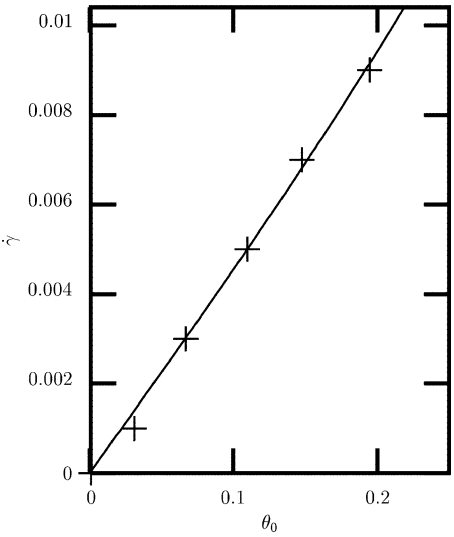

Fig. 13 Strain rate as a function of tilt angle. This form of presenting the data has been chosen to facilitate a direct comparison with the theory, especially (38). The *solid line* is a fit to the data. Extracted from Fig. 5.4 of [54]

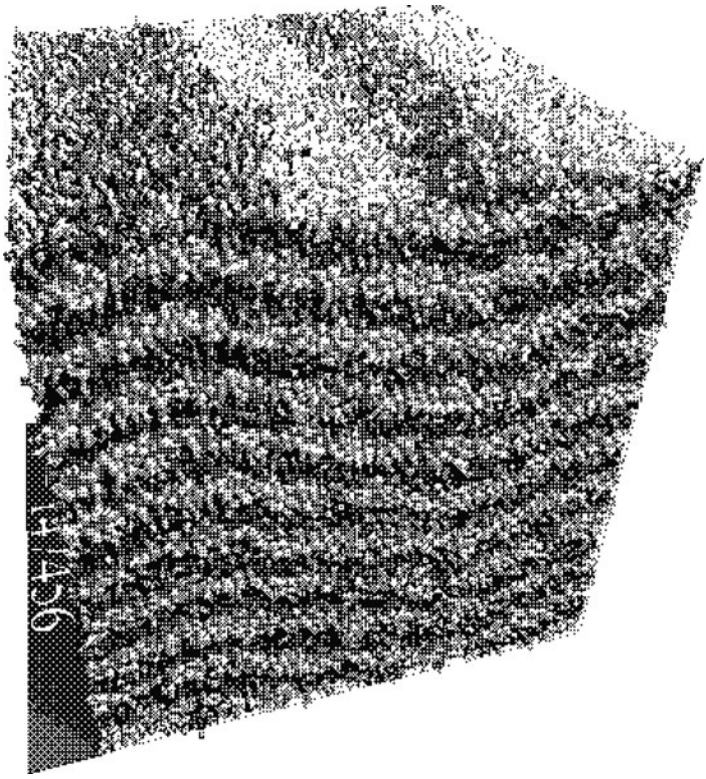

Fig. 14 Undulations in a simulated model system. At a strain rate of $\dot{\gamma} = 0.015$ clearly undulations have developed. As considered in the theory, undulations in the vorticity direction are present. Note that the undulation amplitude does not change along the z- direction. Extracted from Fig. 5.5 of [54]

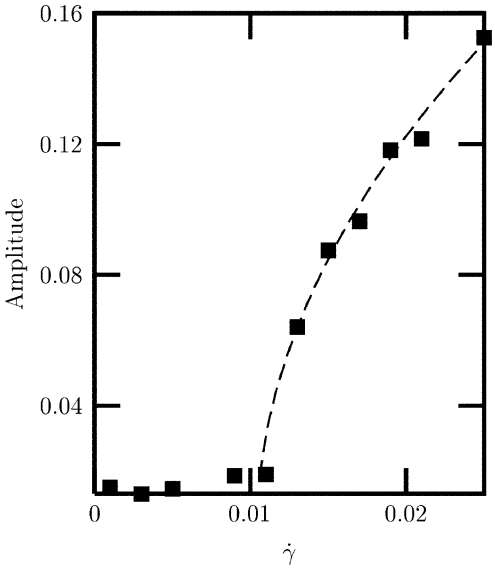

Fig. 15 Undulation amplitude due to shear. The amplitude of the undundulations A is given as a function of the strain rate $\dot{\gamma}$. At a shear rate $\dot{\gamma} \approx 0.01$ undulations set in. The amplitude of these undulations grows continuously with increasing shear rate. The *dashed line* shows a fit to data points starting at $\dot{\gamma} > 0.02$ assuming a square root dependence of the amplitude above the undulation onset. Fig. 5.6 of [54]

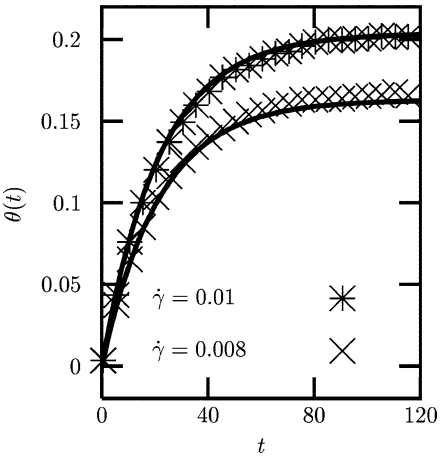

Fig. 16 Time evolution of the director tilt after a step-like start of the shear for two different final shear rates (0.008 and 0.010 in Lennard-Jones units). The lines show the fit to the data using the solution of the averaged linearized form of (27). Fig. 5.12 of [54]

A detailed analysis of the simulation data [53] demonstrated that the analytic theory is in qualitative and frequently even in quantitative agreement with the simulations over the validity range of the linearized theory.

5 Transition to Onions

In this section, we will explore the possibility of having a cylindrical intermediate between the initial lamellar and the final onion state. This possibility has been considered since the shearing experiments of Richtering's group [55, 62] on lyotropic

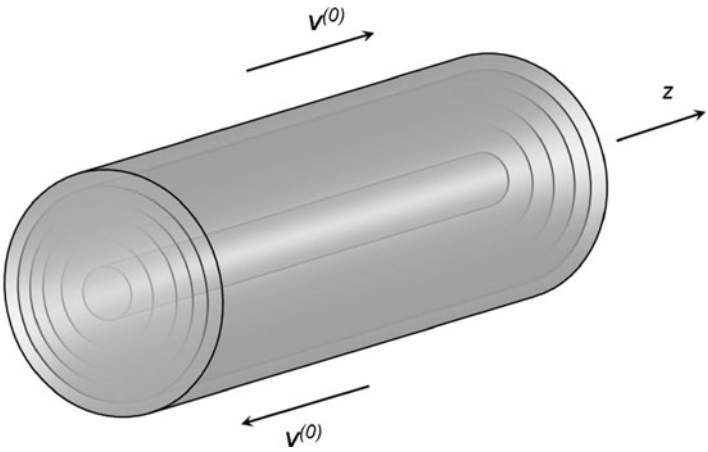

Fig. 17 A schematic representation of the multilamellar cylinder in shear flow. The cylinder axis is aligned along the flow

lamellar phases exhibiting a shear-induced lamellar-to-vesicle (onion) transition. Performing viscosity measurements accompanied by time-resolved small-angle neutron and light scattering, they observe a formation of an intermediate structure exhibiting a scattering pattern corresponding to objects with a cylindrical symmetry oriented in the flow direction. They suggest two possible structures consistent with the overall cylindrical scattering symmetry: multilamellar cylinders with the long axis oriented along the flow, or large amplitude layer undulations with the wave vector in the neutral (vorticity) direction [62].

In what follows, we will explore the first of the two suggested scenarios. Starting with a multilamellar cylinder configuration, we will study its stability under shear flow (Fig. 17). Our aim is to check whether we can find an instability of the cylinder–a secondary instability–that would be responsible for the break-up into onions.

The strategy is as follows. We start by rewriting the equations in cylindrical coordinates (r, ϕ, z). The variables we consider are the layer displacement u (now in the radial direction) from the cylindrical state, the director $\hat{n}$, and the fluid velocity v. The central part of the cylinder, $r < R_1$, containing a line defect, is not included. It is not expected to be relevant for the shear-induced instability. We write down linearized equations for layer displacement, director, and velocity perturbations for a multilamellar (smectic) cylinder oriented in the flow direction (z axis). We are interested in perturbations with the wave vector in the z direction as this is the relevant direction for the hypothetical break-up of the cylinder into onions. The unperturbed configuration in the presence of shear flow (the ground state) depends on r and ϕ and is determined numerically. The perturbations, of course, depend on all three coordinates. We take into account translational symmetry of the ground state in the z direction and use a plane wave ansatz in that direction. Thus, our ansatze for the perturbed variables are

$$u = u^{(0)}(r,\phi) + u^{(1)}(r,\phi,z,t), \tag{54}$$
$$\hat{n} = \hat{n}^{(0)}(r,\phi) + \hat{n}^{(1)}(r,\phi,z,t), \tag{55}$$
$$v = v^{(0)}(r,\phi) + v^{(1)}(r,\phi,z,t), \tag{56}$$

where

$$u^{(1)} = u_0^{(1)}(r,\phi,t)\,\mathrm{e}^{\mathrm{i}kz}, \tag{57}$$
$$\hat{n}^{(1)} = \hat{n}_0^{(1)}(r,\phi,t)\,\mathrm{e}^{\mathrm{i}kz}, \tag{58}$$
$$v^{(1)} = v_0^{(1)}(r,\phi,t)\,\mathrm{e}^{\mathrm{i}kz} \tag{59}$$

and $u_0^{(1)}$, $\hat{n}_0^{(1)}$, and $v_0^{(1)}$ are complex perturbation amplitudes. We use the numerically obtained ground state and evolve the perturbation amplitudes with a selected wave vector in z direction numerically.

The layer normal $\hat{p}$, in first order with respect to u, is

$$\hat{p} = \hat{e}_r - \hat{e}_\phi \frac{\partial u}{r\partial\phi} - \hat{e}_z \frac{\partial u}{\partial z}. \tag{60}$$

Bend of the layers can be conveniently expressed as splay of the layer normal. The bending term (the first term in (3)) is

$$\frac{1}{2}K(\nabla\cdot\hat{p} - \nabla\cdot\hat{e}_r)^2 = \frac{1}{2}K\left(\frac{\partial^2 u}{r^2\partial\phi^2} + \frac{\partial^2 u}{\partial z^2}\right)^2, \tag{61}$$

where we have made the expansion around the curved (cylindrical) ground state. Layer compression (the second term in (3)) to the same order is

$$\begin{aligned}\frac{1}{2}B_0 \Bigg\{ &\frac{\partial u}{\partial r} + 1 - n_r\left[1 - \tfrac{1}{2}\left(\left(\frac{\partial u}{r\partial\phi}\right)^2 + \left(\frac{\partial u}{\partial z}\right)^2\right)\right] \\ &+ n_\phi\frac{\partial u}{r\partial\phi} + n_z\frac{\partial u}{\partial z} - \tfrac{1}{2}\left(\left(\frac{\partial u}{r\partial\phi}\right)^2 + \left(\frac{\partial u}{\partial z}\right)^2\right)\Bigg\}^2,\end{aligned} \tag{62}$$

where we have omitted terms containing u/r or $\partial u/\partial r$ that are smaller than the first term in (62). Finally, the coupling term (the last term in (3)) is

$$\frac{1}{2}B_1\left[\left(n_z\frac{\partial u}{r\partial\phi} - n_\phi\frac{\partial u}{\partial z}\right)^2 + \left(n_z + n_r\frac{\partial u}{\partial z}\right)^2 + \left(n_r\frac{\partial u}{r\partial\phi} + n_\phi\right)^2\right] \tag{63}$$

Dynamics of u and $\hat{n}$ is then given by (16) and (17). For the boundary condition we take $u(R_1) = 0$ at the cut-off radius R_1, and $\frac{\partial u}{\partial r}(R) = 0$ at the surface of the cylinder. It is worth remembering that the functional derivative (14) is rather lengthy

in cylindrical coordinates. For the form of ε as given in (61), (62), and (63), the nonzero terms are

$$\Psi = -\frac{\partial}{\partial r}\frac{\partial \varepsilon}{\partial(\frac{\partial u}{\partial r})} - \frac{1}{r}\frac{\partial \varepsilon}{\partial(\frac{\partial u}{\partial r})} - \frac{\partial}{r\partial\phi}\frac{\partial \varepsilon}{\partial(\frac{\partial u}{r\partial\phi})} - \frac{\partial}{\partial z}\frac{\partial \varepsilon}{\partial(\frac{\partial u}{\partial z})} - \frac{1}{r}\frac{\partial}{\partial r}\frac{\partial \varepsilon}{\partial(\frac{\partial^2 u}{r^2\partial\phi^2})} + \frac{\partial^2}{r^2\partial\phi^2}\frac{\partial \varepsilon}{\partial(\frac{\partial^2 u}{r^2\partial\phi^2})} + \frac{\partial^2}{\partial z^2}\frac{\partial \varepsilon}{\partial(\frac{\partial^2 u}{\partial z^2})}. \tag{64}$$

The velocity is calculated from (18) using a series of approximations. We assume that in the ground state the flow is simple shear flow:

$$v^{(0)} = \dot{\gamma} r \sin\phi\, \hat{e}_z, \tag{65}$$

where $\dot{\gamma}$ is the typical shear rate of the experiment. In our first attempt, we completely neglect the velocity perturbation. The dynamics of layers is thus given solely by permeation (16). This results in a static stability analysis and therefore the fact that permeation is tiny in reality is irrelevant. No instability of the cylinder was found in this case.

From now on, the permeation in (16) is neglected as it is several orders of magnitude smaller than the advection due to the radial component of the velocity v_r (now playing the role of v_z in the planar case). As far as the velocity perturbation is concerned, our aim is to describe its principal effect–the radial motion of smectic layers, i.e., instead of diffusion (permeation) we now have advective transport. In this spirit we make several simplifications to keep the model tractable. The backflow–flow generation due to director reorientation–is neglected, as well as the effect of anisotropic viscosity (third and fourth line of (19)). Thereby (19) is reduced to the Navier-Stokes equation for the velocity perturbation, which upon linearization takes the form

$$\rho\left(\frac{\partial v_i^{(1)}}{\partial t} + v_z^{(0)}\frac{\partial v_i^{(1)}}{\partial z}\right) = -\nabla_i P^{(1)} - = \nabla_j \psi_j^{(1)}\,\delta_{i1} + \eta\nabla^2 v_i^{(1)}, \tag{66}$$

where $-\nabla_j \psi_j^{(1)} = \Psi^{(1)}$ is the force density in the radial direction ($i = 1$) and η is the isotropic viscosity. The z dependence is already captured by the plane wave ansatz (57)–(59), so $\frac{\partial}{\partial z} = \mathrm{i}k$.

Several reduced models for the velocity perturbation $v^{(1)}$ have been systematically tested.

1. Simplest model. The incompressibility condition is not obeyed, the velocity perturbation is stationary (the time derivative in (66) is neglected) and has only a radial direction,
$$v^{(1)} = v_0^{(1)}(r,\phi,t)\,\mathrm{e}^{\mathrm{i}kz}\,\hat{e}_r, \tag{67}$$
with the solution

$$v_0^{(1)}(r,\phi,t) = \frac{1}{\eta k^2 + \mathrm{i}k\rho v_z^{(0)}(r,\phi)} \Psi_0^{(1)}(r,\phi,t). \tag{68}$$

Thus, the r and ϕ components of the velocity gradient are completely disregarded and $v_0^{(1)}$ depends on those coordinates only through the r and ϕ dependence of the (radial) force density and the ground state shear velocity. The quality of this model increases with increasing kR. It is expected that the velocity perturbation is overestimated in this model and thus the hypothetical instability threshold is lowered, which makes the model appealing at least as a first attempt.

2. Improved model. The incompressibility is obeyed. The velocity perturbation is stationary and lies in the rz planes:

$$v^{(1)} = \left[v_{0r}^{(1)}(r,\phi,t)\,\hat{e}_r + v_{0z}^{(1)}(r,\phi,t)\,\hat{e}_z \right] \mathrm{e}^{\mathrm{i}kz} \tag{69}$$

The coordinate ϕ is again only a parameter, i.e., all derivatives with respect to ϕ are neglected. Hence we are left with the one-dimensional problem

$$\rho v_z^{(0)} \mathrm{i}k v_0^{(1)} = -(\nabla_r + \mathrm{i}k\hat{e}_z) P_0^{(1)} + \eta(\nabla_r^2 - k^2) v_0^{(1)} + \Psi_0^{(1)}\,\hat{e}_r \tag{70}$$

and

$$(\nabla_r + \mathrm{i}k\hat{e}_z) \cdot v_0^{(1)} = 0 \tag{71}$$

to solve at every ϕ coordinate. Taking the curl of (70) to eliminate the pressure and omitting all ϕ derivatives, one finally gets

$$\rho v_z^{(0)} \mathrm{i}k \left(\mathrm{i}k v_{0r}^{(1)} - \frac{\partial v_{0z}^{(1)}}{\partial r} \right) - \rho \frac{\partial v_z^{(0)}}{\partial r} \mathrm{i}k v_{0z}^{(1)} = \tag{72}$$

$$\eta \left\{ \left[\frac{1}{r}\frac{\partial}{\partial r}\left(r \frac{\partial}{\partial r} \right) - \left(k^2 + \frac{1}{r^2} \right) \right] \left(\mathrm{i}k v_{0r}^{(1)} - \frac{\partial v_{0z}^{(1)}}{\partial r} \right) \right\} + \mathrm{i}k \Psi_0^{(1)}. \tag{73}$$

At the outer boundary we assume $\frac{\partial v_{0r}^{(1)}}{\partial r}(R) = 0$, $\frac{\partial v_{0z}^{(1)}}{\partial r}(R) = 0$ and at the cut-off boundary $v_{0r}^{(1)}(R_1) = 0$, $\frac{\partial v_{0z}^{(1)}}{\partial r}(R_1) = 0$. The resulting band-diagonal system, (39) and (73), is efficiently solved by the conjugate gradient method [63].

3. Time-dependent velocity model. The approximations are identical to the previous model, except that now the velocity field is not stationary, i.e., the time derivative in (66) is nonzero. This introduces another time scale $\tau_v = \rho R^2/\eta$ to the problem which could be significant for the instability. Now it is convenient to start with (66) containing the pressure. Using (66), the velocity is updated explicitly in time:

$$\frac{v_0^{*(1)} - v_0^{(1)}}{\Delta t} = \frac{1}{\rho}\{\ldots\}, \tag{74}$$

then it is corrected applying a pressure correction δP in an auxiliary step [64]:

$$v_0^{\mathrm{new}(1)} = v_0^{*(1)} - \Delta t \nabla \delta P, \tag{75}$$

such as to satisfy the incompressibility condition (39)

$$\nabla \cdot v_0^{\mathrm{new}(1)} = 0 = \nabla \cdot v_0^{*(1)} - \Delta t \nabla^2 \delta P. \tag{76}$$

Thus at every time step a Poisson equation for the pressure correction is solved, yielding corrections (75) to the velocity and the pressure, $P_0^{\mathrm{new}(1)} = P_0^{(1)} + \delta P$. This leads to the following one-dimensional system:

$$\frac{v_{0r}^{*(1)} - v_{0r}^{(1)}}{\Delta t} = \frac{1}{\rho}\left[-\nabla_r P_0^{(1)} + \eta\left(\nabla_r^2 - \frac{1}{r^2} - k^2\right) v_{0r}^{(1)} + \Psi_0^{(1)}\right], \tag{77}$$

$$\frac{v_{0z}^{*(1)} - v_{0z}^{(1)}}{\Delta t} = \frac{1}{\rho}\left[-\mathrm{i}k P_0^{(1)} + \eta\left(\nabla_r^2 - k^2\right) v_{0z}^{(1)}\right], \tag{78}$$

$$\left(\nabla_r^2 - k^2\right)\delta P = \left(\frac{\partial}{\partial r} + \frac{1}{r}\right) v_{0r}^{*(1)} + \mathrm{i}k v_{0z}^{*(1)}, \tag{79}$$

$$v^{\mathrm{new}(1)} = v^{*(1)} - \Delta t \nabla \delta P, \tag{80}$$

$$P_0^{\mathrm{new}(1)} = P_0^{(1)} + \delta P, \tag{81}$$

which is solved on a staggered grid [64].

We start with the ground state $u^{(0)}$, $\hat{n}^{(0)}$, defined by the simple shear flow $v^{(0)}$, Fig. 17. The principal effect is, as expected, the appearance of a small tilt of the director from the layer normal (flow alignment), predominantly in z direction (Fig. 18). Note that the configuration of layers is also modified by the shear (Figs. 19 and 20), i.e., the cylindrical symmetry is lost. This is analogous to the shear-flow-induced undulation instability of planar layers (wave vector of undulations in the

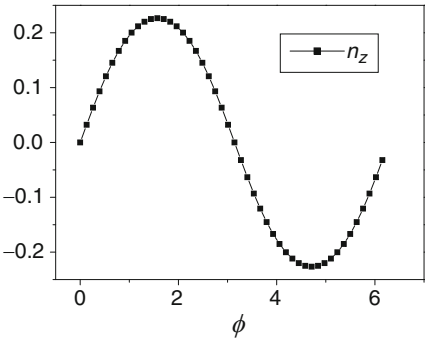

Fig. 18 Ground state flow alignment: director tilt in the z direction $n_z^{(0)}$ at $r = 0.75R$ as a function of the polar angle ϕ. The tilt is zero at $\phi = 0$ and $\phi = \pi$, where the director points in the neutral (vorticity) direction

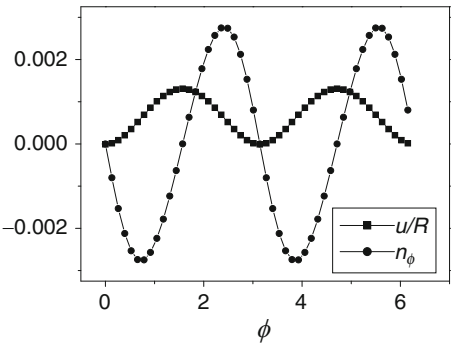

Fig. 19 Second order in $\dot{\gamma}\gamma_1/B_1$ effects: the ground state layer displacement $u^{(0)}$ and $n_\phi^{(0)}$ at $r = 0.75R$ as functions of the polar angle ϕ. Note the quadrupolar deformation of the cylinder

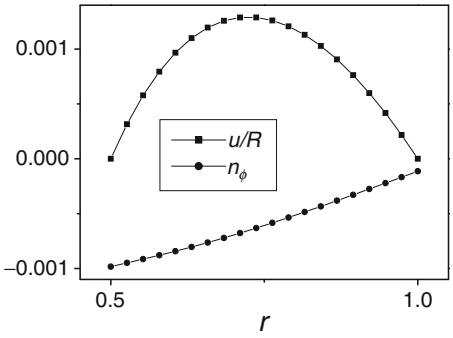

Fig. 20 Radial profile of $u^{(0)}$ and $n_\phi^{(0)}$ close to (but not exactly at) $\phi = \pi/2$. Note the regions of dilatation and compression of the layers caused by the flow alignment

vorticity direction), except that in the case of the cylinder the translational symmetry in the vorticity direction is already broken by construction (in contrast to the planar layers) and hence there exists no instability threshold but rather a continuously growing deformation of the cylinder as the shear rate is increased. In the lowest order of $\dot{\gamma}\gamma_1/B_1$ it can be shown that

$$n_z^{(0)} = \frac{1}{2}\dot{\gamma}\frac{\gamma_1}{B_1}(\lambda + 1)\sin\phi, \tag{82}$$

$$n_\phi^{(0)} = \frac{1}{2}\dot{\gamma}\frac{\gamma_1}{B_1}(\lambda - 1)n_z^{(0)}\cos\phi, \tag{83}$$

i.e., $n_\phi^{(0)}$ is one order smaller than $n_z^{(0)}$. Additionally it can be shown that $u^{(0)}$ is likewise second order in $\dot{\gamma}\gamma_1/B_1$. Note that in the lowest order the tilt in the z direction (82) agrees with the tilt in the planar case (40).

We randomly perturb the ground state and evolve the perturbation with a given wave vector k in time numerically, searching for any exponential increase of its amplitude which would be a signature of the instability. An example of such a perturbation is presented in Fig. 21. For all velocity field models, the parameter space

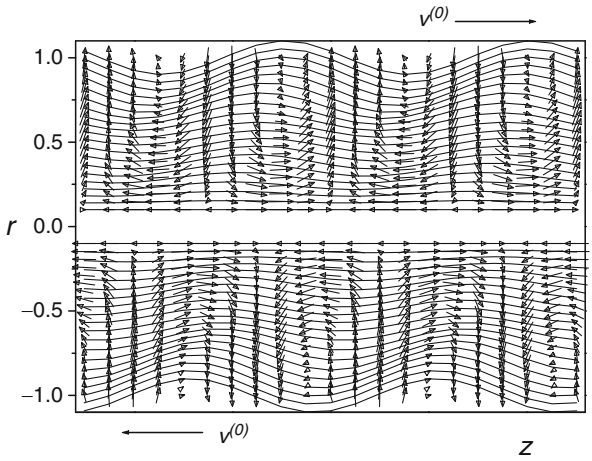

Fig. 21 The shear plane cross section of the layer displacement $u^{(1)}$ (exaggerated) and the corresponding velocity perturbation $v^{(1)}$

is systematically swept. This includes varying the wave vector of the perturbation k, the director tilt (shear rate), the ratio B_1/B_0, and the viscosity η. The result is invariably the same: no instability could be found.

Further, we consider the perturbation $s^{(1)}$ of smectic order $s = s^{(0)} + s^{(1)}$ and check whether it could be important for the instability. We take into account the dependence of the constant B_1 on smectic order:

$$B_1 = B_1^{(0)} + B_1' s^{(1)} \tag{84}$$

to lowest order. A plausible physical picture is the following. Consider the flow-aligned ground state with a small director tilt from the layer normal. The system is frustrated, as the director has a nonzero z component contrasted to the zero z component of the layer normal (no layer curvature in the z direction). Now add a perturbation $s^{(1)}$ with a given wave vector k. In regions of increased order, the director – layer normal coupling is stronger and thus the layer normal should tilt towards the director. In regions of decreased order, on the other hand, the weakened coupling should allow the layers to tilt in the reverse direction and increase the angle between the director and the layer normal. This should result in a sinusoidal perturbation of the layers – undulations with wave vector k. Furthermore, the regions of increased smectic order would thus relieve the frustration and therefore further strengthen the order, whereas the opposite would happen in regions of decreased smectic order, which could be the mechanism responsible for the growth of the perturbation.

To implement this intuitive physical picture, we take into account the smectic order dependence (84) of B_1 in (63), add the energy of smectic order variations (5) to our collection of energy contributions, and regard $s^{(1)}$ as another dynamic variable

with a short relaxation time. Then we repeat the whole procedure of scanning the parameter space and looking for a growing perturbation by the numerical time evolution. Once more the result is: no instability.

The failure of all our attempts to find an instability suggests one of two possibilities: either the cylinders are stable and as such cannot be candidates for the experimentally observed intermediates with the cylindrical scattering symmetry, or an important ingredient of the physics is missing in our description. Repeated reconsiderations of the experimental circumstances, results, and hints of the experimentalists themselves suggest that the cylinders nevertheless remain the strongest candidate for the puzzling transient state. The quest continues and it now appears that a local (in the sense of the energy landscape) instability of the cylinder triggering the formation of onions is unlikely to exist. Therefore it is reasonable to consider another possibility: perhaps it is not a small amplitude instability, but rather a localized large amplitude perturbation that is responsible for the destruction of the cylinder. In other words, the transition to onions may start with a local rupture of smectic layers via previously nucleated layer defects. A schematic picture of the process is just cutting the multilamellar cylinder and then closing the open layers so created to form the multilamellar vesicles. This process is restricted to the vicinity of the cut and leaves the rest of the cylinder unaffected. The description of such processes is nonperturbative and requires a complete description of both the nematic and the smectic phase transition (a complete description of nematic and smectic defects). Moreover, a three-dimensional numerical calculation is necessary in this case.

6 Concluding Remarks

In this chapter we have shown that a modification of the usual smectic hydrodynamics (layer normal and director are no longer forced to be parallel) will lead to a flow aligning behavior and thus to an effective dilatation of the smectic layers A linear stability analysis shows that above a critical shear rate the flow alignment is strong enough to cause an undulation instability and thus to destabilize the layered structure. We point out that the linearized analysis presented here does not allow one to predict which structure will be stable at shear rates above the critical shear rate. To overcome this problem, two strategies can be followed. Either one expands the governing equations in small, but non-vanishing amplitudes (in the vicinity of the threshold) along the lines of the work by Schlüter, Lortz and Busse [65] and Newell and Whitehead [66], or one attacks the full non-linear equations by direct numerical integration. The former procedure results in a hierarchy of equations which have to be solved successively leading at a certain order to an envelope equation for the amplitude. This procedure is from the large field of pattern formation and pattern selection in dissipative systems. For recent overviews to this broad field compare, for example, [67–69].

Following the lines proposed above will give a prediction of the pattern formed above onset. For a transition from undulating lamellae to reorientated lamellae or to multilamellar vesicles, defects have to be created for topological reasons. Since the order parameter varies spatially in the vicinity of the defect core, a description of such a process must include the full (tensorial) nematic order parameter as macroscopic dynamic variables.

An interesting similarity of what we discussed here appears if one deals with mixtures of rodlike and disklike micelles. These systems could behave very similarly to a truly biaxial nematic, but show interesting differences to them. Whereas for the usual orthorhombic biaxial nematics both directors are perpendicular to each other by construction, in mixtures there is no need to impose this restriction. Pleiner and Brand [70] investigated how mixtures are influenced by an external field (magnetic field or shear flow) and found that the angle between the two directors exhibits a flow aligning behavior similar to the one studied in [42, 43].

Experiments by Müller et al. [17] on the lamellar phase of a lyotropic system (an LMW surfactant) under shear suggest that multilamellar vesicles develop via an intermediate state for which one finds a distribution of director orientations in the plane perpendicular to the flow direction. These results are compatible with an undulation instability of the type proposed here, since undulations lead to such a distribution of director orientations. Furthermore, Noirez [25] found in shear experiment on a smectic *A* liquid crystalline polymer in a cone-plate geometry that the layer thickness reduces slightly with increasing shear. This result is compatible with the model presented here as well.

In addition, we have investigated here the question of the lamellar to onion (multilamellar vesicles, MLV) transition. This transition was found experimentally [62] to proceed via two possible structures compatible with the overall scattering geometry: either via multilamellar cylinders with the long axis oriented along the flow, or via large amplitude layer undulations with the wave vector parallel to the vorticity direction. Our detailed stability analysis of a multilamellar cylinder shows that such a structure under shear flow is stable against small amplitude perturbations. From our investigations we conclude that the transition from a lamellar structure to onions proceeds via finite amplitude perturbations and/or a local rupturing of the layering. This result is in agreement with very recent experimental results by Koschoreck et al. [20, 21], using small angle neutron scattering, small angle light scattering, and optical microscopy, who showed that lamellar domains can coexist with onions (similar to a two phase region near equilibrium) and that there is a discontinuous growth of vesicle size. All these findings point towards a hysteretic lamellar to onion transition.

Acknowledgements We wish to thank Guenter Auernhammer, Harald Pleiner, and Walter Richtering for interesting and stimulating discussions. Partial support of this work by the Alexander von Humboldt Foundation (for D.S.) and through SFB 481 'Komplexe Makromolekül- und Hybridsysteme in inneren und äußeren Feldern' of the Deutsche Forschungsgemeinschaft (for H.R.B.) is gratefully acknowledged.

Appendix, Minimal Analytic Model

In our earlier work [42] we considered two independent variables: the layer displacement and the y-component of the director. To compare our present analysis to these results we expand (43) and (44) in power series in θ_0 (up to θ_0^2) and take only the terms connected with ϕ and u:

$$0 = A_\phi \frac{B_1}{\gamma_1}\theta_0 - A_u \frac{B_1}{\gamma_1} q \tag{85}$$

$$0 = -A_u \lambda_p \left[B_1 q^2 + K q^4 + B_0 q_z^2 - \frac{1}{2}\theta_0^2 q^2 (B_0 + 2B_1) \right] + A_\phi \lambda_p B_1 \theta_0 q \tag{86}$$

The solvability condition of (85) and (86) defines the neutral curve $\theta_0(q)$ and its minimum directly gives the critical values θ_c and q_c (within the approximations of this section):

$$q_c^2 = q_z \sqrt{\frac{B_0}{K}} \tag{87}$$

$$\theta_c^2 = 4\, q_z \frac{B_0}{B_0 + 2B_1} \sqrt{\frac{K}{B_0}} \tag{88}$$

$$\dot{\gamma}_c = 4 \frac{B_1}{\gamma_1 (\lambda + 1)} \sqrt{q_z \frac{B_0}{B_0 + 2B_1} \sqrt{\frac{K}{B_0}}} \tag{89}$$

The differences between [42] and (87)–(89) are mainly due to the correct normalization of $\hat{p}$ (see (29)–(31)) used in the present chapter. To summarize, we conclude that our former results are a special case of the present analysis.

References

1. Gupta VK, Krishnamoorti R, Chen Z-R, Kornfield JA, Smith SD, Satkowski M, Grothaus JT (1996) Macromolecules 29:75
2. Wiesner U (1997) Macromol Chem Phys 198:3319
3. Laurer JH, Scott Pinheiro B, Polis DL, Winey KI (1999) Macromolecules 32:4999
4. Zryd JL, Burghardt WR (1998) Macromolecules 31:3656
5. Leist H, Maring D, Thurn-Albrecht T, Wiesner U (1999) J Chem Phys 110:8225
6. Polis DL, Smith S, Terrill NJ, Ryan AJ, Morse DC, Winey KI (1999) Macromolecules 32:4668
7. Winey KI, Patel SS, Larson RG, Watanabe H (1993) Macromolecules 26: 2542
8. Winey KI, Patel SS, Larson RG, Watanabe H (1993) Macromolecules 26:4373
9. Zhang Y, Wiesner U, Spiess HW (1995) Macromolecules 28:778
10. Horn RG, Kleman M (1978) Ann Phys (France) 3:229

11. Safinya CR, Sirota EB, Plano RJ (1991) Phys Rev Lett 66:1986
12. Panizza P, Archambault P, Roux D (1995) J Phys II France 5:303
13. Diat O, Roux D (1993) J Phys II France 3:9
14. Diat O, Roux D, Nallet F (1993) J Phys II France 3:1427
15. Diat O, Roux D, Nallet F (1995) Phys Rev E 51:3296
16. Panizza P, Colin A, Coulon C, Roux D (1998) Eur Phys J B 4:65
17. Müller S, Börschig C, Gronski W, Schmidt C, Roux D (1999) Langmuir 15:7558
(see also Müller S (1998) Struktur und Orientierung lyotroper Flüssigkristalle unter Scherung. Dissertation, Universität Freiburg)
18. Schmidt G, Muller S, Schmidt C, Richtering W (1999) Rheol Acta 38:486
19. Escalante JI, Hoffmann H (2000) Rheol Acta 39:209
20. Koschoreck S, Fujii S, Richtering W (2008) Prog Theor Phys Suppl 175:154
21. Koschoreck S, Fujii S, Lindner P, Richtering W (2009) Rheol Acta 48:231
22. Zipfel J, Lindner P, Tsianou M, Alexandridis P, Richtering W (1999) Langmuir 15:2599
23. Noirez L, Pégy G, Lapp A (1997a) Physica B 234/236:252
24. Noirez L, Lapp A (1997b) Phys Rev Lett 78:70 (and references therein)
25. Noirez L (2000) Phys Rev Lett 84:2164
26. Wang H, Newstein MC, Krishnan A, Balsara NP, Garetz BA, Hammouda B, Krishnamorrti R (1999) Macromolecules 32:3695
27. De Gennes PG (1972) Solid State Commun 10:753
28. Martin PC, Parodi O, Pershan PS (1972) Phys Rev A 6:2401
29. De Gennes PG, Prost J (1993) The physics of liquid crystals, 2nd edn. Clarendon, Oxford
30. Pleiner H, Brand HR (1996) Hydrodynamics and electrohydrodynamics of liquid crystals. Chapter 2. In: Buka A, Kramer L (eds) Pattern formation in liquid crystals. Springer, NY
31. De Groot SR, Mazur P (1962) Non-equilibrium thermodynamics. North-Holland, Amsterdam
32. Forster D (1975) Hydrodynamic fluctuations, broken symmetries, and correlation functions. W.A. Benjamin, Massachusetts
33. Litster JD, Als-Nielsen J, Birgeneau RJ, Dana SS, Davidov D, Garcia-Golding F, Kaplan M, Safinya CR, Schaetzing R (1979) J Phys (Paris) Coll C3 40:339 (and references therein)
34. Clark NA, Meyer RB (1973) Appl Phys Lett 22:493
35. Delaye M, Ribotta R, Durand G (1973) Phys Lett 44A:139
36. Oswald P, Ben-Abraham SI (1982) J Phys (Paris) 43:1193
37. Wunenburger AS, Colin A, Colin T, Roux D (2000) Eur Phys J E 2:277
38. Bruinsma R, Rabin Y (1992) Phys Rev E 45:994
39. Williams DRM, MacKintosh FC (1994) Macromolecules 27:7677
40. Zilman AG, Granek R (1999) Eur Phys J B 11:593
41. Marlow SW, Olmsted PD (2002) Eur Phys J E 8:485
42. Auernhammer GK, Brand HR, Pleiner H (2000) Rheol Acta 39:215
43. Auernhammer GK, Brand HR, Pleiner H (2002) Phys Rev E66:061707; (2005) Phys Rev E71:049901
44. De Gennes PG (1973) Mol Cryst Liq Cryst 21:49
45. Garoff S, Meyer RB (1977) Phys Rev Lett 38:848
46. Forster D, Lubensky TC, Martin PC, Swift J, Pershan PS (1971) Phys Rev Lett 26:1016
47. Liu M (1979) Phys Rev A19:2090
48. Brand HR, Kawasaki K (1986) J Phys C 19:937
49. Marignan J, Parodi O, Dubois-Vioeltte E (1983) J Phys (Paris) 44:263
50. Pleiner H, Brand HR (1999) Physica A 265:62
51. Graf HH, Kneppe H, Schneider F (1992) Mol Phys 77:521
52. Soddemann T, Duenweg B, Kremer K (2001) Eur Phys J E 6:409
53. Soddemann T, Auernhammer GK, Guo HX, Duenweg B, Kremer K (2004) Eur Phys J E 13:141
54. Auernhammer GK (2004) PhD Thesis, University of Bayreuth
55. Zipfel J, Nettesheim F, Lindner P, Le TD, Olsson U, Richtering W (2001) Europhys Lett 53:335
56. Helfrich W (1978) Z Naturforsch 33a:305
57. Nallet F, Roux D, Prost J (1989) J Phys France 50:3147

58. Von Berlepsch H, de Vries R (2000) Eur Phys J E 1:141
59. Johnson D, Saupe A (1977) Phys Rev A15:2079
60. Kumar S (1981) Phys Rev A23:3207
61. Ribotta R, Durand G (1977) J Phys France 38:179
62. Nettesheim F, Zipfel J, Olsson U, Renth F, Lindner P, Richtering W (2003) Langmuir 19:3603
63. Press WH, Flannery BP, Teukolsky SA, Vetterling WT (1986) Numerical recipes. Cambridge University Press, Cambridge
64. Fletcher CAJ (1988) Computational techniques for fluid dynamics, vol II. Springer, Berlin
65. Schlüter A, Lortz D, Busse FH (1965) J Fluid Mech 23:129
66. Newell AC, Whitehead JA (1969) J Fluid Mech 38:279
67. Cross MC, Hohenberg PC (1993) Rev Mod Phys 65:851
68. Buka A, Kramer L (eds) (1996) Pattern formation in liquid crystals. Springer, Berlin
69. Busse FH, Müller SC (eds) (1998) Evolution of spontaneous structures in dissipative continuous systems. Springer, Berlin
70. Pleiner H, Brand HR (1985) J Phys (Paris) 46:615

Adv Polym Sci (2010) 227: 145–198
DOI:10.1007/12_2009_33

Published online: 12 February 2010

Thermal Diffusion in Polymer Blends: Criticality and Pattern Formation

Werner Köhler, Alexei Krekhov, and Walter Zimmermann

Abstract We discuss the dynamic critical properties of a binary blend of the two polymers poly(dimethyl siloxane) (PDMS) and poly(ethyl-methyl siloxane) (PEMS), and we have investigated experimentally and theoretically patterning and structure formation processes above and below the spinodal in the case of a spatially varying temperature. Asymptotic critical scaling is found close to T_c in the range $6 \times 10^{-4} \leq \varepsilon \leq 0.2$ of the reduced temperature ε and a mean field behavior for large values of ε. The thermal diffusion coefficient D_T is thermally activated but does not show the critical slowing down of the Fickian diffusion coefficient D, which can be described by crossover functions for D. The Soret coefficient $S_T = D_T/D$ diverges at the critical point with a critical exponent -0.67 and shows a crossover to the exponent -1 of the structure factor in the classical regime. Thermal activation processes cancel out and do not contribute to S_T. The divergence of S_T also leads to a very strong coupling of the order parameter to small temperature gradients, which can be utilized for laser patterning of thin polymer films. For a quantitative numerical model all three coefficients D, D_T, and S_T have been determined within the entire homogeneous phase and are parameterized by a pseudospinodal model. It is shown that equilibrium phase diagrams are no longer globally valid in the presence of a temperature gradient, and systems with an upper critical solution temperature (UCST) can be quenched into phase separation by local heating. Below the spinodal there is competition between the spontaneous spinodal demixing patterns and

W. Köhler (✉)
Physikalisches Institut, Universität Bayreuth, Universitätsstraße 30, Bayreuth 95447, Germany
e-mail: werner.koehler@uni-bayreuth.de

A. Krekhov
Physikalisches Institut, Universität Bayreuth, Universitätsstraße 30, Bayreuth 95447, Germany
e-mail: alexei.krekhov@uni-bayreuth.de

W. Zimmermann
Physikalisches Institut, Universität Bayreuth, Universitätsstraße 30, Bayreuth 95447, Germany
e-mail: walter.zimmermann@uni-bayreuth.de

structures imposed by means of a focused laser beam utilizing the Soret effect. Elongated structures degrade to spherical objects due to surface tension effects leading to pearling instabilities. Grids of parallel lines can be stabilized by enforcing certain boundary conditions. Phase separation phenomena in polymer blends belong to the universality class of pattern forming systems with a conserved order parameter. In such systems, the effects of spatial forcing are rather unexplored and, as described in this work, spatial temperature modulations may cause via the Soret effect (thermal diffusion) a variety of interesting concentration modulations. In the framework of a generalized Cahn–Hilliard model it is shown that coarsening in the two-phase range of phase separating systems can be interrupted by a spatially periodic temperature modulation with a modulation amplitude beyond a critical one, where in addition the concentration modulations are locked to the periodicity of the external forcing. Accordingly, temperature modulations may be a useful future tool for controlled structuring of polymer blends. In the case of a traveling spatially periodic forcing, but with a modulation amplitude below the critical one, the coarsening dynamics can be enhanced. With a model of phase separation, taking into account thermal diffusion, essential features of the spatio-temporal dynamics of phase separation and thermal patterning observed in experiments can be reproduced. With a directional quenching an effective approach is studied to create regular structures during the phase separation process. In addition, it is shown that the wavelength of periodic stripe patterns is uniquely selected by the velocity of a quench interface. With a spatially periodic modulation of the quench interface itself, cellular patterns can also be generated.

Keywords Cahn-Hilliard model · Diffusion · Nonlinear dynamics · Pattern selection · Polymer blends · Soret effect · Spinodal decomposition · Thermal diffusion

Contents

1 Introduction

When a binary liquid mixture approaches the consolute critical point, the equilibrium restoring forces vanish, the correlation length diverges, and the amplitude of the fluctuations of the order parameter grow according to characteristic power laws. Very close to the critical point the correlation length exceeds by far all microscopic length scales. The fluctuations can be observed macroscopically as critical scattering phenomena like the well-known critical opalescence. At the same time there is a critical slowing down of the diffusion dynamics [1–3] and the system becomes increasingly susceptible to external perturbations.

After crossing the spinodal the mixture immediately becomes unstable and even arbitrarily small composition fluctuations grow exponentially in time. Eventually, the fluid decomposes into two phases that form a labyrinthine spinodal pattern with a characteristic length scale determined by the wave vector at the maximum of the growth rate of small inhomogeneous perturbations. As time proceeds the pattern coarsens and the maximum of the structure factor is shifted towards larger length scales, corresponding to smaller values of the wave vector. Eventually, a new equilibrium is reached with a horizontal meniscus that separates the two phases with the lighter liquid on top of the denser one.

Compared to binary mixtures of low molecular fluids, the critical behavior of polymer blends has been much less explored so far. However, a number of interesting static and dynamic critical phenomena in polymer blends attract increasing attention [4, 5]. Neutron, X-ray, and static light scattering experiments belong to the major techniques for characterizing the static properties of polymer blends. Photon correlation spectroscopy (PCS) has traditionally been the method of choice for the investigation of the dynamics of critical [6–9] and noncritical [10–12] polymer blends.

The vast majority of experimental and theoretical investigations on critical or off-critical polymer blends or solutions has been carried out under isothermal conditions and only a few of them were focusing on the effect of spatially varying temperature fields [13–17]. In all these studies there is no direct effect of a temperature gradient besides the positioning of the different parts of the sample at different locations in the phase diagram. The coupling between the order parameter and the temperature gradients due to the Ludwig–Soret effect – also termed thermal diffusion, thermodiffusion or, briefly, Soret effect – has not been taken into account. While this effect is only weak in most cases of low molecular mixtures away from a phase transition, it can, as will be shown below, become a substantial and sometimes dominating effect in critical polymer blends. The Soret coefficient, which is a measure of the change of the composition induced by a given temperature difference, even diverges at the critical point.

Including the Soret effect, the diffusive mass flow in a multicomponent system contains two contributions, the Fickian diffusion current that is driven by the gradient of the chemical potential and the thermal diffusion current driven by the temperature gradient. To account for this additional transport process, the thermal diffusion coefficient D_T is introduced in addition to the Fickian diffusion coefficient D. Experiments have shown that the direction of the thermal diffusion current is not easily predicted and, in contrast to D, the coefficient D_T can be both positive and negative, and it can change its sign as a function of composition [18–22], temperature [23–26], molar mass [27, 28], or solvent composition [29]. The stationary composition distribution is determined by a competition between thermal and Fickian diffusion, and the Soret coefficient $S_T = D_T/D$ can roughly be interpreted as the relative composition change sustained in the stationary state per temperature difference. Typical numbers for small molecules are only of the order of $S_T \approx 10^{-3}\,K^{-1}$ and the effect generally causes only a minor perturbation for most practical situations. For larger diffusing objects, such as polymers in dilute solution [30–33] or colloids [34–41], significantly higher values of $S_T \approx 0.1 \ldots 1\,K^{-1}$ have been reported.

The Soret effect near a consolute critical point of a simple liquid mixture was first investigated by Thomaes [42] and later by Giglio and Vendramini [43]. Giglio and Vendramini observed a critical divergence of the thermal diffusion factor $k_T = S_T T c(1-c) \sim (T - T_c)^{\nu}$ with the critical exponent $\nu = 0.63$ of the correlation length ξ. c is the concentration (mass fraction) of component one. These results, obtained with an optical beam deflection technique for the aniline/cyclohexane system, have later been confirmed by Wiegand utilizing a transient holographic grating technique [44]. Similar transient gratings had been used for the first time by Pohl to demonstrate qualitatively the divergence of the signal at the critical point of a 2,6-lutidine/water mixture [45]. Buil et al. and Delville et al. have employed transient holographic gratings [46] and focused laser beams [47] for the investigation of first order phase transitions in multicomponent liquids. While there have been a few such studies of the Soret effect in critical low molecular weight liquid mixtures, there were no data available for critical polymer blends. Hence, one of the goals was the investigation of the critical properties related to nonisothermal transport, in particular the crossover from the mean field to the asymptotic critical regime, for a upper critical solution temperature (UCST) polymer blend.

Besides the selection of a characteristic wavelength during spinodal decomposition at a constant temperature, the strong coupling between inhomogeneous temperature fields and the order parameter opens entirely new routes for pattern formation processes in critical polymer blends. Pattern formation in polymer blends via phase separation is an important research topic not only in polymer physics or physical chemistry but also as an interdisciplinary research involving nonequilibrium studies of complex fluids [48, 49], where it became a prototype for pattern forming systems with a conserved order parameter. The phase separation of such systems commonly leads to an isotropic, disordered morphology, such as interconnected domain structure or isolated clusters. These domains grow continuously in space and time and finally become macroscopic. An important research topic regarding phase separation in polymer blends is to fabricate regular structures for their potential application for nanotechnology in diverse fields, ranging from bioactive patterns

[50] to polymer electronics [51]. In fact, polymer mixtures can undergo dramatic changes in response to externally applied perturbations.

Some previous studies have considered the application of external fields like shear flow [52, 53], concentration gradient [54], patterned surface [55], or temperature inhomogeneity [56] to break the symmetry of the phase separation in polymer blends and to produce ordered structures with widely varying morphologies and length scales. Different strategies have been explored to tailor domain patterns of polymer mixtures and obtain new ordered structures. The spontaneous emergence of structures within an initially homogeneous blend and the possibility to generate patterns in a controlled way are not only of interest from the view of basic research but may also lead to technological applications.

Traditional techniques for structuring of polymer films utilize irradiation with UV light, X-rays, or electron beams in combination with some kind of cross-linking photo reaction. Fytas and coworkers have shown that isolated linear structures and periodic gratings can be generated by laser irradiation of homogeneous polymer solutions [57, 58]. Böltau et al. have used patterned surfaces to drive an incompatible polymer blend into pre-defined demixing morphologies [55]. Filler particles can induce composition waves in thin films of demixing polymer blends [59].

Spinodal decomposition in binary liquid mixtures or polymer blends belongs to the universality class of pattern forming systems with a *conserved* order parameter [48]. A variety of interesting effects of spatially varying control parameters in pattern forming systems with *nonconserved* order parameters has been explored during recent years [60–73], but the effects of spatially or temporally varying temperature fields in spinodal decomposition has been investigated only recently. Tanaka and Sigehuzi have periodically driven the system across the spinodal and observed two characteristic superimposed length scales with and without coarsening [74]. Lee et al. performed computational studies on spinodal decomposition with superimposed temperature gradient [16, 17]. Kumaki et al. observed a 20 K shift of the phase boundary after applying a temperature gradient to a ternary polymer mixture [75].

Except for Kumaki, all these authors did not take into account the coupling between temperature gradients and concentration due to the Soret effect. In the second part of the present work, an overview is given of the structure formation processes that occur during spinodal decomposition in the presence of spatially inhomogeneous and/or time dependent temperature fields. It will be shown that the Soret effect may lead to entirely different pattern formation and evolution scenarios in critical and near-critical polymer blends. Introducing a spatially periodic temperature-modulation in a model of phase separation in a polymer blend above a critical modulation amplitude, the coarsening dynamics can be interrupted and a stripe pattern is locked to the periodicity of the external modulation. Similar locking effects are found in the case of a traveling, spatially periodic temperature modulation. In the parameter range where the decomposition is not locked to the external forcing, the coarsening processes can be enhanced by the traveling modulation. With directional quenching a further forcing method is presented. This method turns out to be an effective selection mechanism for the wavelength of the periodic pattern behind the moving quenching interface, where the selected wavelength of the pattern can be uniquely selected by the chosen velocity of the quench interface.

2 Transport Coefficients in a Critical Polymer Blend

2.1 Diffusion in Critical Systems with a Temperature Gradient

First we treat diffusion processes within the homogeneous phase. The presence of a temperature gradient in binary fluid mixtures and polymer blends requires an extension of Fick's diffusion laws, since the mass is not only driven by a concentration but also by a temperature gradient [76]:

$$\mathbf{J} = \mathbf{J}_{\mathrm{m}} + \mathbf{J}_{\mathrm{T}} = -\rho \left[D\nabla c + c(1-c) D_{\mathrm{T}} \nabla T \right]. \tag{1}$$

$c\rho$ is the density and $\mathbf{J}$ the mass flow of component one. D and D_{T} are the mass and the thermal diffusion coefficient, respectively. Since the total mass flow vanishes in the mass-fixed frame of reference, the flow of the second component of concentration $(1-c)$ of the mixture is not independent and need not be considered separately. In the case of vanishing reference velocities and/or small temperature gradients, the continuity equation takes the following form [77, 78]:

$$\frac{\partial c}{\partial t} = -\nabla \cdot \frac{\mathbf{J}}{\rho}. \tag{2}$$

Combining (1) and (2), the evolution equation for the concentration is

$$\frac{\partial c}{\partial t} = \nabla \cdot \left[D\nabla c + c(1-c) D_{\mathrm{T}} \nabla T \right]. \tag{3}$$

All currents vanish in the stationary state, where the amplitude of the induced concentration gradient is determined by the Soret coefficient $S_{\mathrm{T}} = D_{\mathrm{T}}/D$:

$$\nabla c = -S_{\mathrm{T}} c(1-c) \nabla T. \tag{4}$$

The temperature distribution is determined by the heat equation

$$\frac{\partial T}{\partial t} = D_{\mathrm{th}} \nabla^2 T + S(\mathbf{r}, t), \tag{5}$$

including the source term $S(\mathbf{r},t)$. $D_{\mathrm{th}} = \kappa(\rho c_p)^{-1}$ is the thermal diffusivity, κ the thermal conductivity, and c_p the specific heat of the solution.

The formal description of thermodiffusion in the critical region has been discussed in detail by Luettmer-Strathmann [79]. The diffusion coefficient of a critical mixture in the long wavelength limit contains a mobility factor, the Onsager coefficient $\alpha = \alpha^{\mathrm{b}} + \Delta\alpha$, and a thermodynamic contribution, the static structure factor $S(0)$ [7, 79]:

$$D(q=0) = \left(\frac{\alpha^{\mathrm{b}} + \Delta\alpha}{S(0)} \right) = D^{\mathrm{b}} + \Delta D. \tag{6}$$

α^{b} is the background contribution and $\Delta\alpha$ the critical enhancement. Within the random phase approximation the static structure factor of a binary AB polymer blend is given by [4, 8, 80]

$$S(q=0) = \left(\frac{1}{\phi_{\mathrm{A}} N_{\mathrm{A}}} + \frac{1}{\phi_{\mathrm{B}} N_{\mathrm{B}}} - 2\chi \right)^{-1} . \tag{7}$$

ϕ_k and N_k are the volume fraction and the degree of polymerization of polymer k, with $k = \mathrm{A}, \mathrm{B}$. χ is the Flory–Huggins interaction parameter. Introducing the reduced temperature

$$\varepsilon = \frac{T - T_{\mathrm{c}}}{T_{\mathrm{c}}} , \tag{8}$$

the critical temperature dependences of $S(0)$ and the static correlation length ξ are expressed as scaling laws $S(0) \sim \varepsilon^{-\gamma}$ and $\xi \sim \varepsilon^{-\nu}$. Close to the critical point, in the asymptotic critical region, the scaling exponents take the values $\gamma = 1.24$ and $\nu = 0.63$. The mean field values for larger distances from T_{c} are $\gamma = 1.0$ and $\nu = 0.5$. The transition from the classical mean field regime to the asymptotic critical regime is marked by the Ginzburg criterion for the static correlation length, $\xi \approx R_{\mathrm{g}} N^{1/2}$, and occurs at $\varepsilon = Gi$. Gi is the Ginzburg number and R_{g} the polymer radius of gyration. Following the arguments in [79], the background diffusion coefficient scales like $D^{\mathrm{b}} \sim \varepsilon^{\gamma}$, where $\gamma = 1$ in the mean field regime, and the critical enhancement like $\Delta D \sim \varepsilon^{\nu(1+z_\eta)} \approx \varepsilon^{0.67}$, where $z_\eta = 0.063$ is the critical exponent of the viscosity. Because of the larger absolute temperature excursions in the mean field regime, the thermal activation of the Onsager coefficient with an activation temperature T_{a} additionally needs to be taken into account. Hence, we end up with the following temperature dependence of the diffusion coefficient:

$$D \approx \Delta D \sim \varepsilon^{0.67} \quad \text{for } \varepsilon \ll Gi \tag{9}$$

$$D \approx D^{\mathrm{b}} \sim \varepsilon \exp(-T_{\mathrm{a}}/T) \quad \text{for } \varepsilon \gg Gi \tag{10}$$

As discussed in [79], there is no critical enhancement of the thermal diffusion coefficient D_{T}, which retains its background value $D_{\mathrm{T}}^{\mathrm{b}}$ throughout the asymptotic critical regime. It appears reasonable to assume the same activation temperature T_{a} both for α^{b} and $D_{\mathrm{T}}^{\mathrm{b}}$:

$$D_{\mathrm{T}} = D_{\mathrm{T}}^{\mathrm{b}} = D_{\mathrm{T}}^{0} \exp(-T_{\mathrm{a}}/T) . \tag{11}$$

Combining (9), (10), and (11), the critical scaling of the Soret coefficient in the asymptotic critical ($\varepsilon \ll Gi$) and in the mean field regime ($\varepsilon \gg Gi$) is

$$S_{\mathrm{T}} \approx \frac{D_{\mathrm{T}}^{\mathrm{b}}}{\Delta D} \sim \Delta D^{-1} \sim \varepsilon^{-\nu(1+z_\eta)} \sim \varepsilon^{-0.67} \quad \text{for } \varepsilon \ll Gi \tag{12}$$

$$S_{\mathrm{T}} \approx \frac{D_{\mathrm{T}}^{\mathrm{b}}}{D^{\mathrm{b}}} = \frac{D_{\mathrm{T}}^{\mathrm{b}}}{\alpha^{\mathrm{b}}/S(0)} \sim S(0) \sim \varepsilon^{-1} \quad \text{for } \varepsilon \gg Gi \tag{13}$$

Since there had not been any measurements of thermal diffusion and Soret coefficients in polymer blends, the first task was the investigation of the Soret effect in the model polymer blend poly(dimethyl siloxane) (PDMS) and poly(ethyl-methyl siloxane) (PEMS). This polymer system has been chosen because of its conveniently located lower miscibility gap with a critical temperature that can easily be adjusted within the experimentally interesting range between room temperature and 100 °C by a suitable choice of the molar masses [81, 82]. Furthermore, extensive characterization work has already been done for PDMS/PEMS blends, including the determination of activation energies and Flory–Huggins interaction parameters [7, 8, 83, 84].

2.2 The Transient Grating Technique

The transport coefficients have been measured by the transient holographic grating technique of Thermal Diffusion Forced Rayleigh Scattering (TDFRS) that has already been described in more detail in previous works [85–87] and will only be briefly sketched in the following (Fig. 1).

An argon ion laser operating at 488 nm is split into two beams of equal intensities that are brought to intersection within the sample under an angle θ to create a holographic interference grating with a period

$$d = \frac{2\pi}{q} = \frac{\lambda}{2\sin(\theta/2)}. \tag{14}$$

Energy is absorbed from the light field by an inert dye (quinizarin) that is added to the polymer blend in minute quantities. Neither the phase behavior nor the critical

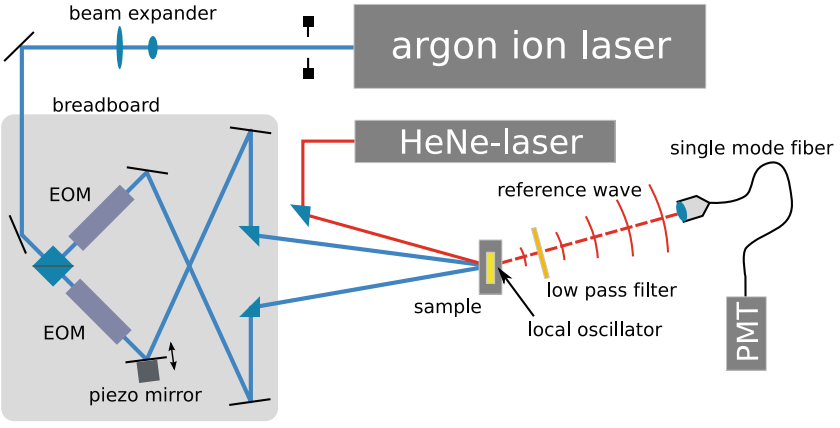

Fig. 1 Setup for transient holographic grating measurements. The electro-optic modulators (EOMs) are used for 180°-phase shifts of the holographic grating. The piezo mirror serves for phase matching between the diffracted beam and the coherent reference wave generated by the local oscillator. The setup is a modified version of the one described in [87]

temperature are influenced by the dye. The temperature grating and the secondary concentration grating both couple to the refractive index grating due to the contrast factors $(\partial n/\partial c)_{p,T}$ and $(\partial n/\partial T)_{p,c}$. The resulting phase grating is read by Bragg diffraction of a readout laser beam (HeNe, 633 nm). The diffracted signal beam is mixed with a coherent reference wave derived from a local oscillator in order to create a heterodyne signal for increased sensitivity at low diffraction efficiencies. Electro-optic modulators (EOMs) are used for switching of the phase of the grating and a piezo-mirror serves for phase stabilization. Details of the stabilization and switching procedure and the separation of heterodyne and homodyne signal components have been described in [88]. A photo multiplier tube operating in photon counting mode is used for detection. It is connected to a counter with a time resolution of 1 µs. For a good signal to noise ratio, typically 10^4–10^5 individual exposure cycles are averaged.

Taking the absorbed optical power density as source term $S = \alpha_\lambda I(\rho c_p)^{-1}$ in the heat equation (5), an analytical expression for the normalized heterodyne diffraction efficiency can be derived as a cascaded linear response [88, 89]:

$$\zeta_{\text{het}}(t) = 1 - \mathrm{e}^{-t/\tau_{\text{th}}} - \frac{\zeta_{\text{c}}}{\tau - \tau_{\text{th}}}\left[\tau\left(1 - \mathrm{e}^{-t/\tau}\right) - \tau_{\text{th}}\left(1 - \mathrm{e}^{-t/\tau_{\text{th}}}\right)\right], \tag{15}$$

$$\zeta_{\text{c}} = \left(\frac{\partial n}{\partial c}\right)_{p,T}\left(\frac{\partial n}{\partial T}\right)_{p,c}^{-1} S_{\text{T}}\, c_0(1 - c_0). \tag{16}$$

α_λ is the optical absorption coefficient, c_p the specific heat, and $I(x,t) = I_q(t)\exp(\mathrm{i}qx)$ the periodic intensity of the light field. The thermal diffusivity and the diffusion coefficient are obtained from the relaxation time constants of the temperature and the concentration grating, which are treated as fit parameters: $\tau_{\text{th}} = (D_{\text{th}}q^2)^{-1}$ and $\tau = (Dq^2)^{-1}$. The description becomes more complex in the case of very thin samples, where heat conduction into the walls is important [90].

The contrast factors have been measured interferometrically [87] and with an Abbe refractometer, respectively. The sample is contained in a fused silica spectroscopic cell with 200 µm thickness (Hellma). The sample holder is thermostated with a circulating water thermostat and the temperature is measured close to the sample with a Pt100 resistor. The amplitude of the temperature modulation of the grating is well below 100 µK and the overall temperature increase within the sample is limited to approximately 70 mK in a typical experiment [91], which is sufficiently small to allow for measurements close to the critical point.

2.3 Measurements on PDMS/PEMS Blends

The measurements near the critical point have been performed with a PDMS/PEMS blend with molar masses of $M_{\text{w}} = 16.4\,\text{kg mol}^{-1}$ (PDMS, $M_{\text{w}}/M_{\text{n}}$=1.10) and $M_{\text{w}} = 22.8\,\text{kg mol}^{-1}$ (PEMS, $M_{\text{w}}/M_{\text{n}}$ =1.11). The corresponding degrees of polymerization are $N = 219$ and $N = 257$, respectively. The phase diagram shows a lower miscibility gap with a critical composition of $c_{\text{c}} = 0.548$ (weight fractions

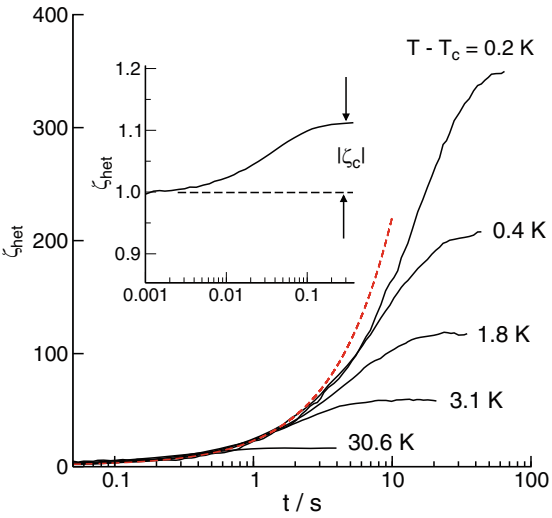

Fig. 2 Typical heterodyne diffraction signals measured for a critical PDMS/PEMS mixture for different distances $T - T_c$ to the critical point. All curves have been normalized according to (15). The *dashed line* indicates the nearly constant initial slope of the concentration signal (an exponential function in the logarithmic plot) caused by the almost constant value of D_T. The *inset* shows, for comparison, a considerably smaller signal for an off critical PDMS/PEMS mixture (860 and 980 g mol^{-1})

of PDMS), which was determined according to the equal volume criterion. This value is in good agreement with the critical volume fraction ϕ_c calculated from the Flory–Huggins-model [91]. The critical temperature is $T_c = 38.6\,^{\circ}\mathrm{C}$. For some measurements off-critical mixtures of varying molar masses have also been employed. The relevant numbers will be given where appropriate.

As predicted by the expressions for the critical divergence of the Soret coefficient in (12) and (13), the heterodyne diffraction efficiency of the induced concentration grating dramatically increases on approach of the critical point. Figure 2 shows normalized heterodyne diffraction efficiencies that have been recorded for different distances $T - T_c$. A few hundred milli-Kelvin away from T_c, the modulation depth, which is proportional to the heterodyne signal, exceeds the values typically found for small molecules and off-critical mixtures by nearly four orders of magnitude.

2.4 The Diffusion Coefficient

The diffusion coefficient D is plotted in Fig. 3 as a function of the reduced temperature ε. The upper x-axis shows the correlation length $\xi = \xi_0 \varepsilon^{-0.63}$ with $\xi_0 = 1.5\,\mathrm{nm}$. The short downward arrow marks the approximate locus of the transition from the asymptotic critical to mean field behavior at $\xi \approx N^{1/2} R_g$ [4]. Below this value, at smaller values of ε and larger correlation lengths, the data are compatible with the asymptotic scaling law of (9). For large values of ε the slope continuously increases due to the transition to the mean field exponent and the growing influence of thermal activation [81].

Data of D as measured previously by PCS on comparable polymer blends have also been included in Fig. 3. Generally, the data of Meier [8] and Sato [92] show

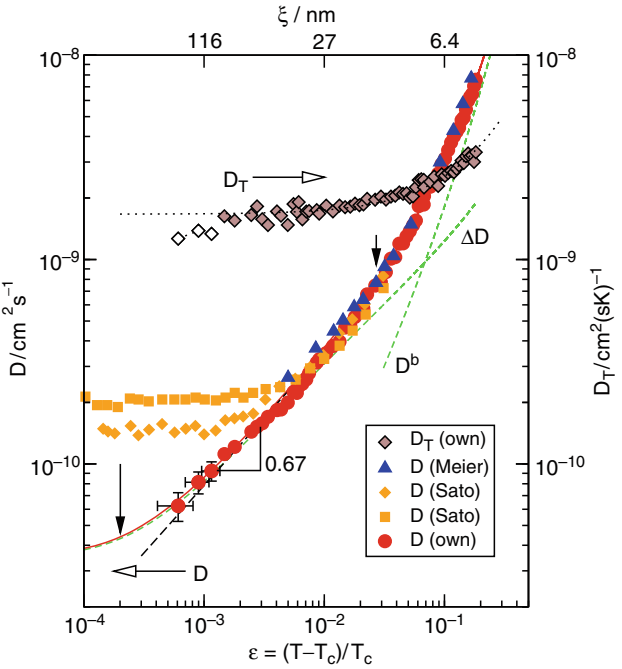

Fig. 3 Mass and thermal diffusion coefficients D and D_T as functions of reduced temperature ε. Literature PCS data for D taken from Meier [8] and Sato [92] (scattering angle 60° (*open diamond*) and 130° (*open square*)). See text for a discussion of the fit functions. Also shown D_T (*upper curve*, *right* y-axis) for the same temperature range together with fit function containing only thermal activation (*dotted line*). *Open diamonds*: data with unclear error bars due to very long equilibration times. Note the different units of the two y-axes

an excellent agreement with our results. Close to T_c (below $\varepsilon \approx 0.01$), however, the PCS data level off and no longer follow the asymptotic scaling law. This transition from a diffusive, $\Gamma = Dq^2 \propto q^2$, to a nondiffusive behavior with $\Gamma \propto q^3$, occurs when the correlation length exceeds the inverse scattering vector, $\xi > q^{-1}$. The q-dependence of the *apparent* diffusion coefficient is evident from the two measurements performed by Sato et al. at different scattering angles.

Since TDFRS works at much lower q-values than PCS, in our case $q \approx 3 \times 10^{-3}\,\mathrm{nm}^{-1}$ compared to $q \approx 3 \times 10^{-2}\,\mathrm{nm}^{-1}$, the critical point can be approached much closer on the ε-axis, thereby still observing scaling behavior and critical slowing down of D. The crossover corresponding to $q^{-1}\xi \approx 1$ is marked with an arrow at $\varepsilon \approx 2 \times 10^{-4}$.

An analytical description of the crossover from a diffusive to a nondiffusive behavior at a finite q-value has been given by Kawasaki [93]:

$$D(q\xi) = D(q \to 0)K(q\xi), \tag{17}$$

$$K(x) = \tfrac{3}{4x^2}\left(1 + x^2 + \left(x^3 - x^{-1}\right)\arctan x\right). \tag{18}$$

A fit of D taking the Kawasaki function (18) into account is included in Fig. 3 (see next paragraph). It shows the expected significant deviation from the scaling law just outside the ε-range of our TDFRS data.

The problem of the dynamic crossover from the asymptotic critical to the mean field regime has been treated by Jacob et al. [94] and by Kostko et al. [95]. Kostko et al. derived a decomposition of $D = D^{\mathrm{b}} + \Delta D$ into a background contribution D^{b} and an enhancement ΔD of the form

$$D^{\mathrm{b}} = \frac{k_{\mathrm{B}}T(1+(q\xi)^2)}{6\pi\eta_{\mathrm{b}}\xi}\,\frac{1}{q_{\mathrm{D}}\xi}\,, \tag{19}$$

$$\Delta D = \frac{k_{\mathrm{B}}T}{6\pi\eta\xi}\,K(q\xi)\left[1+\frac{q\xi}{2}\right]^{z_\eta/2}\,\frac{2}{\pi}\arctan(q_{\mathrm{D}}\xi)\,. \tag{20}$$

η_{b} is the background contribution of the viscosity and q_{D}^{-1} a characteristic cutoff-length. $K(x)$ is the Kawasaki function defined in (18). The solid line in Fig. 3, which interpolates our data quite reasonably, is a fit of the sum of (19) and (20). The correspondingly labeled dashed lines show the decomposition into the two contributions D^{b} and ΔD. The viscosity was assumed to be thermally activated with the same activation temperature of $T_{\mathrm{a}} = 1{,}460\,\mathrm{K}$ as the thermal diffusion coefficient (see below). The weak critical divergence of the viscosity has been neglected. Details of the analysis and questions associated with the proper choice of the correlation length are discussed in more detail in [81].

2.5 The Thermal Diffusion Coefficient

As predicted by Folk and Moser [96], the data for D_{T} in Fig. 3 clearly show, in contrast to the data for D, no critical scaling but only thermal activation. A fit of the expression in (11) to the data in Fig. 3 gives a prefactor $D_{\mathrm{T}}^0 = 1.82\times10^{-7}\,\mathrm{cm^2(sK)^{-1}}$ and an activation temperature of $T_{\mathrm{a}} = 1{,}460\,\mathrm{K}$. Figure 4 shows an Arrhenius plot of the thermal diffusion coefficient according to (11) not only for the D_{T} data from Fig. 3 but also for a number of off-critical PDMS/PEMS blends of different molar masses and PDMS-concentrations of $c = 0.5$. Only the critical mixture has a slightly different concentration of $c_{\mathrm{c}} = 0.548$. Independent of the criticality of the system, all activation energies $k_{\mathrm{B}}T_{\mathrm{a}}$ are identical. A common fit yields an activation temperature of $T_{\mathrm{a}} = 1{,}415\,\mathrm{K}$, which is almost identical to the value of $1{,}460\,\mathrm{K}$ obtained for the critical mixture alone [97]. Also shown in Fig. 4 is a dashed line with the slope corresponding to an activation temperature of $2{,}285\,\mathrm{K}$ as reported in [92] for the viscosity. The reason for the pronounced difference between these two activation temperatures is not clear, and a definite answer would require additional

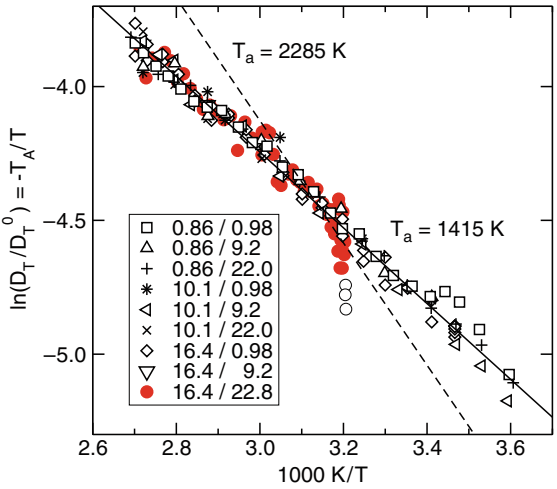

Fig. 4 Arrhenius plot of the ratio D_T/D_T^0 according to (11) for critical (16.4/22.8) and a number of off-critical PDMS/PEMS blends of various molar masses and concentrations $c = 0.5$ [97]. The legends give the PDMS and PEMS molar masses in kg mol^{-1}. Also shown is a line corresponding to the activation energy of the viscosity according to [92]

viscosity measurements for PDMS/PEMS blends as described in this work. A detailed analysis of D_T of PDMS/PEMS mixtures of equal weight fractions has shown that the prefactor D_T^0 can be broken down into a molar mass independent part plus contributions from the end-groups, which vanish for longer chain lengths [97, 98].

2.6 *The Soret Coefficient*

According to (12) and (13) the Soret coefficient $S_T = D_T/D$ diverges on approach of the critical point. This scenario is plotted in Fig. 5. Since D_T is constant to good approximation within this narrow temperature range of only a few Kelvin, the scaling law in the asymptotic critical regime, $S_T \propto \varepsilon^{-0.67}$, is determined by the exponent of the diffusion coefficient. At larger $\varepsilon > Gi$ the Soret coefficient diverges with the mean field exponent of the structure factor $S(0)$, since the thermal activation, which appears both in D and D_T, cancels out. In order to illustrate this crossover of the divergence of S_T from the mean field to the asymptotic critical regime, we have also included in Fig. 5 (besides our own data on D^{-1}) data from previous works on the static structure factor $S(0)$ of a comparable PDMS/PEMS (19.4/30.1) blend [8]. The straight line with a slope of -1 has been included in Fig. 5 to demonstrate that the mean field scaling exponent $\gamma = 1$ can be found for S_T rather than for D, which shows a stronger temperature dependence due to the additional thermal activation of the Onsager coefficient α^b.

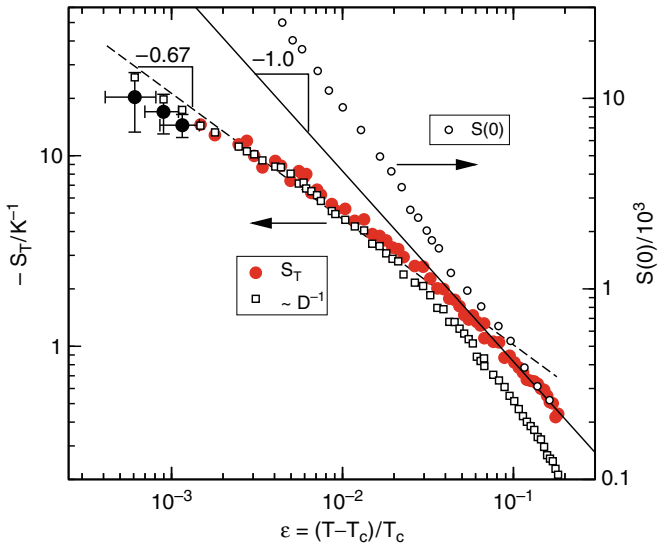

Fig. 5 Soret coefficient S_T as function of the reduced temperature ε [81]. For comparison, D^{-1} with arbitrary multiplicative factor (*both left y*-axis) and the static structure factor $S(0)$ (*open circle*) are shown for a similar blend taken from [8]. Note the identical dynamical range of both *y*-axes

Additional insight into the nature of the Soret coefficient and its critical divergence is obtained from (13) for the classical regime:

$$S_T \approx \frac{D_T}{D^b} = \frac{D_T}{\alpha^b}\, S(0) = K(T)\, S(0). \tag{21}$$

Since both D_T and α^b are thermally activated with the same activation temperature and with prefactors D_T^0 and $\alpha^{b,0}$, the dominating contribution of the temperature dependence cancels out in the ratio and we are left with only a weakly temperature dependent function:

$$K(T) = \frac{D_T}{\alpha^b} = \frac{D_T^0}{\alpha^{b,0}}\,. \tag{22}$$

Experiments have shown that, at least for PDMS/PEMS blends of equal weight fraction, $K(T)$ indeed depends only weakly on temperature and is independent of the molar mass of the constituents [97]. Consequently, the different values of the Soret coefficient in the classical mean field regime are almost exclusively caused by the variation of the static structure factor.

Figure 6 shows the respective data plotted according to (21) for a number of blends with different degrees of polymerization. The left plot shows the Soret coefficients as measured and the right one after normalization to the mean field static structure factor calculated from the Flory–Huggins model, cf. (7). Although the structure factors and the Soret coefficients of the different samples vary by more

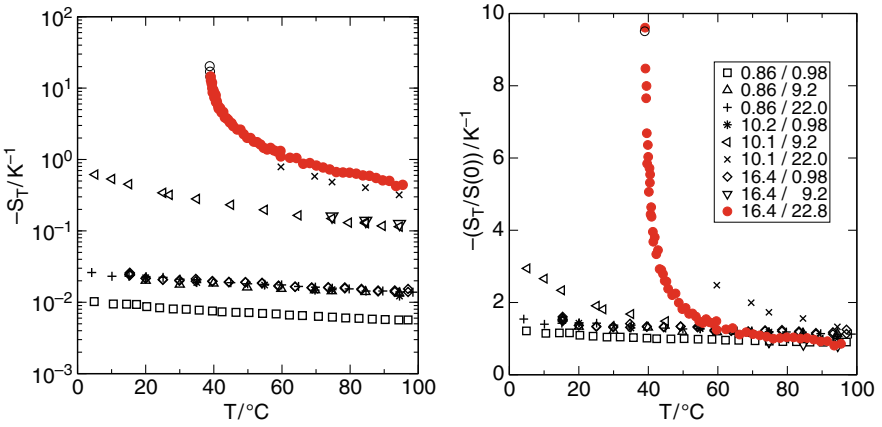

Fig. 6 *Left*: Soret coefficient S_T for a number of PDMS/PEMS blends. The *red bullets* correspond to the critical blend with a critical temperature of $T_c = 38.6\,°C$. *Right*: Same data as left normalized to mean field static structure factor $S(0)$. The legends give the PDMS and PEMS molar masses in kg mol^{-1} [97]

than two orders of magnitude – even at the highest temperature of almost 100 °C – all curves collapse onto one single master curve for a high temperature T. At lower temperatures there is the pronounced deviation from the common curve for the (16.4/22.8) blend in the asymptotic critical regime with the critical divergence of S_T. The slight deviations of two other blends might be first hints of phase transitions at lower temperatures [97].

3 Laser-Thermal Patterning of the Homogeneous Phase

Structuring of polymer films attracts considerable attention, and various radiation sources have been employed to crosslink selectively suitable polymers for, e.g., waveguide fabrication [99]. Incompatible polymer blends have been forced into certain demixing morphologies along pre-patterned surfaces [55]. Persistent structures could be formed by laser radiation in various nonabsorbing polymer solutions, such as polyisoprene in *n*-hexane [57, 58].

In the following we will describe a novel photothermal patterning technique that relies on the Soret effect. The diverging Soret coefficient in a polymer blend close to the critical point leads to a very strong coupling of the order parameter, the local composition, to an externally prescribed inhomogeneous temperature field. This opens an interesting route to the formation of arbitrary composition patterns within an initially homogeneous polymer film. Since there is no photochemistry involved, the whole process is fully reversible and structures can easily be erased by local or global heating of the sample.

Our goal was to provide a detailed experimental characterization and numerical modeling of the photothermal structure formation in a critical polymer blend. Since

the transport coefficients, and in particular the Soret coefficient, strongly depend on temperature and concentration, the structure formation is a highly nonlinear process that requires a detailed knowledge of all relevant coefficients within a broad parameter range. Since useful data on Soret coefficients for polymer blends were not provided by previous works, we started with measurements of Soret coefficients for our model system PDMS/PEMS within the entire one-phase regime above the binodal [100].

3.1 Phase Diagram and Transport Coefficients

To be able also to measure off-critical mixtures down to the binodal within a convenient temperature range, a mixture with a higher critical temperature than for the previous investigation of the critical behavior has been chosen. The system chosen was PDMS ($M_w = 16.4\,\mathrm{kg\,mol^{-1}}$, $M_w/M_n = 1.10$) and PEMS ($M_w = 48.1\,\mathrm{kg\,mol^{-1}}$, $M_w/M_n = 1.19$). It has a critical composition of $c_c \approx 0.6$ and a critical temperature of $T_c \approx 354\,\mathrm{K}$. The phase diagram of this mixture is shown in Fig. 7. The cloud points (squares in Fig. 7), which separate the homogeneous from the phase separated regime, define the binodal and have been determined by turbidimetry. The spinodal and the color-coded Soret coefficient will be discussed later on.

The diffusion, thermal diffusion, and Soret coefficients for nine different PDMS concentrations from $c = 0.09$ to $c = 0.9$ have been measured between the binodal temperature and approximately 368 K. Figure 8 shows on the left side the diffusion and thermal diffusion coefficients. The temperature dependences of the latter are very well described as thermally activated processes according to (11) with a common activation temperature $T_a = 1{,}395\,\mathrm{K}$, which is very close to the 1,460 K obtained for the critical blend in Sect. 2.

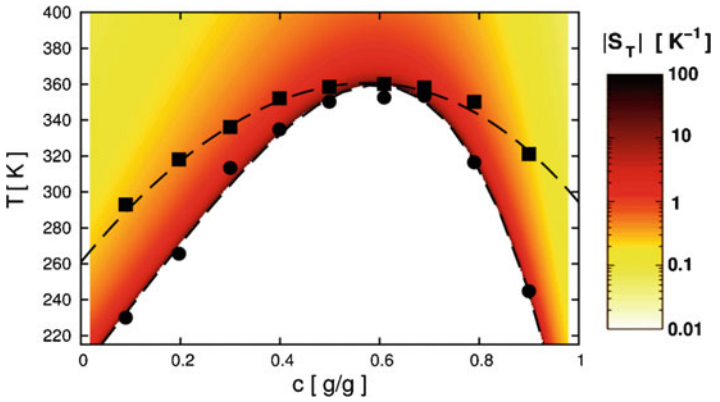

Fig. 7 Phase diagram of PDMS/PEMS (16.4/48.1). The cloud points that mark the binodal (*squares*) have been obtained by turbidimetry. Pseudo-spinodal points are as explained in the text. The color encodes the modulus of the Soret coefficient. Figure from [100]. Copyright (2007) by The American Physical Society

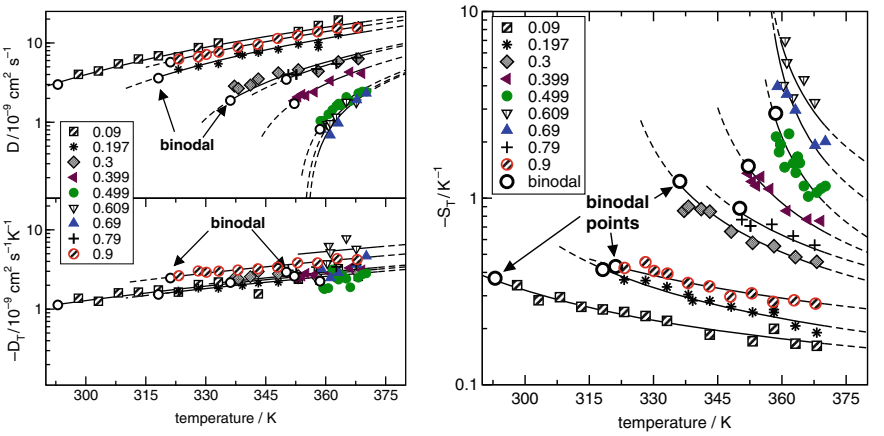

Fig. 8 Diffusion (D) and thermal diffusion (D_T) coefficient of PDMS/PEMS (16.4/48.1) (*left*) and Soret coefficient (*right*) for different PDMS mass fractions given in the legends. *Binodal points* mark the intersection with the binodal. The *dashed line* segments are extrapolations into the two-phase regime. Figures from [100]. Copyright (2007) by The American Physical Society

Within the pseudo-spinodal concept [11, 101] the diffusion coefficient of an off-critical mixture is still described in a similar way to the diffusion coefficient of the critical mixture. Only the critical temperature is now replaced by the temperature T_{sp} of the spinodal:

$$D = a_0 \frac{T - T_{sp}}{T} \exp(-T_a/T)\,. \tag{23}$$

In contrast to the critical temperature T_c, the spinodal temperature T_{sp} is well below the binodal temperature for off-critical mixtures and can hardly be reached due to prior phase separation. The diffusion coefficients in the upper left part of Fig. 8 have been fitted by (23) with a fixed activation temperature determined from D_T. The *binodal points* in Fig. 8 mark the boundary of the homogeneous phase at the binodal. The spinodal temperatures T_{sp} are obtained as a fit parameter for every concentration and together define the (pseudo)spinodal line plotted in the phase diagram in Fig. 7. The Soret coefficient is obtained from (11) and (23) as

$$S_T = \frac{D_T}{D} = \frac{D_T^0}{a_0} \left(\frac{T - T_{sp}}{T} \right)^{-1} \tag{24}$$

and diverges at the spinodal temperature (Fig. 8, right).

Although the asymptotic critical regime with the Ising-like scaling exponents has been neglected in this description, the fit curves in Fig. 8 are a reasonable parameterization for all three coefficients in the one-phase regime. This parameterization then serves as input for the numerical model. A more detailed discussion of the whole procedure can be found in [100].

3.2 Writing Patterns into Polymer Films by Local Laser Heating

The huge Soret coefficient near the critical point can be taken advantage of for the creation of compositional patterns by local heating. Figure 9 shows a setup that has been used in experiments for writing compositional patterns in polymer blends. It consists of an inverted phase contrast microscope equipped with a CCD camera. A laser beam ($\lambda = 515\,\mathrm{nm}$) can be coupled in via a telecentric lens system and a galvano scanner, which allows for arbitrary computer controlled positioning of the laser focus within the sample. The laser is focused down to $r_0 = 0.8\,\mu\mathrm{m}$ and its power can be adjusted between 0.1 and 100 mW. The sample cell is temperature controlled and mounted on an *xyz*-stage. The polymer layer of $L_s = 100\,\mu\mathrm{m}$ thickness is sandwiched between two 1 mm thick sapphire windows that are sealed with a two component epoxy resin (Torr Seal). A small amount of dye (quinizarin) is added for optical absorption. It does not change the critical temperature noticeably.

Pattern writing experiments have been performed with an almost symmetric PDMS/PEMS (16.4/15.9) blend having a critical composition $c_c = 0.48$ and a convenient critical temperature $T_c = 290.15\,\mathrm{K}$. It has been shown in [100] in detail that the parameterization of the transport coefficient determined for the higher PEMS molar mass still yields a good description for this blend too after adjusting the critical concentration and taking $(T - T_{sp})/T$ as dimensionless temperature.

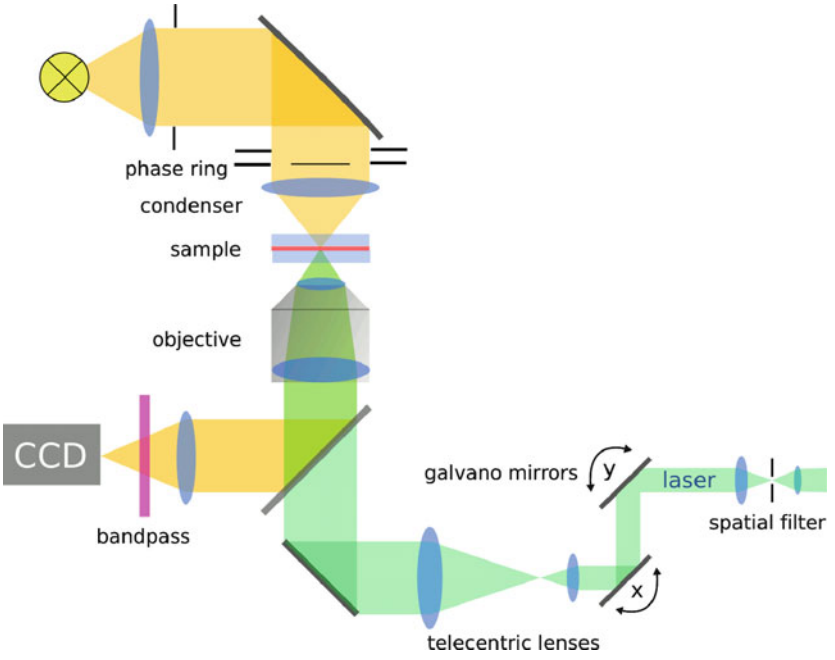

Fig. 9 Inverted phase contrast microscope equipped with a CCD camera and a laser. Galvano mirrors allow for scanning of the laser focus across the sample

The focused laser beam is scanned along an arbitrary path within the *xy*-plane as sketched in Fig. 10. The perspective view with the cross section through the scan path shown in Fig. 10a visualizes the color-coded concentration change due to the Soret effect according to the numerical simulation discussed later on. On the right hand side a phase contrast micrograph is shown where the word *Soret* has been written into the polymer blend.

For a quantitative analysis a short line segment has been written at two different distances $\Delta T = 1\,\mathrm{K}$ and $11.5\,\mathrm{K}$ above T_c, cf. Fig. 11. Because of the positive phase contrast, a darker gray value translates into a higher refractive index. Hence, the polymer with the lower refractive index (PDMS) is enriched within the bright central region. Consequently, PEMS migrates in the opposite direction and causes a dark fringe around the bright lines. This effect also leads to the darker halos around the letters in Fig. 10. This observation is in agreement with the negative sign of S_T reported in Fig. 5 for PDMS/PEMS.

The initial linear growth is proportional to D_T and identical for both distances from T_c, cf. Fig. 11a, d. At longer times the line written at $\Delta T = 11.5\,\mathrm{K}$ quickly saturates, whereas the line written close to T_c continues to grow in intensity due to the much larger Soret coefficient, as indicated in Fig. 11c, f.

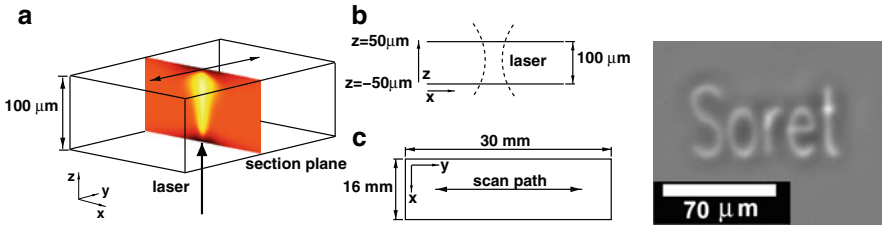

Fig. 10 (**a**) 3D-sketch of the cell; cross section according to Fig. 12. (**b**) Sketch of the laser focus. (**c**) The laser beam is scanned along the *y*-direction. *Right:* phase contrast image of arbitrary pattern written into critical sample. *The bright regions* show an enrichment of PDMS, *the dark ones* a depletion (enrichment of PEMS)

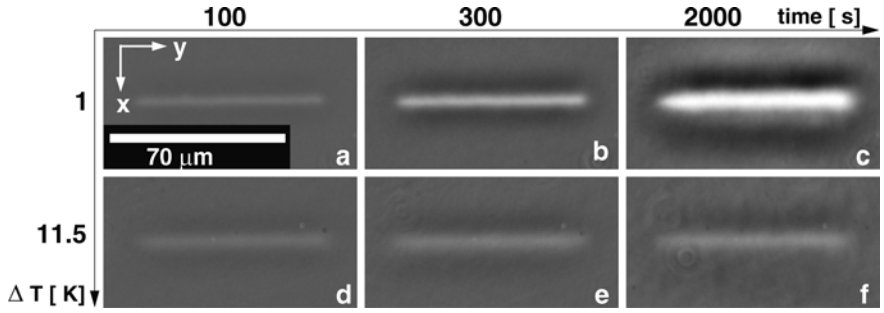

Fig. 11 Phase contrast micrographs of line segment written at 1 K (*upper row*) and 11.5 K (*lower row*) above T_c into PDMS/PEMS blend of critical composition. Images in columns taken after 100, 300, and 2,000 s. Figure from [100]. Copyright (2007) by The American Physical Society

The gray values in Fig. 10 and in Fig. 11 are 2D projections into the *xy*-plane. Because of the phase contrast technique, they are approximately linear functions of the integral over the refractive index along the *z*-direction. The temperature and concentration distribution and, hence, also the refractive index are fully 3D objects. The high thermal conductivity of the sapphire windows enforces a constant temperature boundary condition at the top and bottom windows.

3.2.1 Numerical Model

A more detailed picture of the 3D temperature and concentration distribution can be obtained by an appropriate numerical model. Besides the diffusion equations for heat and mass, convection caused by both thermal and solutal expansion needs to be taken into account.

The temperature profile evolves according to the heat equation (5) with the heat source supplied by absorption of the focused laser beam. An additional advection term accounts for the influence of convection:

$$\frac{\partial T}{\partial t} + (\mathbf{v}\cdot\nabla)\,T = \nabla\cdot(D_{\mathrm{th}}\nabla T) + \frac{\alpha}{\rho c_p} I. \tag{25}$$

The heating Gaussian laser beam is scanned along the *y*-direction. It enters the sample at $z = -L_s/2$ and creates an intensity distribution

$$\begin{aligned} I &= \frac{P_0}{A}\exp\left[-\frac{2\{x^2+(y-s(t))^2\}}{r^2}\right]\exp\left[-\alpha\left(\frac{L_s}{2}-z\right)\right], \\ A &= \pi r^2/2, \\ r^2 &= r_0^2\left[1+\left(\frac{\lambda z}{\pi r_0^2}\right)^2\right]. \end{aligned} \tag{26}$$

The temporally periodic scanning of the laser is described by $s(t)$, which changes from $-L_{\mathrm{line}}/2$ to $+L_{\mathrm{line}}/2$ linearly in time. For coordinate axes see Fig. 10.

As in the case of the heat equation, an advection term must be added to the diffusion equation (3):

$$\frac{\partial c}{\partial t} + (\mathbf{v}\cdot\nabla)\,c = \nabla\cdot[D\nabla c + D_{\mathrm{T}} c(1-c)\nabla T]. \tag{27}$$

Convection is accounted for by the Navier–Stokes equation in the Boussinesq approximation

$$\rho_0\left[\frac{\partial \mathbf{v}}{\partial t} + (\mathbf{v}\cdot\nabla)\mathbf{v}\right] = -\nabla p + \eta_0\nabla^2\mathbf{v} - \rho g\mathbf{e}_z \tag{28}$$

with the incompressibility condition

$$\nabla \cdot \mathbf{v} = 0\,. \tag{29}$$

The density changes because of both thermal and solutal expansion with expansion coefficients $\beta_{\mathrm{T}} = -(1/\rho)(\partial\rho/\partial T)_{\mathrm{c}}$ and $\beta_{\mathrm{c}} = (1/\rho)(\partial\rho/\partial c)_{\mathrm{T}}$, respectively:

$$\rho = \rho_0[1 - \beta_{\mathrm{T}}(T - T_0) + \beta_{\mathrm{c}}(c - c_0)]. \tag{30}$$

ρ_0 is the mean density at temperature T_0.

Since the extension of the induced concentration profile in Fig. 11 along the y-axis is much longer than along the other two directions, we assume translation symmetry and restrict our description to a 2D model within the xz-plane. The intensity of the laser beam is obtained by averaging (26) over the scan period:

$$\begin{aligned} I &= (P_0/A)\exp\left[-\frac{2x^2}{r^2}\right]\exp\left[-\alpha\left(\frac{L_s}{2} - z\right)\right], \\ A &= \sqrt{\frac{\pi}{2}}\,\frac{rL_{\mathrm{line}}}{\mathrm{erf}(L_{\mathrm{line}}/\sqrt{2}r)}, \\ r^2 &= r_0^2\left[1 + \left(\frac{\lambda z}{\pi r_0^2}\right)^2\right]. \end{aligned} \tag{31}$$

The high thermal conductivity of the sapphire windows ensures a fixed temperature $T = T_0$ at the boundaries $z = \pm L_s/2$ and $x = \pm L_x/2$. The boundary condition for the diffusion equation is a vanishing flux at the walls (normal vector $\mathbf{e}_{\mathrm{n}}$):

$$\mathbf{e}_{\mathrm{n}} \cdot [D\nabla c + D_{\mathrm{T}} c(1 - c)\nabla T] = 0. \tag{32}$$

For the velocity one has a nonslip boundary condition at the walls: $\mathbf{v} = 0$. The initial conditions are $T = T_0$, $c = c_0$, and $\mathbf{v} = 0$.

An expression for the transmitted light in ideal phase contrast imaging can be found in [102, 103]. For a more detailed treatment it is also necessary to take the finite width of the phase object into account [104], resulting in

$$\begin{aligned} \frac{I_{Tr} - I_{Tr0}}{I_{Tr0}} &= K\left[\frac{1 + p^2 + t^2 - 2p(\cos\phi + t\sin\phi)}{1 + p^2 + t^2 - 2p} - 1\right], \\ \phi &= \frac{2\pi L_s}{\lambda_{\mathrm{hal}}}\frac{\partial n}{\partial c}(\bar{c} - c_0). \end{aligned} \tag{33}$$

$p^2 = 1$ and $t^2 = 0.4$ are the relative amplitude transmittance of the polymer layer and the microscope objective, respectively. $\phi = \phi(x)$ is the phase shift induced in the layer due to the concentration change, $\lambda_{\mathrm{hal}} = 550$ nm is the wavelength of probing light, $\partial n/\partial c = -2.3 \times 10^{-2}$ is the contrast factor of the PDMS/PEMS mixture, and $\bar{c}$

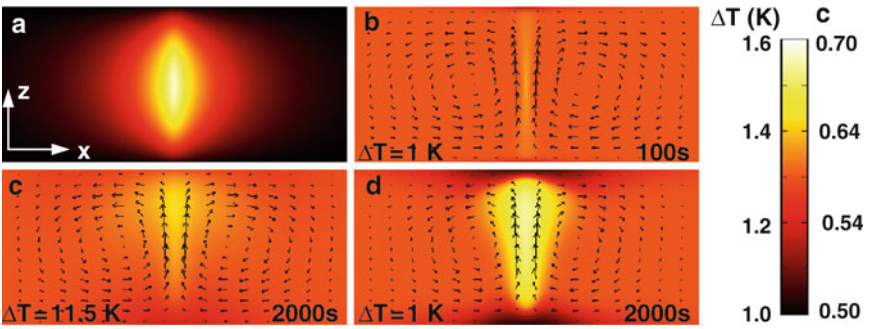

Fig. 12 Vertical cuts (*perpendicular* to *y*-axis) through a linear structure written by the laser. (**a**) Temperature profile. (**b**, **d**) Concentration profiles $c(x,z)$ for a starting temperature of $\Delta T = 1\,\mathrm{K}$ above the critical temperature after 100 s and 2000 s. Part (**c**) visualizes like in (**d**) the temperature and concentration for $\Delta T = 11.5\,\mathrm{K}$. The *arrows* are for visualization of the flow fields. Figure from [100]. Copyright (2007) by The American Physical Society

is the concentration averaged over the layer thickness. K is treated as a fit parameter [100]. The material parameters like viscosity, density, and expansion coefficients are given in [100].

Figure 12 shows the result of the numerical solution of the model above. The images are cross sections through a written line perpendicular to the scan direction of the laser. The vertical dimension, the z-direction, corresponds to a sample thickness of 100 µm. The stationary temperature distribution shown in Fig. 12a is reached very rapidly. Figure 12b shows the concentration profile after 100 s. This image is shown for a distance of $\Delta T = 1\,\mathrm{K}$ above the critical temperature. The early-stage concentration profile does, however, not depend significantly on the absolute temperature because of the almost constant thermal diffusion coefficient. During the initial linear growth period the concentration profile remains very sharp and resembles the profile of the focused Gaussian laser beam. This seems surprising at a first sight, since the driving temperature profile is already rather broad. It is, however, understood from (27), which takes for short times the form

$$\left.\frac{\partial c}{\partial t}\right|_{t\to 0} = D_{\mathrm{T}} c(1-c)\nabla^2 T \ . \tag{34}$$

Hence, the early stage of the concentration profile is proportional to the Laplacian of $T(\mathbf{r},t)$ rather than the temperature field itself. From the stationary solution of (25) it can be seen that $\nabla^2 T(\mathbf{r},t)$ is proportional to the laser intensity, neglecting temperature dependences of the coefficients and convection in a first approach.

At longer times the concentration profile broadens and becomes more intense. The two images at $t = 2{,}000\,\mathrm{s}$ clearly show the much stronger effect close to the critical point, cf. Fig. 12d. Convection causes an asymmetry of the profile and a detailed analysis shows that the main effect of convection is the solutal rather than the thermal expansion of the mixture. Radiation pressure effects due to the laser entering from below are approximately one order of magnitude smaller and negligible.

Due to the optical volume heating and the high thermal conductivity of the sapphire, the strongest temperature gradient develops directly at the window surface. Consequently, PEMS enriches mainly at the windows above and below the heated channel rather than to the left and right, as one might first guess from the 2D projection with the dark halos of Fig. 11. PEMS-rich regions appear darker in Fig. 12.

The color-coding of the hot/cold colormap used in Fig. 12 for the concentration profile can also be interpreted in terms of a refractive index map. The refractive indices of the PDMS/PEMS mixtures are such that the bright channel in the center, which corresponds to a PDMS enrichment, has a lower refractive index and the PEMS-rich layers at the windows have a higher refractive index than the average mixture. However, there may exist other polymer blends where the sign change of the refractive index is in the opposite direction. In this case, the channel-like structures could be used as re-writable optical waveguides. The cladding layers, which automatically form at the windows, would then be of low refractive index and shield the channel from the high refractive index of the window material. Such a structure is sketched in a perspective view in Fig. 13. Written structures are fully reversible and can locally or globally be erased by heating. Long term stability might be achievable with blends of a polymer with a low and a high glass transition temperature, where the dynamics comes to rest during the demixing process [106]. As has been shown for concentrated polymer solutions, the Soret coefficient is not influenced by the increasing viscosity in the vicinity of a glass transition [107–110].

As a direct consequence of the strong temperature and composition dependence of the Soret coefficient near the critical point, S_T (and D) become position dependent within the polymer layer. When the initially homogeneous sample of critical composition is kept slightly above T_c, the very high value of S_T leads to

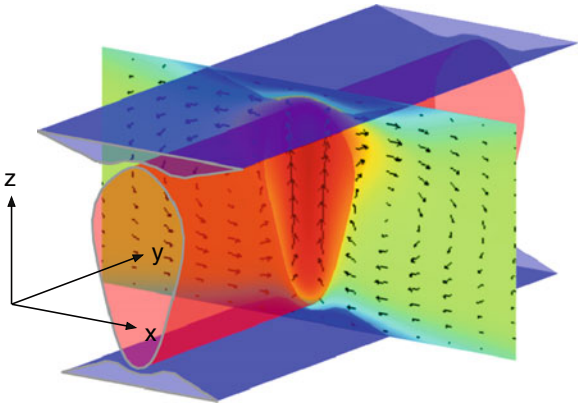

Fig. 13 Perspective view of the channel-like structure of Fig. 12d. A different color coding has been chosen for a better discrimination of the various regions. The PDMS-rich channel in the center (*red*) is sandwiched between two PEMS-rich layers (*blue*). Figure from [105]. Reprinted with permission of the author

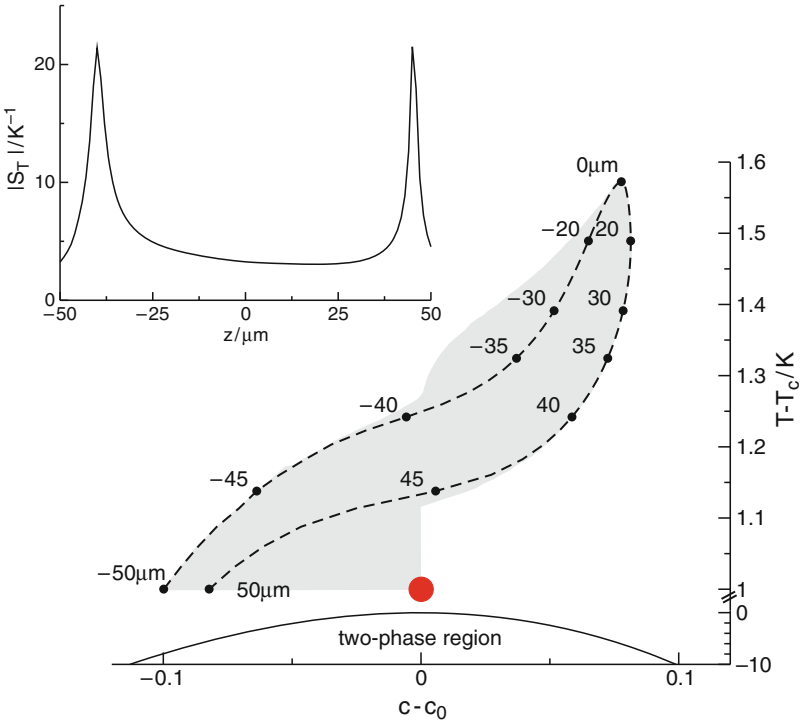

Fig. 14 Trajectory in the phase diagram for a vertical cut through the sample corresponding to Fig. 12d. $z = -50\,\mu$m and $z = -50\,\mu$m correspond to the lower and upper window, respectively. All volume elements of the sample reside inside the *gray region*. The *inset* shows the modulus of the Soret coefficient plotted along the *dashed* trajectory

strong concentration changes even for small temperature gradients. When a volume element is moved away from the critical point in the phase diagram, S_T decreases and the further excursion along the composition axis is efficiently limited.

In order to illustrate this nonlinear mechanism we have plotted the part of the phase diagram occupied by the sample from Fig. 12d in Fig. 14 as a gray region. The red bullet marks the initial position of the homogeneous sample just above the critical point. The dashed curve is a trajectory that corresponds to a vertical cut through the cell along the optical axis of the laser beam. Negative values of $(c - c_0)$ correspond to PEMS, positive values to PDMS enrichment. The Soret coefficient plotted along this trajectory shows a characteristic double peak structure. The two maxima are very close to the position where the concentration crosses the average value $c = c_0$.

Figure 15 shows an example, where the temperature profile has not been created by direct laser heating of the absorbing dyed polymer blend in the volume but rather by optical heating of a colloidal gold particle of 200 nm in diameter [111]. Such a colloid then serves as a microscopic heat source that directly modifies

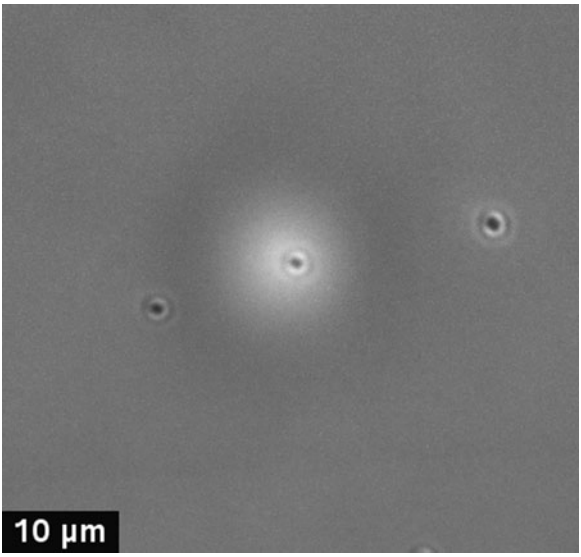

Fig. 15 Phase contrast micrograph of laser-heated gold colloid (*center*) with PDMS enrichment in the surrounding volume (*bright*) and PEMS accumulation at larger distance (*dark*). Only the middle one of the three colloids is heated with a focused laser [111]

the composition of the surrounding polymer blend. The bright region around the colloid, corresponding to PDMS enrichment, is surrounded by a faint darker ring where PEMS, that is displaced from the immediate surrounding of the gold particle, accumulates.

3.3 Quenching of an Off-Critical Blend by Local Heating

Important consequences of the strong coupling between inhomogeneous temperature fields and local composition arise for situations where equilibrium phase diagrams are applied to nonequilibrium systems [112]. Such scenarios have been reported by a number of authors. Lee et al. studied spinodal decomposition in the presence of a temperature gradient [16, 17]. Tanaka et al. investigated the influence of periodically driving the polymer mixture above and below the instability point [74]. Meredith et al. employed a combinatorial method with perpendicular temperature and concentration gradients in order to determine entire polymer phase diagrams in a single experiment [113]. In the following it will be shown that rather unexpected effects can occur in the presence of temperature gradients and that equilibrium phase diagrams do not necessarily give a valid approach to nonequilibrium conditions.

The experiments reported here have been performed with a PDMS/PEMS (16.4/48.1) blend. The mixture is a UCST mixture with a critical composition of $c_c = 0.61$.

The diffusion, thermal diffusion, and Soret coefficients of this system are shown in Fig. 8. Samples of two different off-critical compositions ($c = 0.3$ and $c = 0.9$) were prepared. The temperature was set to a value of a few degrees above the binodal. Hence, the sample was entirely within the homogeneous phase and one would expect that heating could only drive the blend further into the stable one-phase region.

This assumption is indeed true for equilibrium scenarios with a homogeneous temperature distribution. Due to the coupling between heat and mass transport, laser heating gives rise to completely different behavior and can even drive a UCST-mixture locally from the homogeneous into the phase separated state.

The result of such laser writing experiments is shown in Fig. 16, where the focused laser beam has been scanned along simple paths, a line and a circle. The upper two images correspond to the sample with $c = 0.3$ (left of the binodal), the lower two to $c = 0.9$ (right of the binodal). The initial location of either sample in the phase diagram is marked in Fig. 17 with bullets. All four images in Fig. 16 show two distinct features. First, there is smooth variation of the gray values with lighter values along the scan path. This reflects the writing with a concentration change due to the Soret effect, similar to the scenario discussed for the critical sample. Additionally, there are localized droplets, which are characteristic for a nucleation and

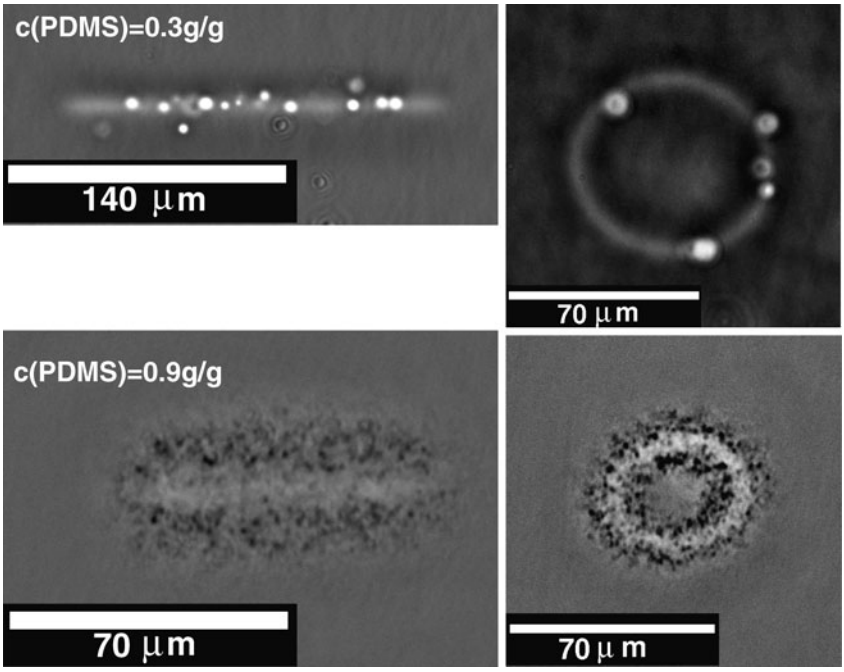

Fig. 16 Forced demixing of an initially homogeneous off-critical PDMS/PEMS blend for $c = 0.3$ (*upper row*) and $c = 0.9$ (*lower row*)

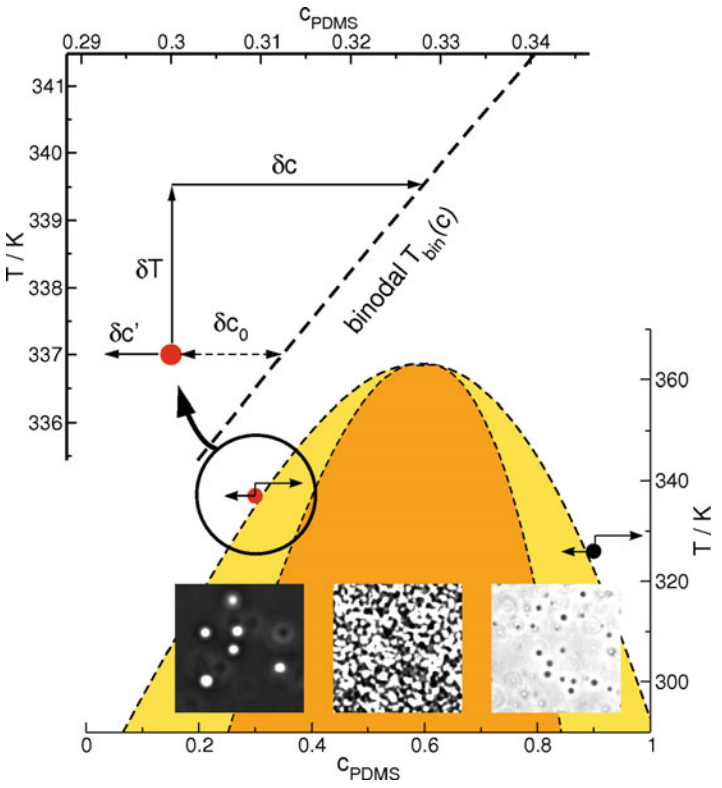

Fig. 17 Phase diagram of a PDMS/PEMS (16.4/48.1) blend. The *dashed lines* are the binodal and the spinodal. The phase contrast micrographs show typical demixing patterns for spinodal decomposition and nucleation and growth in the respective regions. The *bullets* mark the initial sample positions. See text for details. Figure from [112]. Copyright (2007) by the American Chemical Society

growth type demixing scenario. These droplets are bright and appear in the center of the written line, corresponding to the hottest region, for $c = 0.3$. For $c = 0.9$ they are darker than the average gray value and located at the periphery of the line. In either case their number increases with exposure time.

The occurrence of demixing morphologies characteristic for the metastable regime between the binodal and the spinodal can be understood from Fig. 17. The red dot marks the initial position of the sample with $c = 0.3$. Upon laser heating the temperature within the laser focus rises by ΔT and the distance to the binodal first increases. A stationary temperature distribution is rapidly reached and the Laplacian of the temperature field $T(\mathbf{r},t)$ is obtained from the stationary solution of the heat equation (5) with the power absorbed from the laser as source term:

$$\nabla^2 T = -\frac{\alpha}{\kappa} I. \tag{35}$$

Inserting this into the diffusion equation (3) gives an expression for the initial linear growth rate of the concentration profile, where $\nabla^2 c \approx 0$:

$$\frac{\partial c}{\partial t} = -\frac{\alpha}{\kappa} D_{\mathrm{T}} c(1-c) I. \tag{36}$$

Due to the negative Soret coefficient of PDMS/PEMS, the composition in the center of the focus evolves towards higher PDMS concentrations and, hence, towards the two phase region. The mixture crosses the binodal after a time

$$\delta t = \frac{\delta c}{\partial_t c} = -\frac{\delta c_0 + \delta T \left(\mathrm{d}\, T_{\mathrm{bin}}/\mathrm{d}c\right)^{-1}}{D_{\mathrm{T}} c(1-c) I \alpha/\kappa}. \tag{37}$$

δc_0 is the initial distance to the binodal as defined in Fig. 17. $(\mathrm{d}\, T_{\mathrm{bin}}/\mathrm{d}c)$ is the slope of the binodal. $\delta T = 2.5\,\mathrm{K}$ has been obtained from a full 3D-simulation of the thermal part of the problem. Details of this estimation, including estimations for all missing parameters, are discussed in [112]. The estimated time $\delta t \approx 13\,\mathrm{s}$ turned out to be much shorter than the 7 min until first droplets could be observed. Possibly, the much longer waiting time is owed to the metastability of the region between the binodal and the spinodal.

The arrow pointing from the initial location at $c = 0.3$ to the left indicates the evolution of the concentration away from the center of the heated line and at the window surfaces, corresponding to the blue cladding layers in Fig. 12. These regions represent the cold side with a reduced PDMS and increased PEMS concentration that are shifted further into the stable region, away from the phase boundary.

The situation is different for $c = 0.9$, where the PDMS-enriched central part is stabilized and shifted away from the binodal. But now, the regions outside the central area, where PEMS accumulates, cross the phase boundary into the metastable range. The demixing by nucleation and growth is visible in the lower two micrographs in Fig. 16 in the form of a halo of dark droplets around the written structures.

Due to the phase contrast technique, PDMS- and PEMS-rich areas can easily be distinguished, as shown in the three micrographs inserted in Fig. 17. They show characteristic demixing scenarios observed for samples homogeneously quenched into the two-phase region. The image in the middle corresponds to a symmetric spinodal demixing pattern. The image on the left side shows droplet formation characteristic of the metastable region where PDMS-rich droplets form the minority phase. They appear as bright spots with a dark background. Clearly, the forced demixing of the samples with $c = 0.3$ in Fig. 16 corresponds to this scenario.

For samples with high PDMS concentrations $c > c_{\mathrm{c}}$ the situation is the other way round. The droplets of the PEMS-rich minority phase appear dark in front of a bright background. The right micrograph in Fig. 17 and the samples with $c = 0.9$ in Fig. 16 correspond to this situation.

As a consequence of these experiments one has to realize that care is required in situations where equilibrium phase diagrams are applied to nonequilibrium situations [113]. Due to the coupling of heat and mass transport, the local

concentration may change. An excursion along the temperature axis unavoidably leads to a simultaneous excursion along the concentration axis. Due to the large Lewis number, these two effects are characterized by very different characteristic relaxation times.

4 Model for Phase Separation Including Thermodiffusion

A modified Cahn–Hilliard (CH) model [114] is used for the theoretical analysis of the impact of thermal diffusion on phase separation by taking into account an inhomogeneous temperature distribution, which couples to a concentration variation via the Soret effect. The Flory–Huggins model is used for the free energy of binary polymer-mixtures. The composition is naturally measured in terms of volume fraction ϕ of a component A, which can be related to the weight fraction c by

$$c = \frac{\phi\rho_{\mathrm{A}}}{\phi\rho_{\mathrm{A}} + (1-\phi)\rho_{\mathrm{B}}}, \tag{38}$$

where ρ_{A} and ρ_{B} are the densities of the two polymers. For all polymer blends considered in this study, the densities of the two components are assumed to be similar and, therefore, volume and weight fractions can be considered to be identical for all practical purposes. For an incompressible binary A/B mixture (ρ =const) the continuity equation relates the space and time dependence of the local volume fraction $\phi(\mathbf{r},t)$ to the total mass current $\mathbf{J}(\mathbf{r},t)$ and expresses the conservation of mass in the system

$$\frac{\partial\phi(\mathbf{r},t)}{\partial t} = -\nabla\cdot\frac{\mathbf{J}(\mathbf{r},t)}{\rho}, \quad \mathbf{J} = \mathbf{J}_{\mathrm{D}} + \mathbf{J}_{\mathrm{T}}. \tag{39}$$

$\mathbf{J}_{\mathrm{D}}$ is the mass current caused by gradients of the chemical potential $\mu(=\mu_{\mathrm{A}}-\mu_{\mathrm{B}})$ and $\mathbf{J}_{\mathrm{T}}$ is the mass current due to the Soret effect in an inhomogeneous temperature field T [76]

$$\mathbf{J}_{\mathrm{D}}(\mathbf{r},t) = -\rho M(\nabla\mu)_{\mathrm{T}}, \;\; \mathbf{J}_{\mathrm{T}}(\mathbf{r},t) = -\rho D_{\mathrm{T}}\phi(1-\phi)\nabla T(\mathbf{r},t). \tag{40}$$

M is the "mobility" of species A with respect to B and D_{T} is the thermal diffusion coefficient. Both are often treated as constants, although they are generally concentration dependent.

In a Ginzburg–Landau model the chemical potential μ is related to the free energy functional $F[\phi(\mathbf{r},t)]$ by

$$\mu = \frac{\delta F[\phi]}{\delta\phi}, \;\; \frac{F[\phi]}{k_{\mathrm{B}}T} = \frac{1}{v}\int \mathrm{d}\mathbf{r}\left[\frac{f[\phi]}{k_{\mathrm{B}}T} + \kappa(\phi)(\nabla\phi)^2\right], \tag{41}$$

with the Boltzmann constant k_B. The Flory–Huggins (FH) expression for the energy of mixing of an incompressible binary polymer blend has the form [80]

$$\frac{f[\phi]}{k_B T} = \frac{\phi}{N_A} \ln \phi + \frac{(1-\phi)}{N_B} \ln(1-\phi) + \chi \phi (1-\phi), \tag{42}$$

where N_A and N_B describe the degree of polymerization ("chain lengths") of the A and B molecules, respectively. χ is the Flory interaction parameter that describes the interaction strength between the two species A and B. Positive values of χ favor phase separation. This contribution to the free energy has a double-well structure in the two-phase region, and the temperature dependence of the coefficient χ is commonly described by the phenomenological expression

$$\chi = \alpha + \beta T^{-1}. \tag{43}$$

α and β are empirical constants [115].

For positive values of $\kappa(\phi)$ the gradient term in (41) expresses the energy required to create an interface between A-rich and B-rich domains, and this energy contribution is reduced by removing interfaces during the coarsening process in the two phase region. In order to study the case of arbitrary distance from the critical point, the concentration dependence of the gradient term $\kappa(\phi)$ in (41) is taken into account by de Gennes' random phase approximation [116, 117]:

$$\kappa(\phi) = \frac{1}{36} \left[\frac{\sigma_A^2}{\phi} + \frac{\sigma_B^2}{1-\phi} \right], \tag{44}$$

where σ_A and σ_B are the monomer sizes (Kuhn lengths) of the A and B components, respectively.

Since we want to treat polymer blends subjected to an inhomogeneous temperature field (produced, e.g., by light absorption), the heat equation

$$\frac{\partial T(\mathbf{r},t)}{\partial t} = D_{th} \nabla^2 T(\mathbf{r},t) + \frac{\alpha_\lambda}{\rho c_p} I(\mathbf{r},t) \tag{45}$$

has to be taken into account, where D_{th} is the thermal diffusivity. The heat source term is proportional to the light intensity I that corresponds to the local illumination of the polymer film. α_λ is the optical absorption coefficient, ρ is the density, and c_p the specific heat at constant pressure. For typical polymer blends the Lewis number, the ratio between the mass diffusion time and the temperature diffusion time, is of the order of 10^3, and the heat equation (45) can be treated in the stationary limit (neglect the time derivative of the temperature).

A mixture of composition ϕ_0 is unstable against phase separation when $f[\phi]$ has negative curvature at $\phi = \phi_0$. The critical point of spinodal decomposition in model (42) is given by

$$\phi_c = N_B^{1/2} / (N_A^{1/2} + N_B^{1/2}), \quad \chi_c = [N_A^{1/2} + N_B^{1/2}]^2 / (2 N_A N_B), \tag{46}$$

such that the system is miscible for $\chi < \chi_c$ and immiscible for $\chi > \chi_c$ at the critical concentration. Close to (ϕ_c, χ_c) the expression for the free energy in (42) can be approximated by a Taylor expansion with respect to the composition fluctuation $\varphi(\mathbf{r},t) = [\phi(\mathbf{r},t) - \phi_c]$ leading to the Ginzburg–Landau functional in terms of powers of φ (an irrelevant term linear in φ has been omitted)

$$\frac{F_{GL}[\varphi]}{k_B T_c} = \frac{1}{v}\int \mathrm{d}\mathbf{r}\left[\frac{1}{2}b\varphi^2 + \frac{1}{4}u\varphi^4 + \frac{1}{2}K(\nabla\varphi)^2\right], \tag{47}$$

where the coefficients are defined as

$$b = 2(\chi_c - \chi) \approx \frac{2\beta}{T_c^2}(T - T_c), \;\; u = \frac{4}{3}\chi_c^2\sqrt{N_A N_B},$$
$$K = \frac{1}{18}\left[\sigma_A^2(1+\sqrt{N_A/N_B}) + \sigma_B^2(1+\sqrt{N_B/N_A})\right]. \tag{48}$$

Equations (39) and (45) in combination with (40) and (47) define our model close to the critical point:

$$\partial_t\varphi(\mathbf{r},t) = \frac{Mk_B T_c}{v}\nabla^2\left[b(T)\varphi + u\varphi^3 - K\nabla^2\varphi\right] + D_T\phi_c(1-\phi_c)\nabla^2 T, \tag{49}$$

$$D_{th}\nabla^2 T = -\frac{\alpha_\lambda}{\rho c_p}I(\mathbf{r},t). \tag{50}$$

$S_T = D_T/D$ and $D = (Mk_B T_c|b|)/v$ are the Soret and the diffusion coefficient, respectively. In the absence of thermal diffusion, (49) reduces to the well known Cahn–Hilliard equation, which belongs to the universality class described by model B [3]. In fact, (49) gives a universal description of a system in the vicinity of a critical point leading to spinodal decomposition.

5 Temperature Modulations in the Two-Phase Regime

In this section it will be demonstrated how spinodal decomposition patterns in the two phase region can locally be manipulated in a controlled way by heating a polymer blend PDMS/PEMS by a focused laser beam. It will also be shown that the essential spatial and temporal phenomena, as observed in the experiments, can only be reproduced in numerical simulations if thermodiffusion (Soret effect) is taken into account in the basic equations.

The polymer blend PDMS/PEMS with molar masses of $M_w = 16.4$ and $22.3\,\mathrm{kg\,mol^{-1}}$, respectively, is similar to the one which has previously been used for the investigation of transport properties in the critical regime [81]. A 515 nm and 20 mW laser was used for local heating. The blend with a PDMS weight fraction of $c = 0.536$ is almost critical with a critical temperature of $T_c = 37.7°\mathrm{C}$. A minute amount of an inert dye (quinizarin) was added for optical absorption at

the wavelength of the laser. The thickness of the sample was 200 µm, the beam waist approximately 30 µm, the optical density 0.1, and the temperature rise within the beam center was estimated to be approximately 5 K. Images of the sample were recorded by a microscope objective (7×) and a CCD camera, whose image sensor was, without additional optical elements, within the image plane 50 cm behind the objective. The horizontally oriented sample was illuminated with slightly divergent white light from a cold light source, which produces an observable amplitude image from a pure phase object. This method of imaging of spinodal decomposition patterns in mixtures of nonabsorbing liquids of different refractive indices has been discussed in detail in [118].

The sample was quenched into the two-phase region 0.5°C below T_c and 120 min later, where Fig. 18A was also taken, the laser beam was turned on at $t = 0$. At this

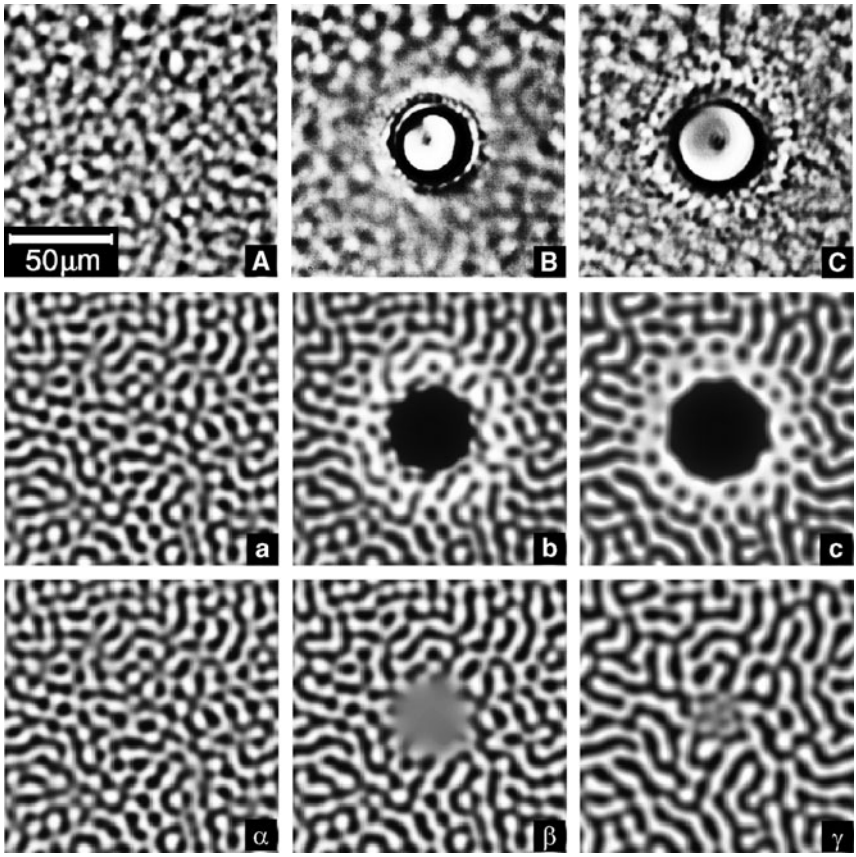

Fig. 18 Temporal evolution of a pattern in a polymer blend at $T = 37.2°C < T_c$ which was exposed locally to laser light during the period $0 < t < 200$ s. Images are taken at $t = 0$ (**A**), $t = 300$ s (**B**), and $t = 700$ s (**C**). The corresponding images (**a–c**) are obtained by simulations with and the images ($\alpha - \gamma$) without taking the Soret effect into account. Figure from [119]. Copyright (2005) by The American Physical Society

moment the spinodal decomposition has already reached a progressed stage, and the Fourier transform of Fig. 18A gives a characteristic length scale of the order of 10 μm. At the time = 200 s the laser beam was turned off, and Fig. 18B was taken at $t = 300$ s. Since the spatial concentration distribution of the two polymers cannot be extracted quantitatively by direct imaging techniques, the gray scales of the experimental images in Fig. 18 have been equalized for optimum contrast.

The spinodal pattern completely disappears in the area where the material was heated by the laser beam beyond T_c. After the laser is switched off, this circular pattern again survives for a long time (Fig. 18B, C) before a somewhat irregular structure develops in this area. It slowly grows in diameter (Fig. 18C) and moves away from the central spot like a spherical wave.

To analyze this phenomenon further, 2D numerical simulations of (49) and (50) were performed using a central finite difference approximation of the spatial derivatives and a fourth order Runge–Kutta integration of the resulting ordinary differential equations in time. Details of the simulation technique can be found in [114, 119]. The material parameters of the polymer blend PDMS/PEMS were used and the spatial scale $\xi = (K/|b|)^{1/2}$ and time scale $\tau = \xi^2/D$ were established from the experimental measurements of the structure factor evolution under a homogeneous temperature quench.

The results of the simulations, including the Soret-effect, are shown in Fig. 18a–c for parameters comparable to the experimental conditions. The dark and bright areas correspond, according to the basic equations, to the A- and B-rich phase. The experimental images, however, are generated by an optical imaging technique, from which only characteristic patterns and length scales are directly comparable. A good quantitative agreement between the model and the experimental results could be obtained for the time evolution of the central spot size. For comparison, simulations were also performed without the Soret effect, cf. Fig. 18$\alpha - \gamma$, by setting $D_T = 0$ in (49). All other parameters of the model were kept constant and the same initial conditions were used in Fig. 18a and Fig. 18α. In this case the laser heated spot is driven into the one-phase regime during the laser light exposure, but the characteristic features of the experimentally observed demixing pattern do not show up without the Soret effect.

Our simulations clearly demonstrate that without thermally driven mass diffusion the spatial variation of the control parameter $b(T)$ due to the local laser heating does not provide the typical pattern evolution observed in the experiments. It is crucial to take the Soret effect in the basic equations into account in order to reproduce the phenomena observed in an experiment with local heating.

We have demonstrated that in the two-phase region the spinodal demixing pattern can be locally manipulated on a mesoscopic length scale by local heating. The smallest achievable structures are expected to be in the range of the diffraction limit of the laser beam. These new effects are not limited to the cylindrical geometries discussed here and may possibly open a new route towards the structuring of polymer blends and towards the creation of gradient materials and embedded gradient structures.

6 Spatially Periodic Forcing of Phase Separation

A number of interesting effects occur in spatially periodically forced pattern forming systems with a nonconserved order parameter, which have been investigated during recent years [60–73, 120]. Here we focus on nearly unexplored effects of spatially periodic forcing in system with a conserved order parameter, as they occur in phase separating systems which are forced by spatial temperature modulations and where thermodiffusion plays a crucial role.

Such forced phase separating systems can be realized, for instance, in optical grating experiments on polymer blends with a spatially periodic light intensity $I(\mathbf{r},t) = I_0 \cos(qx)$ [44, 87]. Such a spatially periodic light intensity leads, together with (50), to the equation

$$\nabla^2 T = -\delta T_0 q^2 \cos(qx), \;\; \delta T_0 = \frac{\alpha_\lambda}{\rho c_p D_{\rm th}} \frac{I_0}{q^2}, \tag{51}$$

which determines the spatially periodic temperature field. The contribution $\nabla^2 T$ in (49) can be replaced with this equation to obtain an additive spatially periodic forcing contribution in (49). On this route dimensionless variables are introduced by choosing the temperature T_0 in the two-phase region as reference temperature ($T_0 < T_c$), leading to

$$\mathbf{r} = \mathbf{r}'\xi, \;\; \xi = (K/|b|)^{1/2}; \;\; t = t'\tau, \;\; \tau = \xi^2/D; \;\; \varphi = \psi(u/|b|)^{-1/2}. \tag{52}$$

All quantities are evaluated at T_0. Then, the rescaled equation for the order parameter $\psi(x,t)$ of the following form (primes are omitted) is obtained:

$$\partial_t \psi(\mathbf{r},t) = \nabla^2 \left[-\varepsilon\psi + \psi^3 - \nabla^2\psi + a\cos(qx) \right], \tag{53}$$

where

$$\varepsilon = \frac{T_c - T}{T_c - T_0}, \;\; a = \frac{D_T}{D} \left(\frac{u}{|b|} \right)^{1/2} \phi_c(1-\phi_c)\delta T_0. \tag{54}$$

Equation (53) describes the dynamics of phase separation in the presence of a spatially periodic forcing following a quench from the stable one-phase region ($\varepsilon < 0$) to a reference temperature in the two-phase region ($\varepsilon > 0$). In the following only the case of a symmetric quench with $\int d\mathbf{r}\psi = 0$ as initial condition at $t = 0$ will be considered.

In the absence of the forcing ($a = 0$) the homogeneous solution $\psi = 0$ becomes unstable for $\varepsilon > 0$ against linear perturbations $\sim \exp(\sigma t + i\mathbf{k}\cdot\mathbf{r})$ with wave number $k \in (0, \sqrt{\varepsilon})$ and the growth rate $\sigma = k^2(\varepsilon - k^2)$. The most unstable (fastest growing) mode is characterized by $k_m = \sqrt{\varepsilon/2}$ with $\sigma_m = \varepsilon^2/4$. If in a 2D phase separating system the spatial extension in one direction is smaller than the wavelength of the fastest growing mode, it can be considered as quasi 1D.

6.1 Spatially Periodic Solutions and Their Stability

For positive values of the control parameter ε, stationary, spatially periodic solutions $\psi_s(x) = \psi_s(x + 2\pi/q)$ of (53) may be found with and without forcing. However, in the case of a vanishing forcing amplitude ($a = 0$) in (53), this equation has a $\pm\psi$-symmetry and one has a pitchfork bifurcation from the trivial solution $\psi = 0$ to finite amplitude periodic solutions as indicated in Fig. 19. In the unforced case, however, periodic solutions of (53) are unstable for any wave number q against infinitesimal perturbations that induce coarsening processes [114, 121].

For finite values of the modulation amplitude a the broken $\pm\psi$-symmetry is indicated in Fig. 19 for $a = 0.01$ by the dashed line and for $a = 0.03$ by the solid line. While there are a trivial solution $\psi = 0$ and two finite solutions with identical amplitudes but of opposite sign in the unmodulated case, there exist three periodic solutions, A_1, A_2, and A_3, of different amplitude in the forced case, as shown for one period in Fig. 19b–d. These three different solutions have been determined by solving (56) by a Galerkin method, namely by expanding the solution $\psi_s(x)$ with respect to periodic functions (Fourier series) and by solving the resulting nonlinear equations for the amplitudes of the periodic expansion functions by means of a Newton method. The A_3- and A_2-solutions are in phase with the external modulation and the preferred A_1-solution is shifted by half a period. One should also note that the A_1 solution already exists in the range $\varepsilon < 0$ and, therefore, in the one phase region without forcing.

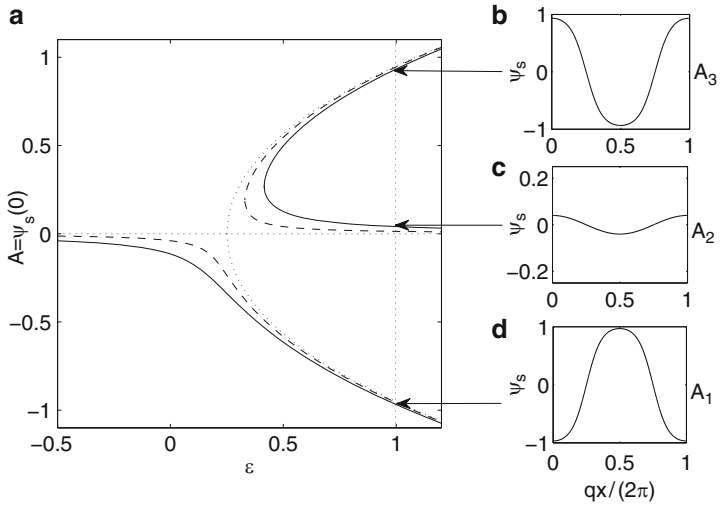

Fig. 19 (**a**) The bifurcation diagram for spatially periodic solutions at a forcing wave number $q = 0.5$ and modulation amplitudes $a = 0$ (*dotted*), $a = 0.01$ (*dashed*), and $a = 0.03$ (*solid*). (**b**)–(**d**) The three solutions $\psi_s(x)$ over one period corresponding to the different branches of the bifurcation diagram for $a = 0.03$ and $\varepsilon = 1$. Figure from [122]. Reprinted with permission by Springer

Besides the existence of the periodic solutions $\psi_s(x)$ of (53), their stability is also of interest. For this purpose we use as ansatz a superposition of the stationary periodic solution $\psi_s(x)$ and a time-dependent perturbation $\psi_1(x,t)$

$$\psi(x,t) = \psi_s(x) + \psi_1(x,t), \;\; \psi_1(x,t) = \mathrm{e}^{\sigma t}\phi(x), \tag{55}$$

where $\psi_s(x)$ satisfies the equation

$$-\varepsilon\psi_s + \psi_s^3 - \partial_{xx}\psi_s + a\cos(qx) = 0 \tag{56}$$

with periodic boundary conditions $\psi_s(0) = \psi_s(2\pi/q)$. Substituting (55) into (53) and linearizing this equation with respect to the perturbation ψ_1 we arrive at a linear eigenvalue problem:

$$\sigma\phi = \partial_{xx}\mathscr{L}\phi, \;\; \mathscr{L} = -\varepsilon + 3\psi_s^2 - \partial_{xx}, \tag{57}$$

where $\phi(x)$ can be represented in Floquet form

$$\phi(x) = \mathrm{e}^{\mathrm{i}sx}\phi_F(x). \tag{58}$$

Here s is the Floquet exponent and $\phi_F(x)$ is $2\pi/q$-periodic. For a given $\varepsilon > 0$ and q we are interested in the largest real part of $\sigma(s,a)$ and therefore in the growth rate of the small perturbation $\psi_1(x,t)$ with respect to each stationary periodic solution A_1, A_2, or A_3. The neutral stability condition $\sigma(a,s,q) = 0$, which separates the parameter range where the periodic solutions are stable from the unstable range, is a condition to determine the critical forcing amplitude $\tilde{a}(s,q)$. For forcing amplitudes larger than this the growth rate of the perturbation is negative and, therefore, the stationary periodic solutions ψ_s are stable with respect small perturbations ψ_1.

In the limit of small wave numbers of the forcing in comparison to the wave number of the fastest growing mode of the unforced system, $q/k_m \ll 1$, the stationary solution ψ_s can be determined and the neutral stability condition $\sigma(a,s,q) = 0$ can be solved analytically in a perturbative way (see [114] for details). With the resulting analytical solution for A_1 the following expression for the critical forcing amplitude is obtained:

$$a_s(s,q) = [1+\cos(\pi s/q)]\varepsilon^{3/2}32(k_m/q)\mathrm{e}^{-2\pi k_m/q}\left[1 + \frac{(\pi q/k_m)^2}{24}\right]. \tag{59}$$

Since the amplitude a_s takes its maximum in the limit $s \to 0$, the periodic solution A_1 becomes at first unstable for long wavelength perturbations.

$\phi_F(x)$ is calculated similar to $\psi_s(x)$ by solving (57) by means of a Galerkin method. In general, the neutral stability condition has to be solved numerically. One finds that the stationary solutions A_2 and A_3 are always unstable with respect to small perturbations. In Fig. 20 the forcing amplitude $a_s(q)$, as given by (59) for $s = 0$, is plotted (solid line) together with the corresponding numerical results (solid circles) and the deviations between both are tiny.

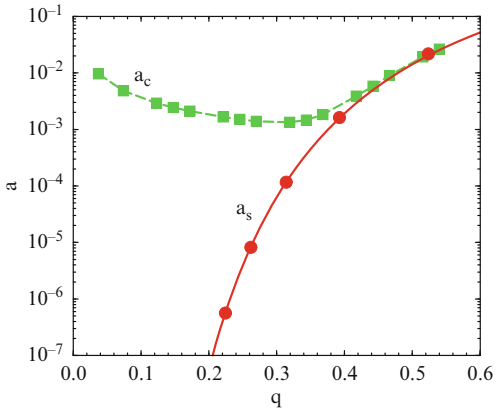

Fig. 20 The forcing amplitude a_s above which the periodic solution A_1 is linearly stable. The *solid line* is the approximate analytical result according to (59) and the *solid circles* are obtained numerically. The critical amplitude a_c above which the evolution of the initially homogeneous system after the quench is locked to the $2\pi/q$-periodicity of the forcing (*solid squares*, obtained numerically). The results are given for $\varepsilon = 1$

The stability of 2D stripe patterns that are periodic along the same direction (here the x direction) as the forcing has been investigated numerically. For this purpose an ansatz similar to the one in 1D has been chosen:

$$\psi_1(x,y,t) = \mathrm{e}^{\sigma t}\mathrm{e}^{\mathrm{i}(sx+py)}\phi_F(x)\,, \tag{60}$$

but now depending on two Floquet exponents: s (x-direction) and p (y-direction). The linear stability analysis shows that additional transversal degrees of freedom do not influence the stability boundary a_s, cf. Fig. 20, as obtained in the case of the 1D model.

As mentioned above, for finite forcing amplitudes one already has periodic A_1 solutions in the range $\varepsilon < 0$. But, when the system is quenched into the two-phase region with $\varepsilon > 0$, where one may choose for reasons of simplicity $\varepsilon = 1$, the spinodal decomposition sets in and the late stage of the phase separation process depends on the forcing amplitude a. It is an interesting question, for which parameter combinations the systems ends up in a A_1 solution that is locked to the periodicity of the external forcing, independent of the initial conditions before the quench.

This question has been investigated by numerical simulations of (53) in one spatial dimension with a typical system size $L = 512$. In order to test the results for their independence of the system size, we also made selected runs for $L = 1{,}024$ and 2,048. As initial condition we took small fluctuations around the homogeneous (single phase) state $\psi = 0$ by assigning to each lattice site a random number uniformly distributed in the interval ± 0.01. In order to average over random initial configurations, 100 runs were performed for each parameter combination. The simulations show that there is a well-defined critical amplitude $a_c = a_c(q)$, above which the time evolution of the system always ends up in the stationary A_1 solution that is locked to the wavelength $2\pi/q$ of the external forcing, independent of the initial conditions. In Fig. 20 the critical amplitude $a_c(q)$ is shown (solid squares) as obtained from the numerical simulations ($\varepsilon = 1$).

Since linear stability of the periodic solution of type A_1 is a necessary condition for it being an attractor one has $a_c(q) \geq a_s(q)$. For q approaching the fastest growing

wave number $k_m = \sqrt{\varepsilon/2}$ one has $a_c(q) \approx a_s(q)$ (see Fig. 20), which is actually not surprising, and this value gives a reasonable estimate for $a_c(q)$ also for smaller values of q.

6.2 Traveling Spatially Periodic Forcing

A spatiotemporal periodic forcing is a rather recent and interesting development for exploring various facets of pattern formation in systems with nonconserved order parameters [69–73]. But also in systems with a conserved order parameter, a forcing traveling with the velocity v provides an interesting possibility to explore various properties of phase separation dynamics. In particular, we consider the effects of traveling spatially periodic forcing in the framework of our extended Cahn–Hilliard model with thermodiffusion [see (49) and (50)]. Using dimensionless variables, as introduced in (52), the modified CH equation is given by

$$\partial_t \psi(\mathbf{r},t) = \nabla^2 \left\{ -\varepsilon\psi + \psi^3 - \nabla^2\psi + a\cos[q(x-vt)] \right\}. \tag{61}$$

The forcing term $a\cos[q(x-vt)]$ is caused by an interplay between a traveling temperature modulation and thermodiffusion (Soret effect). Such a traveling spatially periodic temperature modulation could be created for instance in optical grating experiments [44, 87] with a light intensity of the form $I(\mathbf{r},t) \sim \cos[q(x-vt)]$. Another possibility is to move a sample with a velocity v across a modulated temperature field. The control parameter ε in (61) corresponds to a dimensionless distance to the critical temperature of the binary mixture. Transformation of (61) in the frame comoving with the traveling forcing $x \to x - vt$ gives

$$\partial_t \psi(\mathbf{r},t) = \nabla^2 \left[-\varepsilon\psi + \psi^3 - \nabla^2\psi + a\cos(qx) \right] + v\partial_x\psi. \tag{62}$$

As was shown before, if phase separation is forced by a stationary and spatially periodic temperature modulation, the coarsening dynamics is interrupted above some critical value of the forcing amplitude a and it is locked to the periodicity of the external forcing. However, if this forcing is "pulled" by a velocity $v \neq 0$, the traveling periodic solutions of (61) exist only in a certain range of v depending on a.

Thus we are interested in the conditions of the existence and stability of the spatially periodic solutions $\psi_s(x) = \psi_s(x + 2\pi/q)$ of (62) in the comoving frame. The nonlinear solutions and the bifurcation diagram as given in Fig. 19 are only slightly changed by a small traveling velocity. However, with increasing values of v a phase shift $\Delta\phi$ between the periodic forcing $\sim \cos(qx)$ and the solution $\psi_s(x)$ occurs. The maximum phase shift that can be achieved is about $\Delta\phi_m = \pi/2$ at a certain velocity v_{ex} above which a solution does not exist. Consider $\psi_s(x)$ being a $2\pi/q$-periodic solution of the following equation:

$$\partial_{xx} \left[-\varepsilon\psi_s + \psi_s^3 - \partial_{xx}\psi_s + a\cos(qx) \right] + v\partial_x\psi_s = 0. \tag{63}$$

Equation (63) can be integrated twice. Using the periodicity of ψ_s an integration of the resulting equation with respect to the interval $(0, 2\pi/q)$ gives

$$aq \int_0^{2\pi/q} \sin(qx)\psi_s(x)\mathrm{d}x - v \int_0^{2\pi/q} \psi_s^2(x)\mathrm{d}x = 0. \tag{64}$$

Clearly, the maximum velocity v_{ex}, at which the periodic solution ψ_s still exists, corresponds to the solution which is shifted by $\pi/2$ with respect to the forcing, i.e., for $\psi_s \sim \sin(qx)$.

The linear stability analysis of periodic solutions $\psi_s(x)$ of (63) with respect to small perturbations have been performed numerically (see [122] for details). It has been found that the solutions A_2 and A_3 are again always unstable, whereas the A_1-solution can be stable in a certain range of the parameters. For given values of ε and q the modulation amplitude a has to exceed a certain value $a_s(q)$ (see Fig. 20) to stabilize the A_1-solution. If the traveling velocity v is smaller than a critical velocity $v_{\mathrm{c}}(\varepsilon, a, q)$, the A_1 solution remains stable. The critical velocity $v_{\mathrm{c}}(\varepsilon, a, q)$ is given by the solid line in Fig. 21 and for $v > v_{\mathrm{c}}(\varepsilon, a, q)$ the spatially periodic solution is linearly unstable. The onset of instability occurs for small values of the Floquet exponent $s \to 0$, i.e., it belongs to a long-wave perturbation as in the case of $v = 0$. In Fig. 21 the boundary of the existence range of periodic solutions $v_{\mathrm{ex}}(\varepsilon, a, q)$ is also shown as obtained approximately from (64) (dashed line) and by a full numerical simulation (dotted line). Since the stability boundary (solid line) always lies below v_{ex}, the periodic solution always becomes unstable before the existence range is reached.

The temporal evolution of $\psi(x,t)$ in the laboratory frame, as described by (61) in the 1D case, is shown in Fig. 22 for three regimes of the traveling forcing starting with the initial condition $\psi = 0$ and superimposed with small-amplitude noise. In Fig. 22a the velocity is sufficiently small and belongs to the range where the

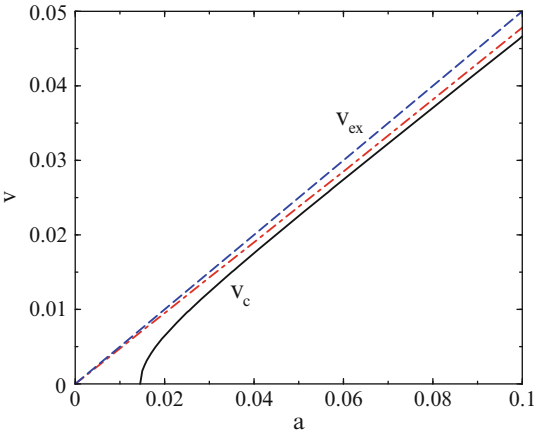

Fig. 21 Above the *solid line* the spatially periodic solution is unstable. The *dashed line* marks the existence boundary above which the spatially periodic solution does not exist due to the criterion given by (64). The *dot-dashed* curve marks the existence boundary obtained numerically from (63). The parameters are $\varepsilon = 1$ and $q = 0.5$

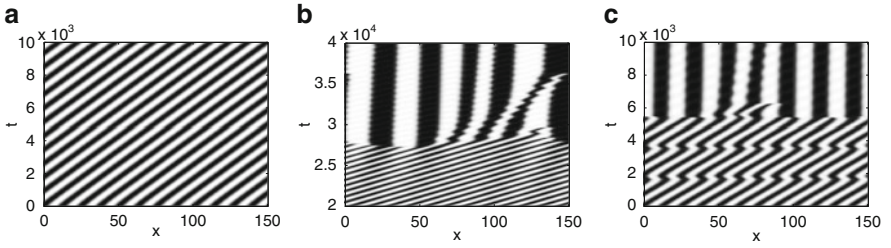

Fig. 22 Temporal evolution of phase separation for $v = 0.015 < v_c$ (**a**), $v_c < v = 0.0185 < v_{ex}$ (**b**), and $v = 0.02 > v_{ex}$ (**c**). The other parameters are $\varepsilon = 1$, $q = 0.5$, and $a = 0.04$. Figure from [122]. Reprinted with permission by Springer

solution is locked to the traveling forcing. In Fig. 22b the velocity is chosen in the range $v_c < v < v_{ex}$, where the solution locked to the traveling forcing still exists, but where it is linearly unstable. In this parameter range the solution is locked during the initial period of phase separation before coarsening takes over. In Fig. 22c the temporal evolution of phase separation is shown for $v > v_{ex}$, where the locked solution does not exist anymore. At this velocity an interesting pinning-depinning behavior can be observed during the initial stage of phase separation. One still has a traveling periodic solution with the same wave number as the forcing but with a velocity smaller than the velocity of the forcing. Due to the velocity mismatch, the phase shift between the solution and the forcing is slowly increased before it reaches about half of the forcing period. From that moment the periodic solution practically stops moving (pinning) until the forcing shifts over the next half of the period. After that, the solution starts moving again (depinning) and the process repeats itself a few times. Later on the wavelengths of the solution and the forcing become different and the coarsening takes place.

6.3 Periodic Patterns in 2D

In two spatial dimensions phase separation can become more complex due to additional degrees of freedom and their consequences are investigated by extended simulations of (53) in two spatial dimensions. We have characterized the simulated patterns by the structure factor

$$S(\mathbf{k},t) = |\hat{\psi}(\mathbf{k},t)|^2, \;\; \hat{\psi}(\mathbf{k},t) = \int \mathrm{d}\mathbf{r} e^{\mathrm{i}\mathbf{k}\cdot\mathbf{r}} \psi(\mathbf{r},t), \tag{65}$$

which can also be measured experimentally and allows direct comparison between experimental and theoretical results. For the unforced case (standard Cahn–Hilliard equation) the structure factor is isotropic $S = S(|\mathbf{k}|,t)$ and possesses at long times the universal scaling behavior $S(k,t) \sim l(t)^d G[kl(t)]$, where the characteristic length

of the domains evolves in time as $l(t) \sim t^{1/3}$ (for $d \geq 2$) [123]. By the spatially periodic forcing the rotational symmetry is broken in the plane and one may expect an anisotropy of the structure factor. The average domain length in the x and y directions can be related to the characteristic length scales

$$l_x(t) = [\langle k_x \rangle(t)]^{-1}, \;\; l_y(t) = [\langle k_y \rangle(t)]^{-1}, \tag{66}$$

where

$$\langle k_x \rangle(t) = \frac{\int \mathrm{d}k_x S(k_x, 0, t) k_x}{\int \mathrm{d}k_x S(k_x, 0, t)}, \;\; \langle k_y \rangle(t) = \frac{\int \mathrm{d}k_y S(0, k_y, t) k_y}{\int \mathrm{d}k_y S(0, k_y, t)}. \tag{67}$$

Numerical simulations of (53) were performed using a central finite difference approximation of the spatial derivatives with fourth order Runge–Kutta integration of the resulting ordinary differential equations in time. The typical system size was $L_x = L_y = 256$. Some test runs were made with $L_x = L_y = 512$ and 1,024. We used a uniform mesh size $\delta x = \delta y = 1$ and time step $\delta t = 2 \times 10^{-2}$. The accuracy of the calculations was checked by choosing $\delta x = \delta y = 0.5$ and $\delta t = 2 \times 10^{-3}$. The dynamics of spinodal decomposition was computed over $6 - 7$ decades in time, which allows monitoring of the late stages of the phase separation process. Starting with random initial conditions with $|\psi| < 0.01$, the characteristic length dynamics was calculated by averaging over 100 runs.

Without driving ($a = 0$) one has the typical scenario of spinodal decomposition and there is no anisotropy in the behavior of l_x and l_y (Fig. 23). Thus, small perturbations grow exponentially and at about $t \sim 15$ (not shown) a nonlinear saturation of the fastest growing mode becomes important and sharp domain boundaries form. At about $t \sim 30$ the late stage coarsening starts and the well-known scaling $l_x \sim l_y \sim t^{1/3}$ is observed. In Fig. 24 snapshots of the phase separation process are presented for a particular run.

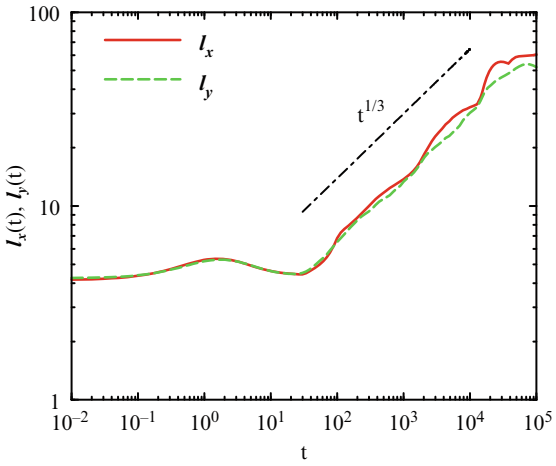

Fig. 23 Dynamics of the characteristic length scales $l_x(t)$ and $l_y(t)$ without forcing ($a = 0$). System size $L_x = L_y = 256$, $\varepsilon = 1$

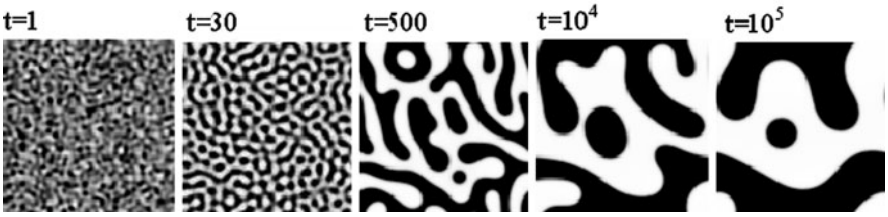

Fig. 24 Snapshots of the phase separation process. The same parameters as in Fig. 23

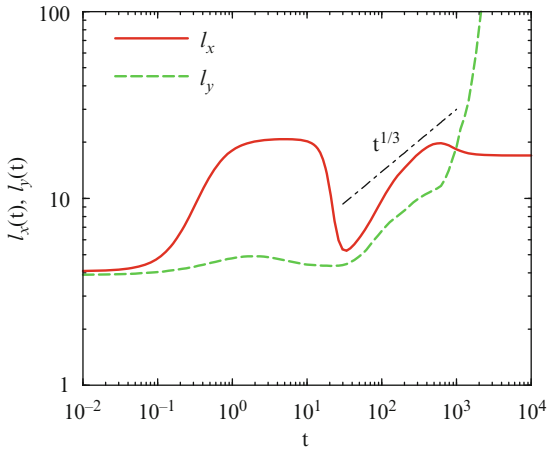

Fig. 25 Dynamics of the characteristic length scales $l_x(t)$ and $l_y(t)$ for the driving amplitude $a = 0.05$ well above the critical. System size $L_x = L_y = 256$, $\varepsilon = 1$, $q = 6\pi/L_x$

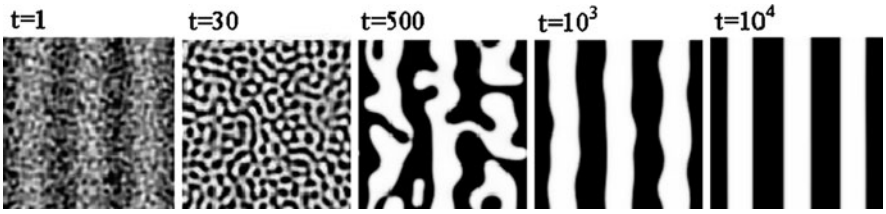

Fig. 26 Snapshots of the phase separation process. The same parameters as in Fig. 25

We have found that in the 2D case, similar to 1D, there exists a critical driving amplitude a_c above which the spinodal decomposition ends up in the stationary periodic solution: a striped structure with the period of the forcing. The critical amplitude turned out to be about three to five times larger than in the 1D case. In particular, for $q = 6\pi/L_x$ with $L_x = 256$ one has in 2D $a_c = 0.014$ whereas for 1D $a_c = 0.0045$. Thus, for 2D the upper curve in Fig. 20 moves slightly upward (the linear stability curve a_s remains unchanged).

In Fig. 25 the dynamics of the characteristic length scales l_x and l_y is presented for the case $a = 0.05 > a_c$. Typical snapshots are shown in Fig. 26. The peculiar nonmonotonic behavior of l_x at early times can be understood as follows: in the linear range the noise-initiated fastest mode grows exponentially as $\psi_0 \exp(t/4)$ and

the forced modulation with wave number q grows linearly as at (its exponential growth is small); see (53). Thus, shortly after the quench the fastest mode determines the average domain size. At a time $t_1 = (\psi_0/a)\exp(t_1/4) \sim \psi_0/a = 0.2$ there is a crossover, beyond which the anisotropy becomes strong and l_x reaches a plateau that is controlled by the wave number of the forcing. Eventually, beyond $t_2 = (\psi_0/a)\exp(t_2/4) \approx 18$, the exponential growth of the fastest mode wins, which leads to a drop of l_x. Although at this time nonlinearities are already noticeable, the suppression of the effect of the forcing remains. Subsequently there is essentially isotropic coarsening until l_x saturates at $1/q$. After this ($t > 500$) the ordering in the y direction becomes exponentially fast. The late stage remains basically unchanged if the forcing is turned on as late as $t \sim 80$, where the average domain size has reached half the driving period. At a later time a forcing amplitude $a = O(1)$ is needed to generate the periodic state.

In Figs. 27 and 28 we also show the dynamics of the characteristic length scales and snapshots for a driving amplitude slightly below the critical one. One can see that at $t \sim 10^3$ there is competition between the influence of the forcing and the coarsening process, which finally wins.

The situation considered here should be applicable to experiments on spinodal decomposition in sufficiently thin polymer films with small periodic temperature modulations created by means of an optical grating technique or by local laser

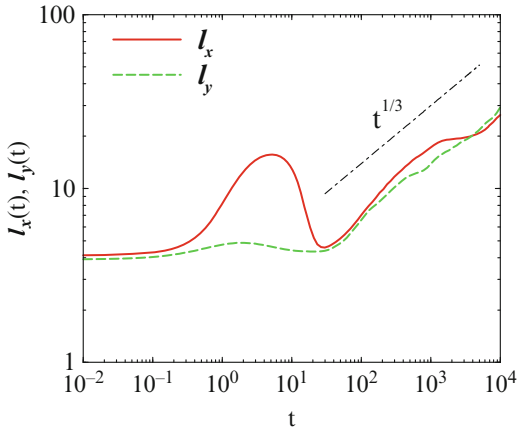

Fig. 27 Dynamics of the characteristic length scales $l_x(t)$ and $l_y(t)$ for the driving amplitude $a = 0.01$ slightly below the critical. System size $L_x = L_y = 256$, $\varepsilon = 1$, $q = 6\pi/L_x$

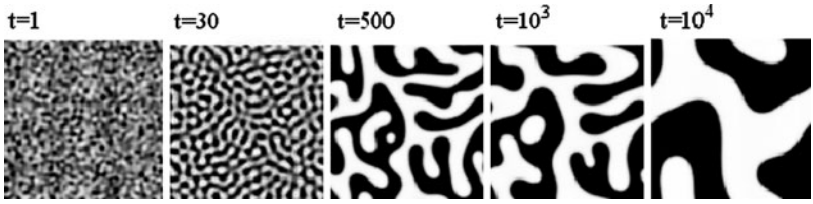

Fig. 28 Snapshots of the phase separation process. The same parameters as in Fig. 27

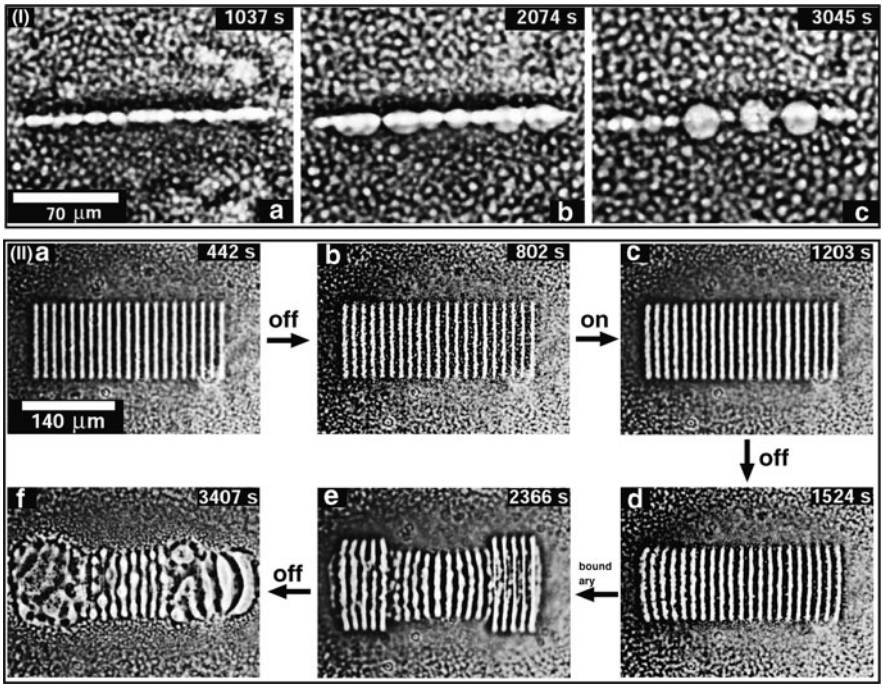

Fig. 29 Temporal evolution of one single line (I) (written from $t = 0\,\mathrm{s}$ until $t = 2,074\,\mathrm{s}$ at 1.3 K below T_c, laser-power 1 mW). 21 parallel lines (II) (written from $t = 0\,\mathrm{s}$ with 8 mW at 1.5 K below T_c; "on" and "off" refer to switching of the laser; "boundary" means that only the outermost lines are written in order to stabilize the central part of the pattern; see text for details)

heating. Then, for polymer blend layers of thickness less than a few micrometers, the temperature variation across the film can be neglected for sufficiently small under cooling. Figure 29(I) shows the time evolution of one single line written into a PDMS(16.4 kg mol^{-1})/PEMS (22.0 kg mol^{-1}) blend ($c = 0.512\,\mathrm{g/g}$, $T_c = 314.7\,\mathrm{K}$, $\alpha \approx 500\,\mathrm{m}^{-1}$, film thickness 100 µm) at a temperature 1.3 K below T_c and a laser power of 1 mW. The width of the laser focus is about 1.6 µm and the length of the line almost 140 µm. Obviously, it is not possible to write a stable line into the sample. After approximately 1,000 s surface tension effects lead to a pearling instability that eventually dominates the structure formation.

Figure 29(II) shows the result if multiple parallel lines are written instead of a single one. A grid pattern evolves with a period comparable to the length scale of the already coarsened spinodal pattern. This grid pattern is stable as long as the writing process continues (A). Turning the laser off for 360 s leads to a beginning degradation (B), but continued writing again stabilizes the imposed structure (C). After turning the laser off, some deformations due to bulging of the left- and rightmost grid lines is observable (D). Continued writing of only the outermost (longer) lines allows for a continued stabilization of the central grid pattern (E). After switching the laser off, surface tension takes over and all parallel lines eventually

decay into spherical structures. Although the patterns observed in these experiments show many similarities to the 2D simulations, we have not attempted a quantitative modeling because of the nonnegligible thickness of the polymer film, asking for a full 3D description.

7 Directional Quenching

With directional quenching we present an effective mechanism to induce periodic stripe patterns in phase separating systems, where the wavelength of the patterns is uniquely selected by the velocity of a quench interface. If an additional spatially periodic modulation of the quench interface is introduced, cellular patterns can also be generated.

For the description of phase separation we choose again the generic Cahn–Hilliard model in one spatial dimension [124, 125]

$$\partial_t \psi = \partial_{xx}(-\varepsilon\psi + \psi^3 - \partial_{xx}\psi), \tag{68}$$

where the real order parameter $\psi(x,t)$ is a measure for the difference of the concentration of one component from its value at the critical point and ε is the control parameter. Here, as in our first approach in [126], thermodiffusion effects are neglected.

Directional quenching is achieved by changing ε from a negative value at $x < x_q$ to a positive one for $x > x_q$, where the point $x_p(t)$ moves in the laboratory frame with the velocity v:

$$\varepsilon(x,t) = \begin{cases} -\varepsilon\ , x < -vt\ , \\ +\varepsilon\ , x > -vt\ . \end{cases} \tag{69}$$

By this moving jump of the control parameter the system is divided into a stable and an unstable region. Numerical simulations of the 1D model in (68) and with the directional quenching (69) show that a periodic solution develops behind the quench interface in the unstable region. Typical examples for large and small values of the

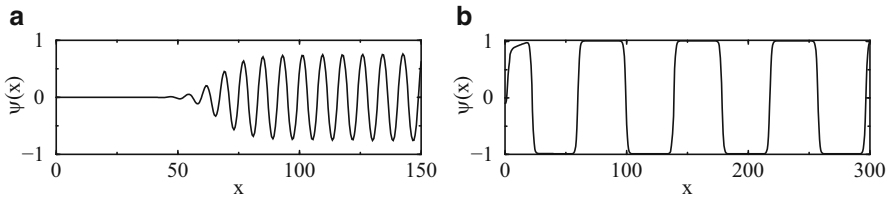

Fig. 30 Solutions of (68) for $\varepsilon = 1$ with the quench interface (69) in the comoving frame at $x = 0$ for $v = 2 > v^\star$ (**a**) and for $v = 0.02 \ll v^\star$ (**b**). Only part of the system of the total length $l_x = 4,096$ is shown [126]

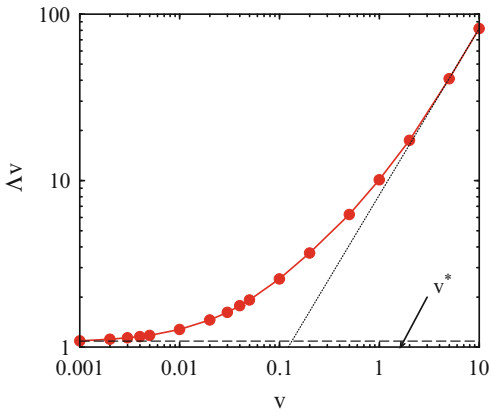

Fig. 31 Period of kink lattice $\Lambda = 2\pi/q$ multiplied by the velocity v of the quench interface as a function of v for $\varepsilon = 1$ (*solid circles* with a *solid line* as a guide to the eye); $v^\star = 1.622$ from (71). The *dashed line* corresponds to (72) [126]

velocity v of the quench interface are shown in Fig. 30. For v above some critical value $v^\star$, the periodic solution detaches from the moving quench interface and the wavelength of the solution becomes independent of v, cf. Fig. 30a. In contrast, for $v < v^\star$ the solution remains attached to the quench interface and the wavelength is uniquely determined by v. Decreasing v, the solution develops into a periodic kink lattice (sharp changes between $\psi = \pm\sqrt{\varepsilon}$), where new kinks are continuously generated at $x = x_q(t) = -vt$ (Fig. 30b). The period of the solution, Λ, turns out to be uniquely defined by the velocity of the quench interface, which is shown in Fig. 31. For $v \to 0$ one has $\Lambda \sim 1/v$, whereas for $v > v^\star$ one finds $\Lambda = 2\pi/q^\star$. Although the periodic solutions far away from the moving quench interface are in principle unstable against period doubling, the coarsening is extremely slow for patterns generated with $q \ll k_\mathrm{m}$ [see (70)]. Thus the extension L_p of the (quasi-ideal) periodic solution behind the quench interface can be estimated as $L_\mathrm{p} = v\Delta t_\mathrm{p} \approx v/\sigma_\mathrm{p}$, where σ_p is the growth rate of the unstable period doubling mode given as [114, 121]

$$\sigma_\mathrm{p} = \varepsilon^2 16 \exp(-2\pi k_\mathrm{m}/q)/(\pi k_\mathrm{m}/q). \tag{70}$$

The two limiting cases of large and small values of the velocity v of the quench interface can be determined analytically. For large v we consider, for instance, the initial condition $\psi = 0$ everywhere except a hump with $\psi > 0$ localized near $x = 0$. Then, the time evolution of this initial perturbation is governed by the motion of wave fronts to the left and to the right with a well-defined velocity $v^\star$ and wave number $q^\star$. These quantities can be calculated by a linear stability analysis of the leading edge of the front in the comoving frame [126]:

$$v^\star = \frac{\sqrt{7}+2}{3}\left(\frac{2}{3}(\sqrt{7}-1)\right)^{1/2}\varepsilon^{3/2}, \quad q^\star = \frac{3(\sqrt{7}+3)^{3/2}}{8\sqrt{2}(\sqrt{7}+2)}\varepsilon^{1/2}. \tag{71}$$

The phase velocity and the wave number of the propagating periodic solutions, as obtained from the numerical simulations of (68), are independent of v in the range $v > v^\star$ and agree perfectly with $v^\star$ and $q^\star$ as given by (71).

In the opposite limit ($v \to 0$) our starting point is a stationary solution of (68) for $v = 0$, interpolating between $\psi = 0$ at $x < 0$ and $\psi = \sqrt{\varepsilon}$ at $x > 0$. It is characterized by a sharp front at $x \approx 0$. If the quench interface according to (69) starts to move, the sharp front will follow at first. But since the spatial average $\langle\psi\rangle$ is conserved, regions with $\psi < 0$ have to be generated in the region $x > x_q$, which leads to the formation of a kink lattice (Fig. 30b). The kink-lattice formation can be understood in terms of a fast switching stage and slow pulling stage: first a new kink is generated in a short time at $x \approx x_q$. During the slow stage this kink is pulled by the quench interface whereby its amplitude and the distance to the next kink behind increase until it exceeds some limiting value, and then a new kink is generated. Repeating this process a regular kink lattice develops in the wake of the quench interface with the period Λ, which is uniquely determined by the velocity v of the moving quench interface (Fig. 31). The equilibrium period Λ can be calculated in the framework of a boundary layer problem that gives [126]

$$\Lambda = \frac{4\sqrt{6}}{9}\frac{\varepsilon}{v} \approx 1.088\frac{\varepsilon}{v}, \tag{72}$$

in perfect agreement with the results of numerical simulations in the limit $v \to 0$ (Fig. 31).

The generalization of the analysis to the off-critical quench, $\langle\psi\rangle \neq 0$, is straightforward and the expressions (71) for $v^\star$ and $q^\star$ hold with the replacement $\varepsilon \to \varepsilon - 3\langle\psi\rangle^2$. In the limit $v \to 0$ the distance λ_+ between two kinks in the range $\psi > 0$ becomes different from the kink-distance λ_- for $\psi < 0$. We find $\lambda_+ - \lambda_- = \langle\psi\rangle\Lambda/\sqrt{\varepsilon}$ and for the resulting period Λ of the kink lattice,

$$\Lambda \equiv \lambda_+ + \lambda_- = \frac{2}{v}\left[2\frac{\sqrt{6}}{9}\varepsilon + (8 - 25\frac{\sqrt{6}}{9})\langle\psi\rangle^2\right]. \tag{73}$$

Similar to the case $\langle\psi\rangle = 0$, we have confirmed the results in (73) by numerical simulations of (68) for $\langle\psi\rangle \neq 0$ in the limit $v \to 0$.

Let us now consider the 2D case $\psi(x,y,t)$, where we numerically study the 2D version of the CH equation (68):

$$\partial_t\psi = \nabla^2(-\varepsilon\psi + \psi^3 - \nabla^2\psi) \tag{74}$$

with the moving quench interface (69). Zero flux boundary conditions have been used at $x = 0, l_x$ and periodic boundary conditions at $y = 0, l_y$. Initially the quench interface is located at $x_q = l_x$, moving from right to left. The system size was $l_x = 512$, $l_y = 256$, and we start with the homogeneous solution $\psi = \langle\psi\rangle$ with small superimposed noise of the strength $\delta\psi$ where $\delta\psi \ll \sqrt{\varepsilon}$ and $\delta\psi \ll \langle\psi\rangle$. Thus the well-known Ginzburg criterion, necessary for the validity of a mean-field descrip-

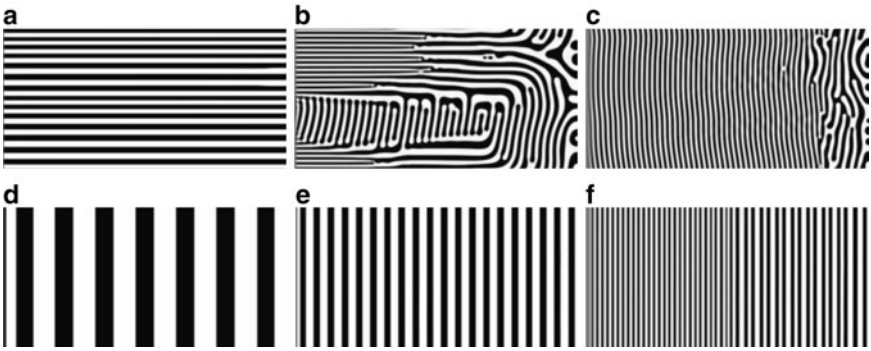

Fig. 32 Snapshots of the phase separation in 2D at the time when the quench interface (69) ($\varepsilon = 1$) almost reaches the left boundary. $\langle\psi\rangle = 0$: $v = 0.01$ (**a**), $v = 0.47$ (**b**), and $v = 1$ (**c**). $\langle\psi\rangle = 0.1$: $v = 0.02$ (**d**), $v = 0.1$ (**e**), and $v = 1$ (**f**)

tion of a phase separation process [5], is satisfied: in fact, the dynamics does not depend on the particular choice of $\delta\psi$.

In the case of the critical quench $\langle\psi\rangle = 0$, the orientation of the domains depends on the velocity of the quench interface (Fig. 32a–c). At small v, periodic patterns with domains perpendicular to the quench interface are formed (Fig. 32a). Then, for v above $v_c \approx 0.45$, the 1D stripe patterns parallel to the quench interface appear (Fig. 32b–c). Finally, $v > v^\star$ eventually leads to irregular patterns similar to the case of a spatially homogeneous quench.

In contrast, for the off-critical quench ($\langle\psi\rangle \neq 0$ when $v < v^\star$) regular stripe patterns with domains parallel to the quench interface were always found (Fig. 32d–f). This situation is covered by a 1D analysis presented before where the period of the structure is uniquely determined by the velocity of the quench interface. In the limit $v \to 0$ the periods of the patterns found in our numerical simulations agree with (73). For $v > v^\star$ irregular coarsening patterns, similar to the case of a spatially homogeneous quench, are observed.

Finally, we have studied the influence of a periodic modulation

$$\varepsilon(x,y,t) = \begin{cases} -\varepsilon\ , & x < l_x + a\cos(py) - vt\ , \\ +\varepsilon\ , & x > l_x + a\cos(py) - vt \end{cases} \tag{75}$$

of the quench interface. In the case of a critical quench we found that the velocity v_c at which the transition from perpendicular stripe patterns (Fig. 33a) to parallel ones (Fig. 33c) occurs depends on the modulation amplitude a. This dependence is very strong for values a of the order of the typical domain size at the initial stage of phase separation ($a \sim \lambda_m = \pi/k_m$). Furthermore, v_c decreases with decreasing modulation wavenumber p. For p smaller than the wavenumber k_m of the fastest growing mode, patterns with a cellular morphology forming behind the moving quench interface have been found (Fig. 33b).

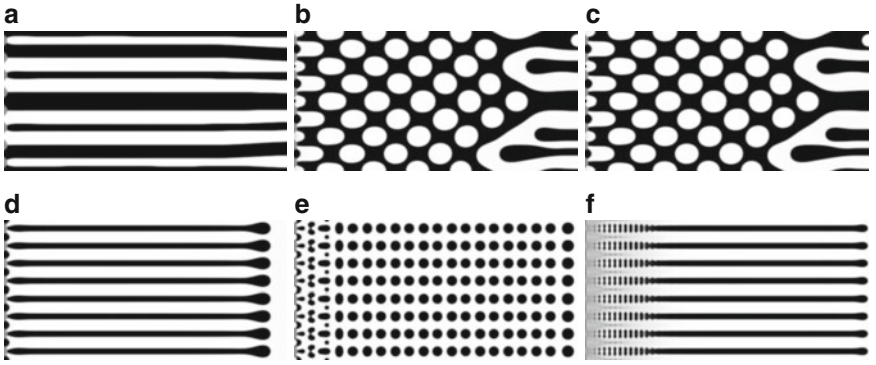

Fig. 33 Snapshots of the phase separation in 2D at the time when the modulated quench interface (75) ($\varepsilon = 1$, $a = 4$, $p = \pi/16$) almost reaches the left boundary. $\langle\psi\rangle = 0$: $v = 0.01$ (**a**), $v = 0.05$ (**b**), and $v = 1$ (**c**). $\langle\psi\rangle = 0.2$: $v = 0.05$ (**d**), $v = 0.2$ (**e**), and $v = 1$ (**f**)

In the case of an off-critical quench we found that $\langle\psi\rangle \neq 0$ favors the formation of regular cellular planforms (Fig. 33e) at intermediate velocities of the quench interface, in analogy to the transition from perpendicular to parallel stripes for $\langle\psi\rangle = 0$.

Thus, we have demonstrated that directional quenching in the CH model leads to the formation of periodic solutions with the wavelength uniquely selected by the velocity of the quench interface. Controlling phase separation by directional quenching turns out to be a promising tool to create regular structures in material science. Although in principle slow coarsening cannot be avoided by directional quenching, long lived periodic patterns can be "frozen in", e.g., by a deep quench, induced polymerization, or chemical crosslinking.

8 Summary and Conclusions

For critical and off-critical PDMS/PEMS polymer blends with an upper critical solution temperature UCST T_c we investigated the coupling between an inhomogeneous temperature field and the order parameter, describing the local composition. In the asymptotic critical regime close to T_c, for $\varepsilon = (T - T_c)/T_c < 0.02$, the system belongs to the 3D Ising universality class. Further away from the critical point, for $\varepsilon > 0.02$, there is a crossover to the classical mean field behavior. Since the employed transient holographic grating technique works at significantly smaller q-values than typically encountered in PCS, the asymptotic critical scaling law of the diffusion coefficient D could be observed much closer to T_c without a conflict between the increasing correlation length ξ and the length scale defined by q^{-1}. A consistent description of D over a broad temperature range is based on a crossover model developed by Jacob and Kostko with an activation energy of the viscosity determined from the temperature dependence of the thermal diffusion coefficient D_T (Fig. 3). The thermal diffusion coefficient D_T shows no critical slowing down and its

temperature dependence can be described by a simple Arrhenius law with identical activation energies both for critical and off-critical mixtures. As a consequence of the insensitivity of D_T to the critical point and the critical slowing down of D, the Soret coefficient $S_T = D_T/D$ of a critical blend diverges on approach of T_c with an exponent of -0.67 in the asymptotic critical regime and with and exponent of -1, characteristic for the structure factor, in the mean field regime (Fig. 5).

Close to the critical point the mixture becomes very susceptible to external perturbations, and only moderate temperature gradients are sufficient to induce significant concentration changes. The highest Soret coefficients measured exceed the values typically found for mixtures of organic solvents, consisting of small molecules, by four to five orders of magnitude. The high susceptibility of the order parameter opens the possibility for writing almost arbitrary composition patterns into a polymer blend by heating with a focused laser beam that can be scanned across the sample. These patterns can then be visualized by phase contrast or differential interference contrast microscopy. Because of the excursions along both the temperature and the concentration axes, a full numerical model requires as input the knowledge of both diffusion coefficients D and D_T over the entire concentration and temperature range of the homogeneous phase. The measured data have been interpolated within the framework of the pseudo-spinodal concept. These data are shown in Fig. 8, and PDMS/PEMS is up to now the only polymer blend where these coefficients are available not only for a critical composition but also for the entire one-phase regime.

Numerical modeling shows that very sharp and localized structures are formed during the initial linear growth regime, although the driving temperature profile has already reached its broadened stationary shape. This at first sight surprising effect can be rationalized by recalling that the evolution of the concentration profile is driven by the Laplacian of $T(\mathbf{r},t)$ rather than the temperature itself. At later times, solutal convection largely exceeds thermal convection and leads to asymmetric vertical cross sections of the patterns even for only 100 µm thick samples (Fig. 12).

The coupling of the order parameter to the temperature gradient also leads to unexpected excursions along the concentration axis in the case of off-critical mixtures. As a consequence, equilibrium phase diagrams lose their usual meaning in thermal nonequilibrium situations, and even an off-critical blend with a temperature above the binodal can be quenched into phase separation by local heating with a laser beam.

After crossing the spinodal from the homogeneous into the two-phase regime, spinodal decomposition sets in and leads to characteristic bicontinuous spinodal patterns with a characteristic length scale that growths during the coarsening stage. The strong Soret effect can not only be utilized to write composition patterns within the homogeneous phase but also opens a route for a controlled local manipulation of the spinodal decomposition patterns below T_c (Fig. 18). After switching the writing laser off, such an enforced perturbation freely evolves in time in competition with the coarsening dynamics of the unperturbed spinodal pattern.

Theoretically we have employed a generalized Cahn–Hilliard model to describe the effects of stationary and traveling spatially periodic temperature-modulations

as well as the effects of moving quench interfaces on spinodal decomposition in binary fluid mixtures and polymer blends. In several phase separating systems, such as the polymer blends investigated experimentally in this work, thermodiffusion plays an important role in the presence of inhomogeneous temperature distributions. Since the model takes thermal diffusion into account, we were able to reproduce the essential features of spatio-temporal dynamics observed in experiments on thermal patterning of polymer blends in the two-phase regime.

In such systems, spatial temperature modulations may cause, via the thermodiffusion effect, concentration modulations in the composition of the polymer blend already above the critical temperature. If the mean temperature crosses the critical temperature from above, phase separation sets in. However, a spatially periodic temperature modulation changes the phase separation process in polymer blends considerably.

If the modulation amplitude of the temperature exceeds a critical value, the spatially periodic forcing interrupts phase separation and the periodicity of the concentration modulation is locked to the wavelength of the temperature modulation. In the case of a traveling temperature modulation, the critical modulation amplitude required for locking the concentration modulation with respect to external forcing depends on the traveling velocity. In a certain parameter range one observes transient locking phenomena of the concentration modulations with respect to the external forcing. If the modulation amplitude is smaller than the critical one, the coarsening processes may be accelerated considerably by traveling temperature modulations in the two-phase regime.

For systems where thermodiffusive effects can be neglected, we have presented results on the effects of directional quenching where the control parameter jumps the critical temperature from above to below and where the location of the jump is moved with a finite velocity v. We have shown how, by this method, regular structures are created during the process of phase separation behind the moving quench interface. Moreover, it was shown that the wavelength of periodic stripe patterns is uniquely selected by the velocity of the quench interface. If an additional spatially periodic modulation of the quench interface is introduced, cellular patterns can also be generated.

Acknowledgements We thank G. Meier and I. Alig for inspiring discussions and T. Wagner and G. Meier for providing part of the samples. The theoretical part of this work was originally initiated by L. Kramer (†). Essential parts of the work have been performed during the PhD theses of W. Enge, A. Voit, M. Hartung and F. Schwaiger and the diploma theses of S. Frank and V. Weith. The work was supported by the Deutsche Forschungsgemeinschaft via the Collaborative Research Center SFB481.

References

1. Sengers JV (1976) Ber Bunsenges Phys Chem 76:234
2. Siggia ED, Halperin BI, Hohenberg PC (1976) Phys Rev B 13:2110
3. Hohenberg PC, Halperin BI (1977) Rev Mod Phys 49:435

4. Binder K (1994) Adv Polym Sci 112:181
5. Binder K (1983) J Chem Phys 79:6387
6. Sato H, Kuwahara N, Kubota K (1994) Phys Rev E 50:R1752
7. Theobald W, Meier G (1995) Phys Rev E 51:5776
8. Meier G, Momper B, Fischer EW (1992) J Chem Phys 97:5884
9. Mayer W, Hoffmann S, Meier G, Alig I (1997) Phys Rev E 55:3102
10. Eckert S, Meier G, Alig I (2002) Phys Chem Chem Phys 4:3743
11. Eckert S, Hoffmann S, Meier G, Alig I (2002) Phys Chem Chem Phys 4:2594
12. Eckert-Kastner S, Meier G, Alig I (2003) Phys Chem Chem Phys 5:3202
13. Mao H, Li C, Zhang Y, Bergbreiter DE, Cremer PS (2003) J Am Chem Soc 125:2850
14. Yamamura M, Nakamura S, Kajiwara T, Kage H, Adachi K (2003) Polymer 44:4699
15. Jasnow D, Viñals J (1996) Phys Fluids 8:660
16. Lee KWD, Chan PK, Feng X (2002) Macromol Theory Simul 11:996
17. Lee KWD, Chan PK, Feng X (2003) Macromol Theory Simul 12:413
18. Kolodner P, Williams H, Moe C (1988) J Chem Phys 88:6512
19. Königer A, Meier B, Köhler W (2009) Philos Mag 89:907
20. Debuschewitz C, Köhler W (2001) Phys Rev Lett 87:055901
21. Wittko G, Köhler W (2005) J Chem Phys 123:014506
22. Artola PA, Rousseau B (2007) Phys Rev Lett 98:125901
23. Kita R, Kircher G, Wiegand S (2004) J Chem Phys 121:9140
24. Wittko G, Köhler W (2007) Europhys Lett 78:46007
25. Iacopini S, Rusconi R, Piazza R (2006) Eur Phys J E 19:59
26. Piazza R, Iacopini S, Triulzi B (2004) Phys Chem Chem Phys 6:1616
27. Stadelmaier D, Köhler W (2008) Macromolecules 41:6205
28. Zhang M, Müller-Plathe F (2006) J Chem Phys 125:124903
29. de Gans BJ, Kita R, Wiegand S, Luettmer-Strathmann J (2003) Phys Rev Lett 91:245501
30. Schimpf ME, Giddings JC (1989) J Polym Sci B Polym Phys 27:1317
31. Rossmanith P, Köhler W (1996) Macromolecules 29:3203
32. Ryskin A, Müller HW, Pleiner H (2003) Phys Rev E 67:046302
33. Luettmer-Strathmann J (2003) J Chem Phys 119:2892
34. Lenglet J, Bourdon A, Bacri JC, Demouchy G (2002) Phys Rev E 65:031408
35. Hoffmann B, Köhler W, Krekhova M (2003) J Chem Phys 118:3237
36. Piazza R, Guarino A (2002) Phys Rev Lett 88:208302
37. Braun D, Libchaber A (2002) Phys Rev Lett 89:188103
38. Dhont JKG, Briels WJ (2008) Eur Phys J E 25:61
39. Dhont JKG, Wiegand S, Duhr S, Braun D (2007) Langmuir 23:1674
40. Dhont JKG (2004) J Chem Phys 120:1642
41. Dhont JKG (2004) J Chem Phys 120(3):1632
42. Thomaes G (1956) J Chem Phys 25:32
43. Giglio M, Vendramini A (1975) Phys Rev Lett 34:561
44. Wiegand S, Köhler W (2002) In: Köhler W, Wiegand S (eds) Thermal nonequilibrium phenomena in fluid mixtures. Springer, Heidelberg, p 189
45. Pohl DW (1980) Phys Lett A 77:53
46. Buil S, Delville JP, Freysz E, Ducasse A (1998) Opt Lett 23:1334
47. Delville JP, Lalaude C, Ducasse A (1999) Physica A 262:40
48. Cross MC, Hohenberg PC (1993) Rev Mod Phys 65:851
49. Bray AJ (1994) Adv Phys 43:357
50. Vörös J, Blättler T, Textor M (2005) MRS Bull 30:202
51. Sirringhaus H (2005) Adv Mater 17:2411
52. Hashimoto T, Matsuzaka K, Moses E, Onuki A (1996) Phys Rev Lett 74:126
53. Chen Z, Kornfeld J, Smith S, Grothaus J, Satkowski M (1997) Science 277:1248
54. Jayalakshmi Y, Khalil B, Beysens D (1992) Phys Rev Lett 69:3088
55. Böltau M, Walheim S, Mlynek J, Krausch G, Steiner U (1998) Nature 391:877
56. Hashimoto T, Bodycomb J, Funaki Y, Kimishima K (1999) Macromolecules 32:952
57. Sigel R, Fytas G, Vainos N, Pispas S, Hadjichristidis N (2002) Science 297:66

58. Loppinet B, Somma E, Vainos N, Fytas G (2005) J Am Chem Soc 127:9678
59. Lee BP, Douglas JF, Glotzer SC (1999) Phys Rev E 60:5812
60. Kelly RE, Pal D (1978) J Fluid Mech 86:433
61. Lowe M, Gollub JP, Lubensky T (1983) Phys Rev Lett 51:786
62. Coullet P, Huerre P (1986) Physica D 23:27
63. Coullet P, Walgraef D (1989) Europhys Lett 10:525
64. Zimmermann W, Ogawa A, Kai S, Kawasaki K, Kawakatsu T (1993) Europhys Lett 24:217
65. Hartung G, Busse FH, Rehberg I (1991) Phys Rev Lett 66:2742
66. Zimmermann W, Schmitz R (1996) Phys Rev E 53:R1321
67. Schmitz R, Zimmermann W (1996) Phys Rev E 53:5993
68. Lin AL, Bertram M, Martinez K, Swinney HL, Ardelea A, Carey GF (2000) Phys Rev Lett 84:4240
69. Utzny C, Zimmermann W, Bär M (2002) Europhys Lett 57:113
70. Miguez DG, Nicola EM, Munuzuri AP, Casademunt J, Sagues F, Kramer L (2004) Phys Rev Lett 93:048303
71. Schuler S, Hammele M, Zimmermann W (2004) Eur Phys J B 42:591
72. Rüdiger S, Miguez DG, Munuzuri AP, Sagués F, Casademunt J (2003) Phys Rev Lett 90:128301
73. Rüdiger S, Nicola EM, Casademunt J, Kramer L (2007) Phys Rep 447:028302
74. Tanaka H, Sigehuzi T (1995) Phys Rev Lett 75:874
75. Kumaki J, Hashimoto T, Granick S (1996) Phys Rev Lett 77:1990
76. de Groot SR, Mazur P (1984) Non-equilibrium thermodynamics. Dover, New York
77. Landau LD, Lifshitz EM (1987) Fluid mechanics. Pergamon, Oxford
78. Hartung M (2007) A detailed treatment of the measurement of transport coefficients in transient grating experiments. Ph.D. thesis, University of Bayreuth
79. Luettmer-Strathmann J (2002) In: Köhler W, Wiegand S (eds) Thermal nonequilibrium phenomena in fluid mixtures. Springer, Heidelberg, p 24
80. de Gennes PG (1979) Scaling concepts in polymer physics. Cornell University Press, London
81. Enge W, Köhler W (2004) Phys Chem Chem Phys 6:2373
82. Enge W, Köhler W (2004) Chem Phys Chem 5:393
83. Schwahn D, Meier G, Mortensen K, Janßen S (1994) J Phys II France 4:837
84. Enders S, Stammer A, Wolf B (1996) Macromol Chem Phys 197:2961
85. Thyagarajan K, Lallemand P (1978) Opt Commun 26:54
86. Köhler W (1993) J Chem Phys 98:660
87. Wittko G, Köhler W (2003) Philos Mag 83:1973
88. Köhler W, Rossmanith P (1995) J Phys Chem 99:5838
89. Kador L, Bausinger R, Leopold A, Haarer D, Köhler W (2004) J Phys Chem A 108:1640
90. Hartung M, Köhler W (2005) Eur Phys J E 17:165
91. Enge W (2004) Thermodiffusion in polymermischungen. Ph.D. thesis, University of Bayreuth
92. Sato H, Kuwahara N, Kubota K (1996) Phys Rev E 53:3854
93. Kawasaki K (1970) Ann Phys 61:1
94. Jakob J, Anisimov MA, Sengers JV, Dechabo V, Yudin IK, Gammon RW (2001) Appl Optics 40:4160
95. Kostko AF, Anisimov MA, Sengers JV (2002) Phys Rev E 66:020803
96. Folk R, Moser G (1998) Phys Rev E 58:6246
97. Enge W, Köhler W (2004) Eur Phys J E 15:265
98. J Rauch, Köhler W (2005) Macromolecules 38:3571
99. Nakayama H, Sugihara O, Okamoto N (2006) Appl Phys Lett 71(14):1924
100. Voit A, Krekhov A, Köhler W (2007) Phys Rev E 76:011808
101. Chu B, Schoenes FJ, Fisher ME (1969) Phys Rev 185:219
102. Beyer R (1977) Handbuch der Mikroskopie, 2nd edn. VEB Verlag Technik, Berlin
103. Born M, Wolf E (1998) Principles of optics. Cambridge University Press, New York
104. Bellair CJ, Curl CL, Allman BE, Harris PJ, Roberts A, Delbridge LMD, Nugent KA (2004) J Microsc 214:62

105. Voit A (2007) Photothermische strukturierung binärer Polymermischungen. Ph.D. thesis, University of Bayreuth
106. Meier G, Vlassopoulos D, Fytas G (1995) Europhys Lett 30:325
107. Rauch J, Hartung M, Privalov AF, Köhler W (2007) J Chem Phys 126:214901
108. Hartung M, Rauch J, Köhler W (2006) J Chem Phys 125:214904
109. Rauch J, Köhler W (2003) J Chem Phys 119:11977
110. Rauch J, Köhler W (2002) Phys Rev Lett 88:185901
111. Schwaiger, F (2009) unpublished results
112. Voit A, Krekhov A, Köhler W (2007) Macromolecules 40:9
113. Meredith JC, Karim A, Amis EJ (2000) Macromolecules 33:5760
114. Krekhov AP, Kramer L (2004) Phys Rev E 70:061801
115. Bates FS, Wignall GD, Koehler WC (1985) Phys Rev Lett 55:2425
116. de Gennes PG (1980) J Chem Phys 72:4756
117. Pincus P (1981) J Chem Phys 75:1996
118. Guenoun P, Gastaud R, Perrot F, Beysens D (1987) Phys Rev A 36:4876
119. Voit A, Krekhov A, Enge W, Kramer L, Köhler W (2005) Phys Rev Lett 94:214501
120. Hammele M, Zimmermann W (2006) Phys Rev E 73:066211
121. Langer JS (1971) Ann Phys (N.Y.) 65:53
122. Weith V, Krekhov A, Zimmermann W (2009) Eur Phys J B 67:419
123. Gunton JD, San Miguel M, Sahni PS (1983) Phase transitions and critical phenomena, vol. 8. Academic, London
124. Cahn JW, Hilliard JE (1958) J Chem Phys 28:258
125. Cahn JW, Hilliard JE (1959) J Chem Phys 31:688
126. Krekhov A (2009) Phys Rev E 79:035302(R)

Adv Polym Sci (2010) 227: 199–252
DOI:10.1007/12_2009_32

Published online: 22 December 2009

Foaming of Microstructured and Nanostructured Polymer Blends

Holger Ruckdäschel, Peter Gutmann, Volker Altstädt, Holger Schmalz, and Axel H.E. Müller

Abstract Foaming of multiphase blend systems can be identified as a promising approach to satisfy the steadily growing demand for cellular materials with enhanced properties. However, combining the sophisticated fields of polymer blends and polymer foams not only offers great chances, but also poses a significant challenge, as the multiphase characteristics of blends and the complexity of foam processing need to be taken into account. Therefore, the foaming behavior of polymer blends is systematically analyzed, correlating the blend structure and the physical characteristics of reference systems to their foam processability and resulting foam morphology. The cellular materials are prepared via batch-foam processing, using carbon dioxide as a blowing agent. Starting with an immiscible poly(2,6-dimethyl-1,4-phenylene ether)/poly(styrene-*co*-acrylonitrile) blend, pathways to tailor the foaming behavior via controlling the micro- and nanostructure of such blends are developed; strategies aiming at reducing the cell size, enhancing the foam homogeneity, and improving the density reduction. As a result of adjusting the blend structure over multiple length scales, cooperative foaming of all blend phases and cell sizes down to several hundred nanometers can be achieved. In the light of the results presented, a general understanding of foaming multiphase blends is developed and guidelines for the selection of blend systems suitable for foaming can be deduced.

Keywords Blend · Foam · Morphology · Compatibilization · Multiphase · Nanostructured

H. Ruckdäschel (✉), P. Gutmann, and V. Altstädt
Department of Polymer Engineering, University of Bayreuth, 95447 Bayreuth, Germany
(*Present address* H. Ruckdäschel: BASF SE, Polymer Research-GKE/T, Ludwigshafen, Germany, e-mail: holger.ruckdaeschel@basf.com)

H. Schmalz and A.H.E. Müller
Department of Polymer Engineering, University of Bayreuth, 95447 Bayreuth, Germany

Contents

1 Introduction

The term foam is defined as a gaseous void surrounded by a much denser continuous matrix, generally a liquid or a solid phase. As a result of the distinct characteristics of the two phases, such cellular materials are able to feature unique properties. Since nature successfully demonstrated their use in manifold examples, such as bones, wood, plant stalks, cork, and sponges, foams have also sparked interest for technical application. Nowadays, a broad range of cellular materials based on metals, ceramics as well as polymers, is readily available, and their structures are as versatile as their applications.

In the early 1930s, the first synthetic polymer foams based on polystyrene (PS) mark the beginning of the era of cellular polymers. Thenceforward, foaming of polymers has evolved into a highly sophisticated field, both from the technological and scientific points of view. As a result, today's foams are able to cover a wide range of applications. Their use as light-weight materials is a prominent example, e.g., allowing the reduction of consumption of fossil fuels in transportation. Other applications aim at exploiting their peculiar physical characteristics, such as low thermal conductivity for heat insulation, good acoustical insulation, and damage-absorbing behavior. Moreover, foams are also used for even more special

applications, e.g., open-porous membranes or sensors. The success of cellular polymers is also reflected in their market volume, which already exceeds bulk polymers when regarding the volume-based consumption.

Foamed plastics can be classified in different ways, for instance by their nature (flexible vs. rigid), chemical composition of the matrix, density, cell size, cell structure (open-celled vs. closed-celled), processing method, and dimensions. It is the aimed combination of these properties that determines the final application of the cellular polymer. As an example, open-celled ultra-low density foams are highly desirable for acoustical insulation, while rigid foams with closed-cells and elevated densities are preferred as load-carrying core materials in composite materials.

As the properties of cellular polymers are closely linked to their structure and density, the development of advanced foams aims at controlling the cell size over multiple length scales down to the nanocellular regime, establishing novel polymeric matrices, adjusting the foam density as well as their open-celled content, and introducing enhanced processing methods. For instance, nanocellular polymers promise a significant reduction in thermal conductivity and an improvement in toughness, factors of relevance for thermal insulation as well as light-weight and tough constructions.

In the light of steadily increasing requirements to the foam performance and functionality, advanced processing routes as well as novel material systems are strongly demanded. Here, exploiting and the knowledge of blending polymers, as an efficient and well-established route to develop materials with tailored properties, is highly attractive. Foaming of multiphase polymer blends, in particular, can be identified as a topic of significant potential interest, both from the scientific and commercial points of view. As an example, the multiphase characteristics promise to tailor the mechanical performance, e.g., via integrating stiffer or tougher phases within the cell walls (Fig. 1). In a similar manner, barrier materials can potentially be formed by adding a low-permeable, highly oriented blend phase into the cellular structure. However, understanding and controlling the foaming behavior of such complex systems is an absolute must for developing novel cellular materials.

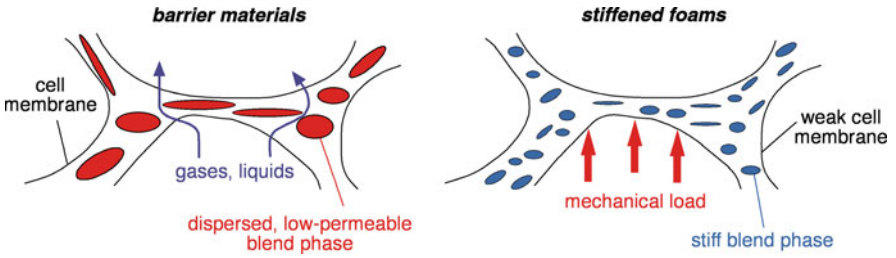

Fig. 1 Enhanced mechanical performance and barrier properties of cellular materials, as examples for the potential of foaming multiphase blends

1.1 Foaming of Blend Systems: An Overview

Notwithstanding the capability to develop new classes of polymer foams, the literature dealing with the foaming of blends is still limited. While foam processing in general has gained a significant technical and scientific sophistication, and the principles controlling the foaming behavior are fairly well understood, most commercial thermoplastic foams are still based on a limited number of polymers such as PS, polyvinylchloride, polyethylene (PE), and polypropylene (PP) [1].

Although the overall number of reviewed scientific contributions on this topic is rather low, an interesting trend has been detected within the last few years (Fig. 2). It appears, as foaming of blends sparks growing interest, to relate to the chance of tailoring polymeric foams. In the following, the state-of-the-art of this topic will be summarized and the most significant publications as well as selected patents are briefly highlighted.

When analyzing the state-of-the-art of foaming blends, one can generally distinguish between one-phase (miscible) and multiphase blend systems. Similar to bulk polymers, understanding and tailoring miscible blend systems is significantly easier, while multiphase blends offer by far more opportunities and challenges. Some general approaches for improving and/or controlling the foaming behavior, both of miscible as well as for multiphase blends, are summarized in Fig. 3.

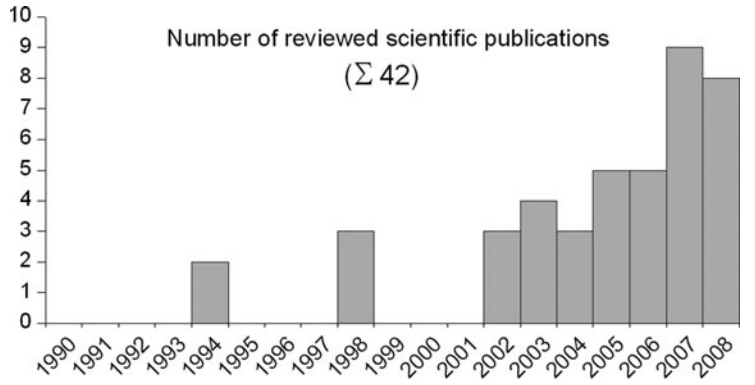

Fig. 2 Number of reviewed scientific papers on foaming thermoplastic blends published since 1990 (Source: ISI Web of Science)

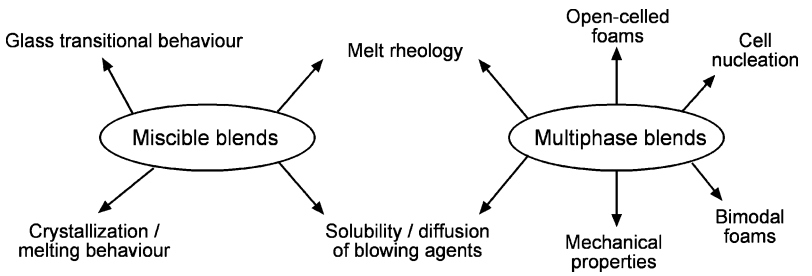

Fig. 3 General strategies for exploiting the blending approach in terms of foaming

1.1.1 Foaming of One-Phase (Miscible) Blends

With regard to miscible polymers, simple blending allows one to develop materials that frequently reveal an intermediate behavior between those of the individual blend components [2, 3]. Such systems can be easily exploited for fine-tuning the foamability, for example by controlling important foaming parameters such as the melt rheology or the gas solubility.

Blending of PPs with different architectures, i.e., linear and long-chain branched grades, is a prominent example for improving the foamability via controlling the melt-rheological behavior. As blending allows one to adjust the drawability as well as the strain-hardening behavior, the cell growth can be controlled and cell coalescence is reduced [4, 5], an approach recently transferred also to other polymers such as polycarbonate [6].

The concept of adding an amorphous component to a semicrystalline, otherwise poorly foamable polymer has been exploited both for blends of poly(methyl methacrylate)/poly(vinylidene fluoride) (PMMA)/(PVDF) as well as PMMA/PLA (poly(lactide acid)) [7, 8]. As a result of the semicrystalline nature – and in part of the low carbon dioxide solubility, both PVDF and PLA exhibit poor foaming behavior. In both cases, PMMA acts as a beneficial blend partner to reduce significantly the cell size and to enhance the foam homogeneity. These phenomena are mainly attributed to the increased gas solubility, the improved melt-rheological behavior, and the suppression of the melting point. Moreover, blending allows inhibiting of the crystallization process and thus shifts the upper limit of the processing window, determined by crystallization, to lower melt-temperatures. As a result, the difference between the processing and the glass transition temperature of the blend is reduced and, in combination with further factors, allows an enhanced control over the cell growth behavior and cell.

In a final example of foamed miscible blends, their potential use for adjusting the solubility behavior is highlighted. Krause et al. investigated the batch-foaming behavior of miscible, amorphous, high-temperature (HT) polymer blends of polysulfone/polyimide (PSU)/(PI) [9]. The carbon dioxide gas sorption capacity of the blends followed a linear rule-of-mixtures. As the content of the blowing agent and the foaming temperature are two factors identified as crucial for the transition from microcellular close-celled to nanocellular open-celled foams, blending allows one to adjust directly the foam structure.

1.1.2 Foaming of Multiphase Blends

While miscible blends can be easily exploited, multiphase blends pose a far greater challenge to control the cellular structure of polymers. Nevertheless, they offer the potential of combining the advantageous properties of each component within the foamed material, and of exploiting the multiphase characteristics for the foaming process. Analyzing the available but limited scientific literature on this topic, multiphase polymer blends have mainly been foamed for the following

purposes: (1) nucleation of foam cells, (2) reducing the foam density, (3) controlling the open-to-closed cell ratio, (4) enhancing the melt-rheological properties, and (5) adjusting the solubility and diffusivity of the blowing agent.

Cell nucleation is regarded as one of the key factors for foam processing, as it determines the cell size and in turn the final properties of the cellular polymer. Generally, high cell densities and small cell size distributions are often desirable [10]. For industrial processing, heterogeneous nucleation is preferred due to its simplicity and high reproducibility. Similar to inorganic, micron-sized materials, a second polymer phase can potentially act as heterogeneous nucleating agent in polymer matrices. As an example, Doroudiani et al. [11] reported a significantly reduced cell size via blending and batch-foaming of isotactic PP (iPP) and high-density PE (HDPE), an effect that was attributed to heterogeneous nucleation effects of foam cells at the interfacial regions. In a similar manner, further authors exploited the weak interfacial interaction and poor adhesion between nonmiscible polyolefin blends as highly effective nucleation sites [12–14].

Cavitation in the rubber particles of PS/high-impact PS (HIPS) was also identified as a heterogeneous nucleation site, using batch-foam processing [15, 16]. The experimentally observed cell densities as a function of the temperature, the rubber (HIPS) concentration, the rubber particle size, and saturation pressure were found to be in good agreement with the proposed nucleation model. Similar nucleation mechanisms of elastomeric particles were claimed for acrylic and di-olefinic latex particles in various thermoplastics [17, 18].

In search of easy dispersible nucleating agents with a high number of nucleants per volume, Spitael et al. [19] investigated the use of nanoscale diblock copolymer micelles on the batch-foaming behavior of PS. The diblock copolymers were composed of a PS block, and either PDMS, PEP, or PMMA as a second block. Several factors were identified as essential for nucleation, e.g., the size of the micelle and the surface tension of the micelle core material.

The size effect of the dispersed phase was also discussed by Han et al. [20, 21] for foaming polymer blends containing nanoparticles, more precisely PMMA/exfoliated montmorillonite (MMT) nanocomposites melt-blended within a PS matrix. Surprisingly, the cell size increased with a decreasing domain size of the dispersed PMMA/MMT phase, locations regarded as potential nucleation sites, a phenomena related to the interfacial and gas transport properties between PS and PMMA. The PMMA/MMT phase with its higher gas solubility acts as an internal gas reservoir. Subsequently, the transfer of carbon dioxide to the interface scales with the domain size of the PMMA/MMT phase, making larger PMMA/MMT domains more efficient for nucleation.

For developing ultra-low density polyolefin foams, blends of PE, a styrenic polymer or copolymer, and/or a PE copolymer allowed one to reduce the density to $10\,g\,l^{-1}$, using a hydrocarbon as blowing agent [22]. In a similar manner, the density of styrenic polymers was strongly reduced by the incorporation of high contents of acrylic homo- and copolymers, showing a higher solubility of the blowing agent [23].

For preparing open-celled foams, melt-heterogeneities during the cell expansion process were identified to promote cell opening, as demonstrated by PS/polyolefin blends [24–27] and further immiscible systems [28]. Besides a sufficiently low cell wall thickness as a necessary criterion, the incorporation of either hard or soft blend phases is able to induce the cell-opening process via (1) geometrical constraints, (2) a low melt strength leading to melt rupture, and/or (3) the presence of shear forces acting on the matrix, as a result of the incorporated second phase (particles). Talcum, added as a nucleating agent, demonstrated synergisms with the two-phase blend, as higher cell density and thus lower thicknesses of the cell walls were induced by nucleation [24, 26].

As a route for improving the melt-elongational properties of semicrystalline polymers, Siripurapu et al. [7] proposed the blending of amorphous and semicrystalline blends of PS and PVDF; nevertheless, their approach showed only limited success. In contrast, Reichelt et al. [29] successfully developed blends of HMS-PP and PP-*b*-PE block copolymers. As could be shown, the melt strength increases with the HMS-PP content, while blends rich in HMS-PP also show the lowest densities.

The chemical nature and the individual chemical groups of the polymer determine the affinity (solubility) and the diffusivity of a specific blowing agent. Due to the low costs and environmental friendliness of carbon dioxide, numerous studies focus on tailoring these transport properties for the polymer/carbon dioxide system. Generally, one aims to overcome the often limited solubility as well as the high diffusivity, both factors complicating the nucleation, growth and stabilization of the polymer foam.

The concept of increasing the solubility was successfully demonstrated for PS-based blends, where CO_2-philic components were added [30–32], e.g., fluoroalkyl, fluoroether, carbonyl and siloxane functional materials. Nevertheless, the benefits on the foam structure and properties could be achieved only in some cases.

Quite similar to these approaches, an immiscible blend of an amorphous PS and a semicrystalline poly(ethylene glycol) (PEG) was investigated, where PEG showed a significantly higher solubility towards the blowing agent carbon dioxide. Foaming revealed a bimodal cell size distribution, formed by larger cells within the PEG phase and smaller cells within the PS phase, respectively. Such behavior was attributed to the inherent differences between PS and PEG. As PEG shows a lower viscosity as well as a higher diffusivity and solubility of the blowing agent carbon dioxide, the nucleation and cell growth rates, and also the tendency towards cell coalescence during growth, are significantly more pronounced. Based on these observations, a morphological evolution mechanism was suggested: bubble nucleation and growth initially starts in the PEG phase and, while the process just starts within the PS phase, the foaming PEG phase already tends to collapse and form large cells as the overall foam structure stabilizes.

Microcellular foaming, bimodal cell size distributions, and high open-celled contents of molecular composites of HT-polymers were reported by Sun et al. [33], investigating blends of a rod-like polymer polybenzimidazole with an aminated PSU and poly(phenyl sulfone) by using carbon dioxide as a blowing agent. The complex foaming behavior was related to phase separation within the otherwise

homogeneous polymer blend. Following a similar concept, foaming of molecular composites of polybenzobisthiazole and poly(ether ketone ketone) led to nonhomogeneous cell structures and high foam densities, but a remarkable enhancement of the mechanical properties [34].

Due to their immiscibility and poor interfacial adhesion, blends of polyolefins with styrenics often demand for compatibilization. Therefore, the foaming of such compatibilized blend systems was claimed in several patents, generally including a large range of compatibilizing agents (e.g., polystyrene-*b*-poly(ethylene-*co*-butylene)-*b*-polystyrene and polystyrene-*b*-polyethylene block copolymers) [35, 36]. In the scientific literature, the effect of compatibilization of PP/HDPE blends by SEBS triblock copolymers on the foam structure was investigated by Sahagun et al. [37]. A model allowed one to develop an understanding of the cellular structure of multiphase foams and to relate the deformation of the cell wall due to foaming to the morphology of the HDPE phase elongated in the PP matrix.

Despite the formidable chances to develop and to tailor cellular polymers, the literature describing the foaming behavior of blends is still rare. Critically analyzing the existing studies, only a few publications systematically discuss the following phenomena:

- Correlation between blend morphology, melt-elongation, and foaming behavior — despite the significant influence only addressed for neat polymers [38], miscible blends [4, 5], and some filled systems [39, 40]
- Knowledge of foaming multiphase blends of amorphous components
- Influence of compatibilization on the foam morphology – despite the significant influence and relevance of compatibilization on the blend structure and interfacial behavior, only partly discussed for polyolefins/styrenics blends [37]
- Foaming of nanostructured blends – so far, only the use of low contents of block copolymers (up to 2 wt%) as nucleating agents was discussed [19]

1.2 Aim of Tailoring the Foaming Behavior Via the Blend Structure

As demonstrated by the literature, multiphase blends potentially provide novel chances to tailor cellular materials, e.g., high cell densities via heterogeneous nucleation, open-celled characteristics by the presence of the second phase, and enhanced properties by incorporating multiple components into the cell wall. Nevertheless, controlling the foamability of such materials demands for understanding both the foam processing and blending technology, as an improved performance, can only be ensured by appropriate selection of the blend composition.

For this purpose, the present work aims at systematically exploiting the multiphase characteristics of blends for foaming, via controlling both the micro- and nanostructure of melt-processed blends. The development of such tailored blend morphologies can be a key factor for optimizing the foamability of complex blends in general. It should be noted that the term *foamability* is often associated with a high foam homogeneity and a sufficiently low cell size, but also with a low density.

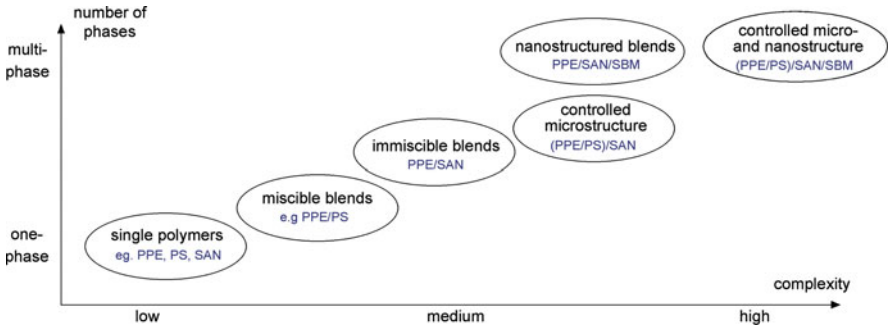

Fig. 4 General strategy for understanding and controlling the foaming behavior of blends

The general proceeding is demonstrated in Fig. 4: Following a detailed evaluation of a binary, immiscible blend, pathways to control the nanostructure (interphase) as well as the microstructure will be introduced. By combining both approaches, the complexity will be further increased stepwise to ensure a superior blend system for foaming. For all blend systems, relationships between structure, processing, and properties will be established, aiming at developing descriptive models on the foaming mechanism of multiphase blends.

Independent of the blend system, the following proceeding proved as ideal for a systematic evaluation of foaming blend systems. Prior to the foaming step the blend morphology, rheological, thermal, and gas transport properties are investigated as factors relevant for foaming. Subsequent batch-foaming experiments using carbon dioxide as the blowing agent are performed to prepare cellular materials under various, accurately controlled processing conditions. It should be noted that temperature-induced batch-foaming was performed, i.e. the materials were first saturated with carbon dioxide (5 MPa, 40°C), and subsequently foamed via heating in an oil bath over a wide range of processing conditions. Finally, the structure and the properties of the foam, as observed by electron microscopy and density measurements, are correlated to the aforementioned blend characteristics and processing parameters.

2 Immiscible Blend Systems (PPE/SAN Blends)

As previously discussed, multiphase blends consisting of at least two components are particularly interesting for materials development, as an exploitation of the advantageous properties of each component appears feasible. In the present case, binary blends of poly(2,6-dimethyl-1,4-phenylene ether) (PPE) and poly(styrene-*co*-acrylonitrile) (SAN) have been identified as a promising system due to the possible combination of the high heat distortion temperature and toughness of PPE with the desirable properties of SAN such as the chemical resistance, good processability, as well as low material costs. In addition, the amorphous nature of both components is likely to allow foaming via common batch-foaming techniques.

As binary PPE/SAN blends form the reference systems and the starting point for the foaming analysis, their miscibility will be considered first. As demonstrated in the literature [41, 42], both miscibility and phase adhesion of PPE/SAN blends are critically dependent on the composition of SAN, more precisely on the ratio between styrene and acrylonitrile (AN). Miscibility at all temperatures occurs up to 9.8 wt% of AN in SAN, whereas higher contents above 12.4 wt% lead to phase separation, independent of the temperature. Intermediate compositions exhibit a lower critical solution temperature behavior (LCST). Taking into account the technically relevant AN content SAN copolymers between 19 and 35 wt%, blends of SAN and PPE are not miscible. As the AN content of the SAN copolymer, selected in this work, is 19 wt%, the observed PPE/SAN blends show a distinct two-phase structure and an interfacial width of only 5 nm [42].

In the following, a systematic evaluation of the batch-foaming behavior of immiscible PPE/SAN blends over a wide compositional range is presented. In order to gain a fundamental understanding of foaming immiscible blends, relationships between the foaming behavior, the processing parameters, and the physical characteristics of the neat components as well as the blend are established. Special emphasis will be placed on the blend structure and on the rheological response of the blend systems under shear and elongational flow.

2.1 Morphology Development and Factors Relevant for Foaming

In the case of two-phase blend systems, one can distinguish between two general phase morphologies: (1) matrix-droplet structures, i.e., one phase is fully dispersed in a matrix phase, and the blend behavior is dominated by this continuous phase, and (2) co-continuous morphologies, i.e., both phases form a continuous network and thus contribute equally to blend behavior. Between these two extremes, a phase regime exists where a partially continuous phase is embedded in a continuous matrix phase. The transition between the fully dispersed and partially continuous structure is also referred to as percolation threshold, and depends – as the phase morphology in general – on the physical characteristics and the processing of the blend system [43, 44].

For controlling the microstructure of immiscible blends, one generally has to consider the following key factors [2, 3]: (1) the content of the individual phases, (2) their rheological behavior, and (3) the interfacial properties between the blend components. In the case of PPE/SAN blends, the shear viscosity of PPE is significantly higher over the complete temperature and shear rate regime (Fig. 5), typically used for processing. As a result, the formation of SAN matrix structures is promoted up to relatively high PPE contents. Following theoretical models, co-continuity of the blend is predicted for PPE contents of around 70 wt% at a shear rate of 50–500 s^{-1}, typical observed during melt-extrusion [46].

According to the theoretical considerations, the following phase morphologies are expected for PPE/SAN blends: (1) PPE contents below the percolation limit of around 19 wt% (according to Utracki [46]: SAN matrix, PPE fully dispersed,

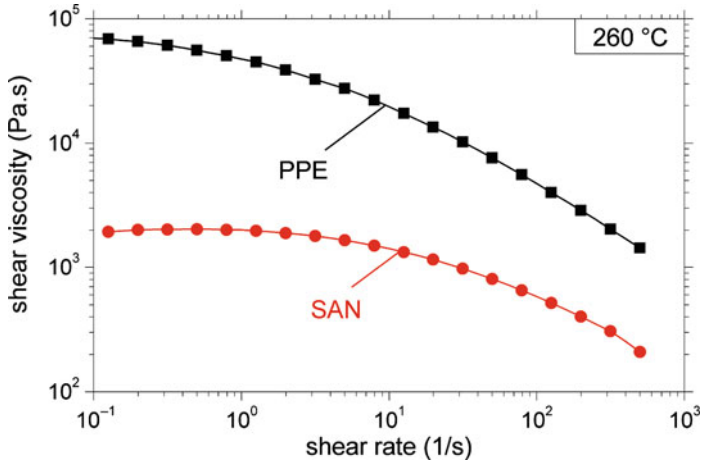

Fig. 5 Shear-rheological behavior of the PPE and SAN, respectively (reprinted from [45])

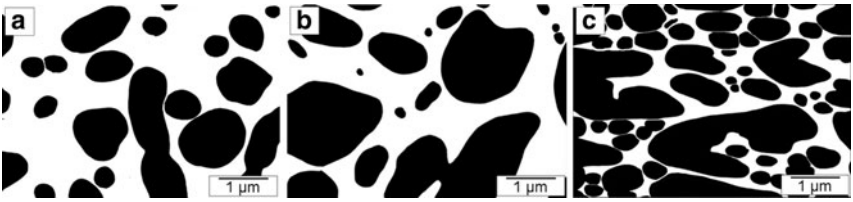

Fig. 6 Morphology of PPE/SAN blends following melt-extrusion: (**a**) PPE/SAN 40/60, (**b**) PPE/SAN 50/50, (**c**) PPE/SAN 60/40 (binary images of SEM micrographs: PPE – *dark*, SAN – *bright*)

(2) PPE contents from 19 to 70 wt%: increasing continuity of the PPE phase within a continuous SAN phase, (3) PPE contents around 70 wt%: co-continuous blend morphologies. At elevated contents, the opposite trend is expected.

Comparison with micrographs, taken from melt-extruded blends at elevated PPE contents, indeed reveals the expected behavior (Fig. 6). Starting at a PPE content of 40 wt%, the PPE phase does not appear fully dispersed, but already shows some degree of continuity. While increasing the PPE content up to 50–60 wt%, the continuity increases further. However, even at 60 wt%, the co-continuity of the blend is not fully approached and SAN still forms the matrix phase. According to the theoretical considerations and the morphological observations, a PPE matrix can only be achieved at elevated contents of the high-viscous PPE on the one hand (approximately 70 wt%). On the other hand, the stepwise increase of the PPE content possesses a strong impact on the blend viscosity and would necessitate melt-temperatures above 270°C. However, as the thermal stability of the selected blend components limits the processing temperatures, the use of PPE contents significantly exceeding 60 wt% required for phase inversion is prevented. In the following, we will therefore discuss only PPE/SAN blends up to 60 wt% of PPE.

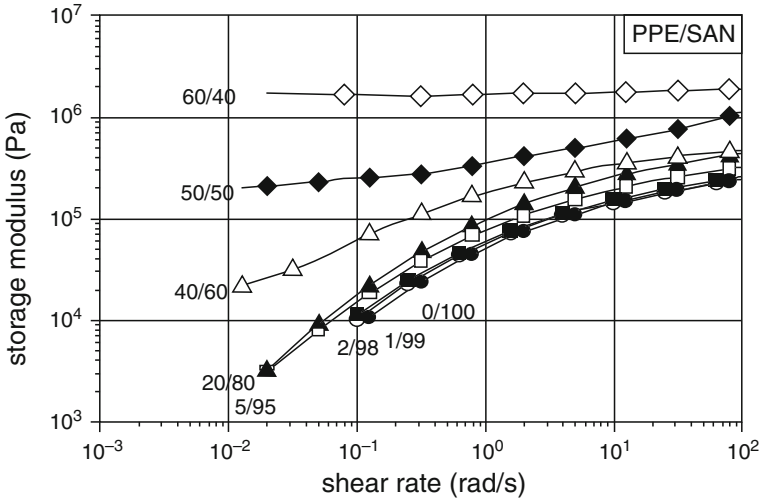

Fig. 7 Storage modulus behavior of PPE/SAN blends observed under oscillatory shear at 180°C (reprinted from [47])

While being a result of the viscosity behavior of PPE and SAN, the microstructure influences the rheological characteristics of the overall blend system again. In the present case, rheological measurements were performed at 180°C in order to allow for a comparison to the foam morphologies shown later (Fig. 7). As the investigated PPE/SAN blend system contains two phases with a significantly different glass transition behavior, it can be simplified to a suspension consisting of a SAN matrix and a glassy-state PPE filler [2]. Dynamic shear measurements can thus provide a detailed insight into the state of the filler dispersion and the filler—filler interactions in polymeric matrices, including the geometry, the content, as well as the interfacial properties of the filler [48–50].

The storage modulus, reflecting the melt elasticity, has proved to be a sensitive measure for such microstructural features. In the present case, distinct differences at lower frequencies are found when comparing systems up to 20 wt% PPE, reflecting the expected percolation limit, to blends with higher PPE contents. Below the percolation threshold, the melt elasticity is only slightly affected by the dispersed PPE particles, as hydrodynamic forces dominate the overall flow behavior. Once the filler content has reached a critical value, the storage modulus, in particular at low angular frequencies, shows a significant increase; a behavior that can be related to a transition from the liquid to a pseudo solid-like behavior as a result of pronounced particle—particle interactions and eventual network formation. The occurrence of a plateau-like regime characterizes pronounced particle—particle interactions [51]. Similar results have also been observed for other filled systems [52, 53].

Besides the blend morphology and the rheological behavior, the solubility of the blowing agent is regarded as key criteria for the foaming behavior. As can be seen in Fig. 8, both neat components reveal a high affinity towards carbon dioxide, as a

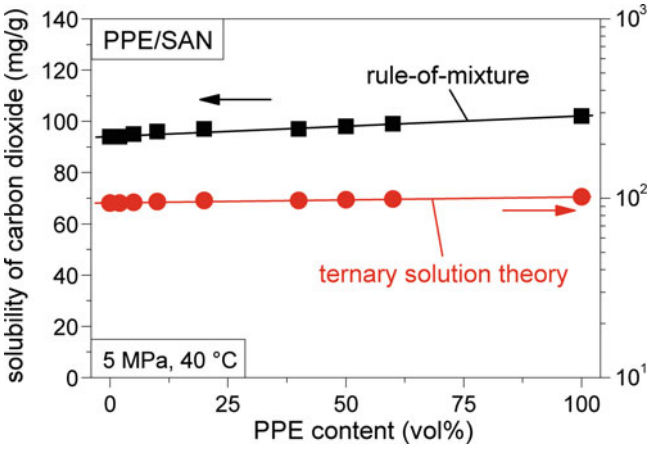

Fig. 8 Solubility of carbon dioxide in PPE/SAN blends at 5 MPa and 40°C

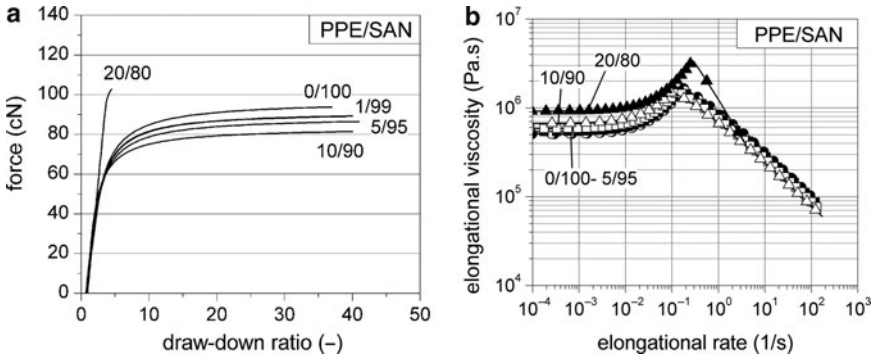

Fig. 9 Melt elongational behavior of PPE/SAN blends at 180°C. (**a**) Rheotens curves. (**b**) Apparent elongational viscosity, as calculated by [57] (reprinted from [47])

result of attractive interaction with the phenylene and ether groups of PPE, and with the phenylene ring and the AN groups of SAN [54, 55]. For the immiscible blend system, the solubility of carbon dioxide nearly scales with the blend composition, as predicted by a simple rule-of-mixture approach. On a closer view, however, a small positive deviation can be detected, an effect which is induced by the higher uptake of carbon dioxide within the interfacial regions between PPE and SAN.

Besides the materials structure and its interaction with the blowing agent, numerous studies on non-blended polymers verified the importance of the melt-elongational behavior for cell growth and stabilization. Factors such as a sufficient level of elongational viscosity, the presence of strain hardening, and a high drawability were frequently related to a homogeneous cell structure and low densities [1, 4, 5, 10, 38–40, 56]. The melt-elongational behavior of the present PPE/SAN blend is shown for a temperature of 180°C (Fig. 9). The shown force vs drawing rate curves are available by so-called Rheotens tests, where the polymer melt is

extruded through a capillary die and continuously drawn by a roller unit, similar to a fiber spinning unit. The draw down rate, as ratio between the draw down velocity and the die exit velocity, and the draw down force are continuously measured at increasing drawing velocity. Figure 9 shows that the materials response under elongational flow remains rather unaffected at low contents of PPE up to 10 wt% (Fig. 9a). Only the melt strength shows a minor decrease with increasing PPE contents [58]. However, the addition of 20 wt% PPE reveals a distinct behavior as the melt strength significantly increases and the drawability simultaneously decreases. Again, the percolation limit of the blend is likely to play a significant role for the observed transition.

For further investigating such effects, the presented Rheotens curves can be further evaluated by an analytical approach of Wagner et al. [57], allowing calculation of the elongational rate and elongational viscosity. As can be seen in Fig. 9b, the addition of PPE, acting as solid-state filler at the selected experimental conditions, leads to a continuous increase in zero elongational viscosity, as predicted for particle-filled systems [59]. Furthermore, the onset of elongational thinning is shifted to lower elongational rates with increasing PPE contents, previously reported also for polyamide 6 (PA6)-clay nanocomposites [60]. More interestingly, strain hardening of the melt, as reflected by the ratio between the maximum elongation viscosity and the zero elongational viscosity, is increasingly suppressed by elevating the PPE content.

The observed behavior is consistent with literature data on particulate-filled polymers up to PPE contents of 10 wt%. As rigid PPE particles are not able to follow the externally applied flow-field, a complex flow near and in-between the particles is found, processes that also involve substantial shear components. As the strain-hardening phenomenon only occurs in elongational flow, this partial conversion to shear flow in the SAN matrix is responsible for the decreasing strain-hardening parameter. Again, the blend with a PPE content of 20 wt% shows a distinct behavior as the strain-hardening parameter is significantly higher as compared to all other blends as well as to the neat SAN. This altered material response under elongational flow is likely related to the onset of particle—particle interactions at these elevated strain rates and to the more complex shapes of the dispersed PPE phase, i.e., the flow behavior is no longer purely hydrodynamically dominated.

2.2 Foaming Behavior

For analyzing the effect of blending on the foaming behavior, batch-foaming was selected as a straightforward and well-established method, as well-defined processing conditions can be ensured. The impact of blending on the cellular structure is demonstrated in Fig. 10, showing SEM micrographs of batch-foamed PPE/SAN blends up to 40 wt% of PPE. Comparing the neat SAN with the blended materials reveals distinct differences in cell size and foam structure. Besides the obvious

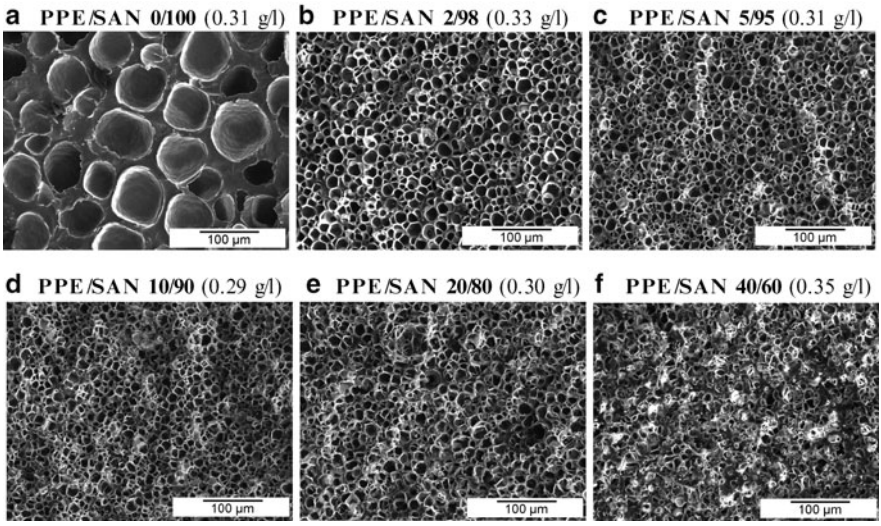

Fig. 10 Foam structure of PPE/SAN blends (foaming time 10 s, temperature 180°C)

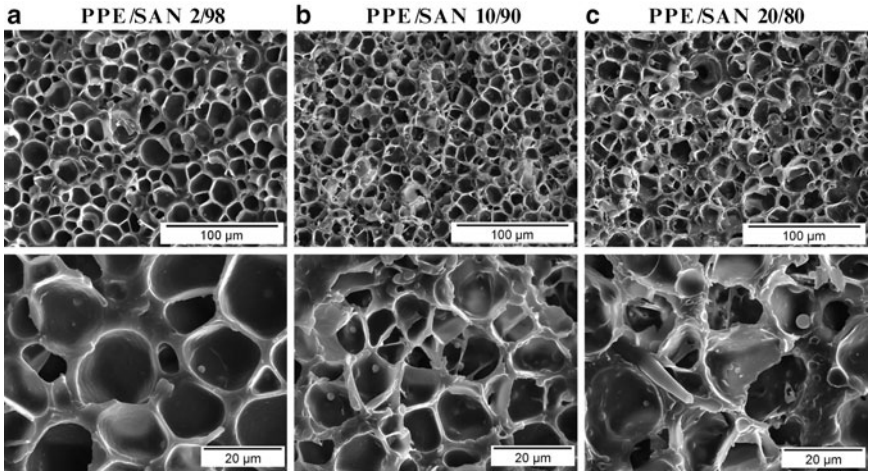

Fig. 11 Details on the cellular morphology of PPE/SAN blends (foaming conditions: time 10 s, temperature 180°C)

reduction in cell size, even by the addition of small PPE contents, the cellular materials become inhomogeneous at higher PPE contents, as can particularly be seen at PPE/SAN 40/60 blends. In addition, the foam density increases at these elevated PPE contents. Micrographs of blends PPE contents beyond 40 wt% are not shown here, as the cell structure of blends becomes even more inhomogeneous and shows macroscopic defects as well as nonfoamed regions.

A more detailed insight into the cellular structure is provided in Fig. 11. At low PPE contents, the PPE phase is homogeneously embedded in the cell walls and is

not affecting the expansion behavior. At increasing contents, however, the homogeneity deteriorates, morphological features occurring during the cell growth which can be related to the melt-elongational behavior and the morphology of the blends. While the addition of PPE to SAN increases the elongational viscosity, it also reduces the strain-hardening behavior and, approaching 20 wt% of PPE, strongly reduces the drawability. The impact of such phenomena on the foam and cell structure can clearly be detected. Besides the reduced homogeneity of the foam, the cell walls tend to be less uniform and reveal coalesced as well as an open-celled structure for elevated PPE contents, both effects reflecting the increased phase size of the blend and the deteriorated elongational behavior. These observations clearly demonstrate that both the shear as well as the melt elongational rheological properties are of significant importance for the cell growth of immiscible blends.

Nevertheless, blending can obviously lead to a significant increase in cell density, indicating that the cell nucleation is strongly controlled by the dispersion of the PPE phase and the overall morphology of the blend. The addition of small amounts of PPE to SAN significantly increases the cell density, indicating a heterogeneous nucleation effect of the PPE phase which dominates over the homogeneous nucleation under the selected experimental conditions.

The efficiency of the PPE phase to nucleate foam cells can be attributed to two phenomena. (1) The interface between PPE and SAN is energetically favored as a nucleation site as a result of the weak interaction between the two blend components, the PPE thereby acts in a similar manner as commonly used solid-state fillers. (2) In contrast to solid-state fillers, the PPE phase solves a significant amount of the blowing agent before the foaming step. During cell nucleation, the mass transfer of the blowing agent to and across the blend interface is highly suitable to induce thermodynamic instabilities which are beneficial for nucleation of foam cells.

The number of PPE particles dispersed in the SAN matrix, i.e., the potential nucleation density for foam cells, is a result of the competing mechanisms of dispersion and coalescence. Dispersion dominates only at rather small contents of the dispersed blend phase, up to the so-called percolation limit which again depends on the particular blend system. The size of the dispersed phase is controlled by the processing history and physical characteristics of the two blend phases, such as the viscosity ratio, the interfacial tension and the viscoelastic behavior. While a continuous increase in nucleation density with PPE content is found below the percolation limit, the phase size and in turn the nucleation density reduces again at elevated contents. Experimentally, it was found that the particle size of immiscible blends, d, follows the relation $d \sim \phi + C\phi^2$, where ϕ is the content of the dispersed phase and C is a material constant depending on the blend system. Subsequently, the theoretical nucleation density, N_{th}, is given by

$N_{\mathrm{th}} \sim \phi$ below percolation ("absence" of coalescence)
$N_{\mathrm{th}} \sim \frac{\phi}{\left(\phi + \mathrm{C}\phi^2\right)^3}$ above percolation (competition of dispersion and coalescence).

It should be noted that the transition is not a prompt as described, but smooth. Nevertheless, an optimum content of the dispersed phase exists for each blend system, where the potential nucleation density approaches its maximum. The

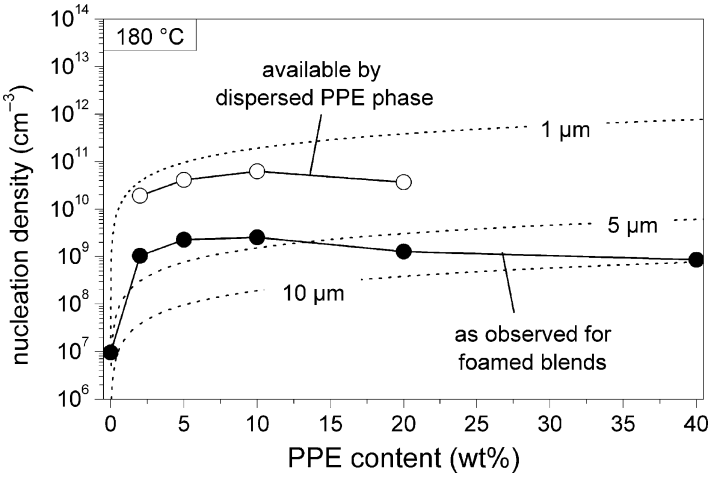

Fig. 12 Nucleation density of foamed PPE/SAN blends vs number of theoretically available nucleation sites (=particle density of the PPE phase). The *dotted lines* represent the theoretical nucleation density at different phase sizes of PPE (reprinted from [47])

experimental values for the investigated PPE/SAN blend verify the described behavior, i.e., the nucleation density available by the dispersed blend phase first increases, before decreasing again, having an optimum around 10 wt% of PPE. As indicated by the full symbols in Fig. 12, the nucleation density of the foam, i.e., the number of cells formed within the initial polymer volume, follows the same trend. Nevertheless, the number of potential nucleation sites is still lower when compared to the potential nucleation density.

Finally, evaluation of the foam densities as a function of the foaming temperature reveals further interesting phenomena. As can be seen by the contour plot in Fig. 13, representing blend systems foamed for 10 s, the density appears to be independent of the blend composition and is a function of the foaming temperature only for low PPE contents up to 20 wt%. For the foaming time of 10 s, a distinct minimum in foam density is obtained at around 200°C. In contrast, further increasing the PPE content leads to increased foam densities, but also reduces the dependence on the foaming temperature. In particular, the density of the PPE/SAN 60/40 blend is nearly independent of temperature, but remains relatively high as compared to the other foams.

The final foam density results of the complex interplay between the main processing steps occurring during foam formation – cell nucleation, growth and stabilization/coalescence. These phenomena can be related to distinct steps during batch-foam processing. Prior to the foaming, the specimens are homogeneously saturated with carbon dioxide under high pressure at a low temperature. After releasing the pressure, the additional heating of the sample leads to thermodynamically instable state by lowering the solubility of the gas in the polymeric matrix. Due to the adequately high heating temperature, the rapid demixing of the blowing agent, the

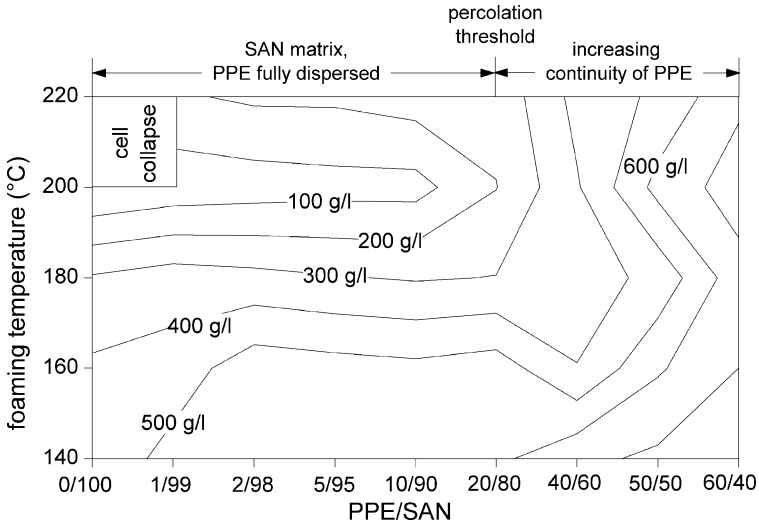

Fig. 13 Foam density of PPE/SAN blends as a function of blend composition (foaming time 10 s)

cell nucleation, is provoked. The following, thermodynamically driven cell growth is mainly controlled by the rheological behavior and the gas transport properties of the immiscible blend system polymer, and determines both the final foam density as well as the cellular morphology.

In the present case, the foam density relates perfectly with the previously observed rheological properties, as a transition in the flow behavior was detected at approximately 20 wt% of PPE (Fig. 13). In the viscoelastic case (below the percolation limit), the PPE content neither significantly influences the foamability nor the blend rheology. At elevated contents (beyond percolation), however, the PPE content strongly affects the rheological response of the blend and, subsequently, degrades the foaming behavior, which is verified by a reduced expandability.

It should further be noted that the onset of continuity of the dispersed blend phase not only deteriorates the overall mobility of the SAN to form cellular structures, but also increases the average phase size of PPE and, thus, sterically hinders the incorporation into the cell walls. In particular, for the PPE/SAN 60/40 blend, showing some co-continuous features and solid-state characteristics at 180 °C, the foamability is limited to such an extent that only local and less defined cell growth proceeds, leading to the highly inhomogeneous foam morphologies.

2.3 Strategies for Enhancing the Foamability of Immiscible Blends

The results demonstrate that, in contrast to blending of miscible polymers, which allows tailoring of both foam morphology and foam processing via controlling the

factors relevant for foaming by the blend composition and the blend partners, foaming of immiscible blends poses a significantly higher challenge. For immiscible blends, additional factors such as the blend morphology, the interfacial properties between the components, and the respective processing characteristics of each phase need to be considered. In addition, both the transport properties of the blowing agent as well as the rheological behavior are not predictable by the simple additivity of the individual components.

Several factors can be identified as being crucial for the foaming of immiscible polymer blends: the blend morphology, the phase size of the blend constituents, the interfacial properties between the blend partners, and, last but not least, the properties of the respective blend phases such as the melt-rheological behavior, the glass transition temperature, the gas solubility, as well as the gas diffusion coefficient. Most of these factors also individually influence the melt-rheological behavior of two-phase blends.

While combining polymer blending and foam processing potentially allows the development of novel cellular materials, the foaming of multiphase blends can still reveal some serious drawbacks. As a result of the distinct processing window of each polymer phase, the overall foamability can be strongly deteriorated, as reflected by volume reduction and the foam homogeneity. These effects become especially obvious if strong differences in the glass transitional and viscosity behavior between the blend phases are present, as exemplarily shown for PPE/SAN. Here, the limitations of foaming blends become particularly evident at elevated PPE contents, leading to a reduced expandability and foam processing window, close to the co-continuity of the blend even resulting in a very poor foam homogeneity, as indicated by macroscopic pores and by nonfoamed regions.

In order to overcome these drawbacks, novel concepts for enhancing the foamability of such immiscible blends need to be introduced. Using the PPE/SAN 60/40 blend as a reference system, the following concepts appear as most promising (Fig. 14):

- Compatibilization/nanostructure formation for achieving a finer blend morphology by the reduction of both the interfacial tension and coalescence, and for ensuring an improved phase adhesion/nanostructure between the blend partners. Thus, the incorporation of the dispersed blend phase into the cell walls should be enhanced while the number of possible nucleating sites is simultaneously increased.
- Selective blending for adjusting the foaming characteristics of each phase individually, particularly reducing the high glass transition temperature and viscosity of the PPE phase, and for controlling the overall blend morphology. Thus, the simultaneous foaming of both phases should be promoted, and the morphology development in presence of the elongational flow during expansion can be tuned.

The fundamental relationships between compatibilization and selective blending on the blend characteristics and the foaming behavior, as demonstrated in the following, will not only be valid for this particular blend system, but will help to understand and control the foaming behavior of multiphase polymer blends in general.

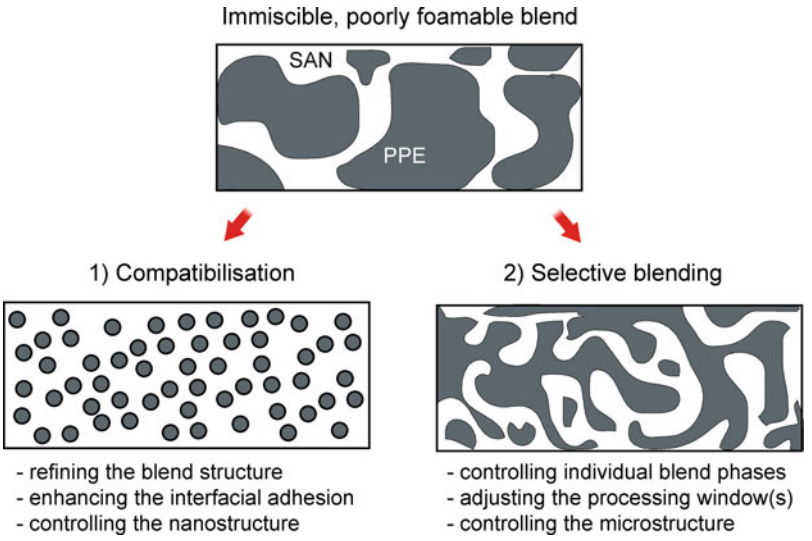

Fig. 14 Potential strategies for enhancing the foaming behavior of immiscible blends

3 Nanostructured Blends Via Compatibilization (PPE/SAN/SBM Blends)

Compatibilization is a well-accepted and efficient method for refining the blend morphology and for enhancing the interfacial adhesion between blend partners [2, 3, 61]. Block copolymers are commonly used as compatibilization agents due to a selective miscibility of the blocks with either blend component [44, 62, 63]. The interfacial presence of such block copolymers not only allows increasing the interfacial strength, but also hinders coalescence and reduces the interfacial tension between the blend partners, leading to more stable blend structures [61]. With regard to PPE/SAN blends, polystyrene-*block*-poly(methyl methacrylate) diblock copolymers (PS-*b*-PMMA, SM) were identified as highly suitable, mainly due to the favorable enthalpic interaction between PS and PPE as well as between PMMA and SAN, respectively [64–66].

Although a notable reduction of the phase size is reported for such compatibilized blends [64–67], the overall mechanical toughness remains unsatisfactorily low [64]. As one reason, thermal stresses at the interface between PPE and SAN, occurring as a result of the different thermal coefficients of expansion during solidification following melt-processing, are identified as a crucial reason for the observed brittle behavior [68].

In order to overcome the build-up of these stresses, the addition of triblock terpolymers as compatibilizing agents with an elastomeric middle block and end blocks of PS and PMMA, respectively, appears advantageous. One example is the use of polystyrene-*block*-poly(1,4-butadiene)-*block*-poly(methyl methacrylate)

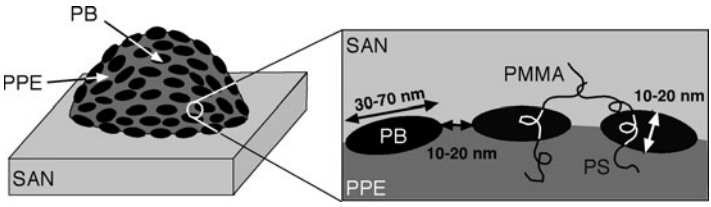

Fig. 15 Schematic of the morphological arrangement in PPE/SAN blends compatibilized by SBM triblock terpolymers – nanostructured "raspberry morphology" (reprinted from [45])

(SBM) as a compatibilizer. As a result of the particular thermodynamic interaction between the relevant blocks and the blend components, a discontinuous and nanoscale distribution of the elastomer at the interface, the so-called raspberry morphology, is observed (Fig. 15). Similar morphologies have also been observed when using triblock terpolymers with hydrogenated middle blocks (polystyrene-*block*-poly(ethylene-*co*-butylene)-*block*-poly(methyl methacrylate), SEBM). It is this discontinuous interfacial coverage by the elastomer as compared to a continuous layer which allows one to minimize the loss in modulus and to ensure toughening of the PPE/SAN blend [69].

The composition of the SBM triblock terpolymers was identified as a key factor for ensuring compatibilization of PPE/SAN blends via melt-processing [45]. SBM triblock terpolymers with equal weight contents of each block were successfully used for melt-blending to give rise to nanostructured blend interfaces. For this reason, the most promising SBM triblock terpolymer, $S_{33}B_{33}M_{33}{}^{94}$, was selected as compatibilizing agent, where the subscripts denote the weight content of the respective blocks and the exponent denotes the total molecular weight. In the following, the $S_{33}B_{33}M_{33}{}^{94}$ will only be referred to as SBM.

The aim of this section, therefore, is to correlate systematically the compatibilization of PPE/SAN 60/40 blends by SBM triblock terpolymers with the foaming behavior of the resulting blend. The reduction of the blend phase size, the improved phase adhesion, a potentially higher nucleation activity of the nanostructured interfaces, and the possibility to adjust the glass transitional behavior between PPE and SAN, they all promise to enhance the foam processing of PPE/SAN blends.

3.1 Controlling the Nanostructure

The blend morphology, as a potential factor for batch-foam processing, is shown in Fig. 16. While the uncompatibilized PPE/SAN 60/40 blend reveals a rather coarse morphology, the compatibilization step by SBM triblock terpolymers, in particular at higher contents, allows one to reduce significantly the phase size and increase in interfacial area. Moreover, a discontinuous interfacial coverage between PPE and SAN can be detected for the compatibilized blend at higher magnification, representing the aforementioned nanostructured raspberry morphology. As previously described for the immiscible PPE/SAN blends, the foam expansion behavior

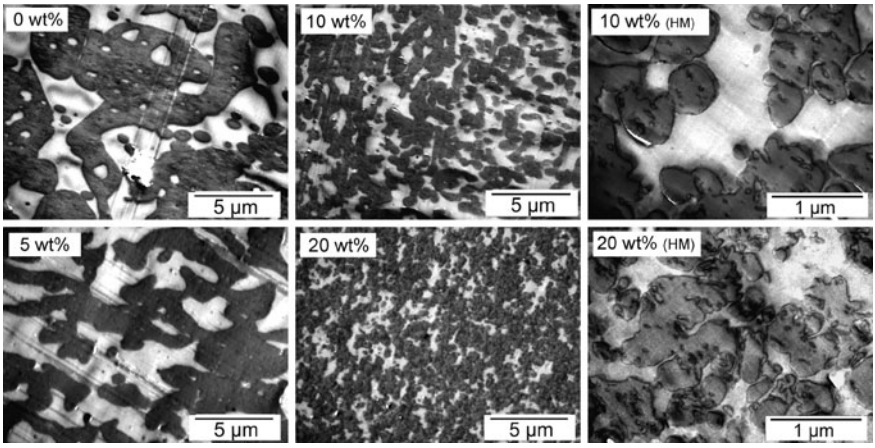

Fig. 16 Morphology of PPE/SAN blends compatibilized by SBM triblock terpolymers (TEM micrographs: PPE – *dark*, SAN – *bright*, PB of SBM – *black*)

of blend systems including a high-T_g and a low-T_g phase, such as PPE and SAN, can, respectively, depend strongly on the co-continuity of the blend. In the present case, as demonstrated elsewhere [70], the co-continuity is strongly and similarly pronounced for each blend system, both for the uncompatibilized and for the SBM-compatibilized blends.

It should be noted that the morphologies of the highlighted compression-molded blends differ from the extruded specimens [45], a phenomenon often reported for multiphase blend systems [3]. During the compression-molding process, the blend system aims at reducing its free energy by reducing the interfacial area between the blend partners [3, 61, 71]. For the uncompatibilized PPE/SAN 60/40 blend, the subsequent coalescence of the PPE phase leads to an increased phase size and an almost co-continuous blend morphology. As mentioned earlier for compatibilization agents in general, the interfacial presence of the SBM block copolymer is able to stabilize the structure via inhibiting this coalescence and coarsening, resulting in morphologies closer to the extruded samples [2, 61].

The solubility of carbon dioxide at the selected saturation conditions of 5 MPa and 40°C, is shown in Table 1. Both the uncompatibilized and the compatibilized PPE/SAN blends absorb similarly high amounts of carbon dioxide in the range of $100, \mathrm{mg\,g^{-1}}$. However, in contrast to one-phase systems, the solubility data of the overall multiphase blend is not sufficient to describe the system, but the content of carbon dioxide in each blend phases needs to be considered. In the case of PPE/SAN blends compatibilized by the SBM triblock terpolymers, one can distinguish three distinct phases, when neglecting interfacial concentration gradients (idealized case): (1) the PPE phase intimately mixed with the PS block, (2) the SAN phase mixed with the PMMA block, and (3) the PB phase located at the interface between PPE/PS and SAN/PMMA.

Table 1 Solubility of carbon dioxide in PPE/SAN/SBM blends at 5 MPa and 40°C. The neat polymers are shown for comparison

Polymer	Solubility of carbon dioxide ($mg\,g^{-1}$)
PPE	102
SAN	94
PS	63
PMMA	121
PPE/SAN 60/40	99
+5 wt% SBM	100
+10 wt% SBM	99
+20 wt% SBM	98

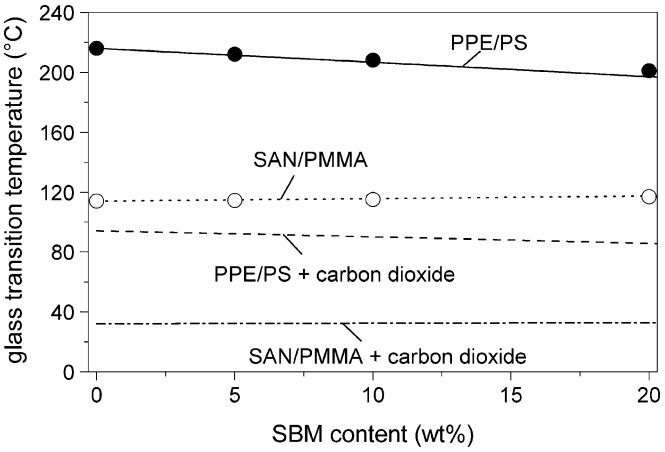

Fig. 17 Effect of compatibilization via SBM triblock terpolymers on the glass transition temperature of PPE/SAN blends, in absence and in presence of carbon dioxide (as predicted by [75] and [76, 77])

In order to predict the solubility of each phase, the solubility of carbon dioxide in the individual components was determined first, using desorption experiments following saturation at 5 MPa and 40°C. PS ($63\,mg\,g^{-1}$) and PMMA ($121\,mg\,g^{-1}$) reveal the lowest and the highest solubility, respectively, while SAN ($94\,mg\,g^{-1}$) and PPE ($102\,mg\,g^{-1}$) show an intermediate behavior. Due to the high diffusion coefficient of PB, its solubility of carbon dioxide could not be determined by the selected method, and only data from the literature is shown [72]. For binary PPE/PS blends, a rather linear dependence between the solubility and the blend composition has been reported [73]; for SAN/PMMA blends, a similar trend can be expected due to the weak interaction between the blend phases [74]. Thus, the gas solubility of each blend phase can be estimated, as a parameter decisive for the cell nucleation and growth process.

The compatibilization activity of the SBM block copolymers significantly influences the glass transitional of the PPE/SAN 60/40, as shown in Fig. 17. The presence

of the PS block ($T_g = 104°C$) in the PPE phase ($T_g = 216°C$) leads to a strong reduction of the glass transition of PPE, which can quantitatively be described by the Couchman equation [77]. Similarly, the addition of the PMMA block ($T_g = 135°C$) to the SAN phase ($T_g = 114°C$) promotes a slight increase in glass transition temperature of SAN, according to the Fox equation [76]. In summary, the presence of 20 wt% SBM triblock terpolymers allows to reduce the difference in glass transition between PPE and SAN from 100 to 80°C.

When discussing the glass transitional behavior of polymeric samples saturated with carbon dioxide, the pronounced plasticizing effect of gas further needs to be taken into account [75]. In the case of simple polymers, the Chow equation has proved to be a rather accurate calculation method for describing the glass transition temperature, T_g, as a function of the weight content of carbon dioxide [56, 75]. The main parameters of the equation are the molar mass of the polymer repeat unit, the molar mass of carbon dioxide, the gas constant, the glass transition of the polymer in the initial state, the heat capacity change associated with the glass transition of the polymer, and the lattice coordination number that depends on the sizes of the gas molecule and the polymer repeat unit, respectively.

For miscible blend phases, these parameters need to be described as a function of the blend composition. In a first approach to describe the behavior of the present PPE/PS and SAN/PMMA phases, these phases will be regarded as ideal, homogeneously mixed blends. It appears reasonable to assume that the heat capacity, the molar mass of the repeat unit, as well as the weight content of carbon dioxide scale linearly with the weight content of the respective blend phase. Moreover, a constant value of the lattice coordination number for PPE/PS and for SAN/PMMA can be anticipated. Thus, the glass transition temperature of the gas-saturated PPE/SAN/SBM blend can be predicted as a function of the blend composition (Fig. 17). Obviously, both the compatibilization by SBM triblock terpolymers and the plasticizing effect of the absorbed carbon dioxide help to reduce the difference in glass transition temperature between PPE and SAN.

Besides the blend structure and the interaction with the blowing agent, the rheological behavior can strongly influence the foam structure. While not explicitly shown here, the melt-rheological behavior under shear and elongational flow remain rather unaffected at high temperatures; at lower temperatures, the reduction in glass transition temperature of PPE by SBM promotes a shift of the solid-state behavior to lower temperatures and thus broadens the processing window of the blend.

3.2 Impact on the Foaming Behavior

As a next step, the effect of compatibilization on the foaming behavior will be discussed. While the density can only be slightly reduced by SBM, and remains at a rather high level, the foam structure reveals distinct differences, exemplarily shown for a foaming temperature of 160°C and at a foaming time of 10 s (Fig. 18). As mentioned earlier, the uncompatibilized blend reveals a highly inhomogeneous structure,

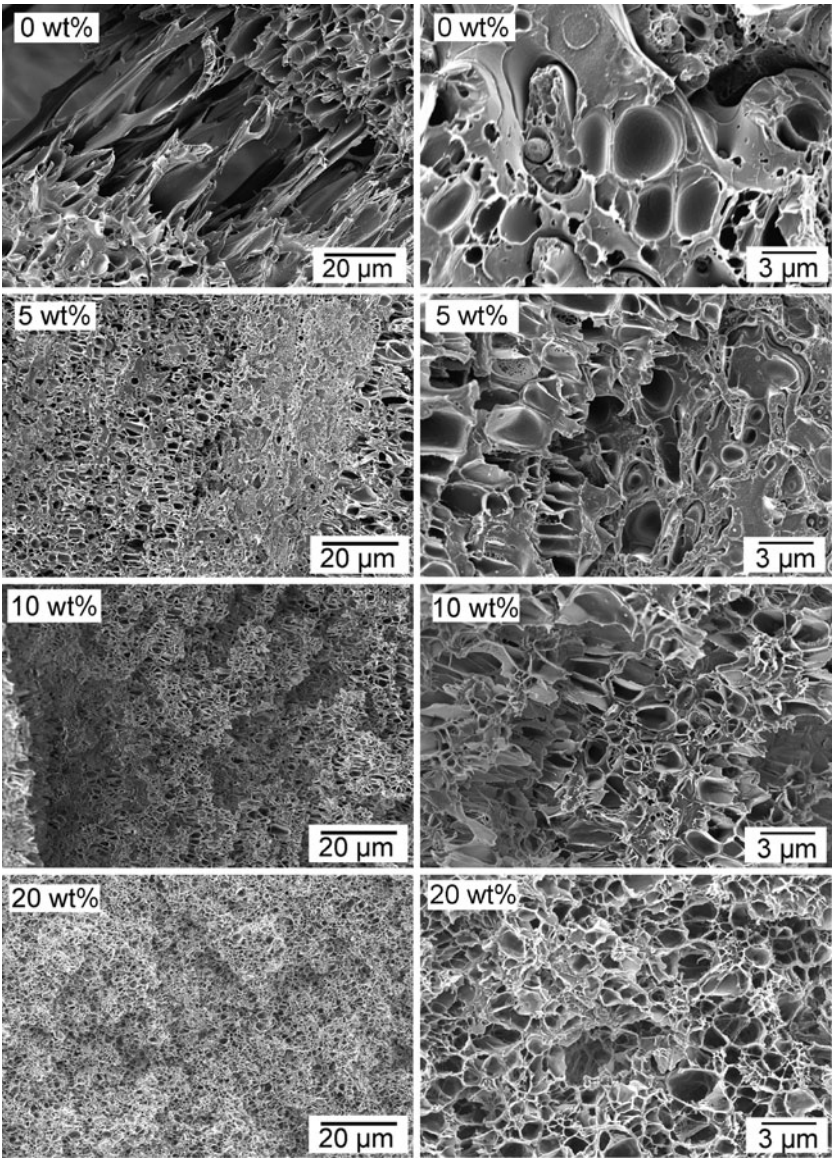

Fig. 18 Foam morphologies of PPE/SAN 60/40 blends as a function of the SBM content, as observed by SEM (foaming time 10 s, foaming temperature 160°C)

as reflected by macroscopic defects, such as pores of several 100 µm, and also nearly nonfoamed regions. The highly viscous PPE clearly restricts the expansion process, while the induced expansion forces locally induce break-up of the foam structure. In addition, the poor phase adhesion between PPE and SAN becomes evident.

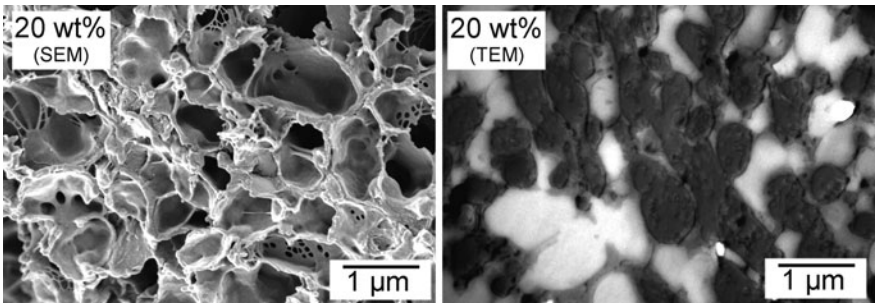

Fig. 19 SEM and TEM micrograph showing the foam morphology and structure of the cell walls of foamed PPE/SAN/SBM 48/32/20 blends (PPE – *dark*, SAN – *bright*, PB of SBM – *black*, foam cell – *white*; foaming time 10 s, temperature 180°C)

Inhomogeneous foam morphologies can also be detected for PPE/SAN blends compatibilized by 5 wt% of SBM, while the overall cell size is notably reduced and macroscopic defects are avoided. A further enhancement in foam morphology is observed for 10 wt% and, in particular, for 20 wt% of the SBM triblock terpolymer. Here, the cell size is in the range of a few microns or even below, down to 350–400 nm, while the homogeneity is high. Moreover, the adhesion between the two blend partners appears to be significantly improved.

One further interesting feature is worth mentioning, becoming obvious at elevated PPE contents: the cell walls partly form cobweb-like structures, contributing to a significant open-cell content. Such morphological phenomena are likely to be induced by both the thin cell structures formed during foaming, by high nucleation densities and by the SBM block copolymer promoting cell wall opening [24] (Fig. 19).

Analyzing the blend and foam structure via both scanning electron and transmission electron microscopy demonstrates that the matrix of the foam cells is formed by the SAN phase, which previously formed the more continuous blend phase. Therefore, it is reasonable to assume that the foam nucleation and growth process proceeded initially in the SAN phase, due to its higher diffusivity and the lower viscosity [78]. The PPE phase appears incorporated into the cell walls, and no foaming within the PPE phase is detectable, an observation which promotes the conclusion that PPE acts as a heterogeneous nucleation agent for the SAN phase. In addition, the sufficiently high adhesion between PPE and SAN phase inhibits delamination of both blend phases, and the nanostructured interface at the blend interface can still be found (raspberry morphology). Thus, such cellular materials can be classified as submicrocellular foams with nanostructured cell walls.

It appears that both compatibilization and the nanostructure formation at the interface play a key role for nucleation. The supposed heterogeneous nucleation activity will therefore be discussed in more detail. Heterogeneous nucleation in general is strongly affected by the particle size and the interfacial properties [79, 80]. As the particle size of the PPE phase is well above the critical radius of nucleation of several nanometers [80], the interface demands closer examination.

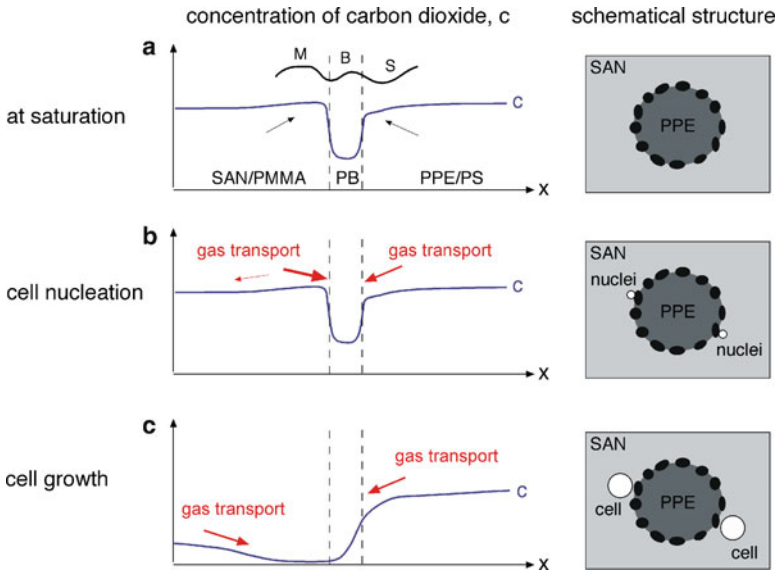

Fig. 20 Proposed interfacial nucleation mechanism in ternary PPE/SAN/SBM blends

The nanostructured interface of this particular PPE/SAN/SBM blend, with a highly diffusive, elastomeric, discontinuous coverage and five different polymers is likely to easily create thermodynamic instabilities as a result of the gas transport between the phases [81, 82]. Subsequently, nucleants can be formed which finally lead to cell growth in the SAN phase. In order to describe more precisely these effects induced by the nanostructured interface, we will revisit the gas solubility of the individual phases (Fig. 20).

Under saturated conditions, the gas solubility of the two major blend phases, SAN/PMMA and PPE/PS, is rather similar, while the solubility of carbon dioxide in PB is significantly lower, leading to a highly nonhomogeneous distribution of the blowing agent along the interface. Without going into detail, we should briefly mention that the gas content within the PPE/PS as well as the SAN/PMMA phase is not absolutely constant. Due to the constraints on the SBM, induced by the chemical bond between the different blocks, the content of both PMMA and PS is slightly higher at the interface. As a result, the gas distribution at the interface may vary slightly (see arrows in Fig. 20a).

As the polymer-blowing agent system is supersaturated by increasing the temperature and reducing the pressure, the carbon dioxide is transported along the concentration gradient, leading to an interfacial enrichment. As a result of this higher gas content at the interface and due to the strong thermodynamic disequilibrium, nucleation close to/within the PB phase is initiated. In addition, two further factors promote this nucleation phenomena: (1) the lower surface tension between the PB and the carbon dioxide compared to the other components [19], and (2) the higher diffusion coefficient within PB [78]. It can be assumed that the cell nuclei

are formed close to the PMMA/SAN phase, as the higher diffusion coefficient of SAN/PMMA (compared to PPE/PS) leads to a stronger driving force.

However, as cell growth proceeds, the physical as well as chemical constraints of the triblock terpolymers inhibit pronounced growth within the PB phase. Instead, the nucleated cells tend to grow into the SAN/PMMA phase. As the PPE/PS phase still stores a significant amount of carbon dioxide, the blowing agent is subsequently transported along the interface towards the foam cells. Apparently the PPE/PS phase still acts similar to a solid phase.

For evaluating the efficiency of the nanostructured interface for cell nucleation, the particle density of PPE, as a measure for the number of nucleating sites available for nucleation, is plotted versus the nucleation density observed for the foam (Fig. 21). For comparison, the previously found values of the uncompatibilized PPE/SAN blend are added. For PPE/SAN, even the relatively high number of PPE particles of around $5 \times 10^{11}\,\mathrm{cm}^{-3}$ only leads to nucleation of approximately 2.5×10^{10} cells cm^{-3}, i.e., only 1/20 of the potentially available PPE particles act as cell nucleating agents. Via compatibilization, however, not only the particle density of PPE and the nucleation density can be increased, but also the efficiency is strongly enhanced. While the number of cells directly scales with particle density, more than two foam cells are nucleated by one PPE particle.

In order to explain this effect, two phenomena can be hypothesized: (1) multiple nucleation of the PPE phases, and (2) break-up the PPE phase and, subsequently an increase of the particle density. Discussing the latter case first, it can be estimated that the time scale for dispersion is not sufficiently high [3, 83]. Therefore, multiple nucleation is likely to induce the higher nucleation densities, making SBM an ideal candidate for nucleation by interfacial effects.

In summary, compatibilization of PPE/SAN blends via SBM triblock terpolymers allows one to enhance significantly the homogeneity of the foam, while simultaneously reducing the cell size by heterogeneous nucleation activity of the

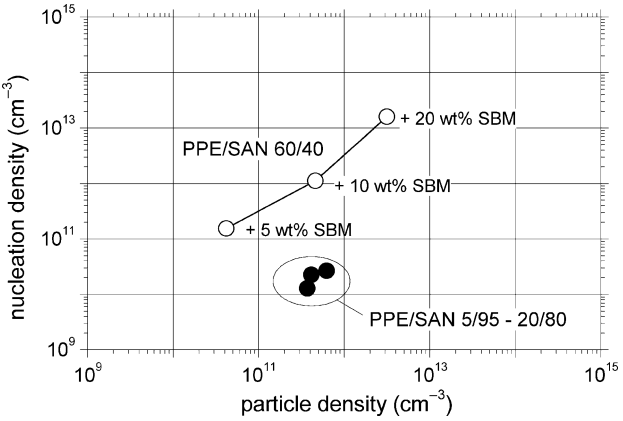

Fig. 21 Nucleation density vs particle density of PPE/SAN blends compatibilized by SMB triblock terpolymers, in comparison to uncompatibilized PPE/SAN blends

interface between the blend components; effects induced by the refined phase size of the blend, the adjusted glass transitional behavior, and the improved adhesion between the blend phases. Moreover, the nanostructured blend morphology of the bulk material can successfully be transferred into the cell walls of the sub-micro- to microcellular foam. However, both the higher number of cells and the multiphase melt-structure also promoted the formation of open-cells. In view of these results, SBM triblock terpolymers can beneficially be used as compatibilization agents in polymer blends for yielding significantly improved foam morphologies.

4 Microstructured PPE/SAN Blends Via Selective Blending (PPE/PS/SAN)

4.1 Controlling the Microstructure

As discussed in the previous sections, the blend morphology as well as the processing window of the individual blend components can be identified as key factors for the foamability of multiphase blend systems [47, 84]. As a first step, compatibilization via SBM triblock terpolymers was exploited for controlling the blend morphology on a nanoscale, and for reducing the difference in processing window between PPE and SAN. However, in order to exploit the benefits of all blend phases, the properties of each blend phase and the overall microstructure of the blend need to be controlled.

For bulk materials, a co-continuous blend structure is often desirable as it offers synergetic effects [71, 85]. For this purpose, numerous investigations on the blend morphology formation were performed, but the precise prediction of the final structure is still rather complex [86–90]. Nevertheless, based on numerous investigations concerning the influence of the processing conditions and the blend composition on the morphology development, two key factors can be deduced [43, 87, 91, 92] – the blend composition and the viscosity ratio.

In order to adjust the viscosity ratio of immiscible blend systems, selective blending can be identified as a promising approach. From the literature it is known that, for multiphase blends containing PPE as one blend phase, PS can be seen as material of choice to adjust the viscosity ratio while only minor changes of the interfacial tension can be observed [91, 92]. With regard to the discussed PPE/SAN blend system, PPE and PS show miscibility over the complete compositional range, while PS is immiscible with SAN, due to the AN content of 19 wt%. The viscosity behavior of the PPE, PS and their miscible blends is compared to neat SAN in Fig. 22. Via blending of PPE and PS, the complete viscosity range between the neat polymers can be covered. Interestingly, the miscible PPE/PS 50/50 blend shows a shear viscosity similar to SAN [93].

For predicting the phase inversion and co-continuous regime in immiscible blend systems, various empirical and semi-empirical models exist [5]. A model, valid for high viscosity ratios and elevated shear rates, was established by Utracki [46]:

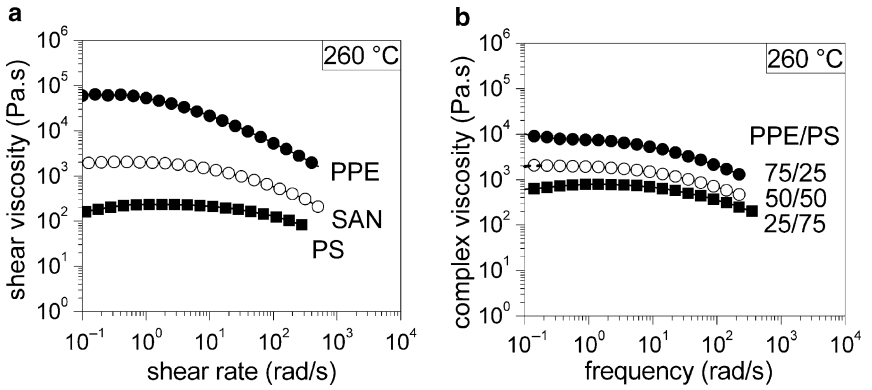

Fig. 22 Shear-rheological behavior at 260°C. (**a**) Neat polymers. (**b**) Miscible PPE/PS blends (reprinted from [93])

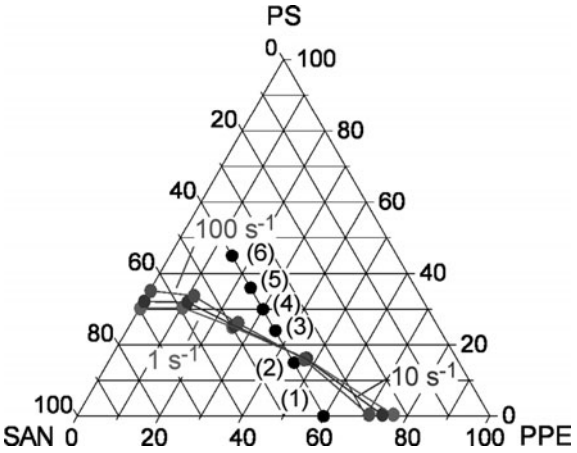

Fig. 23 Phase inversion as function of the shear rate and blend compositions, as calculated by the Utracki model. The dots represent the investigated (PPE/PS)/SAN compositions of (**a**) (60/0)/40, (**b**) (45/15)/40, (**c**) (36/24)/40, (**d**) (30/30)/40, (**e**) (24/36)/40, (**f**) (15/45)/40 (in accordance with [93])

$$\frac{\eta_1}{\eta_2} = \left[\frac{\varphi_m - \varphi_2}{\varphi_m - \varphi_1}\right]^{[\eta]\varphi_m} \tag{1}$$

where ϕ_1 and ϕ_2 denote the volume content at phase inversion of the first and second phase, while $[\eta]$ and φ_m indicate the maximum packaging density of spheres (in vol.%) and the intrinsic viscosity.

The phase inversion composition of (PPE/PS)/SAN blends, as calculated by the Utracki model, is shown by the ternary phase diagram in Fig. 23, highlighting the influence of shear rate and blend composition [93]. The lines separate the regions, where SAN and PPE/PS form the matrix. For example, SAN forms the continuous phase at high SAN contents, while PPE/PS appears as the continuous phase at elevated PPE/PS contents.

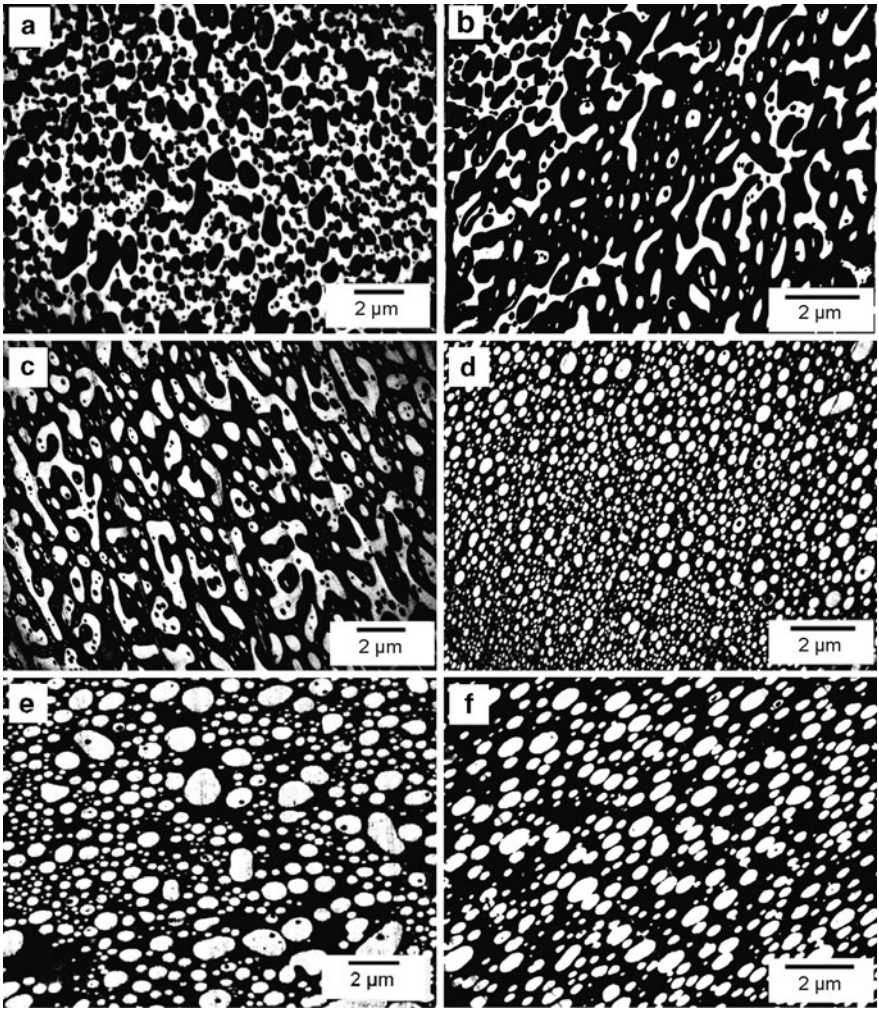

Fig. 24 TEM micrographs of the prepared (PPE/PS)/SAN blend systems. (**a**) (60/0)/40, (**b**) (45/15)/40, (**c**) (36/24)/40, (**d**) (30/30)/40, (**e**) (24/36)/40, (**f**) (15/45)/40 (reprinted from [93])

Comparison of the theoretical prediction with the microstructure of melt-extruded blends, as observed by transmission electron microscopy, reveals good agreement. While the PPE/SAN 60/40 blend system reveals a SAN matrix phase (Fig. 24a), the blend system containing 15 wt% PS shows three distinct blend morphologies (Fig. 24b), both regions showing SAN and PPE/PS as matrix, as well as co-continuous blend morphologies can be found. By further increasing the PS content beyond 30 wt%, PPE/PS forms the matrix, and SAN appears as dispersed phase [93].

Besides the viscosity behavior, blending of PPE with PS also alters the solubility of the blowing agent, a further factor important for foaming [3]. As can be seen in Table 2, PS shows a significant lower solubility of carbon dioxide when compared to PPE. The solubility in the miscible PPE/PS blend systems shows almost linear behavior with a slight negative deviation [73], typical for blends with strong interactions between the blend partners. Such a behavior of miscible blends can be predicted by a log-additivity rule [3]. Even though the solubility of PPE decreases by addition of PS, all systems still reveal a solubility high enough to allow foaming.

The foam processing window of the blend systems is also controlled by the glass transition temperature of the blend phases. With regard to the neat blend system, the addition of PS continuously lowers the glass transition temperature of the PPE/PS phase, as predicted by the Couchman equation [77] (Fig. 25). For the carbon dioxide-laden case, the plastifying effect needs to be taken into account, which lowers the glass transition temperature of both PPE/PS and SAN.

For the PPE/PS phase, the previously described Chow equation can be combined with the Couchman equation to estimate the T_g as a function of the blend composition. The results are highlighted in Fig. 25. For the prediction, the heat capacity and the molar mass of the repeat unit of the PPE/PS blends is regarded to scale linearly with the mass content of the blend partners, and a constant lattice coordination number of $z = 2$ is used [75]. While the addition of PS to PPE allows one to reduce continuously the T_g in presence of carbon dioxide, the plasticization effect is less pronounced, mainly driven by the decreasing solubility via addition of PS.

Table 2 Solubility of carbon dioxide in PPE/PS at 40°C and 50 bar [73]

PPE/PS	0/100	25/75	50/50	75/25	100/0
Solubility ($mg\,g^{-1}$)	63	70	81	91	102

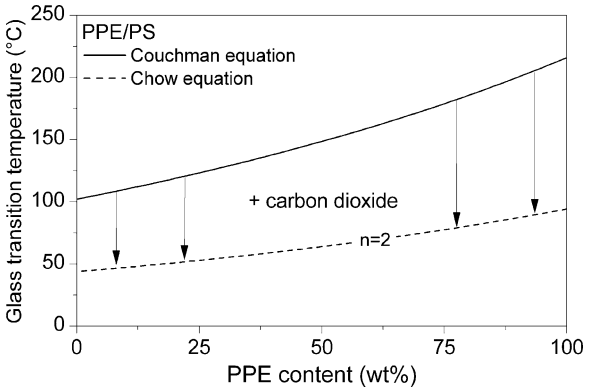

Fig. 25 Glass transition temperature of PPE/PS blends in absence and presence of carbon dioxide, as calculated by the Couchman equation [77] and by the Chow equation [75]

4.2 Influence of Microstructure on Foaming Behavior

As previously shown for PPE/SAN blends, the foaming behavior of immiscible blend systems is affected by both the properties of the blend phases and the overall blend structure [1]. In the present blend system, the viscosity of one specific blend phase is varied; as a result, not only the foaming behavior of the blend phase is altered but also the microstructure of the blend is affected [94]. By investigating blend systems with constant PPE to PS ratios of 75/25 and 50/50, and varying the SAN content in the range of 20–40 wt%, the influence of both the microstructure and the viscosity ratio can be analyzed (Table 3).

The blend morphology is highlighted in Fig. 26, revealing a PPE/PS matrix phase (dark phase) with dispersed SAN particles (bright phase) for all blend systems. Comparing blend morphologies with constant SAN content, only minor differences can be detected, with one exception: at a SAN content of 40 wt%, blends with a PPE to PS ratio of 75/25 are closer to co-continuity compared to blend systems with a PPE to PS ratio of 50/50, as indicated by the elongated SAN particles. In all cases, independent of the viscosity ratio, decreasing the SAN content reduces the coalescence of the dispersed SAN particles, and in turn results in a finer dispersed SAN phase and an increase in SAN particle density [94].

For all investigated blend systems, homogeneous foam structures across the sample thickness were achieved by foaming the carbon dioxide laden blends at 180°C for 10 s. Representative SEM micrographs of the core regions of each foam sample are highlighted in Fig. 27, showing the influence of the PPE/PS ratio and the SAN content. Evaluating the blend systems with a PPE/PS ratio of 75/25, i.e., with a matrix more viscous than the dispersed phase, a bimodal cell size distribution can be detected. In the case of the blend systems with a PPE/PS ratio of 75/25 and a SAN content of 40 wt%, the larger cells are in the range of 10 µm, while the smaller cells are about 1–2 µm in size (Table 3).

In order to understand the highlighted foaming behavior, both the blend morphology and the properties of the individual blend phases need to be taken into account. On the one hand, the less viscous, lower T_g SAN phase reveals a higher tendency to nucleate foam cells, both by homogeneous nucleation within the SAN phase and by heterogeneous nucleation at the interface to PPE/PS. Furthermore, the lower viscosity of the SAN phase promotes rapid cell growth and expansion. As a result of the

Table 3 Blend compositions of the (PPE/PS)/SAN blend systems with constant PPE to PS ratios of 75/25 and 50/50

PPE/PS ratio	PPE (wt%)	PS (wt%)	SAN (wt%)
75/25	45	15	40
	52.5	17.5	30
	60	20	20
50/50	30	30	40
	35	35	30
	40	40	20

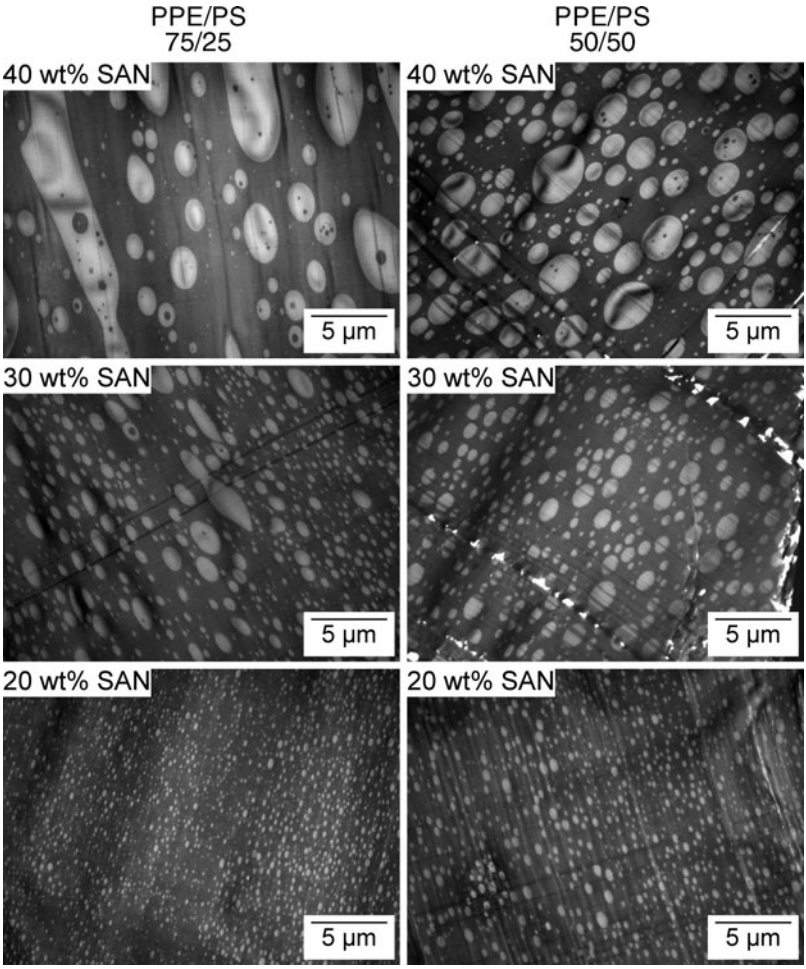

Fig. 26 Microstructure of (PPE/PS)/SAN blend systems following compression-molding, as observed by transmission electron microscopy (PPE/PS – *dark*, SAN – *bright*)

continuous nature and the high viscosity of the PPE/PS phase, expansion of SAN is restricted to some extent, which limits the final cell size. On the other hand, cells nucleated in the PPE/PS phase are restricted in growth due to the high viscosity of PPE/PS, and form a large number of rather small cells incorporated in the cell walls of the foam (Fig. 27). One can thus relate the two populations of the bimodal cell size distribution to the respective blend phases, i.e., the larger cells are formed within the SAN phase, while the smaller cells are induced by the PPE/PS phase.

Reducing the SAN content promotes a finer dispersed and more homogeneous SAN phase, as can be seen by the TEM micrographs in Fig. 26. The altered microstructure shows a strong impact on the cell structure of the foamed blend systems: at a PPE/PS ratio of 75/25 and a SAN content of 30 wt%, the cell size decreases,

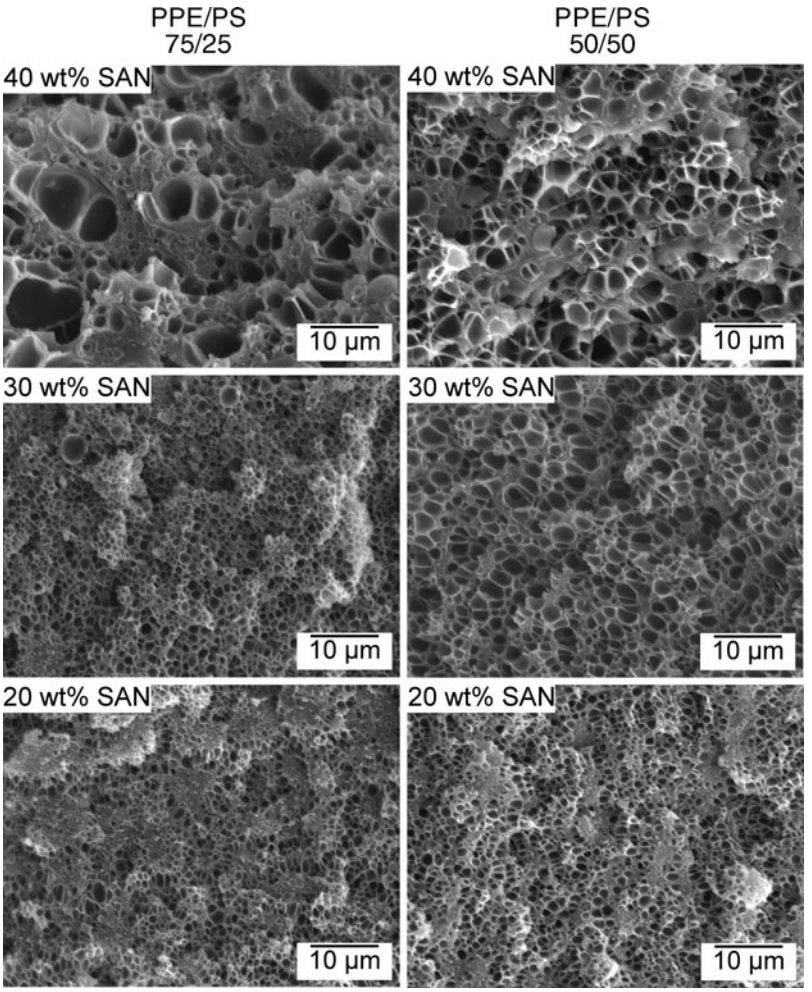

Fig. 27 Foam morphology of (PPE/PS)/SAN blends, as observed by scanning electron microscopy (foaming temperature 180°C, foaming time 10 s)

while the cell density and foam homogeneity is strongly improved. Nevertheless, a bimodal cell size distribution with larger cells in the range of 3 µm and smaller cells below 1 µm can still be detected (Table 4). When further reducing the SAN content to 20 wt%, a detrimental effect on the foam structure is observed. The more viscous PPE/PS phase almost completely restricts cell growth and expansion, resulting in nonfoamed regions and an increase in overall foam density; nevertheless, some cells below 1 µm can still be found.

By foaming an immiscible blend system of a poly(ethylene glycol)PEG/ polystyrene (PEG/PS), Taki et al. detected a similar foaming behavior as well as a bimodal cell size distribution [78]. While smaller cells formed in the more

Table 4 Cell size and cell density as function of the PPE/PS ratio and SAN content of the foamed (PPE/PS)/SAN blend systems. Foaming temperature: 180°C, foaming time: 10 s

PPE/PS ratio	SAN (wt%)	Cell size (μm)	Cell density (cm^{-3})
75/25	40	8.9/1.6	n.a.
	30	2.8/0.65	$6 \times 10^{10}/2 \times 10^{12}$
	20	0.71/–	2×10^{12}/–
50/50	40	9.3/1.1	n.a.
	30	3.3/1.0	$6 \times 10^{10}/6 \times 10^{11}$
	20	1.6/0.66	$1 \times 10^{11}/1 \times 10^{12}$

viscous PS phase, larger cells are induced by the less viscous PEG phase. The foaming behavior was related to the properties of the blend phases, more precisely to the lower viscosity and higher diffusivity of the PEG phase compared to the PS phase. The initial nucleation and enhanced cell growth within the PEG phase leads to an early cell collapse and the formation of large cells. As a result, less blowing agent is available for the PS phase, inducing the formation of smaller cells [78].

A strong similarity is found for the present blends with a PPE/PS ratio of 50/50, as reflected by a similar bimodal cell size distribution for all SAN contents. Small differences can be related to the distinct foaming kinetics of the PPE/PS blend phase. Compared to the PPE/PS 75/25 blend phase, the higher content of PS in the PPE/PS 50/50 phase leads to a cell nucleation and growth kinetics close to the SAN phase. Nevertheless, the PPE/PS phase still appears to restrict the cell growth and expansion in the SAN phase to some extent, and smaller cells are found within the cell walls. Independent of the SAN content, cell growth within the dispersed SAN phase proceeds under the constraints of the continuous, higher T_g PPE/PS phase.

Interestingly, the greater cell size of the bimodal cell size distribution is rather independent of the PPE/PS ratio (Table 4). Although the rheological properties as well as the cell nucleation kinetics differ for both PPE/PS ratios, the blend morphology is likely to possess the strongest influence on foaming behavior, more precisely on the cell structure.

As a further indicator for the foamability, the foam density is highlighted in Fig. 28, showing the influence of the PPE/PS ratio, the SAN content, the foaming temperature, and the foaming time. For a PPE/PS ratio of 75/25 and a foaming time of 10 s, three distinct regimes can be detected:

1. Below 160°C: the foam density increases with increasing PPE/PS content. As the foaming temperature is below the glass transition temperature of the more viscous PPE/PS phase, only a slight expansion appears, as a result of the plasticization by the blowing agent. The density reduction by foaming the blend systems is caused by the less viscous SAN phase. For lower PPE/PS contents, a more continuous SAN phase and therefore an enhanced density reduction is observed.
2. Between 160 and 180°C: slightly above the glass transition temperature of the PPE/PS phase, a similar expansion for all blend systems can be observed.

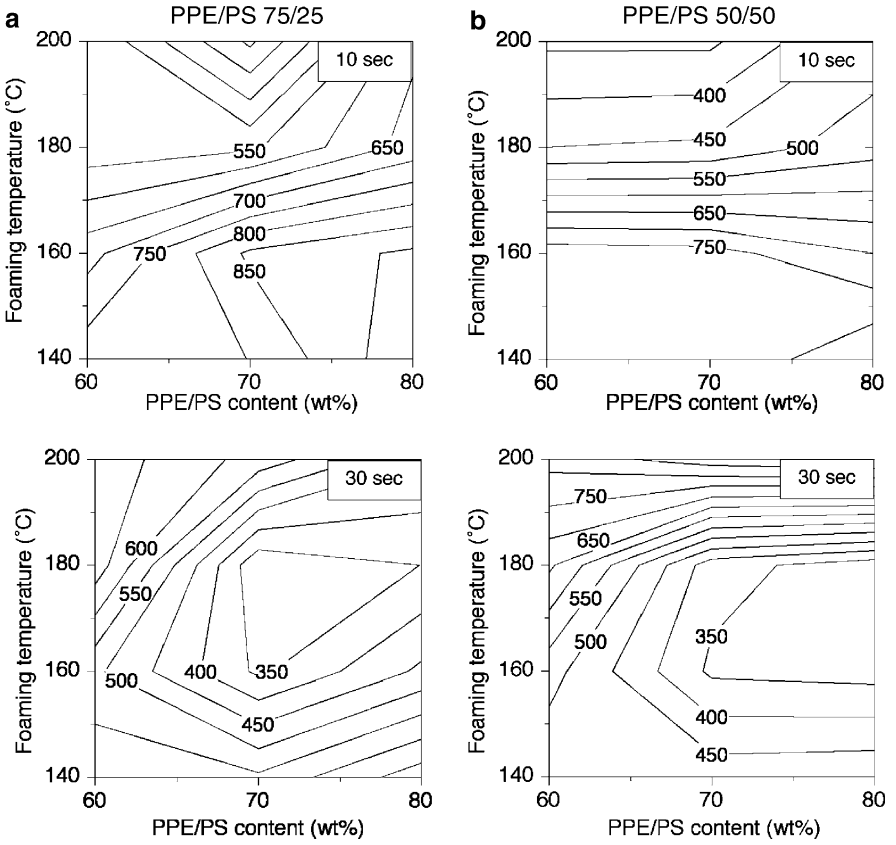

Fig. 28 Foam density as function of the foaming temperature. (**a**) PPE/PS ratio of 75/25. (**b**) PPE to PS ratio of 50/50 (foaming time 10 and 30 s, foam density in $g l^{-1}$)

3. Above 180°C: a further increase of the foaming temperature leads to a coalescence and collapse of the SAN phase, more pronounced for a continuous SAN phase. An increase of the PPE/PS phase to 70 wt% stabilizes the foam structure and therefore can be identified as the most promising system. Higher PPE/PS contents still restrict the expansion and increase the overall foam density.

When increasing the foaming time to 30 s, the minimum in density is shifted from a foaming temperature above 180°C to temperatures between 160 and 180°C. The overall foaming behavior is similar to a foaming time of 10 s. Elevated SAN contents still tend to collapse at elevated foaming temperatures, while an elevated PPE/PS content stabilizes the foam structure. For a PPE/PS ratio of 75/25 the blend system containing 30 wt% SAN shows the best compromise between the density reduction and the cell structure.

As a result of the finely dispersed SAN phase for a PPE/PS ratio of 50/50, the density reduction is almost independent of the SAN content for a foaming time of 10 s. The foam density is generally lower compared to the blend systems with a

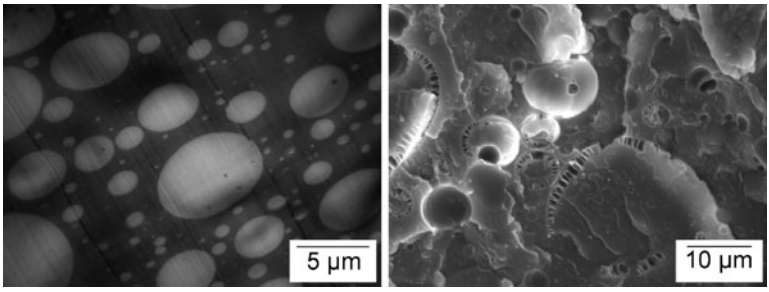

Fig. 29 Blend morphology (*left*) and foam structure (*right*) of (PPE/PS)/SAN blend with a PPE/PS ratio of 25/75 and a SAN content of 40 wt% (foaming temperature 180°C, foaming time 10 s)

PPE/PS ratio of 75/25. The expansion of the SAN phase is less restricted, and the PPE/PS phase tends to foam even at lower foaming temperatures as a result of the lower viscosity and glass transition temperature. By increasing the foaming time to 30 s, again a shift of the minimum density to lower temperatures can be detected.

For further understanding the influence of the viscosity ratio on the foaming behavior, an additional blend system with a PPE/PS ratio of 25/75 and a SAN content of 40 w% was investigated. Due to the high PS content, the PPE/PS matrix phase shows a lower viscosity and a similar glass transition temperature when compared to the dispersed SAN phase. As can be seen in Fig. 29a, the decrease in viscosity of the PPE/PS clearly promotes the formation of elevated SAN phase in comparison to the previously shown blends.

Foaming such materials reveals interesting features, as a completely collapsed PPE/PS matrix phase and partially foamed SAN particles can be observed for all investigated foaming conditions, as exemplarily shown for a foaming temperature of 180°C and a foaming time of 10 s (Fig. 29b). The less viscous PPE/PS matrix phase tends to nucleate first, and promotes rapid cell growth and collapse. The submicron-sized foam cells within the SAN phase are preferentially found at the interface to PPE/PS, as a result of nucleation by the transport of blowing agent out of the SAN phase. The achieved densities of the foamed blend system are rather high and in the range of 700–900 $g\,l^{-1}$.

4.3 Descriptive Foam Model Depending on the Microstructure of the (PPE/PS)/SAN Blend

For establishing a descriptive foam model of such blend systems, the (PPE/PS)/SAN blend with a PPE/PS ratio of 75/25 is exemplarily used (Fig. 30), as it further reveals pronounced differences in microstructure:

1. At high SAN contents of 40 wt%, cell nucleation initially starts in the SAN phase and rapid cell growth appears. The elongated phase structure and the generally elevated phase size of SAN promote rapid cell coalescence, leading to an in-

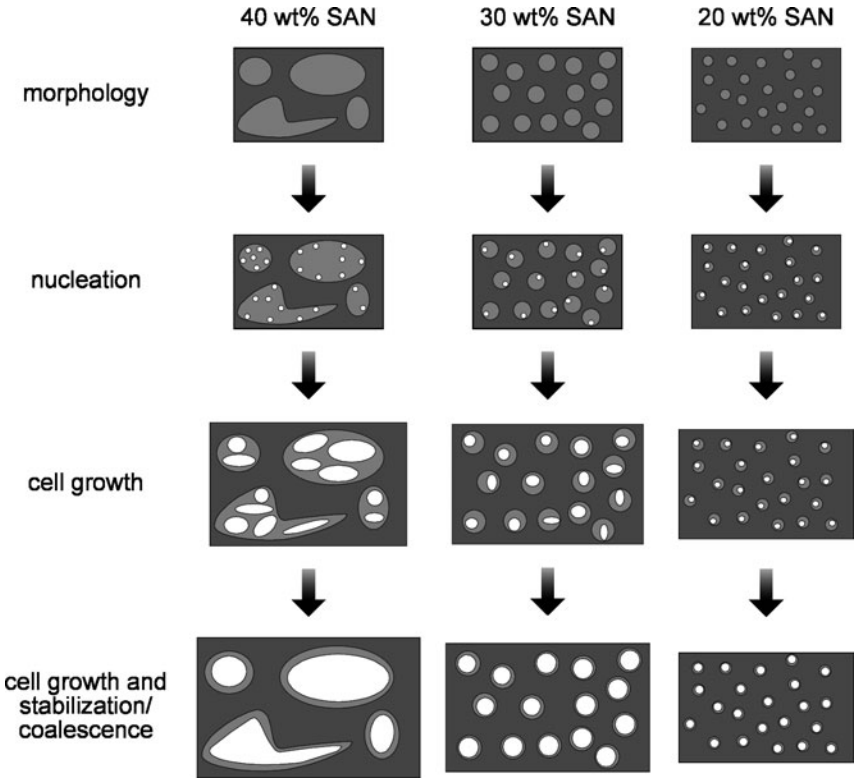

Fig. 30 Schematic foam model of (PPE/PS)/SAN blends with a PPE to PS ratio of 75/25

creased cell size in the SAN phase. Smaller cells are formed by nucleation in the higher viscous PPE/PS phase. In addition, the PPE/PS phase restricts expansion of the SAN phase, limiting the final density reduction.

2. At intermediate SAN contents of 30 wt%, a fully dispersed SAN phase can be detected, leading to an optimum of cell growth in the SAN phase and stabilization by the PPE/PS phase. The lower phase size of the dispersed SAN phase restricts the formation of larger foam cells, while the high SAN particle density and the concurrent nucleation in the PPE/PS matrix induce high cell densities.
3. At SAN contents of 20 wt%, a finer dispersed SAN phase and therefore an elevated cell density is observed. Carbon dioxide is subsequently transferred from the more viscous PPE/PS phase to the less viscous SAN phase showing a higher tendency to nucleate. The PPE/PS phase rapidly vitrifies and cell nucleation is suppressed.

In general, similar properties of the blend phases are beneficial to promote simultaneous nucleation and cell growth in both blend phases. In case of strong differences between the blend phases, a matrix of the higher viscous phase is preferred, as it ensures proper cell stabilization both for the matrix as well as for the lower viscous, dispersed phase.

5 Microstructured and Nanostructured Blend Systems (PPE/PS/SAN/SBM)

In the previous sections the foamability of the PPE/SAN blend systems containing elevated contents of the higher viscosity PPE phase were improved by (1) selective blending with PS as well as (2) compatibilization with SBM.

Selective blending the more viscous PPE phase with PS allowed one to tailor the processing window of the miscible PPE/PS blend phase and the microstructure of the immiscible blend system. Following this approach, simultaneous foaming of both blend phases and more homogeneous cell structures could be achieved. Additionally, the overall foam density could be reduced.

By compatibilizing the immiscible PPE/SAN blend with SBM triblock terpolymers, the overall size of the dispersed PPE particles was reduced, increasing the number of potential nucleating sites and easing the incorporation of PPE in the cell walls. Moreover, nanostructured interface between PPE and SAN was formed, which turned out to be highly beneficial for cell nucleation. As a result, a dramatic increase of the cell density and reduction of the cell size was observed, keeping the density reduction at a similar level.

Finally, the benefits of both strategies – controlling the microstructure by selective blending with PS and controlling the nanostructure by compatibilizing with SBM – will be combined in order to generate synergistic effects. Based on the previous results, a (PPE/PS)/SAN blend with a PPE to PS ratio of 75/25 and a SAN content of 30 wt% was used as reference system, and subsequently compatibilized with 5, 10, and 20 wt% of SBM triblock terpolymers. As the PPE/PS ratio of 75/25 and the SAN content of 30 wt% is fixed, in the following section the blend systems will be described by their SBM content of 0, 5, 10, and 20 wt%.

5.1 Controlling the Microstructure and Nanostructure

Similar to the previously investigated blend systems, selective blending of PPE/SAN with PS allows PPE/PS matrix structures to form in both the noncompatibilized as well as in SBM-compatibilized blend systems (Fig. 31). Already the noncompatibilized (PPE/PS)/SAN blend shows a finely dispersed SAN phase with a particle size in the range of 1 µm (Fig. 31a). The addition of small amounts of SBM to the ternary (PPE/PS)/SAN blend has no significant effect on the particle size of the dispersed SAN phase (Fig. 31b). By further increasing the SBM content to 10 and 20 wt%, a remarkable refinement of the SAN phase can be detected (Fig. 31c,d). While the particle size of the SAN phase is reduced to about 500 nm for 10 wt% SBM, SAN particles far below 300 nm can be detected for the high SBM amount of 20 wt%.

As previously demonstrated, the shear rheological properties are an important factor relevant for the processing and foaming. In addition, morphological features of the blend system can be detected at low shear rates [95]. The shear viscosity and the storage modulus of the present blends are highlighted in Fig. 32. An in-

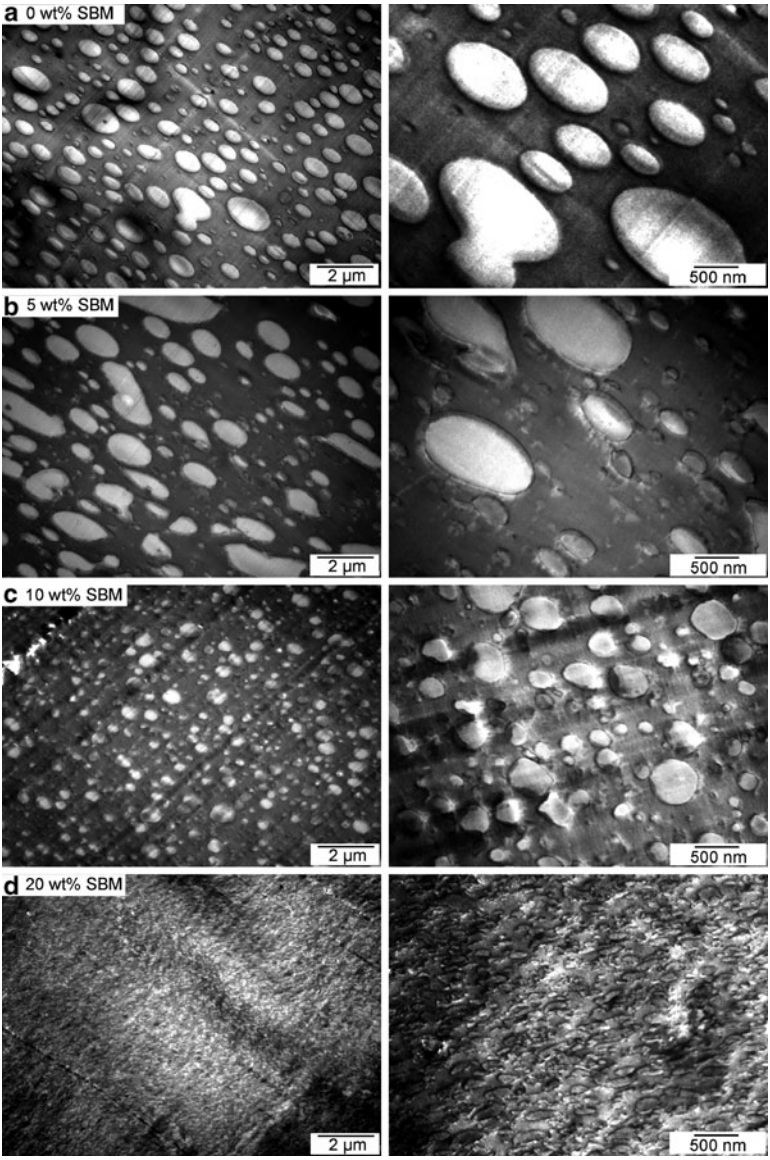

Fig. 31 Morphology of (PPE/PS)/SAN/SBM blends following compression-molding (PPE/PS – *dark*, SAN – *bright*, PB block of the SBM triblock terpolymers – *black*)

creasing viscosity can be detected with increasing SBM content at low frequencies (Fig. 32a). Similar behavior can be observed for filled systems with increasing filler loading, due to network formation [96, 97]. Further evidence on the physical and structural reasons is given by investigating the storage modulus as function of the frequency (Fig. 32b). Again, distinct differences between the blend systems can be

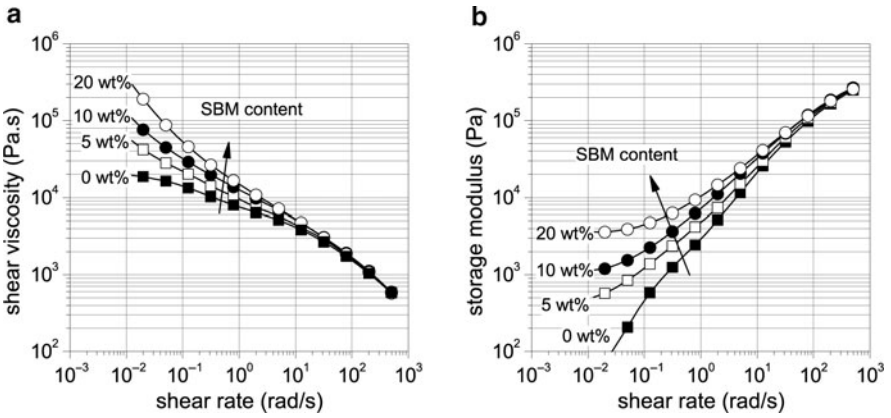

Fig. 32 Shear-rheological behavior at 240°C of (PPE/PS)/SAN blends compatibilized with 0, 5, 10, and 20 wt% SBM. (**a**) Complex viscosity as function of frequency. (**b**) Storage modulus as function of frequency

Table 5 Theoretically calculated solubility of carbon dioxide within the different blend phases of the (PPE/PS)/SAN blend systems compatibilized by SBM

SBM content (wt%)	Solubility in PPE/PS ($mg\,g^{-1}$)	Solubility in SAN/PMMA ($mg\,g^{-1}$)
0	92.5	94.0
5	91.5	94.9
10	90.8	97.0
20	89.1	99.9

observed. At low frequencies the development of a plateau-like regime indicates pseudo-solid behavior and network formation. As no co-continuous morphologies can be detected via transmission electron microscopy, it is likely that the combination of the following two effects leads to the development of a physical network at elevated SBM contents. (1) The SBM at the interphase reduces the mobility and increases the interfacial elasticity due to the intimate entanglement of the end blocks in the respective blend phases. (2) By the decrease of the phase size, the mean distance between the dispersed SAN phase approaches the radius of gyration of the end locks of the block copolymer.

In addition to the blend morphology and the rheological behavior, the gas solubility of the blend phases changes by compatibilization with SBM. As the gas solubility of the individual blend phases is not directly accessible via measurements, theoretical calculations based on the blend phase compositions and on values determined for the miscible PPE/PS and SAN/PMMA blends are presented (Table 5) [75, 77]. Increasing the SBM content results in a decreasing carbon dioxide content in the PPE/PS phase, induced by the higher PS weight fraction. In contrast, the formation of a SAN/PMMA blend by the addition of SBM increases the solubility as result of the high affinity of PMMA to carbon dioxide.

Table 6 Glass transition temperature of (PPE/PS)/SAN blend systems compatibilized by SBM in absence and in presence of carbon dioxide

SBM content (wt%)	Glass transition temperature of PPE/PS (°C)	Glass transition temperature of SAN/PMMA (°C)
0	179 → 78	114 → 32
5	177 → 76	115 → 32
10	174 → 75	116 → 32
20	169 → 73	117 → 32

In order to estimate the plasticizing effect of the blowing agent, the change of the solubility and the glass transition temperature of the respective blend phases by the addition of SBM have to be taken into account. The glass transition temperatures of the PPE/PS and SAN/PMMA phases as function of the SBM as well as the blowing agent content are listed in Table 6. For both phases, concurrent phenomena on the T_g reduction via addition of SBM can be detected. An increasing PS content of the PPE/PS phase reduces the glass transition temperature of this phase, but also lowers the solubility of carbon dioxide. As a result, only minor differences in glass transition temperature of 5°C can be detected between the noncompatibilized and compatibilized blend systems. Similar effects lead to constant glass transition temperature all over the compositional range. Here, the addition of PMMA increases the initial glass transition temperature, but additionally increases the solubility of carbon dioxide.

5.2 Correlation of the Microstructure and Nanostructure to the Foaming Behavior

The cellular structure of the quaternary blend systems after foaming at 180°C for 10 s is highlighted in Fig. 33. An excellent homogeneity down to the microscale can be detected for all foamed blend compositions. As already discussed in the previous section, simultaneous foaming of the PPE/PS and the SAN phase in the noncompatibilized blend leads to a bimodal cell size distribution. Besides larger cells induced by the highly expanded SAN phase, smaller cells are formed in the PPE/PS phase (Fig. 33a).

While the bimodal cell structure is still present for low SBM contents of 5 wt% (Fig. 33b), it vanishes at elevated contents. In parallel, the overall cell size is strongly reduced from 1 µm to several 100 nm (Fig. 33c,d). Similar to the discussed PPE/SAN/SBM blend systems, the interfacial structure developed by the SBM appears highly effective for cell nucleation. Therefore, a dramatic increase in nucleation density can be detected with increasing SBM content (Fig. 34).

As a further feature, an increasing formation of open-cells with increasing SBM content can be detected. As discussed in the literature [24, 26], thin cell walls, appearing by low densities and/or high cell densities, and melt-heterogeneities

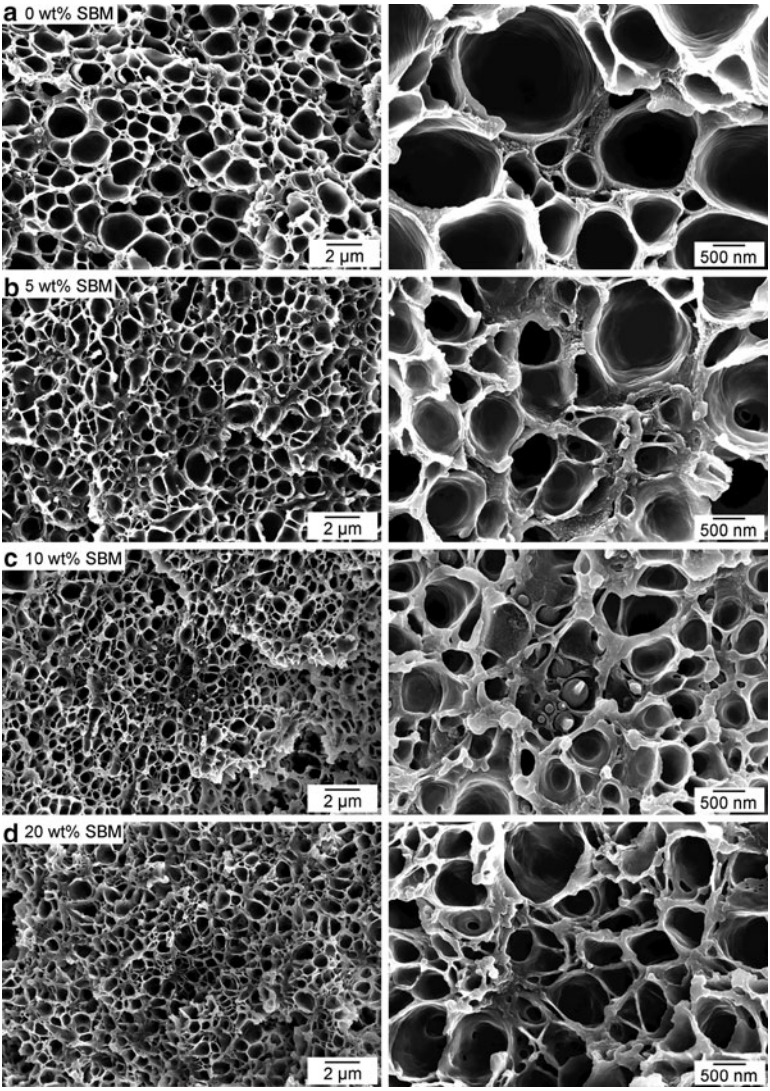

Fig. 33 SEM micrographs of the foam morphology of the (PPE/PS)/SAN blend systems compatibilized with SBM (foaming temperature 180°C, foaming time 10 s)

promote the development of such open-celled foams. As cell nucleation is initiated and cell growth proceeds, the blend system undergoes biaxial stretching. Due to the network-like behavior of the SAN particles, as the mean distance between the dispersed particles is in the range of several ten nanometers, this expansion is strongly hindered. Therefore local failures of the cell walls additionally form an open-cell structure. The cell structure can thus be directly related to the blend morphology as well as to the rheological behavior.

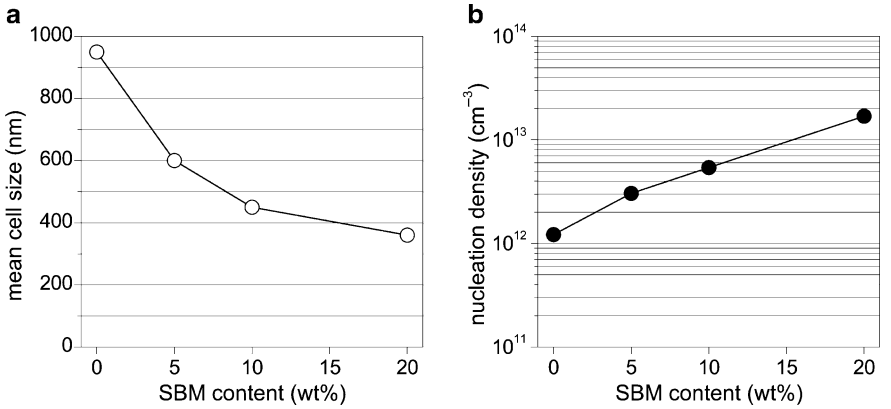

Fig. 34 (**a**) Mean cell size and (**b**) nucleation density as function of the SBM content of the (PPE/PS)/SAN/SBM blend systems (foaming temperature 180°C, foaming time 10 s)

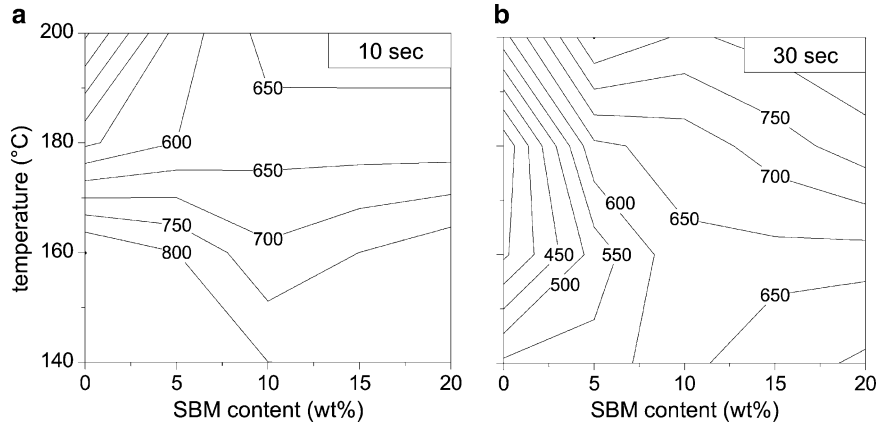

Fig. 35 Foam density of the (PPE/PS)/SAN/SBM blends as function of the foaming temperature and the SBM content. (**a**) Foaming time 10 s. (**b**) Foaming time 30 s

The foam density as function of SBM content and foaming the temperature is highlighted in Fig. 35, showing results at a foaming time of 10 and 30 s. At the shorter foaming time of 10 s, only a minor influence of compatibilization by SBM on the foam density is observed. While a slight decrease in foam density with increasing SBM content can be detected for low temperatures, an increase of the foaming temperature shifts the minimum in foam density to lower SBM contents.

At a foaming time of 30 s, the differences in expansion behavior become more evident. The increase in SBM content leads to an increasing foam density for all foaming temperatures. Besides the previously mentioned reduction of the glass transition temperature of the more viscous PPE phase by the selective blending with PS, subsequently reducing the stabilization effect, the fine blend structure is responsible

for the observed behavior. While a great number of cells is nucleated as result of the micro- and nanostructure, cell rupture and cell coalescence are simultaneously promoted at longer foaming times. As a result, shorter foaming times or lower foaming temperatures are preferable to stabilize the foam structure.

5.3 *Descriptive Foam Model of the Microstructured and Nanostructured Blend Systems*

As previously shown, simultaneous foaming of both PPE and the SAN phase can be achieved by controlling the microstructure, more precisely via selective blending with PS, allowing adjustment of the foaming kinetics of PPE. The compatibilization of the PPE/SAN blends with SBM triblock terpolymers result in a significant reduction of the phase size and an increase in the number of suitable heterogeneous nucleation sites. As a result, the nucleation density of the foamed blend systems is dramatically increased. Additionally, the nanostructured interphase strongly enhances cell nucleation by combining selective blending with PS and, compatibilizing with SBM, the advantages of both approaches can be exploited.

The excellent foamability of the quaternary blend also relates to the microstructure. All selected quaternary blend systems revealed a PPE/PS matrix phase able to stabilize the formed cells, as a result of the higher glass transition temperature and viscosity compared to the dispersed SAN.

A comparison between experimentally observed values of the present thesis and literature data is shown in Fig. 36, summarizing the cell size and the nucleation

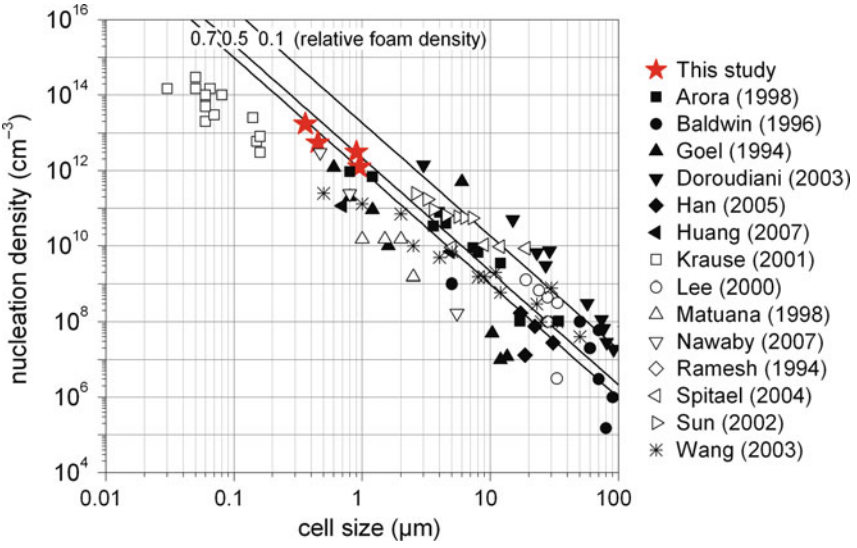

Fig. 36 Cell size and nucleation density as reported in literature, and comparison with the results observed in this study. The *lines* indicate the relative foam density, as theoretically calculated

density of batch-foamed polymers over a broad range. As can be seen, the nucleation density of our foams even exceeds $10^{13}\,cm^{-3}$ leading to cell sizes down to 1 µm, while most other studies reveal significantly lower values in nucleation density. It should be noted that a third parameter, the foam density, is related to both values. As the density of the nonfoamed polymers varies from study to study, the relative foam density as density ratio between the foamed and the neat polymer is selected as an appropriate parameter. Thus, incorporating this interrelated value as a third parameter allows one to verify the quality of the data generally observed in the literature. As can be seen, our data show excellent agreement with theory and reflect the accuracy of our evaluation methods, in contrast to some other studies.

Along with all the advantages, the refined blend structure is more sensitive towards the foaming parameters as foaming temperature and time. The higher number of cells and the elastomeric PB block promote rapid cell coalescence and collapse at elevated foaming temperatures and times. These phenomena can result in an increase in foam density and open-celled or inhomogeneous foam structures.

6 Summary

Controlling the morphology over multiple length scales is regarded as a key factor for the successful development of advanced materials. Tailoring the structure – from macro over micro to nano – allows one to derive materials with superior or even novel properties. In this regard, concepts for developing and foaming micro- and nanostructured polymer blends were established in order to exploit their multiphase characteristics for deriving novel cellular materials. Special emphasis was placed on correlating the blend morphology and the characteristics of the individual phases to the structure of the cellular material.

Even foaming of simple immiscible blends of PPE and SAN turned out to be complex, as a multitude of factors such as the blend morphology, the interfacial properties, and the processing characteristics of each phase need to be considered. For example, the addition of small amounts of PPE to SAN significantly increases the cell density via heterogeneous nucleation activity, which is again controlled by the content and the size of the PPE phase. Depending on the blend composition, the overall foamability, as indicated by the density reduction and the homogeneity of the cell structure, can be strongly deteriorated, as each polymer phase shows a distinct processing window. Such effects become especially evident if the difference in the glass transitional and viscosity behavior between the blend phases is pronounced, e.g., for PPE/SAN blends. While the density reduction of SAN is not influenced by low PPE contents, higher amounts of PPE strongly reduce the foam expansion and homogeneity, in particular close to co-continuity of the blend. In order to overcome these drawbacks, new concepts for enhancing the foamability of such immiscible blends were introduced, using the PPE/SAN 60/40 blend as a reference system.

Melt-compatibilization and nanostructure formation by SBM was identified as a first promising route, significantly enhancing the homogeneity of the foam, and

simultaneously reducing the cell size by heterogeneous nucleation activity at the interface. These effects were related to a refined phase sizes of the blend, an adjusted glass transitional behavior, and an improved adhesion between the blend phases PPE and SAN. In particular, the nanostructured interface between the blend components was identified as an excellent heterogeneous nucleation site, and sub-microcellular and even nanocellular polymeric foams could be derived. However, the density remained rather high due to the absence of cell formation in the highly viscous and high-T_g PPE phase.

In order to overcome this drawback, the concept of selective blending was exploited. Selective blending of PPE with low-viscous PS allowed one to control the microstructure, to refine the phase size, and to adjust the foaming characteristics of the individual phases of PPE/SAN blends. Appropriate blend compositions allowed simultaneous nucleation and cooperative expansion of both phases, generally leading to bimodal cell size distributions in the micron range. Due to cell nucleation and growth in both blend phases, the density could be further reduced when compared to PPE/SAN blends. Moreover, the presence of coalesced foam structure and particularly macroscopic defects could be avoided, and the matrix of the foamed structure was formed by the heat resistant PPE/PS phase.

Finally, both approaches were combined for controlling both the micro- and the nanostructure, for increasing the nucleation density, and promoting simultaneous foaming of quaternary (PPE/PS)/SAN/SBM blends. An excellent foamability was observed, as indicated by nano-sized cells, a remarkable density reduction, and cell densities beyond $10^{13}\,cm^{-3}$. Besides these advantages, the refined blend structure is more sensitive towards processing parameters. The development of polymer foams down to the nanocellular range therefore presents demands not only for establishing suitable material concepts, but also for carefully considering the processing characteristics of these multiphase polymers.

In summary, foaming of blends poses a significant challenge, as the number of influencing and interacting factors increase significantly. Nevertheless, it also provides novel chances to tailor cellular materials, e.g., showing high cell densities, open-celled characteristics, and nanostructured cell walls. The fundamental relationships between the influence of compatibilization and selective blending on the blend characteristics and the foaming behavior demonstrated herein should not only be valid for this particular blend system, but can also help to elucidate the foaming behavior multiphase polymer blends in general and provide guidelines for an appropriate material selection.

7 Perspectives

While the potentials and challenges of foaming multiphase blends were demonstrated for some reference systems, this knowledge now needs to be transferred to other systems and processes, in order to establish general guidelines for foaming polymer blends, all finally aiming at the development of industrial applications and market products.

7.1 Guidelines to Foam Blend Systems

While the foaming behavior of PPE/SAN as well as the effects of compatibilization and selective blending were analyzed in detail, using batch-foaming processing and carbon dioxide as blowing agent, the experience need to be adopted for foaming further blends. These studies should particularly include, but not be limited to, commercially successful blends such as, e.g., PC/ABS, PA/PPE, and PA/ABS. In addition, the transfer to alternative, larger-scale foaming techniques such as foam extrusion and foam injection molding, is highly demanded.

The selection of alternative blowing agents also promises to adjust the foaming behavior of blend systems, which is particularly interesting for multiphase blends. Exploiting the selectivity of the blowing agent, the differences in solubility, diffusivity as well as plasticizing effect of the different phases, they all can contribute to tailor the processing window and foam structure [1, 98–100]. Hydrocarbons, alcohols, and inert gases are promising examples for such blowing agents, which are currently under investigation [1, 98–100]. As an example for the PPE/SAN blend system, selective solubility of *n*-pentane in the more viscous PPE phase can be exploited. As a result, significant density reductions are observed when foaming PPE/SAN blends with an elevated PPE content; in contrast, high SAN contents lead to nonfoamed blends. A similar trend is found for ethanol, due to its low diffusivity and high plasticizing effect in PPE, which allows significant density reductions of PPE/SAN blends with high PPE contents [100].

7.2 Potential Applications of Foamed Blend Systems

Beside the development of new strategies for controlling cellular structure, the potential of foamed blend systems needs to be transferred into industrial applications. As demonstrated, blending allows one to reduce the cell size and to increase the cell density, beneficial for thermal insulation applications, while the mechanical or barrier properties can be improved via multiphase cell walls.

The thermal conductivity of polymer foams is generally composed of four factors: heat conduction by the matrix polymer and the cell gas, heat convection within the cells, and heat irradiation. Regarding standard foams used for insulation in the density range around 15–40 $g\,l^{-1}$ and a cell size of tens of microns; the heat convection can be neglected, while the heat conduction only depends on the foam density. Strategies for further enhancing the thermal barrier properties therefore aim at reducing the contribution of irradiation (e.g., by IR-adsorbing materials such as graphite) or reducing the cell size down to the nanocellular range. Approaching such fine-celled structures, the heat conduction of the cell gas, the most significant factor in the overall heat conduction, is strongly reduced due to the Knudsen effect. The concepts developed in this work allow the formation of such nanocellular structures, identifying efficient nucleation as key criteria. The next steps should aim at verifying the expected low lambda values and at reducing the still rather high density of such systems.

Besides beneficial aspects in terms of reducing the thermal conductivity, foaming of multiphase blends also promises to control the mechanical response and the barrier properties of cellular polymers. The multiphase characteristics of the cell walls can be exploited to set the mechanical properties or to establish cellular barrier materials. For deriving the desired properties of an otherwise weak or highly permeable matrix, the following criteria need to be satisfied. (1) A second phase with significantly higher mechanical properties or a lower permeability towards the gaseous or liquid permeating species is added. (2) As this polymer often shows higher material costs, its content should be reduced to a minimum level. (3) For ensuring a similar processing behavior, the second phase should form the dispersed phase. (4) The dispersed material needs to be incorporated in the cell walls as a highly elongated, platelet-like structure. For this purpose, the elongational behavior, the thermal characteristics and the plasticization effect by the blowing agent need to be carefully adjusted.

Acknowledgments The authors would like to thank all students, technicians, and scientific coworkers contributing to this work, particularly the diploma students Andreas Göldel and Julius Rausch, as well as the lab-technicians Denise Danz and Cornelia Lauble for synthesizing the SBM triblock terpolymers. In addition, BASF SE, Ludwigshafen (Dr. M. Weber), and Mitsubishi Engineering Plastics, Düsseldorf are acknowledged for material support. Financial support by the German Research Foundation (Deutsche Forschungsgemeinschaft, DFG) within the Collaborative Research Center 481 (SFB 481), project A10 is gratefully acknowledged.

References

1. Gendron R (2005) Thermoplastic foam processing. Principles and development. CRC Press, Boca Raton
2. Utracki LA (2002) Polymer blends handbook. Kluwer Academic, New York
3. Paul DR, Bucknall CB (2000) Polymer blends. Wiley, New York
4. Spitael P, Macosko CW (2004) Strain hardening in polypropylenes and its role in extrusion foaming. Polym Eng Sci 44:2090–2100
5. Nam GJ, Yoo JH, Lee JW (2005) Effect of long-chain branches of polypropylene on rheological properties and foam-extrusion performances. J Appl Polym Sci 96:1793–1800
6. Pham HT, Eiffler J (1995) Blend of branched and linear carbonate polymer resin. US Patent 5,414,027
7. Siripurapu S, Gay YJ, Royer JR, DeSimone JM, Spontak RJ, Khan SA (2002) Generation of microcellular foams of PVDF and its blends using supercritical carbon dioxide in a continuous process. Polymer 43:5511–5520
8. Liao X, Nawaby AV, Handa YP (2007) Layered and cellular morphologies in atactic/syndiotactic polystyrene blends. Cell Polym 26:69–81
9. Krause B, Diekmann K, van der Vegt NFA, Wessling M (2002) Open nanoporous morphologies from polymeric blends by carbon dioxide foaming. Macromolecules 35:1738–1745
10. Klempner D, Frisch KC (1999) Handbook of polymeric foams and foam technology. Hanser, Munich
11. Doroudiani S, Park CB, Kortschot MT (1998) Processing and characterization of microcellular foamed high-density polyethylene/isotactic polypropylene blends. Polym Eng Sci 38:1205–1215
12. Huang HX, Wang JK (2007) Improving polypropylene microcellular foaming through blending and the addition of nano-clacium carbonate. J Appl Polym Sci 106:505–513

13. Rachtanapun P, Selke SEM, Matuana LM (2003) Microcellular foam of polymer blends of HDPE/PP and their composites with wood fiber. J Appl Polym Sci 88:2842–2850
14. Zhang P, Zhou NQ, Wu QF, Wang MY, Peng XF (2007) Microcellular foaming of PE/PP blends. J Appl Polym Sci 104:4149–4159
15. Ramesh NS, Rasmussen DH, Campbell GA (1994) The heterogeneous nucleation of microcellular foams assisted by the survival of microvoids in polymers containing low glass-transition particles. 1. Mathematical-modeling and numerical-simulation. Polym Eng Sci 34:1685–1697
16. Ramesh NS, Rasmussen DH, Campbell GA (1994) The heterogeneous nucleation of microcellular foams assisted by the survival of microvoids in polymers containing low glass-transition particles. 2. Experimental results and discussion. Polym Eng Sci 34:1698–1706
17. Campbell GA, Rasmussen DH (1994) Controlling heterogeneous nucleation and growth of foams. US Patent 5,358,675
18. Campbell GA, Rasmussen DH (1994) Controlling heterogeneous nucleation and growth of foams. US Patent 5,369,135
19. Spitael P, Macosko CW, McClurg RB (2004) Block copolymer micelles for nucleation of microcellular thermoplastic foams. Macromolecules 37:6874–6882
20. Han XM, Lee LJ, Tomasko DL (2005) CO_2 foaming of polymer nanocomposite blends. Aust J Chem 58:492–503
21. Han XM, Shen J, Huang HX, Tomasko DL, Lee LJ (2007) CO2 foaming based on polystyrene/poly(methyl methacrylate) blend and nanoclay. Polym Eng Sci 47:103–111
22. Rogers J-V, Kisner RD (1993) Ultra low density polyolefin foam, foamable polyolefin compositions and process for making same. US Patent 5,290,822
23. Smith PJ, Cross BJ (1996) Foamed articles of styrenic and acrylic polymers blend. US Patent 6,063,485
24. Park CB, Padareva V, Lee PC, Naguib HE (2005) Extruded open-celled LDPE-based foams using non-homogeneous melt structure. J Polym Eng 25:239–260
25. Wong CM, Tsai SJ, Ying CH, Hung ML (2006) Effect of low density polyethylene on polystyrene foam. J Cell Plast 42:153–163
26. Lee H, Mall S, He P, Shi DL, Narasimhadevara S, Yeo-Heung Y, Shanov V, Schulz MJ (2007) Characterization of carbon nanotube/nanofiber-reinforced polymer composites using an instrumented indentation technique. Composites Part B 38:58–65
27. Tashiro H, Naito H, Takayama M, Yoshimura I (1983) Fluid transmitting polyolefin foams and method of making the same. US Patent 4,384,032
28. Barry JJA, Nazhat SN, Rose FRAJ, Hainsworth AH, Scotchford CA, Howdle SM (2005) Supercritical carbon dioxide foaming of elastomer/heterocyclic methacrylate blends as scaffolds for tissue engineering. J Mater Chem 15:4881–4888
29. Reichelt N, Stadlbauer M, Folland R, Park CB, Wang J (2003) PP-blends with tailored foamability and mechanical properties. Cell Polym 22:315–327
30. Diaf A, Enick RM, Beckman EJ (1993) Molecular redesign of expanded polystyrene to allow use of carbon-dioxide as a foaming agent. 1. Reversible binding of CO2. J Appl Sci 50:835–844
31. Sarbu T, Styranec TJ, Beckman EJ (2000) Design and synthesis of low cost, sustainable CO2-philes. Ind Eng Chem Res 39:4678–4683
32. Vachon C, Tatibouet J (2004) Effect of additives on the solubility and diffusivity of carbon dioxide in polystyrene. Antec
33. Sun HL, Mark JE, Tan SC, Venkatasubramanian N, Houtz MD, Arnold FE, Lee CYC (2005) Microcellular foams from some high-performance composites. Polymer 46:6623–6632
34. Tan SC, Bai Z, Sun H, Mark JE, Arnold FE, Lee CYC (2003) Processing of microcellular foams from polybenzobisthiazole/polyetherketoneketone molecular composites. J Mater Sci 38:4013–4019
35. Takeda N (1989) Foams of polyolefin/polystyrene resin mixture. US Patent 4,847,150
36. Park CB, Baldwin DF, Suh NP (1995) Effect of the pressure drip rate on cell nucleation in continuous processing of microcellular polymers. Polym Eng Sci 35:432–440

37. Sahagun CZ, Gonzalez-Nunez R, Rodrigue D (2006) Morphology of extruded PP/HDPE foam blends. J Cell Plast 42:469–485
38. Wollecke F (2005) Korrelation dehnrheologischer Kenngrößen mit dem Schäumverhalten von Polymeren, University of Bayreuth, ISBN 3–930400–35–9
39. Werner P, Verdejo R, Wöllecke F, Altstädt V, Sandler JKW, Shaffer MSP (2005) Carbon nanofibers allow foaming of semicrystalline poly(ether ether ketone). Adv Mater 17:2864–2869
40. Nam PH, Maiti P, Okamoto M, Kotaka T, Nakayama T, Takada M, Ohshima M, Usuki A, Hasegawa N, Okamoto H (2002) Foam processing and cellular structure of polypropylene/clay nanocomposites. Polym Eng Sci 42:1907–1918
41. Kressler J, Kammer HW (1987) Miscibility behavior of poly(2,6-dimethylphenylene oxide) and poly(styrene-co-acrylonitrile). Acta Polym 38: 600–602
42. Merfeld GD, Karim A, Majumdar B, Satija SK, Paul DR (1998) Interfacial thickness in bilayers of poly(phenylene oxide) and styrenic copolymers. J Polym Sci B Polym Phys 36:3115–3125
43. Potente H, Bastian M, Bergemann K, Senge M, Scheel G, Winkelmann T (2001) Morphology of polymer blends in the melting section of co-rotating twin screw extruders. Polym Eng Sci 41:222–231
44. Sundararaj U, Macosko CW (1995) Drop breakup and coalescence in polymer blends – the effect of concentration and compatibilization. Macromolecules 28:2647–2657
45. Ruckdäschel H, Sandler JKW, Altstädt V, Rettig C, Schmalz H, Abetz V, Müller AHE (2006) Compatibilization of PPE/SAN blends by triblock terpolymers: correlation between block terpolymer composition, morphology and properties. Polymer 47:2772–2790
46. Utracki LA (1991) On the viscosity-concentration dependence of immiscible polymer blends. J Rheol 35:1615–1637
47. Ruckdäschel H, Rausch J, Sandler JKW, Altstädt V, Schmalz H, Müller AHE (2008) Correlation of the melt rheological properties with the foaming behavior of immiscible blends of poly(2,6-dimethyl-1,4-phenylene ether) and poly(styrene-co-acrylonitrile). Polym Eng Sci 48:2111–2125
48. Le Meins JF, Moldenaers P, Mewis J (2002) Suspensions in polymer melts. 1. Effect of particle size on the shear flow behavior. Ind Eng Chem Res 41:6297–6304
49. Le Meins JF, Moldenaers P, Mewis J (2003) Suspensions of monodisperse spheres in polymer melts: particle size effects in extensional flow. Rheol Acta 42:184–190
50. Van Puyvelde P, Velankar S, Moldenaers P (2001) Rheology and morphology of compatibilized polymer blends. Curr Opin Colloid Interface Sci 6:457–463
51. Krishnamoorti R, Giannelis EP (1997) Rheology of end-tethered polymer layered silicate nanocomposites. Macromolecules 30:4097–4102
52. Jiang L, Lam YC, Tam KC, Chua TH, Sim GW, Ang LS (2005) Strengthening acrylonitrile-butadiene-styrene (ABS) with nano-sized and micron-sized calcium carbonate. Polymer 46:243–252
53. Wu G, Asai S, Sumita M, Hattori T, Higuchi R, Washiyama J (2000) Estimation of flocculation structure in filled polymer composites by dynamic rheological measurements. Colloid Polym Sci 278:220–228
54. Chern RT, Sheu FR, Jia L, Stannett VT, Hopfenberg HB (1987) Transport of gases in unmodified and arylbrominated 2,6-dimethyl-1,4-poly (phenylene oxide). J Membr Sci 35:103–115
55. Nawaby AV, Handa YP, Liao X, Yoshitaka Y, Tomohiro M (2007) Polymer-CO2 systems exhibiting retrograde behavior and formation of nanofoams. Polym Int 56:67–73
56. Lee ST (2000) Foam extrusion. Principles and practice. Technomic Publishing Company, Lancaster
57. Wagner MH, Bernnat A, Schulze V (1998) The rheology of the rheotens test. J Rheol 42: 917–928
58. McInerney LF, Kao N, Bhattacharya SN (2003) Melt strength and extensibility of talc-filled polypropylene. Polym Eng Sci 43:1821–1829
59. Krieger IM (1963) A dimensional approach to colloid rheology. Trans Soc Rheol 7:101–109

60. Seong DG, Kang TJ, Youn JR (2005) Rheological characterization of polymer-based nanocomposites with different nanoscale dispersions. e-Polymers 5
61. Milner ST, Xi HW (1996) How copolymers promote mixing of immiscible homopolymers. J Rheol 40:663–687
62. Creton C, Kramer EJ, Hadziioannou G (1991) Critical molecular-weight for block copolymer reinforcement of interfaces in a 2-phase polymer blend. Macromolecules 24:1846–1853
63. Creton C, Kramer EJ, Hui CY, Brown HR (1992) Failure mechanisms of polymer interfaces reinforced with block copolymers. Macromolecules 25:3075–3088
64. Gottschalk A, Muhlbach K, Seitz F, Stadler R, Auschra C (1994) Blends of poly(2,6-dimethyl-1,4-phenylene oxide) with styrene copolymers. Macromol Symp 83:127–146
65. Auschra C, Stadler R (1993) New ordered morphologies in ABC triblock copolymers. Macromolecules 26:2171–2174
66. Auschra C, Stadler R (1993) Thermal-stability of poly(styrene-b-methyl methacrylate) and poly(styrene-b-ethylene-co-1-butene-b-methyl methacrylate) – a gel-permation. Polym Bull 30:305–311
67. Brown HR, Krappe U, Stadler R (1996) Effect of ABC triblock copolymers with an elastomeric midblock on the adhesion between immiscible polymers. Macromolecules 29:6582–6588
68. Auschra C, Stadler R (1993) Polymer alloys based on poly(2,6-dimethyl-1,4-phenylene ether) and poly(styrene-*co*-acrylonitrile) using poly(styrene-*b*-(ethylene-*co*-butylene)-*b*-methyl methacrylate) triblock copolymers as compatibilizers. Macromolecules 26:6364–6377
69. Ruckdäschel H, Sandler JKW, Altstädt V, Schmalz H, Abetz V, Müller AHE (2007) Toughening of immiscible PPE/SAN blends by triblock terpolymers. Polymer 48:2700–2719
70. Ruckdäschel H, Gutmann P, Altstädt V, Schmalz H, Müller AHE. Cellular polymer blends with nanostructured cell walls. Macromolecules, submitted
71. Quintens D, Groeninckx G, Guest M, Aerts L (1991) Viscoelastic properties related to the phase morphology of 60/40 Pc/San blend. Polym Eng Sci 31:1207–1214
72. Van Krevelen DW (1976) Properties of polymers. Elsevier, Amsterdam
73. Ruckdäschel H, Rausch J, Sandler JKW, Altstädt V, Schmalz H, Müller AHE (2007) Foaming of miscible and immiscible polymer blends. Mater Res Soc Symp Proc 977
74. Chiou JS, Paul DR (1987) Gas permeation in miscible homopolymer copolymer blends. 1.Poly(methyl methacrylate) and styrene acrylonitrile copolymers. J Appl Polym Sci 34:1037–1056
75. Chow TS (1980) Macromolecular interpretation of the glass-transition temperature of polymer-diluent systems. Macromolecules 13:362–364
76. Suess M, Kressler J, Kammer HW (1987) The miscibility window of poly(methyl methacrylate) poly(styrene-co-acrylonitrile) blends. Polymer 28:957–960
77. Couchman PR (1987) Thermodynamics and the compositional variation of glass-transition temperatures. Macromolecules 11:1156–1161
78. Taki K, Nitta K, Kihara S, Ohshima M (2005) CO2 foaming of poly(ethylene glycol)/polystyrene blends: relationship of the blend morphology, CO2 mass transfer, and cellular structure. J Appl Polym Sci 97:1899–1906
79. Shen J, Han XM, Lee LJ (2006) Nanoscaled reinforcement of polystyrene foams using carbon nanofibers. J Cell Plast 42:105–126
80. Colton JS, Suh NP (1987) The nucleation of microcellular thermoplastic foam with additives.1. Theoretical considerations. Polym Eng Sci 27:485–492
81. Tomasko DL, Han XM, Liu DH, Gao WH (2003) Supercritical fluid applications in polymer nanocomposites. Curr Opin Solid State Mater Sci 7:407–412
82. Tomasko DL, Li HB, Liu DH, Han XM, Wingert MJ, Lee LJ, Koelling KW (2003) A review of CO2 applications in the processing of polymers. Ind Eng Chem Res 42:6431–6456
83. Grace HP (1982) Dispersion phenomena in high-viscosity immiscible fluid systems and application of static mixers as dispersion devices in such systems. Chem Eng Commun 14:225–277
84. Ruckdäschel H, Altstädt V, Müller AHE (2007) Foaming of polymer blends – chance and challenge. Cell Polym 26:367–380

85. Kolarik J, Lednicky F, Locati G, Fambri L (1997) Ultimate properties of polycarbonate blends: effects of inclusion plastic deformation and of matrix phase continuity. Polym Eng Sci 37:128–137
86. Harrats C, Thomas S, Groeninckx G (ed) Micro- and nanostructured multiphase polymer blend systems: phase morphology and interfaces. CRC Press, Boca Raton
87. Steinmann S, Gronski W, Friedrich C (2001) Cocontinuous polymer blends: influence of viscosity and elasticity ratios of the constituent polymers on phase inversion. Polymer 42:6619–6629
88. Marin N, Favis BD (2002) Co-continuous morphology development in partially miscible PMMA/PC blends. Polymer 43:4723–4731
89. Pötschke P, Paul DR (2003) Formation of co-continuous structures in melt-mixed immiscible polymer blends. J Macromol Sci Polym Rev C43:87–141
90. Willemse RC (1999) Co-continuous morphologies in polymer blends: stability. Polymer 40:2175–2178
91. Tol RT, Groeninckx G, Vinckier I, Moldenaers P, Mewis J (2004) Phase morphology and stability of co-continuous (PPE/PS)/PA6 and PS/PA6 blends: effect of rheology and reactive compatibilization. Polymer 45:2587–2601
92. Everaert V, Aerts L, Groeninckx G (1999) Phase morphology development in immiscible PP/(PS/PPE) blends influence of the melt-viscosity ratio and blend composition. Polymer 40:6627–6644
93. Göldel A, Ruckdäschel H, Müller AHE, Pötschke P, Altstädt V (2008) Controlling the phase morphology of immiscible poly(2,6-dimethyl-1,4-phenylene ether)/poly(styrene-co-acrylonitrile) blends via addition of polystyrene. e-Polymers 151
94. Gutmann P, Ruckdäschel H, Bangarusampath DS, Altstädt V, Schmalz H, Müller AHE (2009) Influence of the microstructure on the foaming behavior of an immiscible blend system. Antec
95. Palierne JF (1990) Linear rheology of viscoelastic emulsions with interfacial-tension. Rheol Acta 29:204–214
96. Pötschke P, Fornes TD, Paul DR. (2002) Rheological behavior of multiwalled carbon nanotube/polycarbonate composites. Polymer 43:3247–3255
97. Abdel-Goad M, Pötschke P (2005) Rheological characterization of melt processed polycarbonate-multiwalled carbon nanotube composites. J Non-Newtonian Fluid Mech 128:2–6
98. Daigneault LE, Gendron R (2001) Blends of CO2 and 2-ethyl hexanol as replacement foaming agents for extruded polystyrene. J Cell Plast 37:262–272
99. Gendron R, Champagne MF, Delaviz Y, Polasky ME (2006) Foaming polystyrene with a mixture of CO2 and ethanol. J Cell Plast 42:127–138
100. Gutmann P, Hildebrandt K, Altstädt V, Müller AHE (2009) Foaming of an immiscible blend system using organic liquids as blowing agents. Rapra

Index